UNIVERSITY OF Southampton

University of Southampton Research Repository
ePrints Soton

Copyright © and Moral Rights for this thesis are retained by the author and/or other copyright owners. A copy can be downloaded for personal non-commercial research or study, without prior permission or charge. This thesis cannot be reproduced or quoted extensively from without first obtaining permission in writing from the copyright holder/s. The content must not be changed in any way or sold commercially in any format or medium without the formal permission of the copyright holders.

When referring to this work, full bibliographic details including the author, title, awarding institution and date of the thesis must be given e.g.

AUTHOR (year of submission) "Full thesis title", University of Southampton, name of the University School or Department, PhD Thesis, pagination

http://eprints.soton.ac.uk

UNIVERSITY OF SOUTHAMPTON

# Sound Radiation from Perforated Plates

by

Azma Putra

Thesis submitted for the degree of

Doctor of Philosophy

Faculty of Engineering, Science and Mathematics

Institute of Sound and Vibration Research

June 2008

UNIVERSITY OF SOUTHAMPTON

ABSTRACT

FACULTY OF ENGINEERING, SCIENCE AND MATHEMATICS

INSTITUTE OF SOUND AND VIBRATION RESEARCH

Doctor of Philosophy

# SOUND RADIATION FROM PERFORATED PLATES

by Azma Putra

Perforated plates are quite often used as a means of engineering noise control to reduce the sound radiated by structures. However, there appears to be a lack of representative models to determine the sound radiation from a perforated plate. The aim of this thesis is to develop such a model that can be used to give quantitative guidance corresponding to the design and effectiveness of this noise control measure.

Following an assessment of various models for the radiation efficiency of an unbaffled plate, Laulagnet's model is implemented. Results are calculated and compared with those for baffled plates. From this, simple empirical formulae are developed and give a very good agreement with the analytical result. Laulagnet's model is then modified to include the effect of perforation in terms of a continuously distributed surface impedance to represent the holes. This produces a model for the sound radiation from a perforated unbaffled plate. It is found that the radiation efficiency reduces as the perforation ratio increases or as the hole size reduces. An approximate formula for the effect of perforation is proposed which shows a good agreement with the analytical calculation up to half the critical frequency. This could be used for an engineering application to predict the noise reduction due to perforation.

The calculation for guided-guided boundary conditions shows that the radiation efficiency of an unbaffled plate is not sensitive to the edge conditions. It is also shown that perforation changes the plate bending stiffness and mass and hence increases the plate vibration.

The situation is also considered in which a perforated unbaffled plate is located close to a reflecting rigid surface. This is established by modifying the Green's function in the perforated unbaffled model to include an imaginary source to represent the reflected sound. The result shows that the presence of the rigid surface reduces the radiation efficiency at low frequencies.

The limitation of the assumption of a continuous acoustic impedance is investigated using a model of discrete sources. The perforated plate is discretised into elementary sources representing the plate and also the holes. It is found that the uniform surface impedance is only valid if the hole distance is less than an acoustic wavelength for a vibrating rectangular piston and less than half an acoustic wavelength for a rectangular plate in bending vibration. Otherwise, the array of holes is no longer effective to reduce the sound radiation.

Experimental validation is conducted using a reciprocity technique. A good agreement is achieved between the measured results and the theoretical calculation for both the unbaffled perforated plate and the perforated plate near a rigid surface.

# Acknowledgements

*In the Name of God, The Beneficent, The Merciful*

First and foremost, I would like to give sincere tribute to my supervisor, Prof. David Thompson for his guidance and excellent supervision in this research. He provided me motivation and optimism throughout the three years. And also for the generous funding for my first year, which was a first entrance door to my Ph.D study.

I would like also to thank Prof. Frank Fahy for his input to improve the thesis. My work was also made easier with the help from Dr. Anand Thite throughout my experimental work for useful discussions and particularly for teaching me to use the Laser vibrometer.

My appreciation is also addressed to Institute of Sound and Vibration Research (ISVR) for its Rayleigh Scholarship for the second and third year funding. I am proud to be in the ISVR for its excellent environment of study and research. My colleagues in the Dynamics Group also gave a great atmosphere. My Malaysian and Indonesian friends for their warmth of friendship and kindness during my life in the UK of which their names are too numerous to mention.

I wish to express my gratitude to my parents, Abdul Aziz and Maymunah Yatim, for their unlimited love. It is because of their prayer that I have become of what I am. Also for my parents in law, Irawan Yunus and Adawiyah, for their sincere kindness.

Finally but most importantly, for my beloved wife, Amelia, to whom this work is lovingly dedicated. Her unconditional love, support, encouragement and sacrifices have given me a peaceful heart during my study. And also for her gifts from heaven, Faiz Ahmad and Zaid Umar Durrani, who have cheered up my days.

*Read! And your Lord is the Most Bounteous.*
*Who teaches by the pen, Teaches man that which he knew not (Al-Quran: 96, v.3–5).*

# Contents

# Abbreviations

| | |
|---|---|
| EoP | Effect of perforation |
| DFT | Discrete Fourier Transform |
| FFT | Fast Fourier Transform |
| MOF | Modal overlap factor |
| RMSE | Root mean square error |
| SPL | Sound pressure level |
| XLE | Perpendicular ligament efficiency |
| YLE | Parallel ligament efficiency |

# Nomenclature

| | |
|---|---|
| $a$ | Length of plate |
| $a_Q$ | Acceleration due to acoustic excitation from volume velocity $Q$ |
| $b$ | Width of plate |
| $b_x$ | Distance between holes |
| $B$ | Bending stiffness |
| $c$ | Speed of sound |
| $c_L$ | Longitudinal wave speed of plate |
| $c_p$ | Transverse wave speed of plate |
| $C_{pqmn}$ | Acoustic cross-modal coupling terms |
| $d_o$ | Diameter of hole |
| $d_{mn}$ | Modal displacement amplitude |
| $D$ | Distance of plate from a rigid surface |
| $E$ | Young's modulus |
| $E^*$ | Effective Young's modulus of perforated plate |
| $f$ | Frequency |
| $f_c$ | Critical frequency |
| $f_e$ | Starting frequency for edge mode region |
| $f_s$ | Schroeder cross-over frequency |
| $F$ | Excitation force |
| $F_{mn}$ | Modal excitation force |
| $\mathscr{F}^{-1}$ | Inverse Fourier transform |
| $\overline{F^2}$ | Mean-square force |
| $G$ | Green's function |
| $\widetilde{G}$ | Fourier transform of Green's function |
| $h$ | Non-dimensional specific acoustic reactance |
| $h_c$ | Non-dimensional specific acoustic reactance at critical frequency |

| | |
|---|---|
| $j = \sqrt{-1}$ | Imaginary unit |
| $k$ | Acoustic wavenumber |
| $k_{mn}$ | Modal wavenumber or bending wavenumber |
| $k_x, k_y, k_z$ | Wavenumber vector components in $x$,$y$,$z$ directions |
| $m_p$ | Mass per unit area of plate |
| $(m, n)$ | Index of mode order; $m, n = 1, 2, 3, ...$ |
| $M_{mn}$ | Modal mass of plate |
| $M$ | Mass of plate |
| $[\mathbf{M}]$ | Matrix of acoustic impedance |
| $n(\omega)$ | Modal density |
| $N_o$ | Number of holes |
| $p, p_a, p_c$ | Acoustic pressure |
| $\left\langle \overline{p^2} \right\rangle$ | Spatially averaged mean-square pressure |
| $\widetilde{P}$ | Fourier transform of acoustic pressure |
| $P_s$ | Perimeter of plate |
| $Q$ | Volume velocity |
| $r_o$ | Radius of hole |
| $R_r$ | Radiation resistance |
| $R$ | Distance from origin to observation point |
| $R'$ | Distance from source to observation point |
| $S, S_p$ | Area of plate surface |
| $t$ | Time |
| $t_p$ | Thickness of plate |
| $T_{60}$ | Reverberation time |
| $u_{mn}$ | Complex modal velocity amplitude |
| $U_n$, $U_o$, $U_f$, $U_p$ | Uniform velocity (piston motion) |
| $v$ | Normal velocity of plate |
| $v_f$ | Velocity of fluid through hole |
| $V_R$ | Volume of reverberant room |
| $\langle \lvert v \rvert^2 \rangle$ | Spatially averaged squared velocity |
| $\widetilde{V}$ | Fourier transform of velocity |
| $w$ | Normal displacement of plate |
| $W$ | Sound power |

| | |
|---|---|
| $W_{mn}$ | Modal sound power |
| $Y_t$ | Transfer mobility |
| $Y_p$ | Point mobility |
| $\langle \lvert Y_t \rvert^2 \rangle$ | Spatially averaged squared modulus of transfer mobility |
| $z_a$ | Specific acoustic impedance of air |
| $z_h$ | Specific acoustic impedance of hole |
| $Z_h$ | Acoustic impedance of hole |
| $Z_{h,R}$ | Real part of the acoustic impedance of hole |
| $Z_{h,I}$ | Imaginary part of the acoustic impedance of hole |
| $\alpha, \beta$ | Non-dimensional wavenumber vector components in $(x, y)$ directions |
| $\rho$ | Density of air |
| $\rho_p$ | Density of plate material |
| $\rho_p^*$ | Effective density of perforated plate |
| $\eta$ | Damping loss factor |
| $\omega$ | Angular frequency |
| $\omega_{mn}$ | Natural frequency of mode $(m, n)$ |
| $\omega_{mn}^*$ | Natural frequency of mode $(m, n)$ for effective material properties |
| $\sigma$ | Radiation efficiency |
| $\sigma_{mn}$ | Modal radiation efficiency |
| $\tau$ | Perforation ratio |
| $\nu$ | Poisson's ratio |
| $\nu^*$ | Effective Poisson's ratio of perforated plate |
| $\nu_a$ | Viscosity of air |
| $\lambda$ | Acoustic wavelength |
| $\lambda_s$ | Schroeder cross-over wavelength |
| $\varphi_{mn}$ | Mode shape function |

# Chapter 1

# Introduction

## 1.1 Background

Noise exposure of workers, particularly in industry, is one of the major health and safety problems which must be taken seriously. Long-term exposure at certain noise levels, can lead to hearing impairment, hypertension, ischemic heart disease, annoyance and sleep disturbance [1]. For example, a person who is exposed to noise exceeding 85 dB(A) in an average over a working day of 8 hours ($L_{Aeq,8h}$) for a long period of time can suffer a permanent hearing loss [2]. Noise exposure can also create stress, increase workplace accident rates, and stimulate aggression and other anti-social behaviour [3]. Due to these serious effects, the management and control of noise levels, especially in the workplace is the subject of legislation.

The majority of industrial noise sources come from vibrating structures. The accurate prediction of sound radiation from such structures remains a challenging problem. Many structures can be presented in terms of an assemblage of flat plates, for example machinery casings, car body shells, hulls of ships, walls and floors. By reducing the complexity of such structures by approximating them as simple structures like plates, the mechanism of sound radiation can then be modelled considerably more easily by using analytical or numerical approaches. The study of an isolated plate provides the basic understanding of the interaction between the flexural vibration behaviour of a structure and its sound radiation. From this, in many cases, the determination of sound radiation from more complex structures can be estimated reasonably accurately [4].

The sound radiation from a structure is often defined in a dimensionless form known as the radiation efficiency or radiation ratio. Because of its importance throughout the thesis, this is introduced here. The radiation efficiency is the ratio of the acoustic power radiated by a vibrating surface to that produced in an equivalent idealised situation as a function of frequency. This idealised situation can be visualised as follows. When an infinite flat surface vibrates at harmonic frequency $\omega$ with a uniform amplitude and phase where the surface wave speed $c_p$ is greater than the speed of sound in the fluid $c$, it produces plane waves in the acoustic medium. In such a situation, the sound power $W_o$ radiated per unit area is

$$\frac{W_o}{S} = \frac{1}{2}\rho c \left|v\right|^2 \tag{1.1}$$

where $\rho$ is the density of medium enclosing the structure, $S$ is the surface area of the structure and $v$ is the surface velocity amplitude.

The radiation efficiency indicates how much sound power $W$ a given structure radiates compared with the vibrating infinite flat surface for the same area. The radiation efficiency is thus given by [4, 5, 6, 7, 8]

$$\sigma = \frac{W}{W_o} = \frac{W}{\frac{1}{2}\rho c S \left\langle \left|v\right|^2 \right\rangle} \tag{1.2}$$

where $\langle \cdots \rangle$ denotes a spatial average and $v$ is the amplitude of the velocity normal to the surface of the structure. The radiation resistance $R_r$ can be defined as

$$R_r = \rho c S \sigma = \frac{W}{\frac{1}{2}\left\langle \left|v\right|^2 \right\rangle} \tag{1.3}$$

These definitions are often written in terms of the 'mean-square' velocity (over time) in a frequency band in place of $\frac{1}{2}\left|v\right|^2$.

The radiation efficiency depends on the size and shape of the structure and on the distribution of vibration over the surface. Usually at low frequencies the radiation efficiency is very small ($\sigma \ll 1$) but at high frequencies it tends to unity [4]. For relatively simple sources, the radiation efficiency can be determined by analytical models while for more complex structures numerical approaches can be used. In the next section, literature on sound radiation, particularly from plates, is reviewed.

## 1.2 Literature review

### 1.2.1 Analytical models

#### 1.2.1.1 Baffled plate models

A simplified model of the sound radiation from a plate can be made by assuming the source is flat and set in an infinite rigid baffle. If the velocity distribution of the plate is known, and the velocity is assumed to be zero on the baffle, the radiated sound field can be calculated by a Rayleigh integral approach [9]. The sound power can be found either by integrating the far field acoustic intensity over a hemisphere enclosing the plate or by integrating the normal component of the acoustic intensity over the surface of the vibrating plate. A detailed knowledge of the magnitude and phase distribution at each frequency of the vibration velocity is required in both approaches. Since the modes of a plate with simply supported boundaries can readily be determined analytically, such boundaries are often assumed in order to simplify the velocity field.

Many papers have been produced concerning the sound radiation from a baffled plate. Maidanik [5] determined the radiation resistance of a baffled plate for a broadband excitation in terms of a frequency band average. It was assumed that the resonant modes within a frequency band have equal vibrational energies. Several approximate formulae were proposed for calculating the radiation resistance over the whole frequency range. Figure 1.1 from [10] shows a graph based on Maidanik's formulae.

The curve begins with the slope of 6 dB/octave or 20 dB/decade at very low frequency known as the fundamental mode region of the plate. The flat region followed by the increasing trend in the curve up to the critical frequency $f_c$ are the short circuit cancellation regions which will be explained in more detail in Chapter 2. The critical frequency is the frequency at which the speed of sound in the fluid is equal to the wave speed of flexural waves in the plate. Above this frequency is the supersonic region where the plate wave speed is greater than the speed of sound.

Leppington *et al.* [11] found that near the critical frequency, Maidanik's prediction overestimates the radiation resistance by a factor of about 2, for a large plate aspect ratio. An alternative asymptotic formula at the critical frequency was therefore

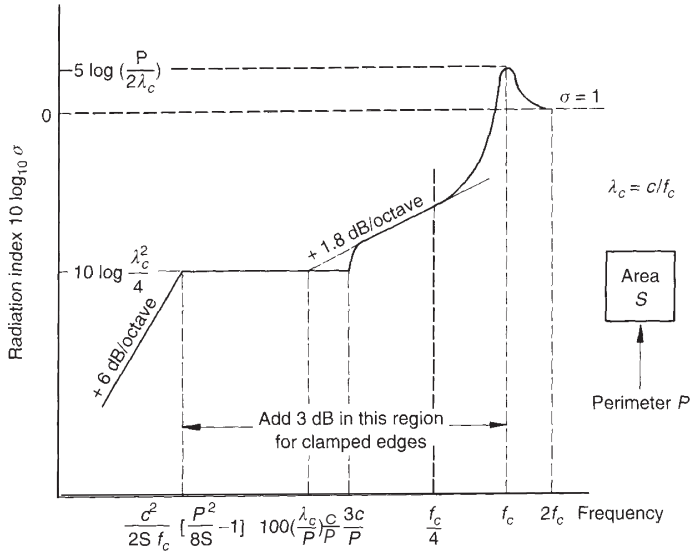


FIGURE 1.1: Theoretical modal average radiation efficiency of a baffled rectangular plate [10].

proposed.

Wallace [6] studied the radiation efficiency of a finite, simply supported rectangular plate in an infinite baffle. The radiation efficiency was determined for individual modes using a Rayleigh integral to calculate the total energy radiated to the farfield. Asymptotic solutions for low frequencies were also presented. Figure 1.2 shows example radiation efficiency results from Wallace [6] for several low and high order modes. For each mode $(m, n)$ results are plotted against $\gamma = k/k_{mn}$ where $k$ is the acoustic wavenumber and $k_{mn}$ is the plate bending wavenumber. The results from Wallace were used by Xie *et al.* [12] to form a summation over the contributions of individual modes. This was used to obtain the radiation efficiency in forced vibration. It was found that using an average over many uncorrelated force point locations, the cross-modal coupling terms average to zero.

Bonilha and Fahy [13] also proposed a model of sound radiation from a baffled flat plate in multi-modal response. It was assumed that the modal density of a plate is sufficiently large for there to be a considerable number of resonant modes of vibration within a frequency band of analysis. The model gave a good agreement with Leppington's numerical estimate [14] except at low frequencies.

A restrained edge plate, e.g. clamped plate, was also studied by several authors [15, 16, 17]. Maidanik [15] found that the radiation efficiency of a clamped plate is 3 dB greater than that of a simply supported plate for frequencies up to half the critical

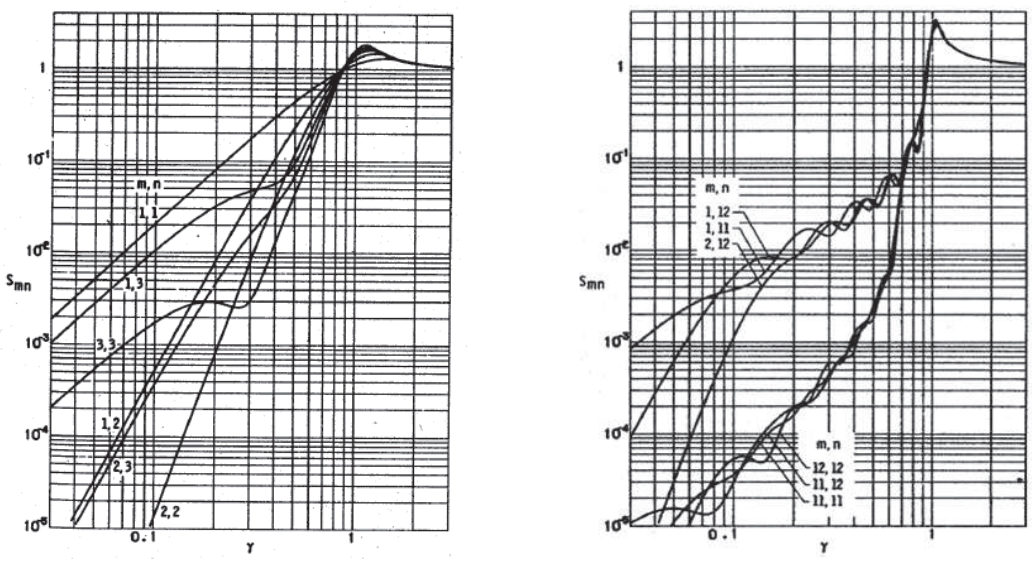


(a) (b)

FIGURE 1.2: Radiation efficiency from Wallace [6] for: (a) low modes and (b) high modes of a rectangular plate.

frequency. The prediction was validated by the measurement of radiation efficiency of a gypsum board nailed in wooden frame which gave good agreement. Leppington *et al.* [16] also suggested that for a clamped plate, a correction of roughly 3 dB should be applied to the estimate for a simply supported plate below the critical frequency.

Gompert [18] used the flexural modes of uniform beams to derive expressions for the sound radiation from a rectangular plate. The radiation efficiency formulae were developed for general boundary conditions but only where the plate has the same edge conditions on both sides. Gompert [19] then proposed an extended model for two-dimensional radiation problems for five different ideal boundary conditions ranging from free to restrained edges. Simple approximation formulae for low frequencies were also given. It was found that below the resonance frequency, a guided-guided plate has a lower radiation efficiency than that of a simply supported plate. It was also found that a plate with simply supported-clamped edges (or vice versa) has almost the same radiation efficiency (difference $< 1$ dB) as a simply supported plate.

A formulation for general boundary conditions was also proposed by Berry *et al.* [20]. A Rayleigh-Ritz method was used by selecting a family of trial functions satisfying the geometry of the boundary conditions. Later in [21] it was found that only one set of trial functions was required to represent the plate displacement. Berry *et al.* [20] found

that in low-order modes up to the mode (2,2), the simply supported plate has a slightly higher radiation efficiency than that of the clamped plate. For all other modes, the opposite situation applies with a maximum factor of 2.5 (4 dB). The radiation efficiency for multi-modal responses for a single forcing location was also calculated up to 3 kHz. In an average sense, the radiation efficiency level was found to be almost equal for the clamped and simply supported plates, apart from the antisymmetric resonances appearing for the two cases. The same phenomenon was also found between the cases of guided-guided and free-free edges.

Williams and Maynard [22] used a scheme based on the Fast Fourier transform (FFT) to calculate the radiation from a baffled plate. Rayleigh's integral formula was evaluated numerically for baffled planar radiators, with specified velocity in the source plane using the FFT algorithm. Bias errors appearing using this technique were also described. Williams [23] also proposed a series expansion technique of the acoustic power radiated from planar sources. A Maclaurin expansion of the Fourier transform of the velocity was used to calculate the first few terms of the acoustic power. This was later used by Li [24] to solve the Green's function to derive analytical solutions for the self and mutual radiation resistances of a rectangular plate.

Vitiello *et al.* [25], Cunefare and Koopmann [26], Elliott and Johnson [27] and Gardonio *et al.* [28] used an approach based on elementary radiators. The plate was divided into rectangular sources, where for each source, the normal time-harmonic velocity was defined at its centre position. The interaction among the elementary sources, i.e. the pressure at one source position as a result of contributions from the remaining sources, was expressed by a radiation resistance matrix. The power radiated by the plate can be found from the contributions of these sources provided that the elementary source dimensions are small compared with both structural and acoustic wavelengths [4].

As described above, models for the sound radiation from a baffled plate are well established. They began in the 1960s when Maidanik [5] proposed formulae for the frequency band average due to the modal response of a lightly damped plate. In the 1970s, Wallace [6] presented the radiation efficiency of a baffled plate for single modes. Later on in the 1990s and more recently, the averaged radiation efficiency was calculated by summation over these individual modes [4, 12]. This method is still being expanded to fulfil many practical situations. However, the baffle in the model is used

for mathematical convenience rather than picturing the practical case. Often, plates are mounted without a baffle. The model for this unbaffled condition is more complicated as account has to be taken of the interaction of sound between the two sides of the plate.

#### 1.2.1.2 Unbaffled plate models

The infinite rigid baffle frequently used as an approximation never exists in practical cases. A more practical situation for flat plates is often an unbaffled plate. The problem of the radiation from an unbaffled flat plate is more difficult as the velocity is known over the plate surface whereas elsewhere in the plane of the plate the pressure is known (zero) due to anti-symmetry but the velocity is unknown. This creates a mixed boundary condition which has to be overcome. However, several methods have been developed to solve the problem.

Williams [29] applied an FFT based iterative technique to evaluate numerically the acoustic pressure and particle velocity on and near unbaffled thin plates vibrating in air. However, this technique suffers from convergence problems at low frequencies which is the region where the sound radiation of baffled and unbaffled plates shows significant differences.

Atalla *et al.* [30] gave a numerical solution for the sound radiation of an unbaffled plate with general boundary conditions. The Kirchhoff-Helmholtz equation allows the pressure to be defined anywhere within the volume enclosing the plate. Applying Euler's equation, the plate displacement solution was obtained, which involved a surface integral of the Green's function. The plate displacement was then solved using a variational approach [31]. From this, the pressure jump was neglected when calculating the velocity of the plate, allowing any boundary conditions to be derived analytically at the plate edges. The simulation was compared with a measurement result from [32] and showed good agreement. However, the numerical implementation was found to be incorrect at high frequencies due to convergence problems. The model implied that the radiation efficiency of an unbaffled plate started to exceed that of the equivalent baffled plate at frequencies below the critical frequency.

Laulagnet [33] gave an alternative solution by also using the Kirchhoff-Helmholtz equation to represent the acoustic pressure. The surface integral for the Green's function was solved analytically by implementing a two-dimensional spatial Fourier transform. Both the pressure jump and the plate displacement were developed in terms of a series of the simply supported plate modes. The matrix of modal coupling coefficients was calculated numerically and later was used to define the accuracy of the radiation efficiency. In the paper, the author used the normalized cross-modal radiation impedance rather than the radiation efficiency. The real and imaginary parts of the radiation impedance were plotted for certain modes and were compared with those of the baffled plate.

Nelisse *et al.* [34] proposed a study on the radiation of both baffled and unbaffled plates. A Rayleigh-Ritz approach was used to develop the plate displacement in the baffled case, as well as the pressure jump in the unbaffled case. The plate mode shape function was defined by applying a set of trigonometric functions for arbitrary boundary conditions [35]. As in Laulagnet's model [33], the pressure jump was also expanded in terms of a series of modes. The radiation efficiency was obtained by first determining sets of matrices, namely radiation impedance, mass and stiffness matrices. Intended for general boundary conditions, the calculation is more complicated than Laulagnet's model. In the paper, the radiation efficiency of an unbaffled clamped plate in water was presented against frequency up to moderate frequencies and compared with that of the baffled plate.

Oppenheimer and Dubowsky [36] introduced heuristic correction factors in the formula for a baffled plate and then used curve-fitting based on measured results to determine the various coefficients. This method is not sufficiently rigorous to be considered further here but it is practical from an engineering point of view.

More recently, Fahy and Thompson [37] developed a wavenumber domain scheme involving inversion of a matrix equation. However, the model was only applied to a one-dimensional strip piston. Intended for perforated strips, this method can also be applied to an unbaffled strip although the results were found to be poor in this case due to a singular matrix produced (see Appendix A). In terms of its concept, the model provides a useful insight to a case of mixed boundary conditions. The acoustic pressure was defined as a function of the acoustic impedance which could be different

in the region above the strip and beyond it, creating the mixed boundary conditions. The acoustic power was then calculated in the wavenumber domain.

Models for the radiation from an unbaffled plate are much less widely considered than for the baffled plate. From the existing methods, particularly in [29] and [33], the results presented were only focused on single modes. The radiation efficiency due to vibration in multiple modes was calculated in [30, 33, 34] but only up to relatively low frequency. However, this is not still adequate to give a thorough analysis, particularly to provide a complete investigation into the difference between the radiation from the baffled and unbaffled plate.

### 1.2.2 Numerical models

Alternative approaches are available using numerical methods such as the finite element method (FEM) or boundary element method (BEM). The FEM is used to obtain solutions to the differential equations that describe, or approximately describe a wide variety of physical (and non-physical) problems [38, 39]. The BEM is basically derived through the discretisation of an integral equation that is mathematically equivalent to the original partial differential equation [40]. The FEM and BEM allow arbitrary geometry to be considered but do not provide the same physical insight as analytical methods. The FEM is usually first used for analysing the vibration of a structure. Once motion of the vibrating structure is obtained, the BEM is employed to solve the equation of motion of the acoustic medium [41]. Several studies relating to the sound radiation have been proposed based on these methods. For heavy fluid loading, FEM/BEM can also be used in fully a coupled mode to allow for the effect of the fluid on the structure.

Nolte and Gaul [42] investigated the sound radiation from a vibrating structure in water. The pressure field in the fluid domain and the velocity field were determined by using BEM with input data of surface velocities obtained from a FEM calculation of modal analysis. The sound radiation can be identified by determining the intensity vector in the acoustic near field. For a comparison, the sound radiation calculated by using BEM was compared with the results obtained by a superposition of monopole sources (pulsating spheres). Mattei [43] presented a formulation and a numerical

solution using a simple BEM model of a boundary integral equation for a baffled plate, and also developed an analytical method for the constrained plate.

Zhao *et al.* [44] proposed a method to calculate the radiation efficiency of arbitrary structures by combining BEM and general eigenvalue decomposition. The surface pressure of the structure was calculated using BEM and as the impedance matrix is positive definite and the mean square velocity is real symmetric and also positive definite, the sound radiation can be decoupled using general eigenvalue decomposition. The method was validated with the prediction for radiation efficiencies of a pulsating sphere and a radiating cube.

Although FEM can also be used for acoustic fields, it cannot be used directly for open problems such as sound radiation from structures. However, it is possible to use the scheme called the 'infinite element method' to simulate non-reflecting boundaries. This can be implemented to solve an unbounded acoustical problems [45, 46] as an alternative to the BEM.

### 1.2.3 Experimental work and methods

Many experimental investigations using various methods have also been carried out to validate models for the sound radiation from a vibrating structure. To determine the radiation efficiency, the experimental work requires two sets of measurement i.e. the acoustical measurement for the sound power and the mechanical measurement for the squared surface velocity. Mostly, the methods only differ in the means of measuring the sound power. This can be obtained in several ways:

1. by measuring the nearfield, sound intensity using the sound intensity probe [47, 48]

2. by measuring the direct field far from the plate [49]. This can be done accurately in an anechoic chamber, a special room having walls with high absorption to suppress the reflected sound. For a sound source with high directivity, the sound pressure must be taken at many measurement positions.

3. by measuring the diffuse field in a reverberant chamber [50, 51, 52]. At a certain distance from the sound source where the direct field is negligible compared

with the reverberant field, the sound pressure is approximately uniform across the room. A smaller number of measurement locations than for the anechoic chamber is therefore sufficient.

To prevent unwanted noise from the mechanical exciter, such as a shaker, the reciprocity technique can be applied to obtain the radiated power for a given squared input force [50, 51, 53]. Instead of exciting the structure mechanically, the structure is now excited acoustically by a broadband sound. The sound pressure over the room and the surface velocity or acceleration of the structure are measured. This technique, in many cases of practical application in noise control engineering, can provide information in a simpler, faster and cheaper than by direct test methods [54].

Ramachandran and Narayanan [52] implemented experimental statistical energy analysis (SEA) to determine the radiation efficiency of a stiffened cylindrical shell. The estimated modal density was obtained from the measured point mobility of the cylinder. The cylinder was then excited by a diffuse sound field in a reverberant chamber. From this, experimental SEA was employed to obtain the coupling loss factors (CLFs) and the damping loss factors (DLFs). The radiation efficiency is proportional to the CLF between the cylinder and the acoustic subsystem. A correction factor, as in [36], was applied below the critical frequency as the experiment was conducted in unbaffled condition. The results showed a good agreement between the experiment and predictions for stiffened and unstiffened cylinders.

Hashimoto [55] proposed a combination between theoretical calculation and measurement for obtaining the radiation efficiency using both vibration measurements and calculations of self and mutual radiation impedances. The plate was divided into rectangular elements smaller than the acoustic wavelength at the critical frequency. To have a simple formula to calculate the radiation impedance, each element was approximated as a circular piston. The sound power was then obtained by using the measured surface velocity of the structure at the centre of each element in combination with the calculated radiation impedance. The radiation efficiency calculated from this method was validated by comparison with Rayleigh's integral [9] for uniform vibration of the plate surface and with Maidanik's formulae [5] for diffuse vibration, the latter being obtained from FEM. The results showed a reasonably good agreement. This method offers an advantage that the acoustic (sound power) measurement is not required.

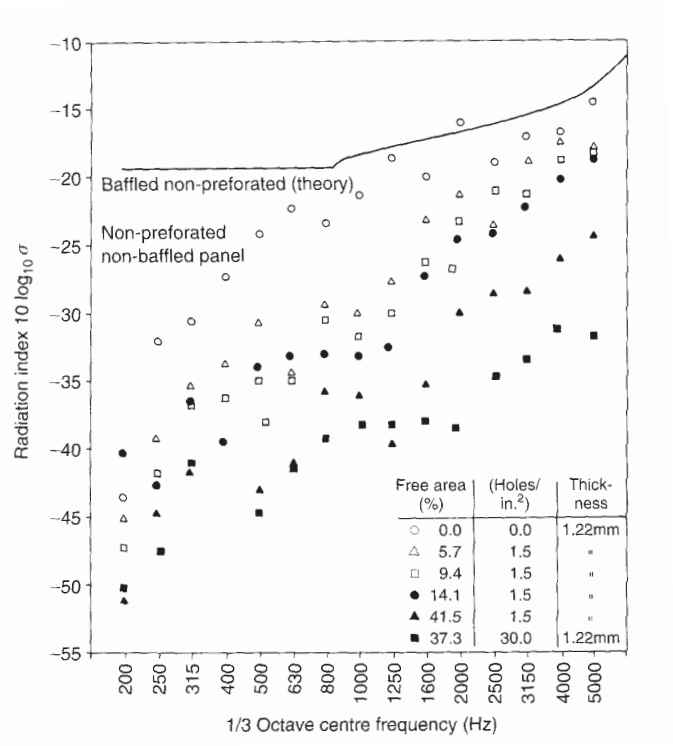


FIGURE 1.3: Measured radiation efficiencies of some unbaffled perforated plates [56].

However, the paper does not provide results comparing measured data with the theoretical results to demonstrate that the method could be a good alternative for the conventional method. Furthermore, the method is applicable only for a flat baffled plate.

### 1.2.4 Perforated plate models

The main aim in studying the sound radiated by vibrating plates is usually to determine how to reduce the sound radiation. For this purpose, several schemes have been developed, one of which is to introduce perforation over the area of the plate. Although not applicable in every situation, this technique is known to be very effective [4]. Figure 1.3 shows measured data [56] of radiation efficiencies from 1 mm thick perforated unbaffled steel plates with various perforation ratios. It can be seen that the perforated plates produce less sound radiation than the solid plate does.

Perforated plates can be seen in many practical applications, for example safety guard enclosures, such as the protective cover over flywheels and belt drives as seen in Figure 1.4(a), and product collection hoppers as shown in Figure 1.4(b). They are also

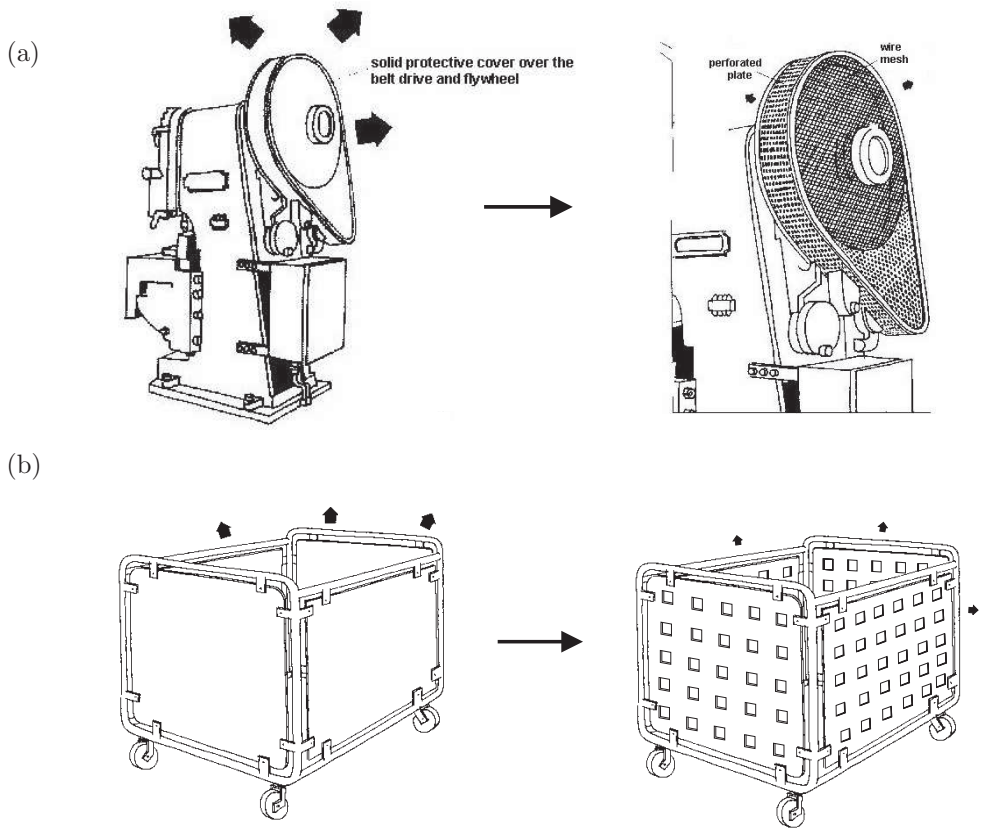


FIGURE 1.4: Applications of perforated plates for reducing the sound radiation [62]: (a) cover of a belt drive and (b) product collection hopper.

widely used in sound absorption applications, as flexible panels covering a porous material [57] or backed by an air cavity [58, 59, 60]. In such applications, it has been shown that the vibration of the perforated plate has the effect of increasing the absorption coefficient [58]. In developing models for the sound absorption from a perforated plate, the acoustic impedance of a hole was approximated by the analytical solution for wave propagation in a small tube having a circular cross section, as proposed by Maa [61].

Very few models have been proposed to calculate the sound radiation from a perforated plate. Janssens and van Vliet [63] studied the sound radiation from a vibrating steel railway bridge, and investigated the potential effect of perforating various bridge components. Measurements were carried out on a set of perforated plates by varying the perforation ratio, the hole density and the hole diameter. An empirical formula was then derived for the effect of perforation on the radiation efficiency.

Fahy and Thompson [37] started with a model of radiation by plane bending waves

propagating in an unbounded plate with uniform perforation to calculate the radiation efficiency of a simply supported rectangular perforated plate. The assumptions imply that the plate is effectively mounted in a similarly perforated rigid baffle, which would not be found in practice. This model replaces the perforations by an equivalent continuous impedance, based on an assumption that the hole size is much smaller than the acoustic wavelength.

The model was then extended to the situation where the plate and the baffle have different specific acoustic impedances. The relation between velocities and pressures was derived in the wavenumber domain as a matrix problem and then solved by matrix inversion. As a preliminary case, this was applied to the radiation by a perforated strip piston, in one dimension, vibrating in an infinite baffle. Good results were obtained for the case of a perforated strip piston in a perforated baffle and in a rigid baffle. However, problems were found with this model at low frequencies for an unbaffled perforated strip. A very low acoustic impedance of the boundary (relative to the acoustic impedance of the hole) led to a singular or nearly singular matrix which reduced the quality of the results from the inverted matrix. In addition, expanding this model into the two-dimensional case is found to require intensive computational effort. Results from this model have been reproduced and are given in Appendix A.

A somewhat different study was carried out by Toyoda and Takahashi [59] who proposed a model for the sound radiation from an infinite, thin elastic plate under a single normal point force excitation in the presence of a perforated plate used as an absorptive facing to the vibrating plate. The analysis was carried out under the assumption that the perforated board was rigidly attached to the vibrating plate via a honeycomb structure so that both plates have an identical motion. The problem was examined as a one-dimensional situation. The basic model for the sound power radiated by the flexural vibration of a perforated plate was adopted from [57]. In [60], the problem was extended to three-dimensions but still using a normal point force excitation at a particular location on the plate. A large reduction in sound radiation due to perforation on the facing was found around a narrow frequency of the Helmholtz resonator formed by the air cavity inside the honeycomb structure and the perforated plate.

In terms of the effect of perforation in reducing the radiated sound over a wider frequency range, which can be achieved by perforating the vibrating main structure,

if possible, there is still a lack of quantitative models that can accurately determine the level of sound reduction due to the perforation.

## 1.3 Objectives and scope of the thesis

The main objective of this thesis is to develop models for the sound radiation from vibrating perforated plates, with or without a baffle. These should be applicable in practical cases and be usable to give quantitative guidance especially relating to the noise reduction potential. The emphasis is therefore placed on a vibrating rectangular plate rather than simpler case of a strip. Extensive measurements are presented to validate these models.

Most emphasis is placed on simply supported boundary conditions although the model can in principle be extended to other edge conditions. A guided-guided boundary condition is highlighted as a comparison for perforated baffled and unbaffled plates. The plate is also assumed to be immersed in air so that the effect of fluid loading can be neglected.

Perforation introduced to a solid plate will also change the dynamic properties of the plate, i.e. the effective Young's modulus, the Poisson's ratio and the density, depending on the ratio of the perforation [64, 65]. This will thus change the resonance frequencies of the plate. The models proposed assume that the perforation does not affect these properties significantly, although it will be shown later from the experimental results that this also affects the radiation efficiency particularly for thin, light plates. In addition, the model proposed is based on regular evenly spaced holes so that the mode shapes are unchanged.

## 1.4 Thesis outline

The structure of the thesis is as follows:

Chapter 2 reviews several existing models for calculating the radiation efficiency of a plate set in an infinite baffle. The accuracy and computational efficiency of methods

from Xie *et al.* [12], Fahy [4] and Williams [22] are compared and their advantages and disadvantages are discussed. The radiation efficiency is calculated for multi modal responses and averaged over force positions. The variability of the radiation efficiencies due to the location of a single point force is also investigated.

In Chapter 3 models for the unbaffled plate are reviewed. Similar to the baffled plate in Chapter 2, the accuracy and computational efficiency of the existing models are discussed. Methods from Williams [23] and Laulagnet [33] are implemented to calculate the radiation efficiency of an unbaffled plate. The results are plotted and also compared with those of the baffled plate. From this, simple empirical formulae, equivalent to Maidanik's formulae for the baffled plate, will be derived.

In Chapter 4 the effect of the plate edge condition on the radiation efficiency is sought. This is calculated in particular for the combination of simply supported and guided-guided boundary conditions both for baffled and unbaffled plates.

Chapter 5 extends the problem to consider the sound radiation from a perforated plate. The impedance of the hole and its approximations in terms of fluid viscosity and near field effects are described. The model from Fahy and Thompson [37] for the perforated plate in an infinite perforated baffle is implemented. Some results are plotted including the effect of perforation. For the latter, an approximate formula is developed. The sound radiation from a perforated unbaffled plate is then modelled by extending Laulagnet's model [33]. The result is compared with the model of a perforated plate in an infinite perforated baffle. An approximate formula is also developed for the effect of perforation at low frequency. The unbaffled perforated plate model is also extended further to consider the case where the plate is close to a reflecting rigid surface.

In Chapter 6 a model is developed for a perforated plate in a rigid baffle based on discretisation of the Rayleigh integral to simulate a distribution of discrete monopole sources. The concept is similar to [25, 26] where the plate is divided into small elementary radiators. This allows an investigation of the limitation of using a uniform specific acoustic impedance to represent the holes.

Chapter 7 presents experimental work to validate the model for the sound radiation from an unbaffled plate. The experiments are conducted with two types of boundary

conditions, namely simply supported and free-free. A validation experiment is also made for the radiation from a plate close to a rigid surface.

Chapter 8 summarises the main findings of the thesis and proposes further work.

## 1.5 Thesis contributions

The main contributions from this thesis can be summarised as follows:

(a) An assessment is made of existing methods for calculating the averaged radiation efficiency of baffled plates. The variability of the radiation efficiency due to the forcing location has been established. It is shown that the highest variability lies in the corner mode frequency region. The variability depends on plate thickness whereas it is largely independent of damping and plate dimensions.

(b) Existing models of the sound radiation from unbaffled plates have been implemented and assessed. It is shown that Laulagnet's model is the most powerful and reliable model to calculate the results up to high frequency. Simple empirical formulae for calculating the radiation efficiency of an unbaffled plate have been introduced. For engineering purposes, these are found to be very useful in terms of calculation time.

(c) The effect of plate boundary conditions on the radiation from multi-modal responses have been determined by comparing results for simply supported and guided-guided boundaries both for baffled and unbaffled plates. For the unbaffled case, the plate boundary conditions are found to have less influence on the radiation efficiency than for the baffled case.

(d) By modifying Laulagnet's model, a model for sound radiation from an unbaffled perforated plate is proposed. It is found that the radiated sound can be reduced by increasing the perforation ratio or by introducing a smaller hole size for a constant perforation ratio.

(e) A model for sound radiation from a baffled perforated plate is developed by using a discrete sources approach. This model demonstrates that the assumption of a continuous impedance is only valid when the distance between holes is less than

an acoustic wavelength for a rectangular piston and less than half an acoustic wavelength for a plate in bending vibration.

(f) The unbaffled perforated plate model is extended to consider the case where the plate is close to a rigid surface. It is found that at low frequency, the effect of perforation on the sound radiation is greater than that when the rigid surface is absence.

(g) Experimental validation of the models is provided which gives good agreement between measured results and the predictions. It also confirms point (c) above because a good agreement is achieved for the prediction calculated using simply supported edges while the experiment is actually conducted with free-free edges.

# Chapter 2

# Radiation efficiency of a baffled plate

The purpose of this chapter is to compare different methods of calculating the radiation efficiency of a rectangular plate set in an infinite baffle, for a case of a point force excitation. Since plate vibrations generally involve many superimposed modes, the radiation efficiency of a plate, in principle, can be obtained by summing over all the modes that contribute significantly in the frequency range under consideration [12]. Methods described in this chapter and in Chapter 3 apply this theory to obtain the radiation efficiency of baffled and unbaffled plates respectively. In each case an average over possible point force locations is taken. Simply supported plate boundaries will be considered for simplicity. The methods are described in detail as they form a basis for later sections on perforated plates.

## 2.1 Spatial domain approach

### 2.1.1 Power radiated in terms of plate modes

Figure 2.1 shows a rectangular plate of length $a$ and width $b$ set in an infinite rigid baffle. Harmonic motion at frequency $\omega$ is assumed. The complex acoustic pressure amplitude $p(\mathbf{r})$ at position $\mathbf{r}$ can be written in terms of the plate surface velocity using the Rayleigh integral [9] evaluated over the plate surface $S$, since the velocity is zero

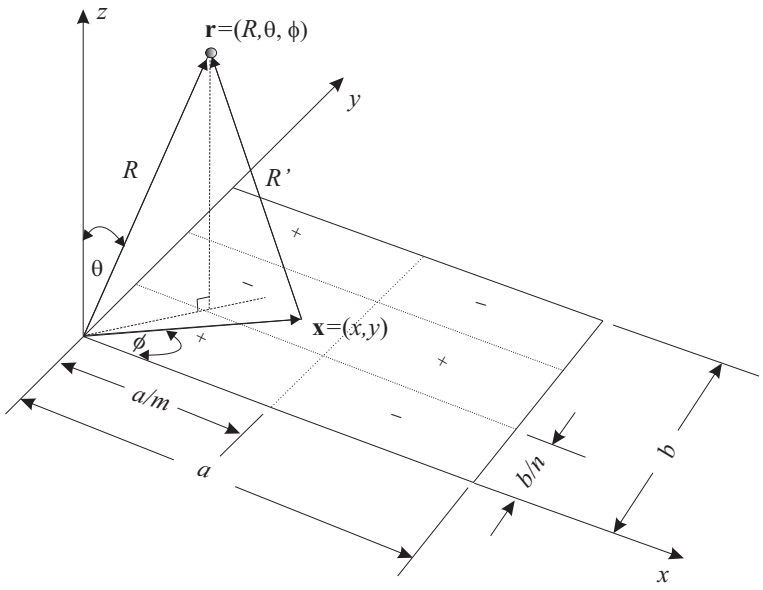


FIGURE 2.1: Co-ordinate system of a vibrating plate.

elsewhere on the baffle

$$p(\mathbf{r}) = \frac{jk\rho c}{2\pi} \int_s v(\mathbf{x}) \frac{e^{-jkR'}}{R'} d\mathbf{x} \tag{2.1}$$

where $v(\mathbf{x})$ is the complex velocity amplitude normal to the surface at location $\mathbf{x} = (x, y)$, $k$ is the acoustic wavenumber ($k = \omega/c$), $\rho$ is the density of air, $c$ is the speed of sound and $R' = |\mathbf{r} - \mathbf{x}|$ is the distance from the location on the plate to the observation point. The term $e^{-jkR'}/2\pi R'$ is the half space Green's function [4]. A time dependence of $e^{j\omega t}$ is assumed, where $t$ is time.

Following the method of Xie *et al.* [12], by integrating the far field acoustic intensity over a hemisphere of radius $R$, the total radiated acoustic power can be written as

$$W = \int_0^{2\pi} \int_0^{\pi/2} \frac{|p(\mathbf{r})|^2}{2\rho c} R^2 \sin\theta \, d\theta \, d\phi \tag{2.2}$$

where the location $\mathbf{r}$ is expressed in spherical co-ordinates as $\mathbf{r} = (R, \theta, \phi)$.

The radiated power can also be calculated by integrating the acoustic intensity over the surface of the vibrating plate. This calculation is not developed further here as there are singularities when $R' = 0$, hence more effort would be needed to overcome the problems in the Rayleigh integral. One approach is to use series expansions. For a further description of this approach, one can refer to reference [66] or [67].

The velocity $v(\mathbf{x})$ at any location $\mathbf{x}$ on the plate can be found by summing over all the modes of structural vibration of the plate,

$$v(\mathbf{x}) = \sum_{m=1}^{\infty} \sum_{n=1}^{\infty} u_{mn} \varphi_{mn}(\mathbf{x}) \tag{2.3}$$

where $u_{mn}$ is the complex velocity amplitude of mode $(m, n)$, which depends on the form of excitation and on frequency, and $\varphi_{mn}(\mathbf{x})$ is the value of the associated mode shape function at $\mathbf{x}$.

For a plate with simply supported edges, the mode shape function $\varphi_{mn}(\mathbf{x})$ is the product of two sinusoidal functions along the $x$ and $y$ directions (see Appendix B)

$$\varphi_{mn}(x, y) = \sin\left(\frac{m\pi x}{a}\right) \sin\left(\frac{n\pi y}{b}\right) \tag{2.4}$$

From Cremer *et al.* [7], the modal velocity amplitude due to a point force applied at a location $(x_0, y_0)$ is given by

$$u_{mn} = \frac{j\omega F \varphi_{mn}(x_0, y_0)}{[\omega_{mn}^2(1 + j\eta) - \omega^2] M_{mn}} \tag{2.5}$$

where $F$ is the force amplitude, $\omega_{mn}$ is the natural frequency, $\eta$ is the damping loss factor, and $M_{mn}$ is the modal mass which, for the simply supported boundaries, is given by

$$M_{mn} = \int_s \rho_p t_p \varphi_{mn}^2(x, y) dS = \frac{1}{4} \rho_p t_p ab = \frac{M}{4} \tag{2.6}$$

where $\rho_p$, $t_p$ and $M$ are the density, thickness and mass of the plate respectively.

The natural frequencies $\omega_{mn}$ are given by

$$\omega_{mn} = \left(\frac{B}{\rho_p t_p}\right)^{1/2} \left[\left(\frac{m\pi}{a}\right)^2 + \left(\frac{n\pi}{b}\right)^2\right] \tag{2.7}$$

where $B = Et_p^3/[12(1 - \nu^2)]$ is the bending stiffness of the plate, in which $E$ is the Young's modulus and $\nu$ is the Poisson's ratio.

By substituting Eq.(2.3) into Eq.(2.1), the sound pressure is thus given by

$$p(\mathbf{r}) = \sum_{m=1}^{\infty}\sum_{n=1}^{\infty} u_{mn}\left\{\frac{jk\rho c}{2\pi}\int_s \varphi_{mn}(\mathbf{x})\frac{e^{-jkR'}}{R'}d\mathbf{x}\right\} \tag{2.8}$$

or it can also be expressed as

$$p(\mathbf{r}) = \sum_{m=1}^{\infty}\sum_{n=1}^{\infty} u_{mn}A_{mn}(\mathbf{r}) \tag{2.9}$$

where $A_{mn}(\mathbf{r})$ is the term in the brackets in Eq.(2.8).

Wallace [6] has produced an analytical solution for $A_{mn}(\mathbf{r})$, which is given by

$$A_{mn}(\mathbf{r}) = \frac{jk\rho c}{2\pi}\left(\frac{e^{-jkR}}{R}\right)\Phi \tag{2.10}$$

where

$$\Phi = \frac{ab}{\pi^2 mn}\left[\frac{(-1)^m e^{j\mu}-1}{(\mu/(m\pi))^2-1}\right]\left[\frac{(-1)^n e^{j\chi}-1}{(\chi/(n\pi))^2-1}\right]$$

$$\mu = ka\,\sin\theta\,\cos\phi, \quad \chi = kb\,\sin\theta\,\sin\phi \quad \text{and} \quad r = |\mathbf{r}|$$

Since $p.p^* = |p|^2$, substituting Eq.(2.9) into Eq.(2.2) gives the total radiated power as

$$W = \sum_{m=1}^{\infty}\sum_{n=1}^{\infty}\sum_{m'=1}^{\infty}\sum_{n'=1}^{\infty}\left\{u_{mn}u^*_{m'n'}\int_0^{2\pi}\int_0^{\pi/2}\frac{A_{mn}(\mathbf{r})A^*_{m'n'}(\mathbf{r})}{2\rho c}R^2\sin\theta\,d\theta\,d\phi\right\} \tag{2.11}$$

where $m$ and $n'$ denote the values of $m$ and $n$ in the conjugate form. This equation shows that the total radiated power depends on the contributions of combinations of modes. The contribution is usually referred to as the self-modal radiation for $m = m'$ and $n = n'$, and cross-modal radiation for either $m \neq m'$ or $n \neq n'$. According to Snyder and Tanaka [66], the cross-modal coupling can only occur (non-zero value) between a pair of modes with the same parity, i.e. both odd or both even in each of the $x$ and $y$ directions. Li and Gibeling [67] have shown that the cross-modal coupling could have a significant impact on the radiated power, depending upon frequency and load condition. In particular it is found that the effect is significant between pairs

of low order modes. Without taking the cross-modal contribution into account, the sound power may be over- or under-estimated. However, Xie *et al.* [12] arrive at the conclusion that the contribution of the cross-modal coupling can be neglected when the plate is excited with uncorrelated point forces averaged over all positions on the plate. This is explained in the next section.

### 2.1.2 Average over forcing points

Following the procedure of [12], consider a point force applied on the plate at location $(x_0, y_0)$ producing a radiated power $W(x_0, y_0)$. It is possible to average the radiated power for all possible locations of uncorrelated point forces on the plate. Such excitation, known as "rain on the roof", is often used in statistical energy analysis (SEA) [68] where geometrical details of a system are neglected. It can be considered as an ensemble average. This average is written as

$$\overline{W} = \frac{1}{ab} \int_0^a \int_0^b W(x_0, y_0)\, dx_0\, dy_0 \tag{2.12}$$

Substituting Eq.(2.11) into Eq.(2.12) gives

$$\overline{W} = \sum_{m=1}^{\infty} \sum_{n=1}^{\infty} \sum_{m'=1}^{\infty} \sum_{n'=1}^{\infty} \left\{ \frac{1}{ab} \int_0^a \int_0^b u_{mn} u^*_{m'n'} dx_0 dx_0 \right. \\ \left. \int_0^{2\pi} \int_0^{\pi/2} \frac{A_{mn}(\mathbf{r}) A^*_{m'n'}(\mathbf{r})}{2\rho c} R^2 \sin\theta\, d\theta\, d\phi \right\} \tag{2.13}$$

where

$$\int_0^a \int_0^b u_{mn} u^*_{m'n'} dx_0\, dy_0 = \\ \int_0^a \int_0^b \left( \frac{j\omega F \varphi_{mn}(x_0, y_0)}{[\omega^2_{mn}(1 + j\eta) - \omega^2] M_{mn}} \right) \left( \frac{-j\omega F \varphi_{m'n'}(x_0, y_0)}{[\omega^2_{m'n'}(1 - j\eta) - \omega^2] M_{m'n'}} \right) dx_0\, dy_0$$

For a uniform structure with a constant mass per unit area, due to the orthogonality of the eigenfunctions, Eq.(2.13) can be simplified to [12]

$$\overline{W} = \sum_{m=1}^{\infty}\sum_{n=1}^{\infty}\left\{\frac{1}{ab}\int_0^a\int_0^b u_{mn}u_{mn}^*\,dx_0\,dy_0\int_0^{2\pi}\int_0^{\pi/2}\frac{A_{mn}(\mathbf{r})A_{mn}^*(\mathbf{r})}{2\rho c}R^2\sin\theta\,d\theta\,d\phi\right\} \tag{2.14}$$

This verifies that the total radiated power averaged over forcing locations is a summation of the power radiated by each single mode. The cross-modal coupling terms have now been eliminated.

Eq.(2.14) can also be expressed as

$$\overline{W} = \sum_{m=1}^{\infty}\sum_{n=1}^{\infty}\overline{W}_{mn} \tag{2.15}$$

where $\overline{W}_{mn}$ is given by

$$\overline{W}_{mn} = \overline{|u_{mn}|^2}\int_0^{2\pi}\int_0^{\pi/2}\frac{A_{mn}(\mathbf{r})A_{mn}^*(\mathbf{r})}{2\rho c}R^2\,d\theta\,d\phi \tag{2.16}$$

and $\overline{|u_{mn}|^2}$ is the squared modal velocity amplitude $u_{mn}$, averaged over all forcing positions.

From Eq.(2.5), for simply supported boundaries $\overline{|u_{mn}|^2}$ can be calculated as

$$\overline{|u_{mn}|^2} = \frac{1}{ab}\int_0^a\int_0^b u_{mn}u_{mn}^*\,dx_0\,dy_0 = \frac{4\omega^2|F|^2}{[(\omega_{mn}^2-\omega^2)^2+\eta^2\omega_{mn}^4]M^2} \tag{2.17}$$

Recalling Eq.(1.2), the modal radiation efficiency $\sigma_{mn}$ can be given by

$$\sigma_{mn} = \frac{\overline{W}_{mn}}{\frac{1}{2}\rho cab\left\langle|v_{mn}|^2\right\rangle} \tag{2.18}$$

where $\left\langle|v_{mn}|^2\right\rangle$ is the spatially averaged squared velocity amplitude of a single mode at one forcing location given by

$$\left\langle|v_{mn}|^2\right\rangle = \frac{1}{ab}\int_0^a\int_0^b|u_{mn}|^2\varphi_{mn}^2(x,y)\,dx\,dy = \frac{|u_{mn}|^2}{4} \tag{2.19}$$

Averaging $\left\langle|v_{mn}|^2\right\rangle$ over all possible forcing positions gives

$$\overline{\langle |v_{mn}|^2 \rangle} = \frac{1}{ab}\int_0^a \int_0^b \langle |v_{mn}|^2 \rangle \, dx_0 \, dy_0$$
$$= \frac{1}{ab}\int_0^a \int_0^b \frac{1}{4}|u_{mn}|^2 \, dx_0 \, dy_0 = \frac{\overline{|u_{mn}|^2}}{4} \tag{2.20}$$

Therefore by substituting Eq.(2.16) and (2.20) into (2.18) yields the modal radiation efficiency averaged over all forcing positions

$$\sigma_{mn} = 4\int_0^{2\pi} \int_0^{\pi/2} \frac{A_{mn}(\mathbf{r}) A^*_{mn}(\mathbf{r})}{(\rho c)^2 ab} R^2 \, d\theta \, d\phi \tag{2.21}$$

After algebraic manipulation, Eq.(2.21) can be expressed as

$$\sigma_{mn} = \frac{64abk^2}{\pi^6 m^2 n^2}\int_0^{\pi/2} \int_0^{\pi/2} \Theta \, \sin\theta \, d\theta \, d\phi \tag{2.22}$$

where

$$\Theta = \left\{ \frac{\begin{array}{c|c} \cos(\xi/2) & \cos(\varrho/2) \\ \sin(\xi/2) & \sin(\varrho/2) \end{array}}{[(\xi/m\pi)^2 - 1][(\varrho/n\pi)^2 - 1]} \right\}^2$$

in which $\cos(\xi/2)$ and $\sin(\xi/2)$ are used when $m$ is an odd or even integer respectively. Similarly, $\cos(\varrho/2)$ and $\sin(\varrho/2)$ are used when $n$ is an odd or even integer respectively.

Since $\sin(\xi/2 + p\pi/2) = \pm\cos(\xi/2)$ and $\sin(\xi/2 + q\pi/2) = \pm\sin(\xi/2)$ where $p$ is odd and $q$ is even, $\Theta$ can be expressed more efficiently as

$$\Theta = \left\{ \frac{\sin(\xi/2 + m\pi/2)\sin(\varrho/2 + n\pi/2)}{[(\xi/m\pi)^2 - 1][(\varrho/n\pi)^2 - 1]} \right\}^2 \tag{2.23}$$

As an example, Figure 2.2 plots the radiation efficiency of modes (1,1) and (10,1) of a rectangular plate having dimensions 0.65×0.5×0.003 m (details given in Section 2.4) in terms of normalised frequencies $k/k_{mn}$, where $k_{mn} = \sqrt{(m\pi/a)^2 + (n\pi/b)^2}$. The frequency resolution used is 40 points per decade spaced logarithmically to ensure a good resolution at the resonance.

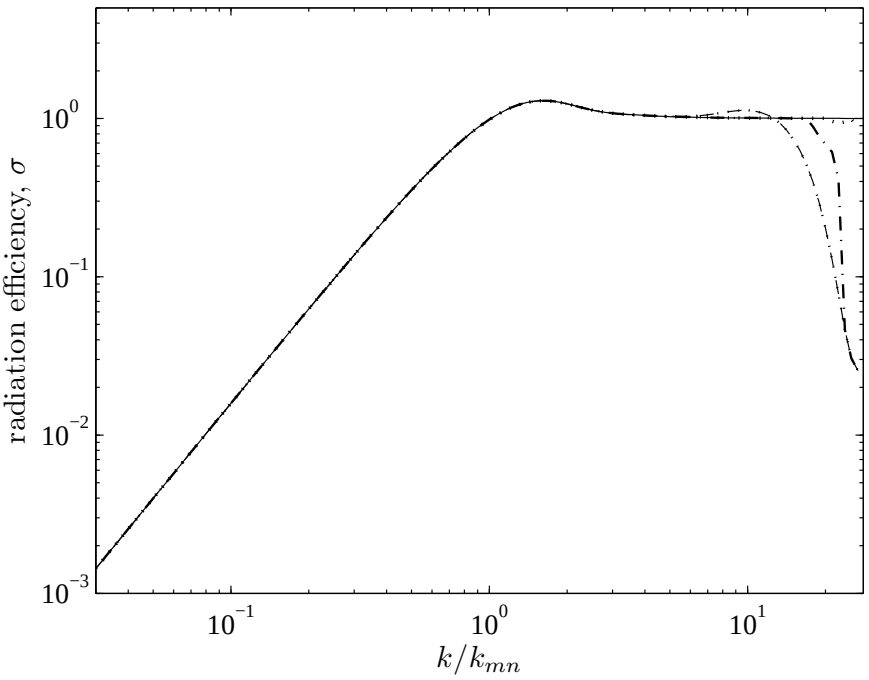


(a)

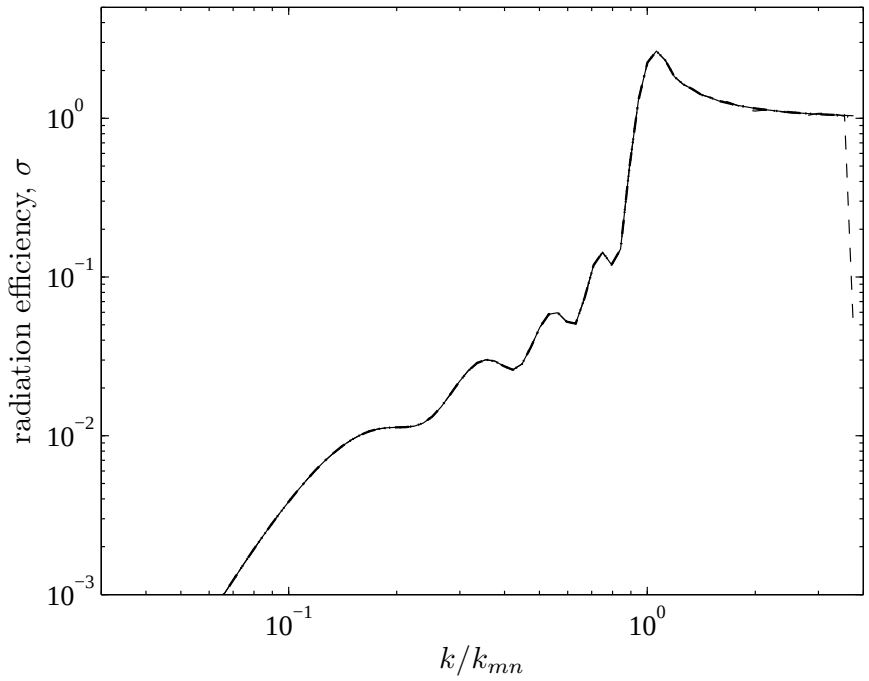


(b)

FIGURE 2.2: Radiation efficiency of (a) mode (1,1) and (b) mode (10,1) of a simply supported baffled plate using the spatial domain approach: $e = --10^{-3}$, $- \cdot -10^{-5}$, $\cdots 10^{-7}$, —$10^{-9}$.

The double integral in Eq.(2.22) is evaluated using a built-in function in MATLAB implementing the two-dimensional Simpson quadrature with various error tolerances, $e$. The results show that the radiation efficiency increases as the frequency increases and then converges to unity above the maximum peak at $k \approx k_{mn}$. As $e$ is reduced, the curve converges.

Finally, the general average radiation efficiency $\sigma$ is given by

$$\sigma = \frac{\sum_{m=1}^{\infty}\sum_{n=1}^{\infty}\overline{W}_{mn}}{\frac{1}{2}\rho cab\overline{\langle|v|^2\rangle}} = \frac{\sum_{m=1}^{\infty}\sum_{n=1}^{\infty}\sigma_{mn}\overline{\langle|v_{mn}|^2\rangle}}{\overline{\langle|v|^2\rangle}} \tag{2.24}$$

where according to Cremer *et al.* [7], $\overline{\langle|v|^2\rangle}$ is the result of summation of the spatially averaged modal squared velocity $\overline{\langle|v_{mn}|^2\rangle}$, averaged over forcing locations, i.e.

$$\overline{\langle|v|^2\rangle} = \frac{\omega^2|F|^2}{2M^2}\sum_{m=1}^{\infty}\sum_{n=1}^{\infty}\frac{1}{[(\omega_{mn}^2-\omega^2)^2+\eta^2\omega_{mn}^4]} = \sum_{m=1}^{\infty}\sum_{n=1}^{\infty}\overline{\langle|v_{mn}|^2\rangle} \tag{2.25}$$

Eq.(2.25) indicates that, as the cross-modal contributions vanish due to averaging over forcing locations, the modal responses are uncorrelated. In other words, the modes act individually, and are all excited with the same input power.

Therefore by substituting Eq.(2.20) and Eq.(2.17) gives

$$\begin{aligned}\sigma &= \frac{\sum_{m=1}^{\infty}\sum_{n=1}^{\infty}\sigma_{mn}\overline{\langle|v_{mn}|^2\rangle}}{\sum_{m=1}^{\infty}\sum_{n=1}^{\infty}\overline{\langle|v_{mn}|^2\rangle}} \\ &= \frac{\sum_{m=1}^{\infty}\sum_{n=1}^{\infty}\sigma_{mn}[(\omega_{mn}^2-\omega^2)^2+\eta^2\omega_{mn}^4]^{-1}}{\sum_{m=1}^{\infty}\sum_{n=1}^{\infty}[(\omega_{mn}^2-\omega^2)^2+\eta^2\omega_{mn}^4]^{-1}}\end{aligned} \tag{2.26}$$

Example results of $\sigma$ will be given in Section 2.4 below.

## 2.2 Wavenumber domain approach

### 2.2.1 Governing equations

The sound radiation from a mode of vibration of a finite plate set in an infinite baffle can also be determined by wavenumber decomposition of the spatial distribution of velocity in the mode [4].

Consider first a one-dimensional infinite vibrating plate, having velocity $v(x)$, which is in contact with a fluid in the semi-infinite space $z > 0$ as shown in Figure 2.3. A plane transverse wave is travelling in the plate with arbitrary frequency $\omega$ and wavenumber $\kappa$ in the $x$ direction. Sound is radiated by the plate into the fluid with the same wavenumber component in the $x$ direction.

As the propagation of a plane wave in a two-dimensional space is expressed by

$$p(x, z, t) = p\, e^{-j(\kappa x + k_z z)} e^{j\omega t} \tag{2.27}$$

the condition must be satisfied that $\kappa < k$, i.e. the plate wave speed $c_p$ is greater than the speed of sound $c$ in the fluid, to allow the wave to propagate away from the plate surface. Also to fulfil this distinct condition, the positive sign must be chosen for $k_z$, whereas the negative sign is disallowed as no wave can propagate towards the surface of the plate.

Assuming a light fluid (for example air), the dependence of the acoustic field in the fluid in the $x$ direction must be the same as that of the plate, i.e. $k_x = \kappa$ so that the wavenumber relationship is given by

$$k_z = \pm(k^2 - k_x^2)^{1/2} \tag{2.28}$$

where $k$ is the acoustic wavenumber, $k = \omega/c$.

The radiated pressure field can be related to the surface normal velocity distribution through the specific acoustic impedance. The specific acoustic impedance is defined as

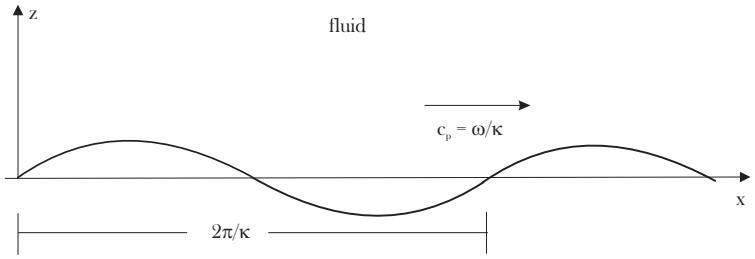


FIGURE 2.3: Propagating wave in a plate

the ratio of complex amplitudes of pressure and particle velocity at a single frequency and wavenumber.

The linearized equation of momentum conservation in the $z$ direction is given by

$$\rho\frac{\partial v_z}{\partial t} + \frac{\partial p}{\partial z} = 0 \tag{2.29}$$

where $v_z$ is the component of particle velocity in the $z$ direction and $p$ is the pressure.

For harmonic motion at frequency $\omega$, this gives, in terms of complex amplitudes

$$j\omega\rho v_z + \frac{dp}{dz} = 0 \tag{2.30}$$

Therefore for the case of the plane travelling wave given by Eq.(2.27), this yields

$$v_z = \frac{-1}{j\omega\rho}\frac{dp}{dz} = \frac{k_z}{\omega\rho}p \tag{2.31}$$

For a given wavenumber $k_x$ from Eq.(2.28), the acoustic impedance $z_a$ can be written as

$$z_a = \frac{p}{v_z} = \frac{\omega\rho}{k_z} = \frac{\omega\rho}{(k - k_x^2)^{1/2}} \tag{2.32}$$

Consider now the spatial Fourier transform of an arbitrary velocity distribution $v(x)$ on the plate

$$\widetilde{V}(k_x) = \int_{-\infty}^{\infty} v(x)e^{-jk_x x}dx \tag{2.33}$$

and its inverse Fourier transform

$$v(x) = \frac{1}{2\pi}\int_{-\infty}^{\infty} \widetilde{V}(k_x) e^{jk_x x} dk_x \tag{2.34}$$

For a finite plate in a rigid baffle, if $v(x)$ represents the plate velocity, or zero on the baffle, the velocity distribution of the plate can also be expressed as an integral over wavenumber. Similarly the pressure at $z = 0$ can be Fourier transformed with respect to $k_x$.

Thus in terms of the wavenumber transforms, Eq.(2.32) can be written as

$$\left[\widetilde{P}(k_x)\right]_{z=0} = \widetilde{V}(k_x) z_a(k_x) = \left(\frac{\omega\rho}{(k^2 - k_x^2)^{1/2}}\right) \widetilde{V}(k_x) \tag{2.35}$$

Considering now a plane wave travelling in the plate surface with a component in the $x$ and $y$ directions, having wavenumber components $k_x$ and $k_y$, $k_x^2$ is then replaced by $k_x^2 + k_y^2$. The direction of travel is at an angle $\theta = \tan^{-1}(k_y/k_x)$ to the $x$-axis. Thus from Eq.(2.35), the surface pressure wavenumber component is related to the velocity wavenumber component by

$$\left[\widetilde{P}(k_x, k_y)\right]_{z=0} = \frac{\omega\rho}{(k^2 - k_x^2 - k_y^2)^{1/2}} \widetilde{V}(k_x, k_y) \tag{2.36}$$

Referring to Eq.(2.34) for a two-dimensional case, the surface pressure field and the surface normal velocity are

$$[p(x,y)]_{z=0} = \frac{1}{4\pi^2}\int_{-\infty}^{\infty}\int_{-\infty}^{\infty} [\widetilde{P}(k_x, k_y)]_{z=0}\, e^{j(k_x x + k_y y)}\, dk_x\, dk_y \tag{2.37}$$

$$v_n(x,y) = \frac{1}{4\pi^2}\int_{-\infty}^{\infty}\int_{-\infty}^{\infty} \widetilde{V}(k_x, k_y)\, e^{j(k_x x + k_y y)}\, dk_x\, dk_y \tag{2.38}$$

The radiated power per unit area is calculated by

$$W = \frac{1}{2}\Re\left\{\int_S p(x,y)\, v_n^*(x,y)\, dx\, dy\right\} \tag{2.39}$$

where $\Re$ denotes the real part.

Therefore by substituting Eq.(2.37) and (2.38) into (2.39) this gives

$$W = \frac{1}{32\pi^4}\Re\left\{\int_S\left[\int_{-\infty}^{\infty}\int_{-\infty}^{\infty}[\widetilde{P}(k_x,k_y)]_{z=0}\,e^{j(k_x x+k_y y)}\,dk_x\,dk_y \times \int_{-\infty}^{\infty}\int_{-\infty}^{\infty}\widetilde{V}^*(k'_x,k'_y)\,e^{-j(k'_x x+k'_y y)}\,dk'_x\,dk'_y\right]dxdy\right\} \tag{2.40}$$

The range of double integration over the surface $S$ can be extended to $-\infty$ to $\infty$ because the particle velocity $v$ is ensured to be zero outside the plate boundary.

Thus substituting Eq.(2.36) into (2.40) gives

$$W = \frac{1}{32\pi^4}\Re\left\{\int_{-\infty}^{\infty}\int_{-\infty}^{\infty}\left[\int_{-\infty}^{\infty}\int_{-\infty}^{\infty}\frac{\omega\rho}{(k^2-k_x^2-k_y^2)^{1/2}}\,\widetilde{V}(k_x,k_y)\,e^{j(k_x x+k_y y)}\,dk_x\,dk_y \times \int_{-\infty}^{\infty}\int_{-\infty}^{\infty}\widetilde{V}^*(k'_x,k'_y)\,e^{-j(k'_x x+k'_y y)}\,dk'_x\,dk'_y\right]dx\,dy\right\} \tag{2.41}$$

If the integration is first performed over $x$ and $y$, by changing the order of integration, the Dirac delta functions are obtained i.e.

$$\int_{-\infty}^{\infty}\int_{-\infty}^{\infty}e^{-j(k_x-k'_x)x}e^{-j(k_y-k'_y)y}dx\,dy = 4\pi^2\delta(k_x-k'_x)\delta(k_y-k'_y) \tag{2.42}$$

Hence Eq.(2.41) can be simplified as

$$W = \frac{1}{8\pi^2}\Re\int_{-\infty}^{\infty}\int_{-\infty}^{\infty}\frac{\omega\rho}{(k^2-k_x^2-k_y^2)^{1/2}}\,|\widetilde{V}(k_x,k_y)|^2\,dk_x\,dk_y \tag{2.43}$$

In addition only wavenumber components satisfying the condition $k_x^2+k_y^2 \le k^2$ contribute to sound power radiation; elsewhere the term $(k^2-k_x^2-k_y^2)^{1/2}$ is imaginary. The range of integration can therefore be limited to give

$$W = \frac{\rho c}{8\pi^2}\int_{-k}^{k}\int_{-\sqrt{k^2-k_y^2}}^{\sqrt{k^2-k_y^2}}\frac{k}{(k^2-k_x^2-k_y^2)^{1/2}}\,|\widetilde{V}(k_x,k_y)|^2\,dk_x\,dk_y \tag{2.44}$$

In the two-dimensional spatial Fourier transform, the velocity distribution of an individual mode $(m,n)$ is decomposed into a continuous spectrum of spatially harmonic,

travelling plane wave components, each having a certain wavenumber vector which is given by

$$\widetilde{V}_{mn}(k_x, k_y) = \int_0^a \int_0^b u_{mn}\, \varphi_{mn} e^{-j(k_x x + k_y y)}\, dx\, dy \tag{2.45}$$

where $\widetilde{V}_{mn}(k_x, k_y)$ is the complex amplitude of the wavenumber component. Integration yields

$$\widetilde{V}_{mn}(\alpha, \beta) = u_{mn} \Lambda k^{-2} (\varepsilon + j\vartheta)(\gamma + j\varsigma) \tag{2.46}$$

where

$$\Lambda = \frac{\left(\frac{m\pi}{ka}\right)\left(\frac{n\pi}{kb}\right)}{\left[\alpha^2 - \left(\frac{m\pi}{ka}\right)^2\right]\left[\beta^2 - \left(\frac{n\pi}{kb}\right)^2\right]}$$

$$\varepsilon = (-1)^m \cos(\alpha k a) - 1,\ \vartheta = (-1)^{m+1} \sin(\alpha k a)$$

$$\gamma = (-1)^n \cos(\beta k b) - 1,\ \varsigma = (-1)^{n+1} \sin(\beta k b)$$

in which $\alpha = k_x/k$ and $\beta = k_y/k$ are the non-dimensional wavenumbers and $a$ and $b$ are the plate dimensions. The derivation of Eq.(2.46) is given in Appendix C.

Referring to the co-ordinates in Figure 2.1 for wavenumber components, it is found that $k_x = k\, \sin\theta\, \cos\phi$ and $k_y = k\, \sin\theta\, \sin\phi$.

Thus by relating Eq.(2.46) to Eq.(2.10), it can also be found that

$$\widetilde{V}_{mn}(k, \theta, \phi) = u_{mn}\, \frac{\Phi}{(ka)(kb)} \tag{2.47}$$

Substituting Eq.(2.46) into Eq.(2.44), the sound power radiated by a single mode is thus

$$W_{mn} = \frac{\rho c \overline{|u_{mn}|^2}}{8\pi^2 k^2} \int_{-1}^{1} \int_{-\sqrt{1-\alpha^2}}^{\sqrt{1-\alpha^2}} \Lambda^2 \frac{(\Gamma^2 + \Pi^2)}{(1 - \alpha^2 - \beta^2)^{1/2}}\, d\beta\, d\alpha \tag{2.48}$$

where $\Gamma = (\varepsilon\gamma - \vartheta\varsigma)$ and $\Pi = (\vartheta\gamma + \varepsilon\varsigma)$. Note that the integrand in Eq.(2.48) forms an even function, so that the limit of integration can be simplified

$$W_{mn} = \frac{\rho c \overline{|u_{mn}|^2}}{2\pi^2 k^2} \int_{0}^{1} \int_{0}^{\sqrt{1-\alpha^2}} \Lambda^2 \frac{(\Gamma^2 + \Pi^2)}{(1 - \alpha^2 - \beta^2)^{1/2}}\, d\beta\, d\alpha \tag{2.49}$$

Because only spectral components of $\widetilde{V}_{mn}$ with $\alpha^2 + \beta^2 \leq 1$ can radiate sound to the far field, the integrands over $\alpha$ and $\beta$ are calculated for the area of non-dimensional wavenumber space enclosed by a quarter of a circle of unit radius centred on the origin (see Figure 2.4(a)).

The bar above the squared modal velocity amplitude $\overline{|u_{mn}|^2}$ indicates the excitation force averaged over all possible positions $(x_0, y_0)$, i.e.

$$\overline{|u_{mn}|^2} = \frac{1}{ab} \int_0^a \int_0^b |u_{mn}|^2 \, dx_0 \, dy_0 \tag{2.50}$$

From Eq.(2.18), as $\overline{\langle |v_{mn}|^2 \rangle}$ equals $\overline{|u_{mn}|^2}/4$ (see Eq.(2.20)), the modal radiation efficiency averaged over forcing positions is

$$\sigma_{mn} = \frac{4}{\pi^2 (ka)(kb)} \int_0^1 \int_0^{\sqrt{1-\alpha^2}} \Lambda^2 \frac{(\Gamma^2 + \Pi^2)}{(1 - \alpha^2 - \beta^2)^{1/2}} \, d\beta \, d\alpha \tag{2.51}$$

### 2.2.2 Singularity solution

A singularity problem occurs in evaluating the integrals when the values of sample points over $\alpha$ and $\beta$ coincide with the radiation circle $\alpha^2 + \beta^2 = 1$ or $k_x^2 + k_y^2 = k^2$. Although not rigorous, the following approach is found to give reasonable results. If $k_p^2 = k_x^2 + k_y^2$, the infinity when $k_p = k$ can be avoided by taking the sample points in the middle of rectangular integration segments of length $dk_p$ (see Figure 2.4). Thus the calculation of the double integral in Eq.(2.51) is implemented by selecting suitable sample spacing $d\alpha$ and $d\beta$.

Of course, the sample spacing must be chosen to be sufficiently small to obtain such a smooth result, especially to ensure that the radiation efficiency converges to unity above the critical frequency. Figure 2.5 shows the results for the same plate dimensions as those in the previous section with different values of $d\alpha$ or $d\beta$. It shows that the radiation efficiency converges as the sampling precision increases. For $d\alpha = d\beta = 0.05$, the curve converges to unity above the bending wavenumber $k_{mn}$. It can also be seen that using the wavenumber domain approach, the results are exactly the same as the results of the spatial domain approach, given in Figure 2.2. To find the average

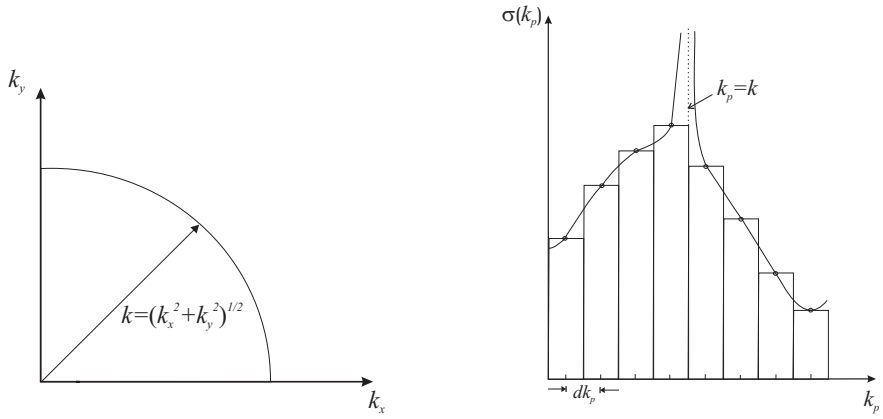


FIGURE 2.4: (a) Radiation circle and (b) Integration performed as a series of rectangles defining the area under the graph. The sample points are taken at the middle of the rectangles.

radiation efficiency over all modes, Eq.(2.26) can be applied. Example results are given in Section 2.4 below.

## 2.3 The Fast Fourier Transform (FFT) approach

The Fourier transform of the velocity in the calculation, as defined in Eq.(2.33), can be solved much faster by using the Fast Fourier Transform (FFT). Compared with numerical integration of the conventional Fourier transform, the FFT can reduce the number of computations needed for $N$ points from $2N^2$ to $2N \log_2 N$ [69]. In addition, as many programming languages, such as MATLAB, provide a built-in FFT function, the task of programming it is much reduced.

### 2.3.1 Steps of calculation and bias error

Williams [22] first implemented the numerical evaluation of the radiation efficiency using the FFT method. Using Figure 2.1 for the plate co-ordinates, Rayleigh's formula as expressed in Eq.(2.1) is rewritten in convolution form

$$p(x, y, d) = v(x, y) \otimes h_g(x, y, d) \tag{2.52}$$

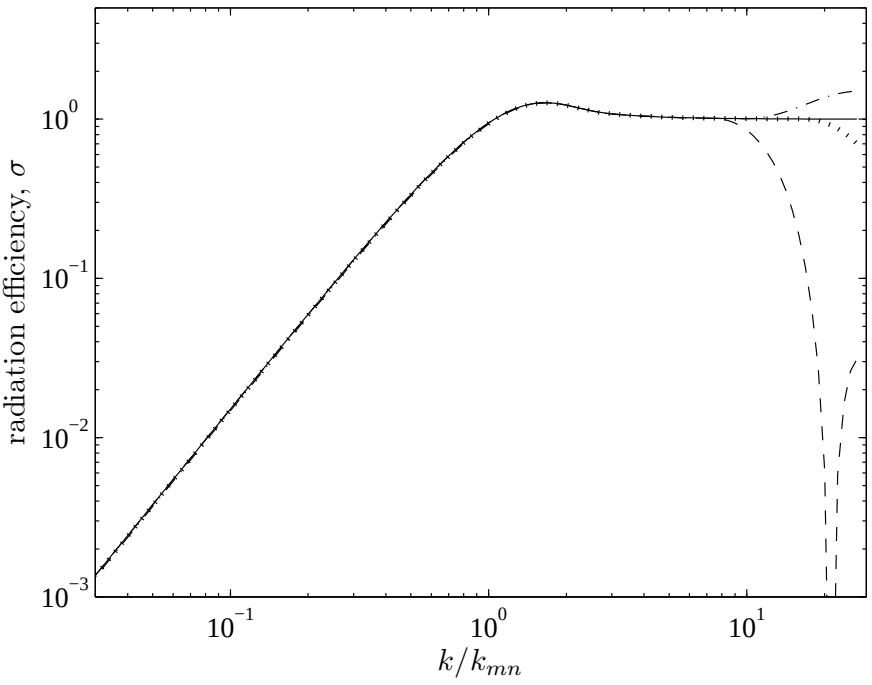


(a)

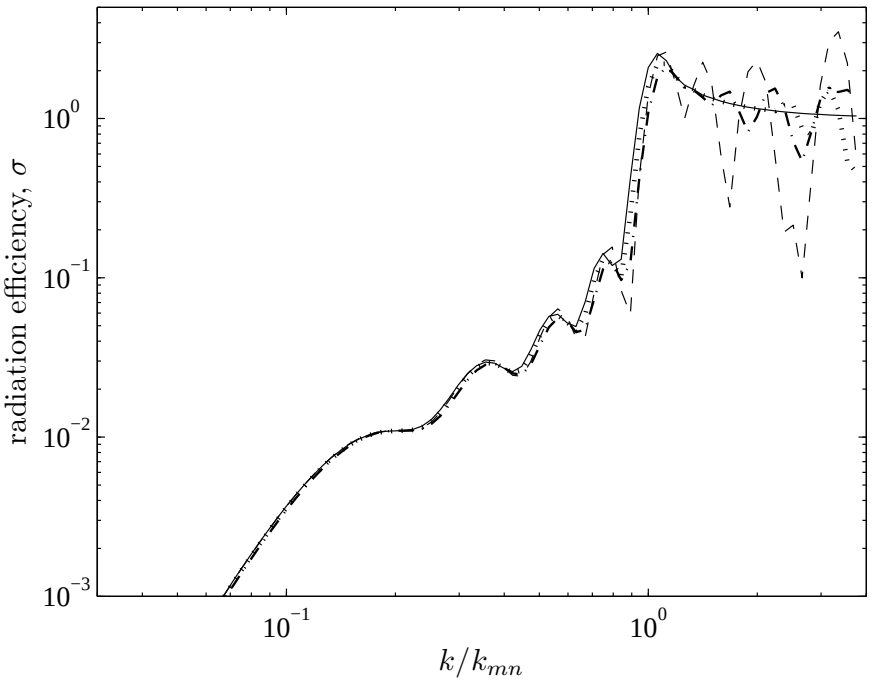


(b)

FIGURE 2.5: Radiation efficiency of (a) mode (1,1) and (b) mode (10,1) of a simply supported baffled plate using the wavenumber domain approach: $d\alpha = d\beta = --0.20$, $- \cdot -0.15$, $\cdots 0.09$, —0.05 m.

where $h_g$ is given by[1]

$$h_g(x,y,d) = j\omega\rho G(x,y,d) = \frac{j\omega\rho}{2\pi}\left(\frac{e^{-jk(x^2+y^2+d^2)^{1/2}}}{(x^2+y^2+d^2)^{1/2}}\right) \tag{2.53}$$

where $G(x,y,d)$ is the half-space Green's function evaluated at $z=d$.

Thus by applying the convolution theorem, one can obtain

$$p(x,y,d) = \mathscr{F}^{-1}\left[\widetilde{V}(k_x,k_y)\widetilde{H}_g(k_x,k_y,d)\right] \tag{2.54}$$

where $\mathscr{F}^{-1}$ denotes the inverse Fourier transform, $\widetilde{V}$ is the Fourier transform of $v$ and $\widetilde{H}_g$ is the Fourier transform of $h_g$, given by

$$\widetilde{H}_g(k_x,k_y,d) = j\omega\rho\widetilde{G}(k_x,k_y,d) = \omega\rho\frac{e^{-jk_zd}}{k_z} \tag{2.55}$$

where

$$k_z = \begin{cases} (k^2-k_x^2-k_y^2)^{1/2}, & k^2 \geq k_x^2+k_y^2 \\ i(k_x^2+k_y^2-k^2)^{1/2}, & k^2 \leq k_x^2+k_y^2 \end{cases}$$

From a knowledge of $v(x,y)$, a process of calculating $p(x,y,d)$ using the FFT can be performed as follows:

1. Calculate the discrete Fourier transform (DFT) of $v(x,y)$ using the two-dimensional FFT algorithm to obtain $\widetilde{V}_D(k_x,k_y)$.
2. Calculate $\widetilde{H}_g(k_x,k_y,d)$ from Eq.(2.55).
3. Multiply results of 1 and 2.
4. Calculate the inverse DFT of result 3.

The velocity $v(x,y)$ is defined on every point of a baffle having dimensions of $L\times L$. The points are sampled with the sample spacing of $a_s$. The plate itself occupies a region in the centre of this baffle as can be seen in Figure 2.6. The velocity on the rest of the baffle is zero. However due to the truncation of the FFT, the region beyond that

[1]Note that Williams [22] uses the time dependence of $e^{-j\omega t}$ instead of $e^{j\omega t}$. This has been changed here for consistency with the remainder of this thesis.

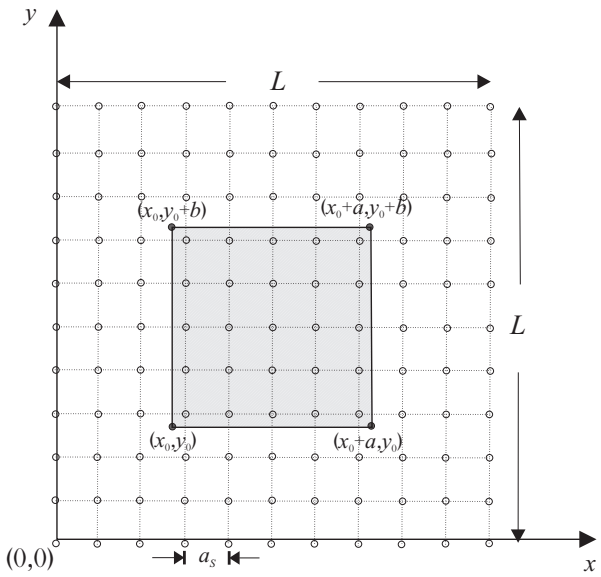


FIGURE 2.6: Diagram of a plate in a sampled baffle for sound radiation calculation using the FFT.

shown in Figure 2.6 is effectively periodic. This produces so-called replicated sources. Thus $L$ must be chosen to be sufficiently large to prevent overlapping the pressure field $p(x, y)$ with that from the replicated sources causing a bias error in the analysis.

The two-dimensional DFT of $v(x, y)$ can be written as

$$\widetilde{V}_D(r\Delta k, s\Delta k) = \frac{1}{N^2} \sum_{p=-N/2}^{N/2-1} \sum_{q=-N/2}^{N/2-1} v(pa_s, qa_s) e^{-j2\pi(rp+sq)/N} \tag{2.56}$$

where $N = L/a_s$ and $\Delta k = 2\pi/L$.

### 2.3.2 Modified Green's function

From Eq.(2.55) it can be seen that the Green's function $\widetilde{G}(k_x, k_y, d)$ becomes infinite when $k_z = 0$, although the integral is finite. To avoid another bias error in the resulting integral, the averaged Green's function $\overline{\widetilde{G}}$ over an annulus $k_1 \leq k_0 \leq k_2$ in wavenumber space is introduced [22]. For $d = 0$, this yields[2]

[2]In Williams [22], a typing mistake is made on the operator of the denominator in the second term, i.e. $k_2^2 + k_1^2$. The fourth term has been added here as another important condition of $\overline{\widetilde{G}}$.

$$\overline{\widetilde{G}} = \begin{cases} \dfrac{-2j[(k^2-k_1^2)^{1/2}-(k^2-k_2^2)^{1/2}]}{(k_2^2-k_1^2)}, & k_2 \leq k \\ \dfrac{-2j(k^2-k_1^2)^{1/2}+2(k^2-k_2^2)^{1/2}}{(k_2^2-k_1^2)}, & k_1 \leq k \leq k_2 \\ \dfrac{2[(k^2-k_1^2)^{1/2}-(k^2-k_2^2)^{1/2}]}{(k_2^2-k_1^2)}, & k \leq k_1 \\ \dfrac{-j}{k}, & k_0 = 0 \end{cases} \tag{2.57}$$

where $k_1 = k_0 - \Delta k/2$, $k_2 = k_0 + \Delta k/2$ and $k_0 = (p^2+q^2)^{1/2}\Delta k$.

Therefore $\widetilde{G}$ from Eq.(2.55) is now replaced with $\overline{\widetilde{G}}$ from Eq.(2.57). Substituting this into Eq.(2.54), the acoustic pressure on the source plane ($d = 0$) is now

$$p(x,y,0) = j\omega\rho\mathscr{F}^{-1}\left[\widetilde{V}_D(k_x,k_y)\overline{\widetilde{G}}(k_x,k_y,d)\right] \tag{2.58}$$

Finally, the radiated power from the plate can be calculated in the spatial domain, given by

$$W = \frac{1}{2}\int_0^L \int_0^L \Re\left[p(x,y,0)\right] v(x,y)\, dx\, dy \tag{2.59}$$

since $v(x,y)$ is real. Alternatively, in the wavenumber domain, the radiated sound power is given by

$$W = 2\int_0^k \int_0^{\sqrt{k^2-k_y^2}} \Re\left[\widetilde{P}^*(k_x,k_y)\widetilde{V}_D(k_x,k_y)\right]\, dk_x\, dk_y \tag{2.60}$$

where $k_x = r\Delta k$ and $k_y = s\Delta k$ and * denotes the complex conjugate. The wavenumbers are filtered so that only those satisfying $k_x^2+k_y^2 < k^2$ are retained in the calculation, and again use has been made of symmetry of the integrand. The radiation efficiency can be found by applying Eq.(1.2).

Figure 2.7 presents the results for modes (1,1) and (10,1) using various numbers of points in the FFT, i.e. using different baffle lengths $L$ and sample spacing $a_s$. From Figure 2.7(a), using $L = 6.4$ m and $a_s = 0.1$ m, a bias error appears at low frequency. It can be seen that the error is then reduced by using larger values of $L$ (larger baffle).

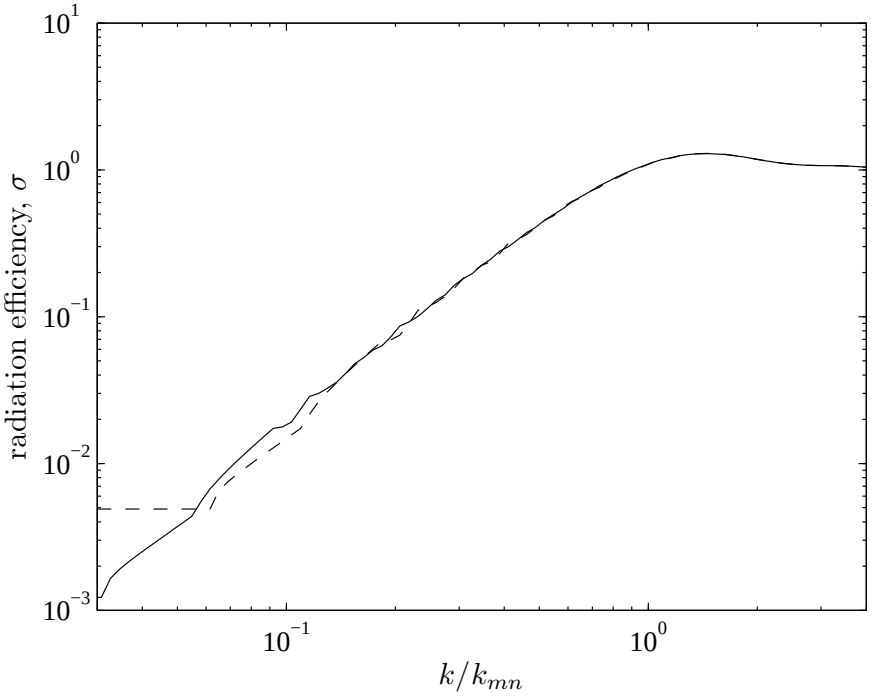


(a)

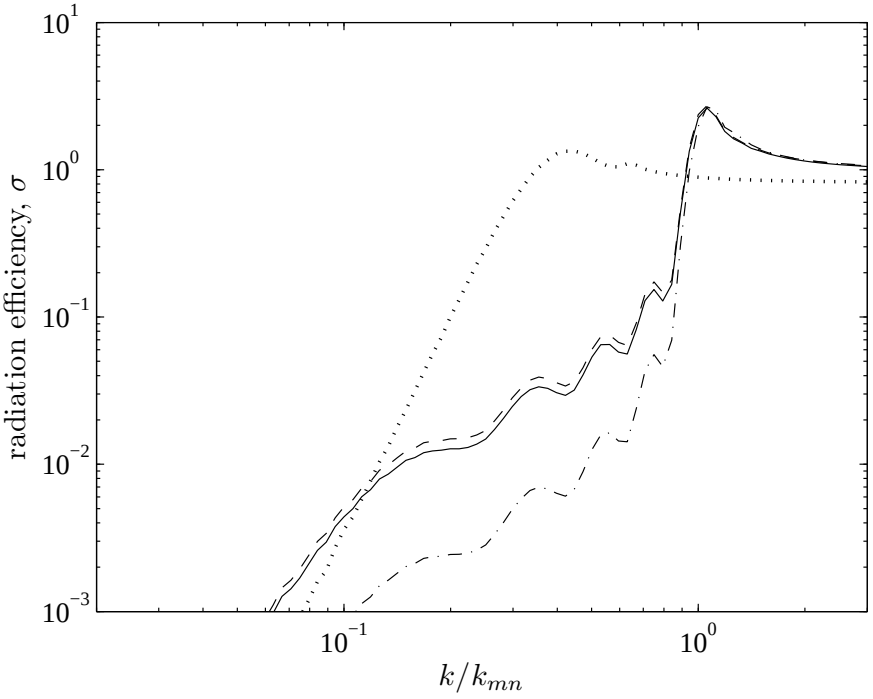


(b)

FIGURE 2.7: Radiation efficiency of a simply supported baffled plate using FFT method. (a) mode (1,1): $--L = 6.4$ m, $a_s = 0.1$ m; —$L = 12.8$ m, $a_s = 0.1$ m and (b) mode (10,1): $L = 6.4$ m; $\cdots a_s = 0.1$ m, $-\cdot- a_s = 0.05$ m, $--a_s = 0.04$ m, —$a_s = 0.03$ m.

For the higher order mode, the bias error is very small at low frequency and is not shown in the plot. However, without changing the baffle length, a finer resolution of sample points is required to obtain the true result of the radiation efficiency. This can be explained as follows. In mode (10,1), there are 5 structural wavelengths in the plate length $a$. In this case $a = 0.65$ m is used, therefore $\lambda = 0.65/5 = 0.13$ m. Meanwhile more than two points are required to represent one wavelength digitally. Therefore the sample spacings needed are $a_s \ll 0.13/2 = 0.065$ m. Figure 2.7(b) presents the radiation efficiency using $L = 6.4$ m and different values of $a_s$. It is clear that for $a_s = 0.1$ m, the result does not capture the interference due to the modal pattern. For $a_s < 0.065$ m, the results converge to the true value of radiation efficiency as the resolution of the sample spacing gets finer. It appears that 3 or more points per wavelength are required to obtain a good accuracy of result.

## 2.4 Comparison of the methods for a baffled plate

### 2.4.1 Example results

Three different methods have been described for determining the radiation efficiency of a baffled plate. A comparison is made of the above methods by applying them to calculate the average radiation efficiency of a rectangular aluminium plate having dimensions of $0.65 \times 0.5 \times 0.003$ m, density $\rho_p = 2700$ kg/m$^3$, Young's modulus $E = 7 \times 10^{10}$ N/m$^2$, and damping loss factor $\eta = 0.1$. The frequency resolution is 40 points per decade, spaced logarithmically. For these parameters, the first plate mode occurs at 48 Hz and the critical frequency is 4022 Hz. The critical frequency $f_c$ is given by

$$f_c = \frac{c^2}{2\pi}\left(\frac{\rho_p t_p}{B}\right)^{1/2} \tag{2.61}$$

Figure 2.8 presents the modal and average radiation efficiencies calculated using the wavenumber domain approach. The spatial domain approach gives identical results, hence these are not presented here. The calculation is made up to 10 kHz for $20 \times 20$ modes. However, the modal resonance frequency for mode (21,1) is 7.6 kHz, which is much lower than the resonance frequency for mode (20,20), i.e. 18.6 kHz. This means

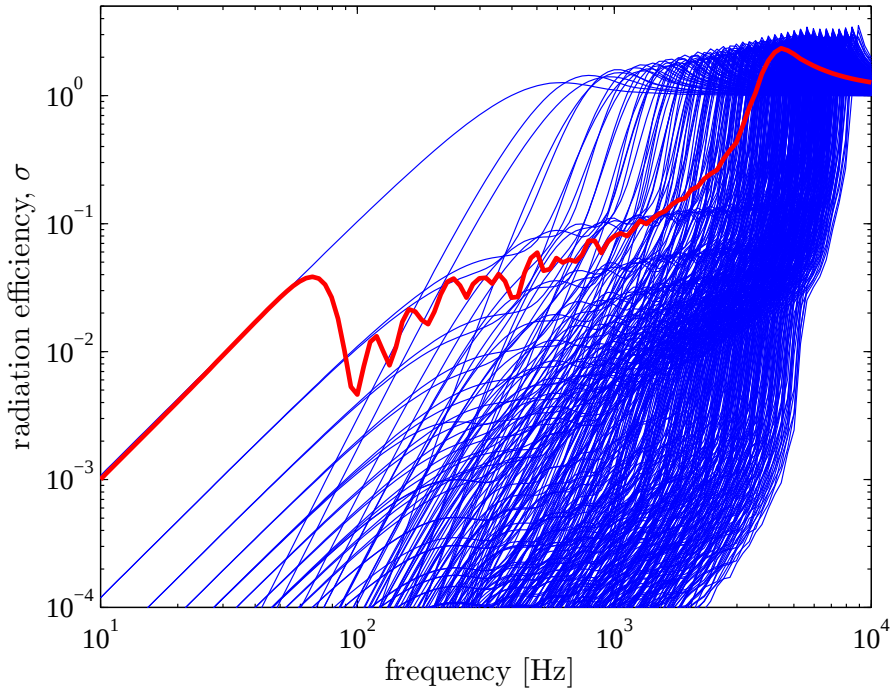


FIGURE 2.8: Modal and average radiation efficiency of a simply supported rectangular baffled plate ($0.65 \times 0.5 \times 0.003$ m aluminium plate with $\eta = 0.1$) using wavenumber decomposition: —modal radiation efficiency; — average radiation efficiency.

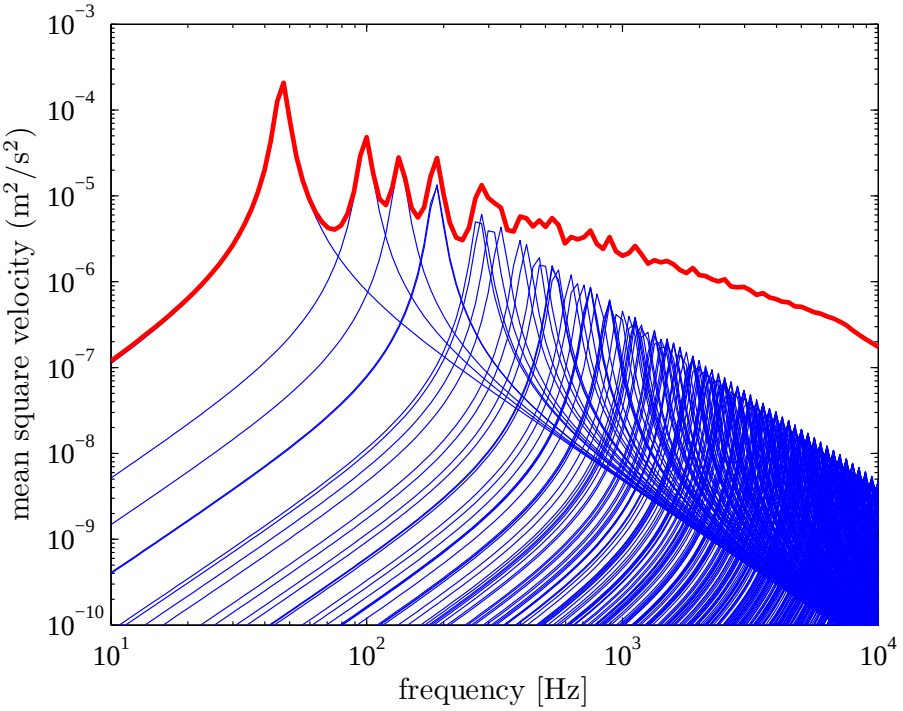


FIGURE 2.9: Contibution of modal mean square velocity (—) to total mean square velocity ( — ) of a rectangular plate ($0.65 \times 0.5 \times 0.003$ m aluminium plate with $\eta = 0.1$).

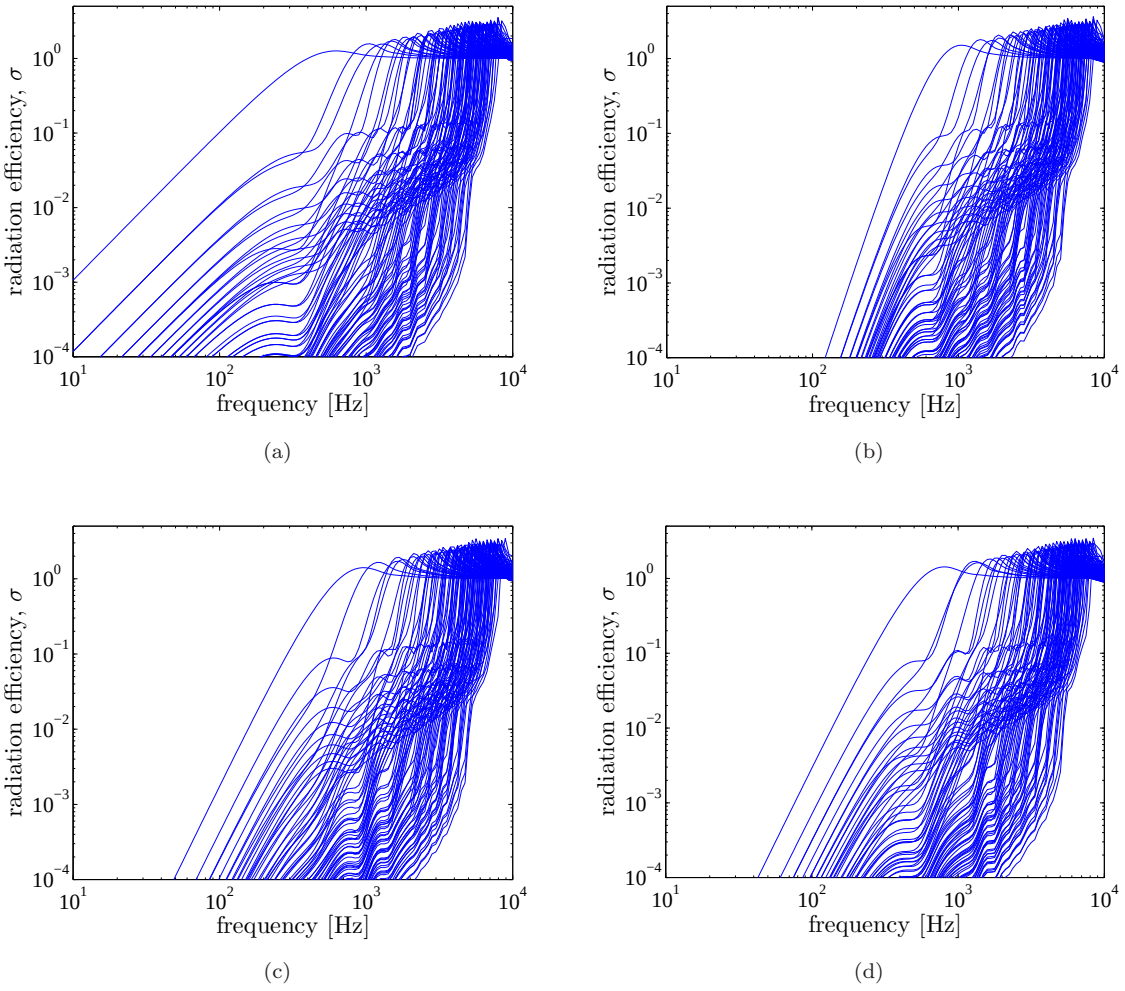


FIGURE 2.10: Self-radiation efficiency of each mode of a baffled plate (0.65 × 0.5 × 0.003 m aluminium plate with $\eta = 0.1$): (a) odd-odd modes; (b) even-even modes; (c) odd-even modes and (d) even-odd modes.

above this frequency for the number of modes given, there are not enough modes to obtain the true average of radiation efficiency up to 10 kHz. Nevertheless, as this is above the critical frequency, i.e. 4 kHz, the result still gives a good convergence to unity as expected.

It can be seen from the average radiation efficiency that the overall result below 70 Hz is determined by the first mode (mode (1,1)). The velocity of the plate, shown in Figure 2.9, indicates that the first mode dominates the response in this frequency region, and moreover it has the highest modal radiation efficiency. Above 70 Hz, the average radiation efficiency suddenly drops and then rises gradually until it reaches the maximum at about 4 kHz. This peak at about 4 kHz is the critical frequency.

Note that the plate resonances shown by the peaks in Figure 2.9 are the dips in the

radiation efficiency plot as seen in Figure 2.8. This is because the radiation efficiency is inversely proportional to the mean-square velocity (see Eq.(1.2)).

Figure 2.10 shows the modal radiation efficiencies of the various modes, separated into odd-odd, even-even, odd-even and even-odd modes. From Figure 2.8, the slope of the average radiation efficiency at frequencies below 70 Hz is 20 dB/decade ($\sigma \propto k^2$). It can be seen that this corresponds to the slope for the odd-odd modes, where the first mode (1,1) is dominant. Acting like monopole sources below 250 Hz, the odd-odd modes make the highest contributions to the sound radiation, see Figure 2.10(a). The odd-even in Figure 2.10(c) and the even-odd modes in Figure 2.10(d), with 40 dB/decade slope below 250 Hz, act like dipole sources ($\sigma \propto k^4$). They radiate sound less effectively than the odd-odd modes. Meanwhile the even-even modes resemble a quadrupole source behaviour. They have the lowest contributions to the sound radiation, with a slope of 60 dB/decade ($\sigma \propto k^6$) below 250 Hz, see Figure 2.10(b).

It is interesting to note that these slopes apply at low frequencies up to around 250 Hz. Above 250 Hz, where the greatest width of the plate (0.65 m) is more than half an acoustic wavelength, the curves are more complex, due to interference effect between the travelling waves that leads to a spatial variation in amplitude, before each rising to a peak at a frequency where the acoustic wavenumber equals the plate wavenumber in their mode.

### 2.4.2 Mode regions

From Figure 2.8, the fluctuation seen in the radiation efficiency between the first peak at low frequency (70 Hz) and the critical frequency is dominated by the 'corner' modes ($m\pi/a > k$ and $n\pi/b > k$) and 'edge' modes ($m\pi/a > k$, $n\pi/b < k$ or $m\pi/a < k$, $n\pi/b > k$). For corner modes the sound is radiated effectively from the plate corners, while the edge modes radiate sound from along the two plate edges on opposite sides. Close to the critical frequency where the radiation efficiency rises dramatically, all four edges of the plate effectively become a good radiator ($m\pi/a < k$, $n\pi/b < k$; but $((m\pi/a)^2 + (n\pi/b)^2)^{\frac{1}{2}} > k$) [4, 11]. Above the critical frequency, the whole plate surface effectively radiates sound into the air. Figure 2.11(a) illustrates the classification of mode regions in wavenumber space and Figure 2.11(b) shows the

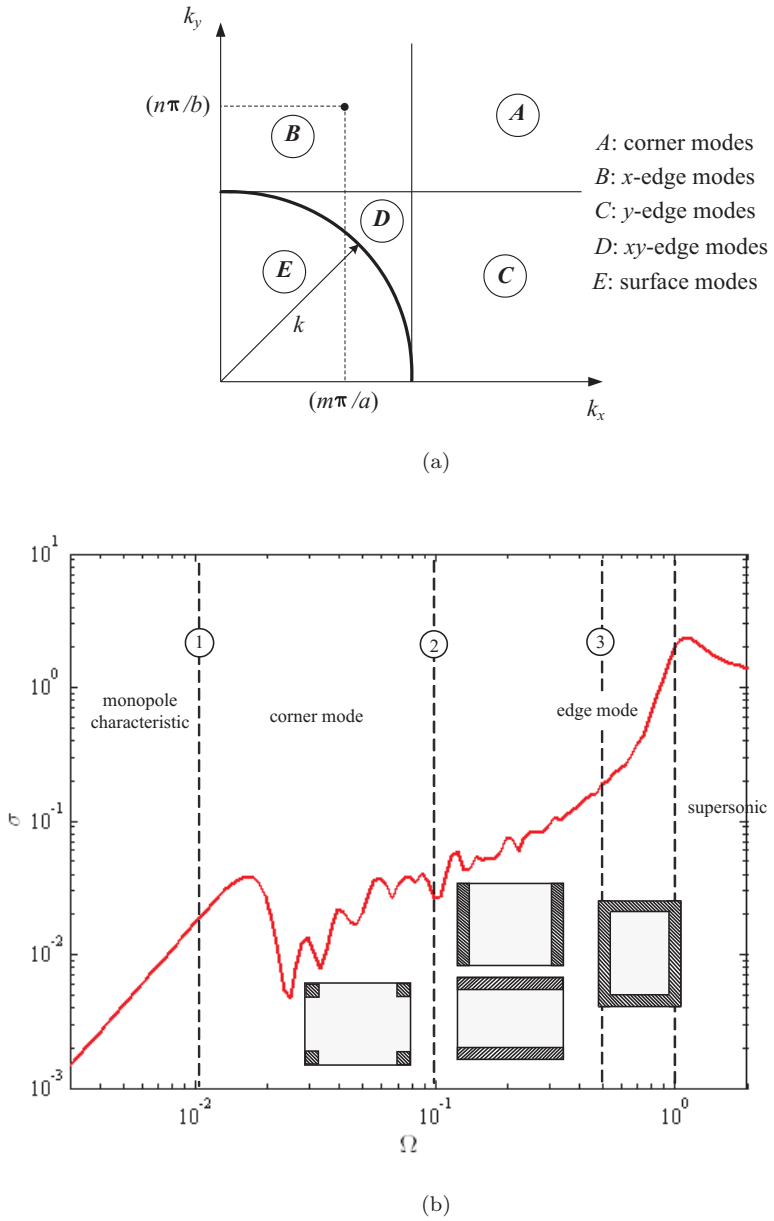


FIGURE 2.11: (a) classification of modes in wavenumber space relative to the acoustic wavenumber $k$ and (b) example of mode regions in the radiation efficiency curve.

regions in the radiation efficiency curve for the example of the plate given above, but now plotted against the normalised frequency $\Omega = f/f_c$. Note that the curve in Figure 2.11(b) is only applicable for thin plates with a moderate aspect ratio, $0.1 \leq \gamma \leq 1$ ($\gamma = a/b$, $a \leq b$). For a smaller plate dimensions with a greater thickness, the corner and edge mode regions will be narrower. The radiation efficiency curve for the case of a strip type plate ($\gamma \leq 0.1$) can be seen in [12].

The boundaries 1,2, and 3 in Figure 2.11(b) in terms of non-dimensional frequency $\Omega$ are given by [4, 10]

$$\begin{aligned}\Omega_1 &= \frac{\pi^2 B}{c^2 \rho_p t_p}\left(\frac{1}{a^2}+\frac{1}{b^2}\right)\\ \Omega_2 &= \frac{6\pi}{cP_s}\left(\frac{B}{\rho_p t_p}\right)^{1/2}\\ \Omega_3 &= 0.5\end{aligned} \tag{2.62}$$

where $P_s$ is the perimeter of the plate. In terms of frequency $f$, Eq.(2.62) can be written as

$$\begin{aligned}f_1 &= \frac{\pi}{2}\sqrt{\frac{B}{\rho_p t_p}}\left(\frac{1}{a^2}+\frac{1}{b^2}\right)\\ f_2 &= \frac{3c}{P_s}\\ f_3 &= \frac{f_c}{2}\end{aligned} \tag{2.63}$$

It can be seen from Eq.(2.63) that the boundary between corner and edge mode regions ($f_2$) depends only on the plate dimensions and not on the plate thickness.

In this thesis, the terminology "fundamental mode", "corner mode" and "edge mode" regions will be used to denote the frequency region in the radiation efficiency. In the remainder of the thesis, all results will be plotted as a function of dimensional frequency (Eq.(2.63)). This is chosen because, although non-dimensional frequency can eliminate the critical frequency, it does not eliminate the influence of bending stiffness, mass or thickness, as seen in Eq.(2.62).

### 2.4.3 Effect of damping

Figure 2.12 presents the average radiation efficiency for various values of the damping loss factor. This shows that the significant effect of damping on the sound radiation lies in the corner and edge mode regions. It can also be seen that the radiation from the first mode, which has the form of a monopole source, is not affected by the damping. The radiation efficiency is also independent of the damping above the critical frequency. However, the greatest damping effect can be seen between around 450 Hz and 4 kHz, i.e. in the edge mode region.

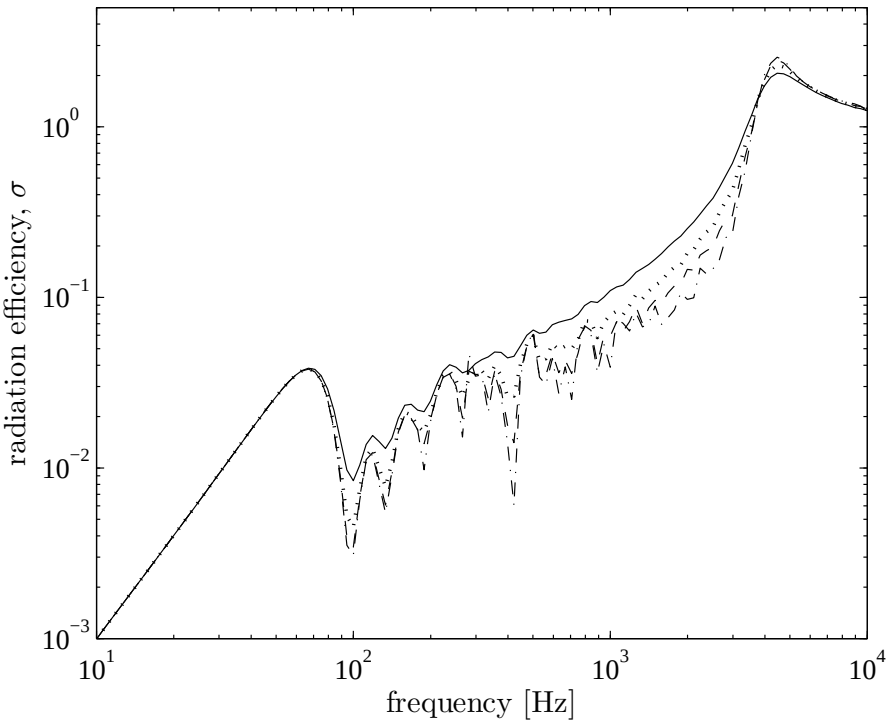


FIGURE 2.12: The average radiation efficiency of a baffled plate with different damping loss factors: —, 0.2; $\cdots$, 0.1; $--$, 0.05; $-\cdot-$, 0.01.

The modal velocity amplitude around each resonance decreases as the damping increases, see Eq.(2.5), and this also decreases the spatially averaged velocity. With higher damping, waves propagating from the force point decay faster so that the effect of the nearfield close to the force point has a greater importance relative to the contribution of resonant modes [4]. In the limit for high damping, the nearfield may dominate the sound radiation, which becomes independent of the damping. However the radiation efficiency is normalised by the spatially averaged squared velocity and consequently the radiation efficiency rises with increased damping.

It can be seen that the radiation efficiency curves, particularly for low damping, have considerable fluctuations at low frequency and become smoother as the frequency increases. This can be related to how many modes contribute in the frequency range of interest. It can be understood in terms of the response of the plate shown in Figure 2.9. Individual modes can still be differentiated at low frequencies (up to about 300 Hz), but at high frequencies, the modes are very dense so that the average response becomes almost a smooth curve. The modal density $n(\omega)$ determines the average number of natural frequencies in a unit frequency band. For bending waves on a plate, it is independent of frequency and is given by [7]

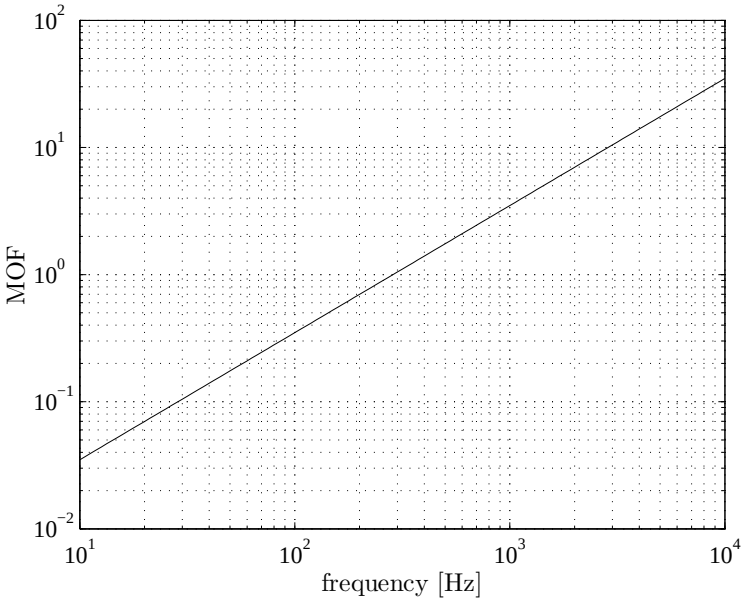


FIGURE 2.13: Modal overlap factor of the plate ($0.65 \times 0.5 \times 0.003$ m aluminium plate with $\eta = 0.1$).

$$n(\omega) = 0.276 \frac{S}{t_p c_L} \tag{2.64}$$

where $S$ is the plate area, $t_p$ is the plate thickness and $c_L = \sqrt{E/\rho_p(1-\nu^2)}$ is the longitudinal wavespeed in the plate. The modal overlap factor is given by

$$\text{MOF} = n(\omega)\omega\eta \tag{2.65}$$

where $\eta$ is the damping loss factor. This is shown in Figure 2.13 for $\eta = 0.1$. This indicates that MOF $= 1$ occurs at around 300 Hz. For a flat plate at high frequency, where MOF $\gg 1$, the contribution of single modes is of less interest than the average over several modes. In Figure 2.12 it can be seen that in this example the radiation efficiency curves become smoother above 300 Hz for $\eta = 0.2$, 600 Hz for $\eta = 0.1$ and 1200 Hz for $\eta = 0.05$, i.e. for MOF $> 2$.

### 2.4.4 Calculation time

Considering Eq.(2.22) in the spatial domain approach, the modal radiation efficiency is calculated by integrating over a hemisphere of farfield positions. Using the wavenumber domain scheme, the radiation efficiency is found directly for each wavenumber, but

integration is then performed over wavenumber components which contribute to the radiated sound. This method can also be used to plot the spectrum of the plate velocity [4] as a function of wavenumber. This gives a better insight into the mechanism of sound radiation.

Both methods involve double integrals. However in the spatial approach, the calculation has to deal with integrating factors of the form of $\sin(\sin(A)\cos(B))$ as expressed in Eq.(2.10), Eq.(2.22) and (2.23). To obtain a good accuracy of result, this form must be solved with a good resolution of integration segments. Consequently, this increases the calculation time. On the other hand in the wavenumber domain approach, the calculation can be performed more efficiently as the integration only employs the multiplication of the form of $\sin(A)$ or $\sin(B)$ (see Eq.(2.51)). Using a sufficient resolution, not necessarily as fine as that used in the spatial domain, this method can save a significant amount of calculation time.

Using MATLAB on a personal computer with the specification as in Table 2.1, the calculation using the wavenumber domain approach with $d\alpha = d\beta = 0.03$ based on 400 modes takes approximately 8 minutes. For the spatial domain approach to have a good convergence for frequencies up to 10 kHz, the error tolerance needed is $10^{-9}$. With the same number of modes, the calculation of the radiation efficiency takes more than 4 hours.

Despite the advantages of the FFT algorithm, the FFT approach is not found to be an efficient method to calculate the radiation efficiency. It is time consuming as the averaged Green's function $\overline{\overline{G}}$ needs to be constructed first before implementing the inverse FFT of the plate velocity for each frequency, and later calculating the acoustic power. As described in section 2.3, an accurate result needs a good resolution of sample points and a larger baffle is required to overcome the bias error at low frequency, especially in the first mode. The calculation of a single modal radiation efficiency for a $64 \times 64$ points FFT takes 11 seconds. The equivalent calculation is estimated to take more than 15 hours for the average over 400 modes. Therefore, the calculation of the average radiation efficiency using this method has not been pursued further here.

TABLE 2.1: Computer specification used for calculation

| | |
|---|---|
| Processor | Pentium IV |
| Processor speed | 3 GHz |
| Memory | 0.99 GByte |

## 2.5 Variability in radiation efficiency due to forcing position

In the previous sections, the average radiation efficiency of a simply supported plate was obtained from the summation over vibration modes. This method has the advantage that information is provided about the contribution of the various modes to the sound radiation. Moreover, no account is needed of the cross-modal radiation. However, often in practice the plate will be excited at a particular location and the sound radiation may differ from the result averaged over all possible point force positions.

In this section the distribution of the radiation efficiencies from several discrete point force positions is studied for a baffled plate. Despite the limitations of the FFT method noted above, it is found to be efficient to use the FFT approach for this investigation since it implicitly takes account of cross-modal radiation.

### 2.5.1 Method

The velocity of the plate $v(x, y)$ due to a single point force position at a location $(x_0, y_0)$ can be calculated as a sum of modes. Recalling Eq.(2.3), the expression is given by

$$v(x,y) = \sum_{m=1}^{\infty}\sum_{n=1}^{\infty} u_{mn}\varphi_{mn}(x,y) \tag{2.66}$$

where $\varphi_{mn}$ is the mode shape function from Eq.(2.4) and $u_{mn}$ is the complex velocity amplitude of the mode from Eq.(2.5).

The velocity in the wavenumber domain $\widetilde{V}(k_x, k_y)$ can then be obtained by applying the two-dimensional FFT to $v(x,y)$. Therefore, for each frequency, the FFT method

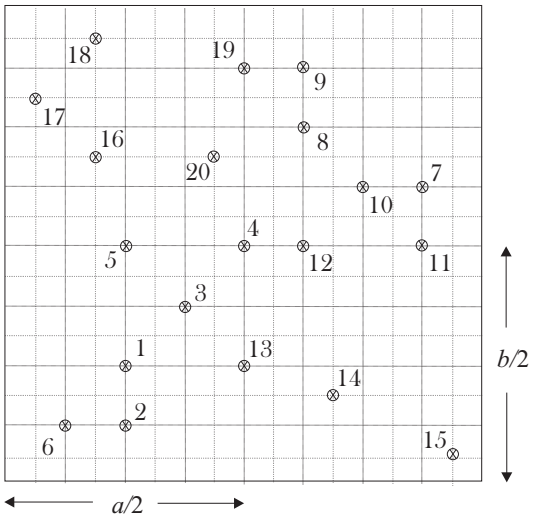


FIGURE 2.14: Locations of the point force on the plate surface.

for a simply supported baffled plate described in section 2.3 can be implemented, but now it is for the total velocity at each frequency, not on a mode-by-mode basis.

Results are calculated for 20 force points, scattered over on the plate surface as shown in Figure 2.14. The plate dimensions and properties are still the same as those in the previous sections. In the FFT method, the baffle length $L = 12.8$ m and the spacing sample $a_s = 0.03$ m are used. The radiation efficiencies obtained are plotted together in Figure 2.15.

### 2.5.2 Results

The results show the same trend as that of the average radiation efficiency, see Figure 2.8. It is clear that the radiation efficiencies from different point force positions only vary between about 50 Hz and the critical frequency around 4 kHz, i.e. mainly in the corner and edge mode regions. As these regions are the focus of observation, the bias error clearly seen at very low frequency due to the application of the FFT method can be ignored. It is also interesting to see that some high peaks appear in the variation. These peaks show that certain modes become dominant due to the absence of other certain modes. For instance from Figure 2.15, the radiation efficiency having the highest peak at around 140 Hz is obtained when the point force is applied at the middle of the plate (point No.4 in Figure 2.14). The excitation at the middle of the plate does not generate modes (2,1) or (1,2) because the force is applied exactly at

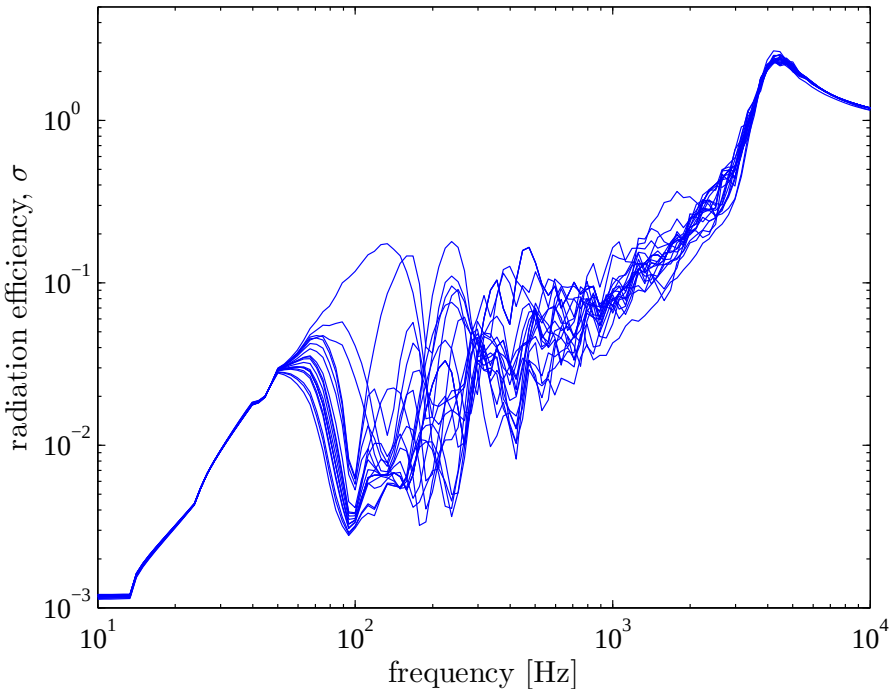


FIGURE 2.15: Distribution of radiation efficiency over 20 point force positions on the plate ($0.65 \times 0.5 \times 0.003$ m aluminium plate with $\eta = 0.1$).

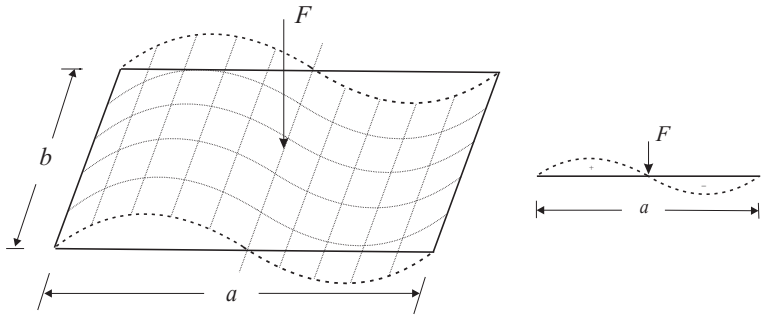


FIGURE 2.16: Excitation at the node point of mode (2,1).

the nodal point of these modes. This is illustrated in Figure 2.16. Mode (1,1) then becomes dominant in the response over a wider frequency range, leading to a higher overall radiation efficiency. That is why the knowledge of modes of vibration is useful at low frequencies especially when structural sensors and actuators are embedded in a structure in active control systems to reduce the sound radiation [4].

Figure 2.17 shows the range of the variation from the results such as Figure 2.15 corresponding to the 10% and 90% bands at each frequency in narrow bands and also in $\frac{1}{3}$ octave bands. These are arranged with increasing damping ($\eta = 0.05$, $\eta = 0.1$, $\eta = 0.2$) from top to bottom to investigate the variation with damping loss factor. As seen in the figure, the average radiation efficiency (calculated directly using the

wavenumber domain method) lies among the variations. It can also be seen that there is no significant change due to damping in the extent of the variation, except at a few specific frequencies.

Figure 2.18 shows the averaged and 10/90 percentile curves of the radiation efficiency for three different plate dimensions. These are calculated for different plate areas and aspect ratios. On average, this also shows that the variation of the radiation efficiency does not change significantly with the plate dimensions, although for a larger plate area as in Figure 2.18(a)-(b), the corner mode region has a slightly greater range of radiation efficiency compared with the same region in Figure 2.18(c)-(d) and Figure 2.18(e)-(f).

However, a clear change of variation can be seen in Figure 2.19. This maintains the plate dimensions but changes the thickness of the plate. It can be seen that the range of variation, especially in corner mode region, reduces as the thickness increases. This is due to the increasing of the plate bending stiffness as the thickness increases. For the same input power, a stiffer plate has less modes which then produces a smaller variation in the radiation efficiency.

Figure 2.20 shows the variability of the radiation efficiency for each case in narrow and $\frac{1}{3}$ octave bands plotted in decibels (dB) given by

$$\text{variability} = 10 \log_{10} \left( \frac{\sigma_{10}}{\sigma_{90}} \right). \tag{2.67}$$

where $\sigma_{10}$ and $\sigma_{90}$ denotes the radiation efficiency from 10 and 90 percentiles, respectively. It can be seen that all cases produce similar pattern of variability where it is high in corner mode region and then it declines in the edge mode region with increasing frequency.

In Figure 2.20(a)-(b), no consistent effect of damping can be clearly observed, except around the peaks at 160 Hz and 230 Hz where the variation increases with reduced damping.

The same phenomenon can also be seen in In Figure 2.20(c)-(d). The variation is similar except that the curves are shifted due to different location of the corner mode region in frequency with differing plate dimensions (perimeter), see Eq.(2.63). From

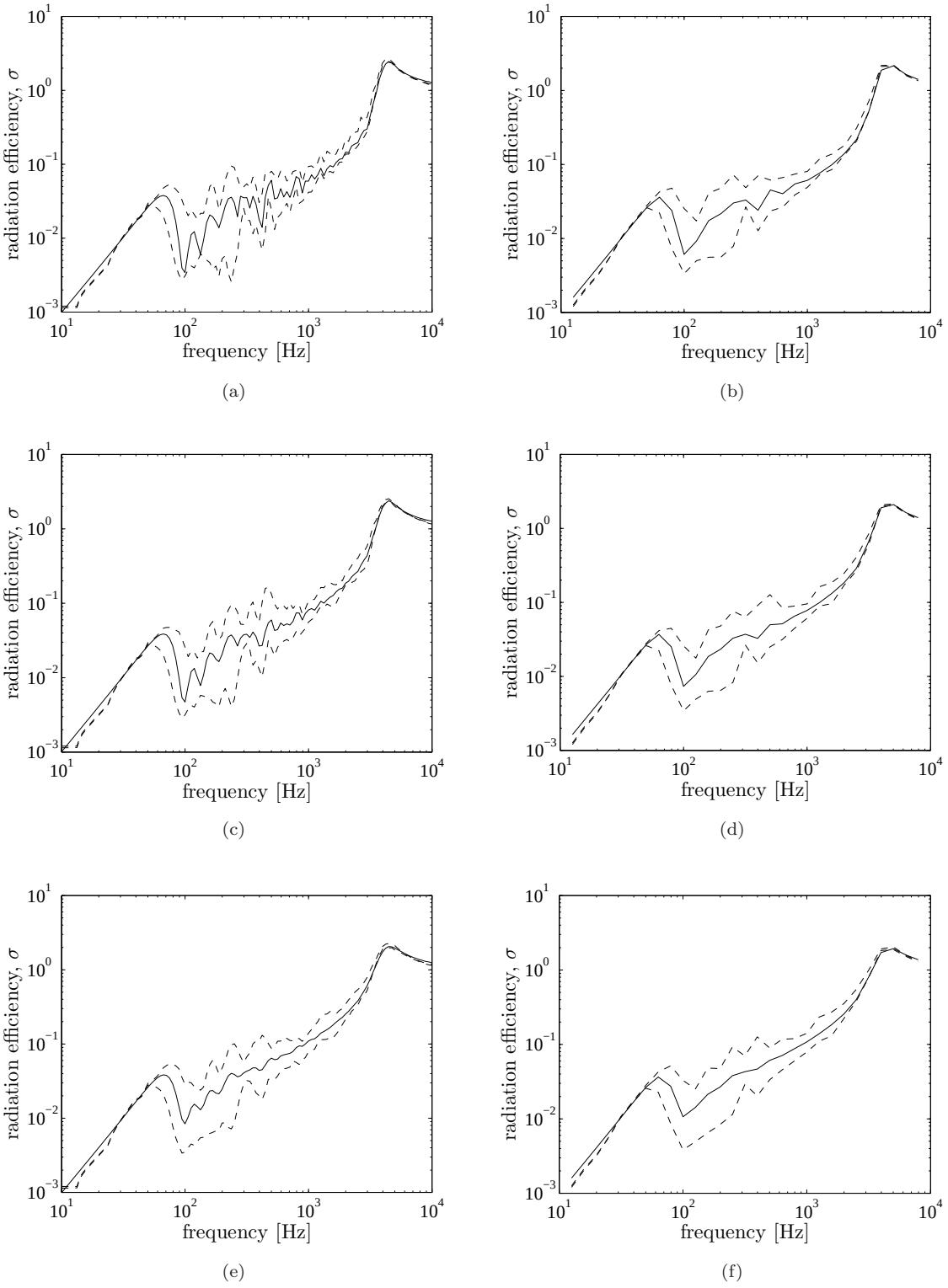


FIGURE 2.17: Range of radiation efficiency variation using 10/90 percentiles (−−) and average radiation efficiency (—) in narrow band (left column) and $\frac{1}{3}$ octave bands (right column) ($0.65 \times 0.5 \times 0.003$ m aluminium plate with: (a)-(b) $\eta = 0.05$, (c)-(d) $\eta = 0.1$, (e)-(f) $\eta = 0.2$).

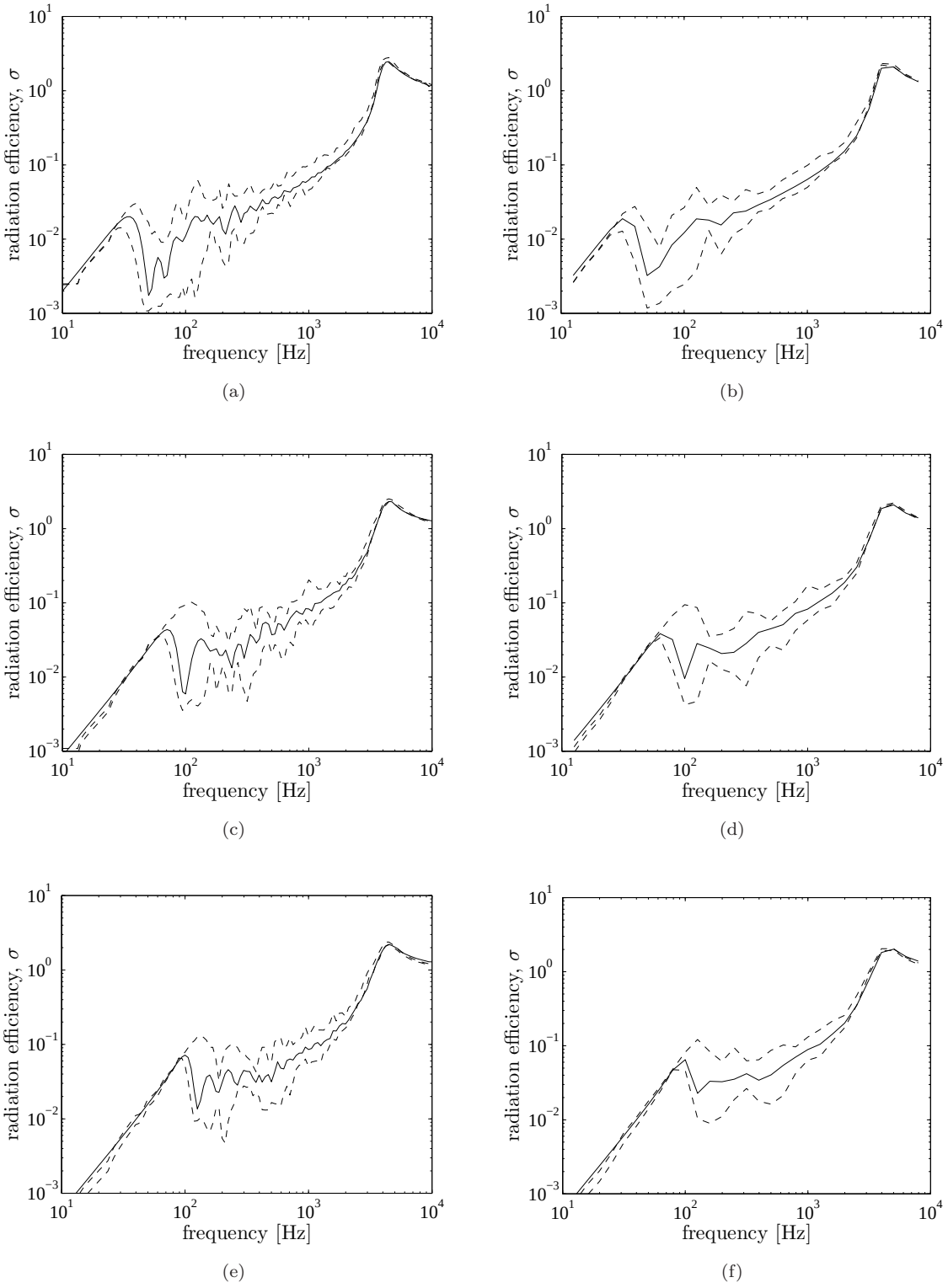


FIGURE 2.18: Range of radiation efficiency variation using 10/90 percentiles (−−) and average radiation efficiency (—) in narrow band (left column) and $\frac{1}{3}$ octave bands (right column) (aluminium plate, $\eta = 0.1$; (a) $0.9 \times 0.7 \times 0.003$ m, (b) $0.4 \times 0.75 \times 0.003$ m and (c) $0.8 \times 0.3 \times 0.003$ m).

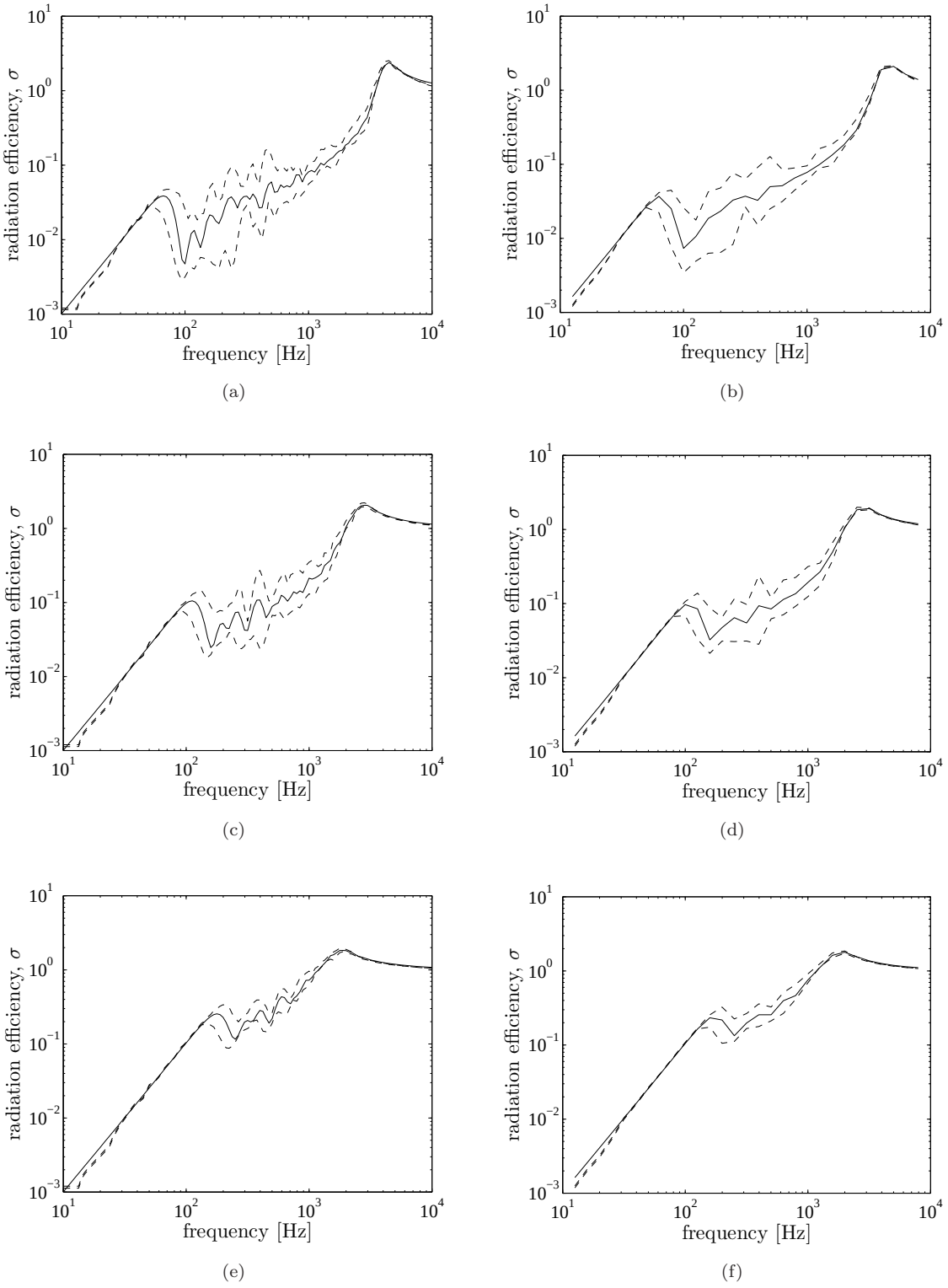


FIGURE 2.19: Range of radiation efficiency variation using 10/90 percentiles (−−) and average radiation efficiency (—) in narrow band (left column) and $\frac{1}{3}$ octave bands (right column) (aluminium plate, $\eta = 0.1$; (a) $0.65 \times 0.5 \times 0.003$ m, (b) $0.65 \times 0.5 \times 0.005$ m and (c) $0.65 \times 0.5 \times 0.008$ m).

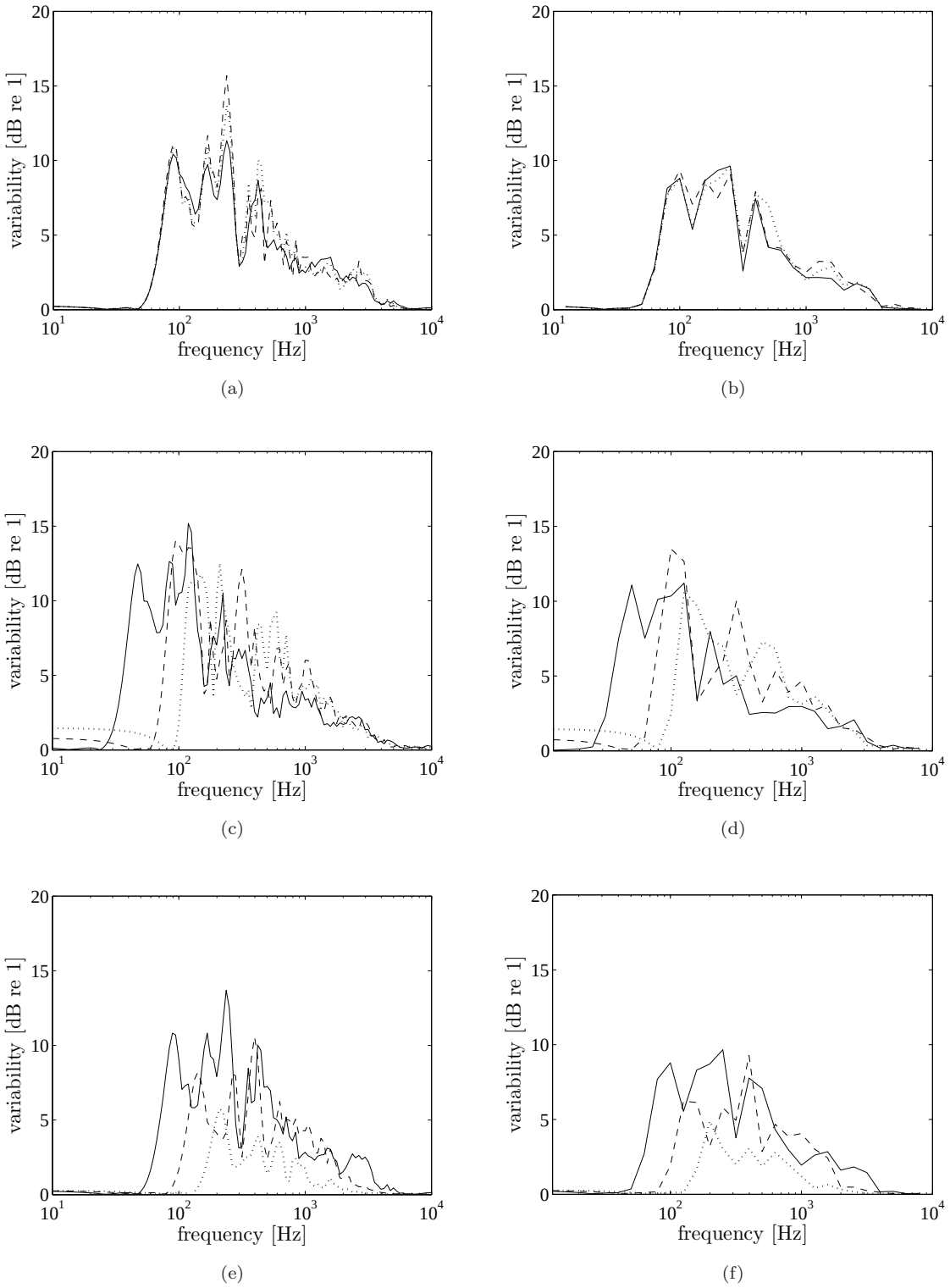


FIGURE 2.20: Variability of radiation efficiency of an aluminium rectangular plate from 10/90 percentiles in narrow band (left column) and $\frac{1}{3}$ octave bands (right column): (a)-(b) $0.65 \times 0.5 \times 0.003$ m; $\cdots \eta = 0.01$, —$\eta = 0.05$, $--\ \eta = 0.1$, (c)-(d) $\eta = 0.1$; —$0.9 \times 0.7 \times 0.003$ m, $--\ 0.4 \times 0.75 \times 0.003$ m, $\cdots 0.8 \times 0.3 \times 0.003$ m, (e)-(f) $\eta = 0.1$; —$0.65 \times 0.5 \times 0.003$ m, $--\ 0.65 \times 0.5 \times 0.005$ m, $\cdots 0.65 \times 0.5 \times 0.008$ m.

Figure 2.20(b) and Figure 2.20(d), it is shown that for a 3 mm thick plate, the variation of the radiation efficiency in $\frac{1}{3}$ octave bands is around $\pm 5$ dB in the corner mode region.

Figure 2.20(e)-(f) shows the effect of the plate thickness on the variability. It is clearly shown that the variability reduces as the plate thickness increases.

Another interesting phenomenon is that the variability is lower at the plate resonances. From Figure 2.20(a), one can note that the dips in the variability, for example around 140 Hz and 190 Hz, correspond to peaks in the mean-square velocity of the plate, i.e. the resonances, as seen in Figure 2.9. Conversely, one can see that the peaks in the variability correspond to the dips in the mean-square velocity of the plate, not to resonances. A similar phenomenon occurs in each case in Figure 2.18 and Figure 2.19.

## 2.6 Conventional modal-average radiation efficiency

Besides the analytical method described in the previous sections, predictions of the sound radiation from a rectangular plate set in an infinite baffle are widely used, particularly using the simple modal-average formulae of Maidanik [5]. This approach is more efficient although more restricted in its assumptions. This model was based on the assumption of equal modal vibration energy in a number of modes in a frequency band (requiring a high modal density and an average over force locations) for a lightly damped plate. The formulae have been summarized in [70] as follows

$$\sigma = \begin{cases} \dfrac{4S}{c^2} f^2 , & f < f_{1,1},\ f_{1,1} = \dfrac{\pi}{2}\sqrt{\dfrac{B}{\rho_p t_p}}\left(\dfrac{1}{a^2}+\dfrac{1}{b^2}\right) \\ \dfrac{4\pi^2}{c^2 S}\dfrac{B}{\rho_p t_p} , & f_{1,1} < f < f_e,\ \ f_e = \dfrac{3c}{P_s} \\ \dfrac{P_s c}{4\pi^2 S f_c} \times \dfrac{(1-\alpha^2)\ln\left(\dfrac{1+\alpha}{1-\alpha}\right)+2\alpha}{(1-\alpha^2)^{3/2}} , & f_e < f < f_c,\ \ \alpha = \sqrt{\dfrac{f}{f_c}} \\ 0.45\sqrt{\dfrac{P_s f_c}{c}} , & f = f_c \\ \left(1-\dfrac{f_c}{f}\right)^{-1/2} , & f > f_c \end{cases} \tag{2.68}$$

where $P_s$ is the perimeter of the plate, $f_{1,1}$ is the fundamental frequency of the plate, $B$ is the bending stiffness, $\rho_p t_p$ is the mass per unit area of the plate and $f_c$ is the critical frequency.

The first term is the monopole characteristic of the fundamental mode. This has also been derived by Wallace [6] for the radiation efficiency below the fundamental natural frequency

$$\sigma_{1,1} = \frac{32k^2 S}{\pi^5} = \frac{128}{\pi^3 c^2} S f^2 \approx \frac{4S}{c^2} f^2 \tag{2.69}$$

The second term is the approximation for the corner mode region. However, according to Leppington *et al.* [11] and Xie *et al.* [12], the first and second terms are only valid for moderate aspect ratio, $0.1 \leq \gamma \leq 1$ ($\gamma = a/b$, $a \leq b$). For the case of a strip ($\gamma \leq 0.1$), the edge modes will dominate the corner mode region.

The third term in Eq.(2.68) is the edge mode region. For this region, a second term is presented in [70] but this is often neglected and is not presented here.

For a point-excited plate with a higher damping loss factor $\eta$, the effect of damping can be included into the formulae by introducing an equivalent radiation efficiency to account for the near-field of a point force [4, 7] i.e.

$$\sigma_n = \frac{4f}{\pi f_c}\eta, \qquad f < f_c \tag{2.70}$$

As explained in Section 2.4, when the damping increases, the plate displacement becomes concentrated only in the vicinity of the driving force. Therefore for a plate with high damping, it can be misleading to average the plate surface velocity when the velocity which is relatively far from the excitation point is much less than that near the excitation point. Thus according to Eq.(1.2) the radiation efficiency increases as the spatially averaged mean-square velocity decreases due to the increased damping, assuming that the sound power from the near-field is unchanged. Eq.(2.70) supports this assumption. Therefore it is less appropriate to judge the radiated noise from a plate having a high damping by its 'radiation efficiency' rather than by its radiated 'sound power' per unit mean square force. In other words, the definition of 'radiation efficiency' is less useful if a plate has a high damping.

The prediction of the radiation efficiency including the effect of damping can be written as

$$\sigma = \sigma_0 + \sigma_n \tag{2.71}$$

where $\sigma_0$ is the radiation efficiency for a very lightly damped plate. This technique has been implemented by Xie *et al.* [12] and has been compared with the prediction results from the modal summation approach. Figure 2.21 reproduces the results for the plate geometry considered here for various damping loss factors. This shows a good agreement over a wide range of frequency. The prediction from Eq.(2.68, 2.70, 2.71) overestimates the dips in the corner mode region and also underestimates the result at around 100 Hz which is dominated by the first mode.

## 2.7 Summary

Several analytical and numerical methods for calculating the radiation efficiency of a vibrating plate set in an infinite baffle have been implemented and evaluated. It was found that the wavenumber domain approach is the most effective method to calculate the radiation efficiency, particularly in terms of the summation of the modal responses.

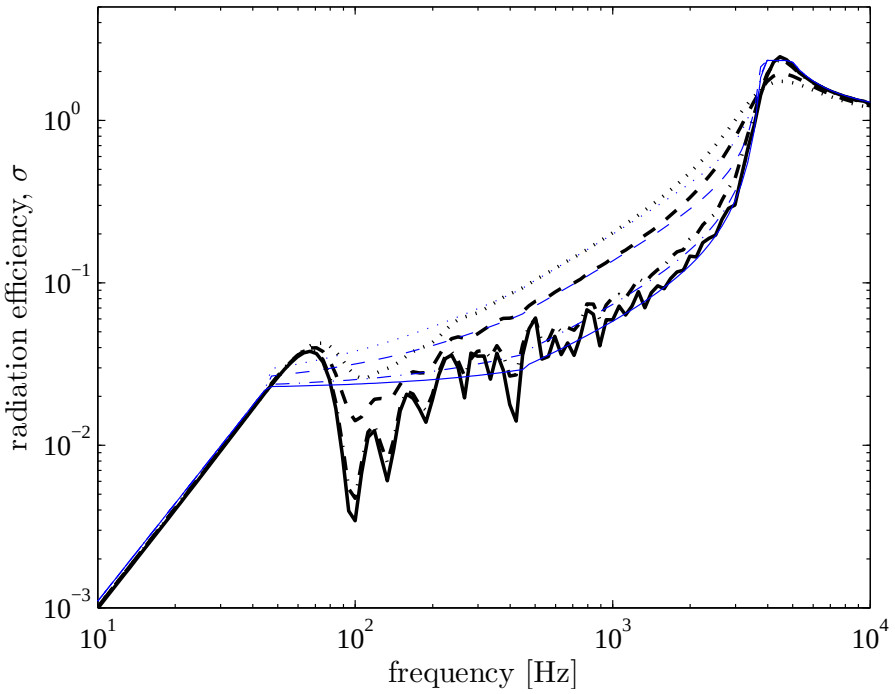


FIGURE 2.21: The average radiation efficiency of a simply supported baffled plate from Eq.(2.71) (thin line, blue) and the modal summation approach (thick line) : —$\eta = 0.05$, $-\cdot-\eta = 0.1$, $--\eta = 0.3$, $\cdots\eta = 0.5$.

The spatial domain approach needs a higher resolution of integration segments to obtain a result with a good accuracy, which increases the calculation time considerably. The FFT method is also not effective where more integration segments are needed to define the baffle. At low frequency, this requires a larger baffle and hence more sample points to overcome the bias error due to the overlapped pressure. Moreover, a finer resolution is needed to give a good accuracy for higher modes which are important at high frequencies.

The variability in radiation efficiency of a typical plate due to variations in the location of a single forcing point is found to be higher in the corner mode region. For 3 mm thick plate, the variation relative to the average radiation efficiency is around a factor of three ($\pm$ 5 dB). This variation reduces as the plate thickness increases. It is important to consider this variation in practice, for example in experimental statistical energy analysis (SEA) where 'acoustic' power is injected to a subsystem by an impact hammer excitation at several locations on the plate [68].

# Chapter 3

# Radiation efficiency of an unbaffled plate

In practice, vibrating plates are not set in a baffle and the opposite extreme of an unbaffled plate is also important. As long as the sound field from one side can interact with that from the other side of the plate, the plate condition can be categorised as unbaffled. Unlike the baffled plate, where the velocity is known to be zero on the rigid baffle, for the unbaffled plate the particle velocity is not known outside the plate region. However, it is known that the pressure is zero beyond the plate in its plane. This makes the task of solving the sound radiation from an unbaffled plate more complicated than that from the baffled plate. This chapter discusses existing methods for calculating the radiation efficiency from an unbaffled plate. Simply supported boundary conditions of the plate are again used for simplicity.

## 3.1 Iterative scheme using the FFT

### 3.1.1 Algorithm

Continuing the FFT method for calculating the sound radiation for baffled plates, Williams [29] also developed this method for application to unbaffled, finite plates. This involves using an iterative scheme based on the Rayleigh integral and its inverse

expressed in the wavenumber domain. The FFT algorithm is then implemented to evaluate them.

Applying the averaged Green's function used in the baffled plate calculation in section 2.3, Eq.(2.58) gives the Rayleigh integral formula as

$$p(x,y,0) = j\omega\rho\mathscr{F}^{-1}\left[\widetilde{V}(k_x,k_y)\overline{\widetilde{G}}(k_x,k_y,0)\right] \tag{3.1}$$

Inverting Eq.(3.1) gives

$$v(x,y) = -(j/\omega\rho)\mathscr{F}^{-1}\left[\widetilde{P}(k_x,k_y)/\overline{\widetilde{G}}(k_x,k_y,0)\right] \tag{3.2}$$

In the case of a baffled plate, the velocity is defined on the plate and is zero on the baffle. This velocity is then used to determine the pressure everywhere. For an unbaffled plate, neither the velocity nor the pressure are fully known and therefore an iterative procedure is employed. The velocity is used to estimate the pressure on the plate, and then the pressure is used to calculate the velocity beyond the plate. Eq.(3.1) and (3.2) are the basic formulae used in the iteration process, as explained below.

Assuming $\mathbb{P}$ is the plate region and $\mathbb{E}$ is the exterior region in the plane of the plate, the mixed boundary condition for the unbaffled plate is $v(x,y) = v_i(x,y)$ on $\mathbb{P}$ and $p(x,y,0) = 0$ on $\mathbb{E}$, where $v_i(x,y)$ is the given velocity. Note that in the FFT method, $\mathbb{E}$ is only defined over an aperture of dimensions $L \times L$.

The following iteration algorithm is used:

1. Start with the boundary condition for the baffled plate, i.e. $v(x,y) = v_i(x,y)$ on $\mathbb{P}$ and $v(x,y) = 0$ on $\mathbb{E}$ on the plane at $z = 0$. For a simply supported plate, Eq.(2.3) is used for $v_i(x,y)$. Implement the two dimensional FFT to find $\widetilde{V}(k_x,k_y)$ (see section 2.3).

2. Use Eq.(3.1) to obtain $p(x,y,0)$. Retain this solution for $\mathbb{P}$ but set $p(x,y,0) = 0$ on $\mathbb{E}$.

3. Find $\widetilde{P}(k_x, k_y)$ using the FFT and calculate the new $v(x, y)$ for the whole plane at $z = 0$ from Eq.(3.2).

4. Check the root mean square error (RMSE) of the reconstructed velocity field on $\mathbb{P}$ from

$$\epsilon = \sqrt{\frac{1}{N}\sum_{0}^{N} \mid [v(x,y) - v_i(x,y)] \mid^2} \tag{3.3}$$

where $N$ is the total number of points considered on the plate region $\mathbb{P}$.

5. If the RMSE is more than a certain tolerance, the iteration is repeated from the first step by setting $v(x, y) = v_i(x, y)$ on P and leaving $v(x, y)$ unchanged on $\mathbb{E}$.

When the iteration is stopped, the boundary condition in the exterior region $\mathbb{E}$, $p(x, y, 0) = 0$ should also be closely achieved. Williams [29] found that for RMSE less than 0.005, for a unit maximum amplitude of $v_i(x, y)$, the pressure magnitude on $\mathbb{E}$ was generally three orders of magnitude below its maximum value on $\mathbb{P}$.

Equivalent approaches for calculating the radiated power as those used for the baffled plates can be employed, either by integrating over the spatial domain or over the wavenumber domain using Eq.(2.59) or Eq.(2.60) respectively.

### 3.1.2 Convergence problem

Figure 3.1 plots the radiation efficiency of mode (1,1) using both approaches (spatial or wavenumber domains) to calculate the radiated power (Eq.(2.59) and Eq.(2.60)) for a plate having the same dimensions and properties as in the previous sections. From Figure 3.1(a) and (c), it can be seen that using the spatial domain integration, the calculation results in a discontinuity below 100 Hz. Some results are actually negative. This limitation of using the spatial domain could be because the calculation includes all the wavenumbers; those outside the radiation circle that contribute to the non-propagating waves may not cancel each other at low frequencies due to numerical inaccuracies. Meanwhile, positive results are obtained over the whole frequency range using the wavenumber domain integration for $a_s = 0.1$ m, but the slope of the graph deviates below 50 Hz for $L = 6.4$ m. This is due to a bias error from the replicated

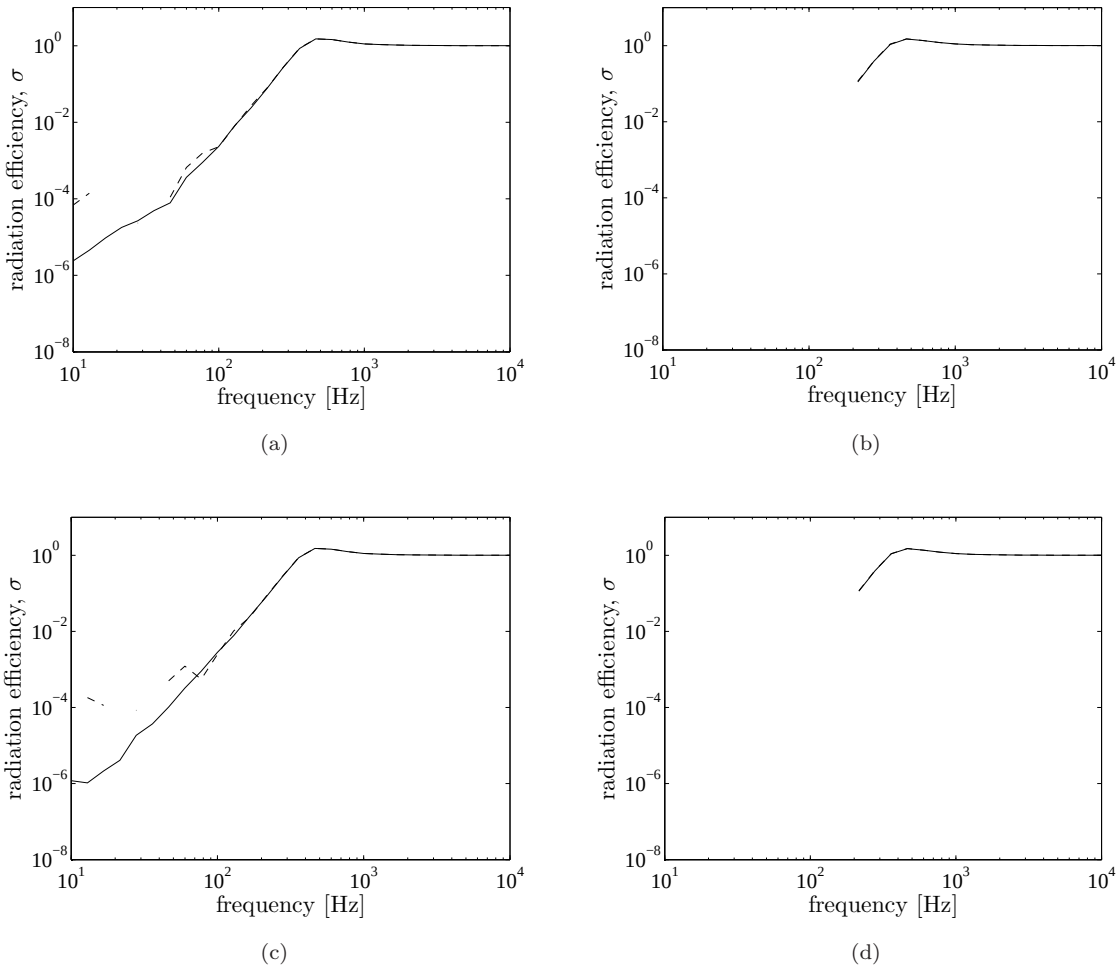


FIGURE 3.1: Radiation efficiency of mode (1,1) of a simply supported unbaffled plate using the FFT method: (a) $L = 6.4$ m, $a_s = 0.1$ m, (b) $L = 6.4$ m, $a_s = 0.05$ m, (c) $L = 12.8$ m, $a_s = 0.1$ m and (d) $L = 12.8$ m, $a_s = 0.05$ m. $--$, spatial domain; —, wavenumber domain (aluminium plate: $0.65 \times 0.5 \times 0.003$ m, $\eta = 0.1$).

sources (outside the window $L \times L$) as explained in section 2.3.1. This can be overcome by using a larger aperture, i.e. in this case $L$ is increased to 12.8 m, see Figure 3.1(c).

Convergence problems appear due to the sample spacing used, $a_s$. It is found that using $a_s \leq 0.05$ m, the results for both values of $L$ fail to converge below 200 Hz as seen in Figure 3.1(b) and (d). This might be due to the pressure discontinuity at the plate edge. It is interesting to note that, for an unbaffled disc of radius $a$, Williams [29] found that the mean square error did not converge for $ka < 1.7$. The results shown here suggest that this is connected with the sample spacing $a_s$ rather than the size of the radiating plate. Unfortunately finer resolution is required to represent higher order modes so that it appears that this iterative FFT method cannot cope satisfactorily with higher order plate modes.

## 3.2 Wavenumber domain using modal basis

Laulagnet [33] has proposed a numerical evaluation for calculating the sound radiation from a simply supported unbaffled plate, where the pressure jump and the plate displacement are developed as a sum over the plate modes. This method is explained in this section.

### 3.2.1 Derivation of equations

Consider a flat thin unbaffled plate with a surface area $S_p$ located in an infinite medium, excited by a harmonic force distribution $F(x, y)$ of angular frequency $\omega$. $\Delta p(x, y)$ is the difference of the acoustic surface pressure on the two side of the plate. Thus the pressure jump across the plate due to the transverse motion is given by

$$\Delta p(x, y) = p^-(x, y) - p^+(x, y) \tag{3.4}$$

where $p^-(x, y)$ and $p^+(x, y)$ are the surface pressure at $z = 0_-$ and $z = 0_+$ respectively. By symmetry $p^- = -p^+$.

The force distribution is assumed to act normal to the plate. One can apply the equation of motion expressed as

$$B\nabla^4 w(x, y) - m_p\omega^2 w(x, y) = F(x, y) + \Delta p(x, y) \tag{3.5}$$

where $B$ is the bending stiffness, $m_p$ is the mass per unit area, $w(x,y)$ is the transverse displacement of the plate and $\nabla^4$ is given by

$$\nabla^4 = \frac{\partial^4}{\partial x^4} + \frac{2\partial^4}{\partial x^2\, \partial y^2} + \frac{\partial^4}{\partial y^4} \tag{3.6}$$

The pressure anywhere in the volume encompassing the plate can be found by using the Green's function, see Figure 3.2. Applying the Kirchhoff-Helmholtz (K-H) integral theorem, the pressure in the surrounding fluid can be expressed by [4, 71]

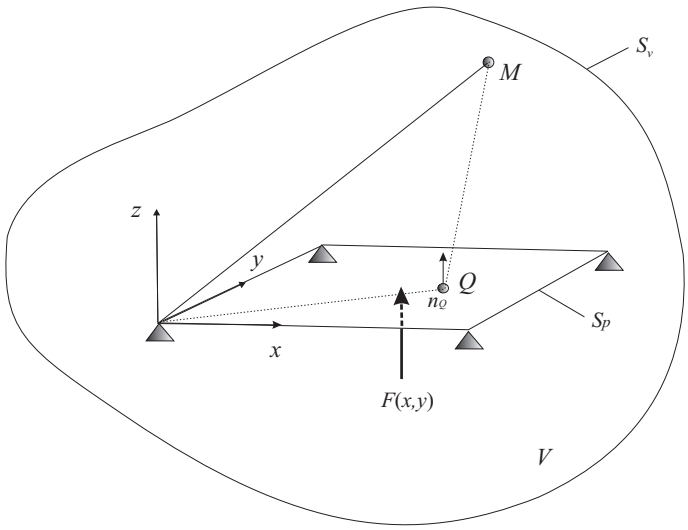


FIGURE 3.2: A simply supported plate enclosed by a volume $V$ in the medium with its bounding surface $S_v$.

$$p(M) = \int_{S_v} \left( p(Q) \frac{\partial G(Q,M)}{\partial n_Q} - G(Q,M) \frac{\partial p}{\partial n_Q} \right) dS_v \tag{3.7}$$

where $M$ denotes a point in the medium, $n_Q$ is the normal to the surface taken at point $Q$ on the plate, $G(Q,M) = e^{-jkR}/4\pi R$ is the free-field Green's function with $R$ the distance between points $Q$ and $M$. The surface $S_v$ covers both sides of the plate plus a surface at infinity.

Considering that only outgoing waves from the plate are allowed in the calculation, the surface integral in Eq.(3.7) can be reduced to $S_p$, i.e. the whole surface of the plate, $S_{p+}$ and $S_{p-}$. The surface at infinity is neglected since it is assumed that there is no wave reflected back to the plate.

To help visualise this equation, the plate can be considered as consisting of discrete elementary sources. The first term in the K-H equation is the dipole term representing the presence of a body in obstructing the free passage of sound, both that generated by its own normal motion (monopole source) and that incident upon it due to any other sources [71]. As the sound pressure appears both in the left and right hand sides of the equation, the sound pressure on the surface is a dependent variable. The elementary sources cannot be treated as isolated monopole sources because they are operating in the presence of other elementary sources from the remainder of the body [4]. The second term represents the monopole contribution which is proportional to the normal acceleration of the plate surface. From the linearized equation of momentum

conservation

$$\frac{\partial p}{\partial n_Q} = -\rho \frac{\partial v_n}{\partial t} \tag{3.8}$$

where $v_n$ is the normal plate velocity at $Q$.

The free field Green's function $G$ must satisfy

$$\nabla^2 G(Q, M) + k^2 G(Q, M) = \delta(x - x_0)\delta(y - y_0)\delta(z - z_0) \tag{3.9}$$

where $\delta$ is the Dirac delta distribution; $Q$ is at $(x,\ y,\ z)$ and $M$ is at $(x_0, y_0, z_0)$. By using the two dimensional spatial Fourier transform of Eq.(3.9), the Green's function can be expressed as [72]

$$G = \frac{j}{8\pi^2} \int_{-\infty}^{\infty} \int_{-\infty}^{\infty} \frac{e^{jk_x(x-x_0)} e^{jk_y(y-y_0)} e^{jk_z|z-z_0|}}{k_z}\, dk_x\, dk_y \tag{3.10}$$

where $k_z = \sqrt{k^2 - k_x^2 - k_y^2}$.

Restricting attention to the pressure at a point $M$ above the plate (in the half space $V^+$, $z_0 \geq 0$), by considering the normal vector $\mathbf{n}$ parallel to the $z$-axis and pointing into the fluid as illustrated in Figure 3.3, the K-H integral in Eq.(3.7) can be decomposed as

$$\begin{aligned} p(M) = &\int_{S_{p+}} p^+(Q) \frac{\partial G(Q, M)}{\partial z_Q}\, dS_{p+} - \int_{S_{p-}} p^-(Q) \frac{\partial G(Q, M)}{\partial z_Q}\, dS_{p-} \\ &- \int_{S_{p+}} G(Q, M) \frac{\partial p^+}{\partial z_Q}\, dS_{p+} + \int_{S_{p-}} G(Q, M) \frac{\partial p^-}{\partial z_Q}\, dS_{p-} \end{aligned} \tag{3.11}$$

where $M \in V^+$.

Since the plate thickness is assumed to be very small compared with its length and width, the normal velocity can be assumed equal on $S_{p+}$ and $S_{p-}$. From Eq.(3.8) therefore $\partial p / \partial z_Q$ is equal on both side of plate. Thus from Eq.(3.11), it is obtained that

$$\int_{S_p} G(Q, M) \left( \frac{\partial p^-}{\partial z_Q} - \frac{\partial p^+}{\partial z_Q} \right) dS_p = 0\,, \qquad Q \in S_p \tag{3.12}$$

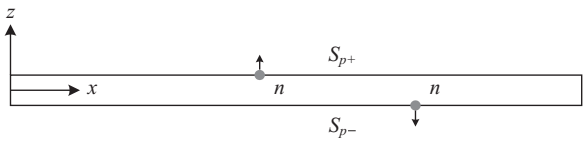


FIGURE 3.3: Agreement of normal vector **n** on the plate

Therefore the monopole term vanishes, leaving only the dipole term, which is related the discontinuity of the acoustic surface pressure

$$p(M) = -\int_{S_p} \Delta p \frac{\partial G(Q,M)}{\partial z_Q}\, dS_p \tag{3.13}$$

Substituting Eq.(3.5) for $\Delta p$ into Eq.(3.13) yields

$$p(M) = \int_{S_p} \left[F(x,y) + m_p\omega^2 w(x,y) - B\nabla^4 w(x,y)\right] \frac{\partial G(Q,M)}{\partial z_Q}\, dS_p \tag{3.14}$$

where $Q \in S_p$, $M \in V^+$.

The two unknown fields, i.e. the acoustic field $p(M)$ and the vibration of the plate $w(Q)$ in Eq.(3.14) can be related using Eq.(3.8). Since $v_n = j\omega w\, e^{j\omega t}$, in the plane of the plate at $z$=0

$$\begin{aligned} \frac{\partial p}{\partial z}(M)\Big|_{z=0} &= \rho\,\omega^2 w(M) \\ &= \int_{S_p} \left[F(Q) + m_p\omega^2 w(Q) - B\nabla^4 w(Q)\right] \frac{\partial^2 G(Q,M)}{\partial z_Q \partial z_M}\, dS_p \end{aligned} \tag{3.15}$$

where $\partial/\partial z_Q$ and $\partial/\partial z_M$ are the derivatives in the $z$ direction at $Q$ and $M$ respectively. Eq.(3.15) can be solved to find the displacement $w$.

### 3.2.2 Integral solution using modal summation

The displacement can be considered as the summation of a series of plate modes. Similar to Eq.(2.3) for the velocity, the displacement can be expressed as

$$w(x,y) = \sum_{m=1}^{\infty}\sum_{n=1}^{\infty} d_{mn}\varphi_{mn}(x,y) \tag{3.16}$$

where $d_{mn}$ is the modal displacement amplitude and $\varphi_{mn}$ is the associated mode shape function as in Eq.(2.4).

The same form of modal series can also be applied for the excitation force,

$$F(x,y) = \sum_{m=1}^{\infty}\sum_{n=1}^{\infty} F_{mn}\varphi_{mn}(x,y) \tag{3.17}$$

where $F_{mn}$ is the generalized force density for mode $(m,n)$. This can be recovered by multiplying by $m_p\varphi_{pq}(x,y)$ and integrating over the plate area $S_p$

$$F_{pq} = \frac{m_p}{M_{pq}}\int_{S_p} F(x,y)\varphi_{pq}(x,y)\,dx\,dy \tag{3.18}$$

where $M_{pq}$ is the modal mass as in Eq.(2.6) i.e.

$$M_{pq} = \int_{S_p} m_p\,\varphi_{pq}^2\,dS_p \tag{3.19}$$

while $\int_{S_p} m_p\,\varphi_{mn}\varphi_{pq}\,dS_p = 0$ for $m \neq p$ or $n \neq q$ by orthogonality of the mode shapes.

Substituting Eq.(3.16) and Eq.(3.17) into Eq.(3.15), this can then be written as

$$\begin{aligned}\rho\omega^2 \sum_{m=1}^{\infty}\sum_{n=1}^{\infty} d_{mn}\varphi_{mn}(x_0,y_0) = \\ \int_{S_p}\sum_{m=1}^{\infty}\sum_{n=1}^{\infty}\left[F_{mn}\varphi_{mn}(x,y) + m_p\omega^2 d_{mn}\varphi_{mn}(x,y) - Bd_{mn}\nabla^4\varphi_{mn}(x,y)\right] \\ \times \frac{\partial^2 G}{\partial z\partial z_0}(x,x_0,y,y_0,z=z_0=0)\,dx\,dy\end{aligned} \tag{3.20}$$

By multiplying both sides by $\varphi_{pq}$ and then integrating over the plate area, this yields

$$\frac{\rho\omega^2}{m_p} d_{pq} M_{pq} = \int_{S_p}\int_{S_p} \sum_{m=1}^{\infty}\sum_{n=1}^{\infty} \left[F_{mn}\varphi_{mn}(x,y) + m_p\omega^2 d_{mn}\varphi_{mn}(x,y) - B d_{mn}\nabla^4\varphi_{mn}(x,y)\right] \times \varphi_{pq}(x_0,y_0)\frac{\partial^2 G}{\partial z \partial z_0}(x,x_0,y,y_0,z=z_0=0)\,dx\,dy\,dx_0\,dy_0 \tag{3.21}$$

The mode shape $\varphi_{mn}$ must satisfy

$$\nabla^4\varphi_{mn}(x,y) = k_{mn}^4\varphi_{mn}(x,y) = \left(\frac{m_p\omega_{mn}^2}{B}\right)\varphi_{mn}(x,y) \tag{3.22}$$

where $\omega_{mn}$ is the modal natural frequency. Substituting Eq.(3.22) into Eq.(3.21) yields

$$\frac{\rho\omega^2}{m_p} d_{pq} M_{pq} = \sum_{m=1}^{\infty}\sum_{n=1}^{\infty}\left[F_{mn} - m_p(\omega_{mn}^2 - \omega^2)d_{mn}\right] C_{pqmn} \tag{3.23}$$

where $C_{pqmn}$ is the acoustical cross-modal coupling term expressed by

$$C_{pqmn} = \int_{S_p}\int_{S_p} \varphi_{pq}(x_0,y_0)\frac{\partial^2 G}{\partial z\partial z_0}(x,x_0,y,y_0,z=z_0=0)\,\varphi_{mn}(x,y)dxdydx_0dy_0 \tag{3.24}$$

Substituting Eq.(3.10) into Eq.(3.24) and performing the two integrals over $S_p$ yields

$$C_{pqmn} = \frac{j}{8\pi^2}\int_{-\infty}^{\infty}\int_{-\infty}^{\infty} k_z\,\widetilde{\varphi}_{pq}^*(k_x,k_y)\widetilde{\varphi}_{mn}(k_x,k_y)\,dk_x\,dk_y \tag{3.25}$$

where $\widetilde{\varphi}_{mn}(k_x,k_y)$ is the Fourier transform of the mode shape $\varphi_{mn}(x,y)$ which is expressed by

$$\widetilde{\varphi}_{mn}(k_x,k_y) = \int_0^a\int_0^b \varphi_{mn}(x,y)e^{-j(k_x x + k_y y)}\,dx\,dy \tag{3.26}$$

For a simply supported plate, by substituting Eq.(2.4) into Eq.(3.19), the modal mass $M_{pq}$ gives

$$M_{mn} = m_p\frac{S_p}{4} \tag{3.27}$$

Substituting Eq.(3.27) into Eq.(3.23) gives

$$\rho\omega^2\frac{S_p}{4}d_{pq} = \sum_{m=1}^{\infty}\sum_{n=1}^{\infty}\left[F_{mn} - m_p(\omega_{mn}^2 - \omega^2)d_{mn}\right]C_{pqmn} \tag{3.28}$$

where the modal natural frequency $\omega_{mn}$ for a simply supported plate is given in Eq.(2.7).

Evaluating analytically Eq.(3.26) for the simply supported mode shape gives

$$\widetilde{\varphi}_{mn}(k_x, k_y) = \frac{ab}{\pi^2 mn}\left[\frac{(-1)^m e^{-j\mu} - 1}{(\mu/(m\pi))^2 - 1}\right]\left[\frac{(-1)^n e^{-j\chi} - 1}{(\chi/(n\pi))^2 - 1}\right] \tag{3.29}$$

where $\mu = k_x a$ and $\chi = k_y b$. Note that this is identical with $\Phi$ in the spatial domain as in Eq.(2.10). The derivation of Eq.(3.29) can be found in Appendix C.

For the conjugate form of the mode shape $\varphi_{pq}^*(x, y)$, the result is identical except that the sign of the exponentials is changed from negative to positive, i.e.

$$\widetilde{\varphi}_{pq}^*(k_x, k_y) = \frac{ab}{\pi^2 pq}\left[\frac{(-1)^p e^{j\mu} - 1}{(\mu/(p\pi))^2 - 1}\right]\left[\frac{(-1)^q e^{j\chi} - 1}{(\chi/(q\pi))^2 - 1}\right] \tag{3.30}$$

From Eq.(3.26), it can be found that the integrand, with respect to $k_x$, is an even function when the mode orders $(p, m)$ are of the same parity. Also, with respect to $k_y$, it is an even function when the mode orders $(q, n)$ are of the same parity.

Therefore Eq.(3.25) can be simplified as

$$C_{pqmn} = \frac{j}{2\pi^2}\int_0^{\infty}\int_0^{\infty} k_z\, \widetilde{\varphi}_{pq}^*(k_x, k_y)\widetilde{\varphi}_{mn}(k_x, k_y)\, dk_x\, dk_y \tag{3.31}$$

when $p$ and $m$ are of the same parity and $q$ and $n$ are also of the same parity. The remaining cases will have $C_{pqmn} = 0$.

Finally after substituting Eq.(3.29) and Eq.(3.30) into Eq.(3.31), it is found that

$$C_{pqmn} = C_{mnpq} = \frac{2j}{pqmn}\left(\frac{ab}{\pi^3}\right)^2\int_0^{\infty}\int_0^{\infty} k_z \Upsilon\, \Omega\, dk_x\, dk_y \tag{3.32}$$

where $\Upsilon = \dfrac{1 - (-1)^p\cos\mu}{((\mu/p\pi)^2 - 1)((\mu/m\pi)^2 - 1)}$, $\Omega = \dfrac{1 - (-1)^q\cos\chi}{((\chi/q\pi)^2 - 1)((\chi/n\pi)^2 - 1)}$.

In practice, the infinite limits of the double layer integrals over $k_x$ and $k_y$ can be limited, as in [33], to

$$k_x^{max} = (1+K)\frac{p\pi}{a}, \quad k_y^{max} = (1+K)\frac{q\pi}{b} \tag{3.33}$$

for some $K \geq 1$.

To avoid the singularities in the integration, the method used in the wavenumber domain method in Section 2.2.2 can be applied.

From Eq.(3.28), after numerically evaluating $C_{mnpq}$, the displacement modal amplitude $d_{pq}$ can be found by solving the linear matrix equation

$$[C_{mnpq}]\{m_p(\omega_{pq}^2 - \omega^2)d_{pq}\} + \rho\omega^2\frac{S_p}{4}[I]\,\{d_{pq}\} = [C_{mnpq}]\{F_{pq}\} \tag{3.34}$$

where $[C_{mnpq}]$ is the complex cross coupling matrix, $[I]$ is the identity matrix of size $N \times N$ and $\{\}$ indicates a column vector.

After inverting $C_{mnpq}$ this gives

$$\{m_p(\omega_{pq}^2 - \omega^2)d_{pq}\} + \rho\omega^2\frac{S_p}{4}[C_{mnpq}]^{-1}\,\{d_{pq}\} = \{F_{pq}\} \tag{3.35}$$

Here, the matrix $[C_{mnpq}]$ has to be inverted first. Thus the solution strongly depends not only on the accuracy of the calculated $[C_{mnpq}]$ but also on the size of the matrix $[C_{mnpq}]$ to be inverted. In order to simplify the calculation and avoid the matrix inversion, an approximation can be applied in which the off-diagonal terms in $C_{mnpq}$ are neglected. In other words, as in the baffled plate case in section 2.1.2, only the self-modal radiation contributions are taken into account in the calculation. The effect of the cross-modal coupling is eliminated. Laulagnet [33] showed that, compared with the exact solution, this gives a very good approximation in light fluid such as air. This approach is still consistent with the objective of this thesis where the study is limited only for the radiation into the air. However, it was found that for a plate with a heavy fluid loading such as water, the off-diagonal terms become important, particularly for the radiated sound power [33].

Therefore Eq.(3.35) can written as

$$m_p(\omega_{pq}^2 - \omega^2)d_{pq} + \rho\omega^2 \frac{S_p}{4}\left(\frac{1}{C_{pqpq}}\right) d_{pq} = F_{pq} \tag{3.36}$$

Multiplying by $S_p/4$ gives

$$M_{pq}(\omega_{pq}^2 - \omega^2)d_{pq} + \rho\omega^2 \left(\frac{S_p}{4}\right)^2 \left(\frac{1}{C_{pqpq}}\right) d_{pq} = \hat{F}_{pq} \tag{3.37}$$

where $M_{pq} = m_p(S_p/4)$ and $\hat{F}_{pq} = F_{pq}(S_p/4)$ are the generalized mass and the generalized force for the simply supported plate. $\hat{F}_{pq}$ now has units of Newtons.

Eq.(3.37) can be solved to find the complex displacement amplitude of mode $(p, q)$, $d_{pq}$. The plate velocity for each mode is given by

$$v_{pq}(x, y) = \frac{\partial w}{\partial t} = j\omega d_{pq}\varphi_{pq}(x, y) \tag{3.38}$$

where $\varphi_{pq}$ is the value of the corresponding mode shape function.

The spatially average squared velocity of a mode can be expressed as

$$\left\langle |v_{pq}|^2 \right\rangle = \frac{1}{S_p}\int_{S_p} |v_{pq}(x, y)|^2 \, dx \, dy \tag{3.39}$$

Substituting Eq.(3.38) for the case of a simply supported plate gives

$$\left\langle |v_{pq}|^2 \right\rangle = \frac{\omega^2}{4} |d_{pq}|^2 \tag{3.40}$$

For a plate immersed in light fluid, the fluid loading has a negligible effect on the vibrational behaviour of the plate. The second term in Eq.(3.37) i.e. the fluid loading part is very small compared with the first term. The displacement $d_{pq}$ can therefore be calculated by neglecting this term.

Referring to Figure 3.3, the total radiated sound power from both sides of the plate can be defined as

$$
\begin{aligned}
W &= \frac{1}{2}\int_{S_p} \Re\left\{\sum_{p=1}^{\infty}\sum_{q=1}^{\infty} p_+(x,y)\mathbf{v}^*_{pq}(x,y)\cdot\mathbf{n}\, dS_{p+} + p_-(x,y)\mathbf{v}^*_{pq}(x,y)\cdot\mathbf{n}\, dS_{p-}\right\} \\
&= \frac{1}{2}\int_{S_p} \Re\left\{\sum_{p=1}^{\infty}\sum_{q=1}^{\infty} (p_+(x,y)-p_-(x,y))v^*_{pq}(x,y)\right\} dS_p \\
&= -\frac{1}{2}\int_{S_p} \Re\left\{\sum_{p=1}^{\infty}\sum_{q=1}^{\infty} \Delta p(x,y)v^*_{pq}(x,y)\right\} dS_p
\end{aligned} \tag{3.41}
$$

As in Eq.(3.4), the acoustic pressure is determined from the pressure difference $\Delta p(x,y)$ between the two sides of the plate surface. To obtain a convenient calculation, the pressure difference $\Delta p(x,y)$ can also be written as a sum of plate mode shapes

$$
\Delta p(x,y) = \sum_{m=1}^{\infty}\sum_{n=1}^{\infty} p_{mn}\varphi_{mn}(x,y) \tag{3.42}
$$

where $p_{mn}$ are the corresponding amplitudes.

Therefore by using the orthogonality relationship for the simply supported conditions, the radiated sound power can be written as

$$
\begin{aligned}
W &= -\frac{1}{2}\int_{S_p} \Re\left\{\sum_{m=1}^{\infty}\sum_{n=1}^{\infty} p_{mn}\varphi_{mn} \times (j\omega)\sum_{p=1}^{\infty}\sum_{q=1}^{\infty} d^*_{pq}\varphi_{pq}\right\} dS_p \\
&= -\frac{\omega}{2}\left(\frac{S_p}{4}\right)\ \Re\left\{j\sum_{p=1}^{\infty}\sum_{q=1}^{\infty} p_{pq}d^*_{pq}\right\}
\end{aligned} \tag{3.43}
$$

Substituting Eq.(3.42), Eq.(3.5) can then be written as

$$
\begin{aligned}
&\sum_{m=1}^{\infty}\sum_{n=1}^{\infty} m_p(\omega^2_{mn}-\omega^2)d_{mn}\varphi_{mn}(x,y) \\
&\qquad = \sum_{m=1}^{\infty}\sum_{n=1}^{\infty} F_{mn}\varphi_{mn}(x,y) + \sum_{m=1}^{\infty}\sum_{n=1}^{\infty} p_{mn}\varphi_{mn}(x,y)
\end{aligned} \tag{3.44}
$$

Again, applying the orthogonality relationship yields

$$
m_p(\omega^2_{pq}-\omega^2)d_{pq} = F_{pq} + p_{pq} \tag{3.45}
$$

Eliminating $p_{pq}$ in Eq.(3.43) using Eq.(3.45)

$$W = \frac{\omega S_p}{8} \Re \left\{ j \sum_{p=1}^{\infty} \sum_{q=1}^{\infty} \left( F_{pq} - m_p(\omega_{pq}^2 - \omega^2) d_{pq} \right) d_{pq}^* \right\} \tag{3.46}$$

In terms of the acoustic cross-modal coupling $C_{pqpq}$, from Eq.(3.37) the sound power $W$ can also be written as

$$W = \frac{\omega S_p}{8} \Re \left\{ j \sum_{p=1}^{\infty} \sum_{q=1}^{\infty} \left[ \rho \omega^2 \left( \frac{S_p}{4} \right)^2 \left( \frac{1}{C_{pqpq}} \right) d_{pq} \right] d_{pq}^* \right\} \tag{3.47}$$

The total radiation efficiency $\sigma$ can be found from this using

$$\sigma = \frac{W}{\frac{1}{2} \rho c S_p \sum_{p=1}^{\infty} \sum_{q=1}^{\infty} \overline{\langle |v_{pq}|^2 \rangle}} \tag{3.48}$$

where $\overline{\langle |v_{pq}|^2 \rangle}$ is the spatially averaged squared velocity, averaged over all possible forcing locations $(x_0, y_0)$. As in Eq.(2.20), it is given by

$$\overline{\langle |v_{pq}|^2 \rangle} = \frac{1}{ab} \int_0^a \int_0^b \langle |v_{pq}|^2 \rangle \, dx_0 \, dy_0 \tag{3.49}$$

Eq.(3.48) is the average radiation efficiency which is defined as a summation over the contributions of modes (modal summation approach). As in Eq.(2.25) in the baffled plate case, here it is also assumed that the individual modes are uniformly excited simultaneously and each mode acts as an independent energy reservoir (uncorrelated) [7]. The same assumption should also be applied to the modal force $F_{pq}$ in Eq.(3.18) where all modes produce equal excitation energy.

The modal radiation efficiency $\sigma_{pq}$ can be calculated from

$$\sigma_{pq} = \frac{W_{pq}}{\frac{1}{2} \rho c S_p \overline{\langle |v_{pq}|^2 \rangle}} \tag{3.50}$$

where $W_{pq}$ is the modal radiated sound power given by one term in Eq.(3.47)

$$W_{pq} = \frac{\omega S_p}{8} \Re \left\{ j \left[ \rho \omega^2 \left( \frac{S_p}{4} \right)^2 \left( \frac{1}{C_{pqpq}} \right) d_{pq} \right] d_{pq}^* \right\} \tag{3.51}$$

The radiation efficiency of the unbaffled plate takes into account the fluid loading on both sides of the plate but has been normalised only by the area of one side. To have an equivalency to the radiation efficiency of the baffled plate, as a consequence, it has to be further divided by two.

## 3.3 Results and comparison with baffled plate

Figure 3.4 shows example results for different mode orders, i.e. odd-odd, even-odd, odd-even and even-even. The results for the baffled plate are also plotted for comparison. The plate is a rectangular plate having the same dimensions and properties as the baffled plate described in section 2.4. It can be seen that the radiation efficiency is much reduced for the unbaffled plate at low frequencies. For mode (1,1) in Figure 3.4(a), the slope below the modal coincidence frequency is 40 dB/decade ($\sigma \propto k^4$) instead of 20 dB/decade found for the baffled plate. This is a dipole type radiation. A similar phenomenon can be seen for other types of modes where the slope at very low frequency in the unbaffled plate is 20 dB/decade steeper than that of the baffled plate. From Figure 3.4(b) and (c), the even-odd modes and the odd-even modes have a dependency of 60 dB/decade ($\sigma \propto k^6$) at low frequencies. As in the baffled plate case, the lowest radiation is found for the even-even mode as in Figure 3.4(d) where the slope is 80 dB/decade ($\sigma \propto k^8$).

The difference between the radiation efficiency of the unbaffled plate and the baffled plate can also be noted from the mathematical point of view. Eq.(3.32) for the acoustical cross-modal coupling term in the unbaffled case is identical with Eq.(2.10) in the baffled case. However, the former becomes the denominator due to the matrix inversion in the equation of motion (Eq.(3.37)), while the latter becomes the numerator in the radiation efficiency equation (Eq.(2.51)).

Figure 3.5 shows a result for the averaged radiation efficiency obtained using the modal summation approach as in Eq.(3.48). The radiation efficiencies of individual modes

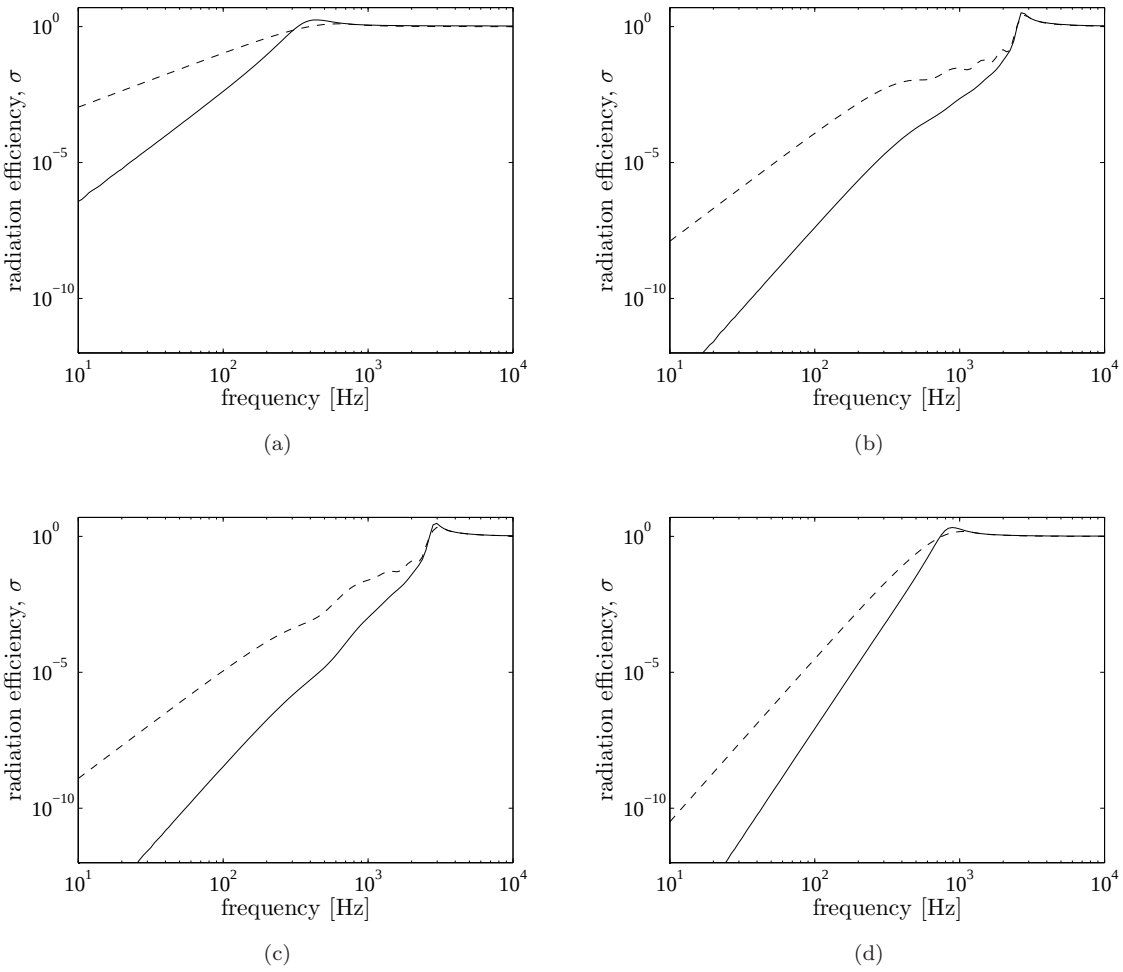


FIGURE 3.4: Comparison of modal radiation efficiencies of unbaffled (—) and baffled (−−) plates: (a) mode (1,1), (b) mode (10,1), (c) mode (3,8) and (d) mode (2,2).

are also shown. It can be seen that, at low frequencies below 70 Hz, the overall result is dominated by mode (1,1), as found for the baffled plate.

Figure 3.6 compares the average radiation efficiency of the baffled and unbaffled plates. As well as the difference in slope noted at low frequency, the unbaffled plate has a lower radiation efficiency than the baffled plate in the region of acoustic short-circuiting between 100 and 3 kHz. Without the baffle, the surface velocity sources from one side of the plate partially cancel the field produced by the surface velocity sources from the other side of the plate. The extent of this cancellation depends on the acoustic wavelength and becomes less effective as the frequency increases. It appears that, in this region, the frequency dependence is approximately 20 dB/decade for the unbaffled plate compared with 10 dB/decade for the baffle plate.

Using the same personal computer specification and the same frequency resolution as

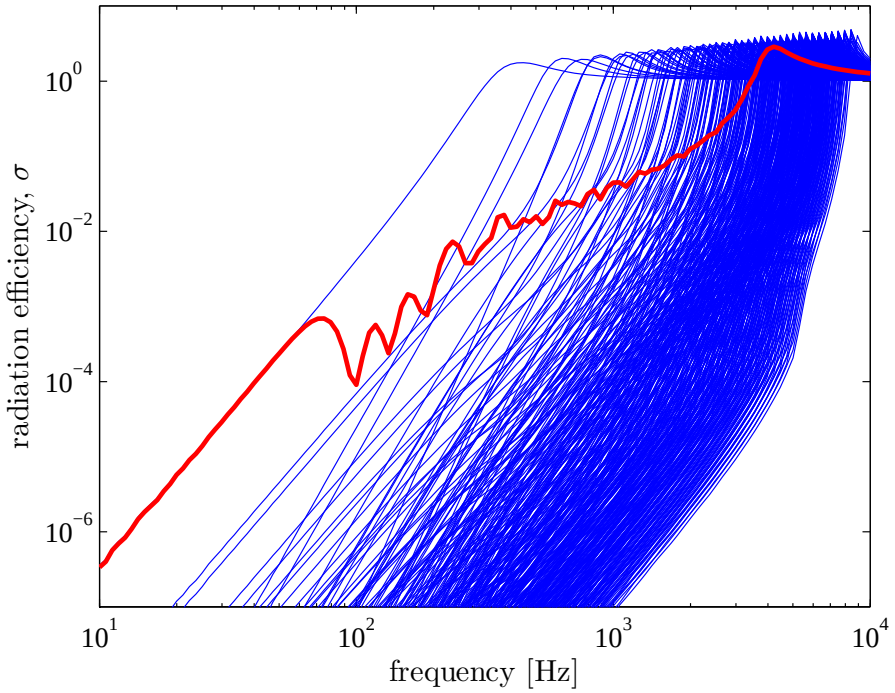


FIGURE 3.5: Modal and average radiation efficiency of a simply supported unbaffled plate ($0.65 \times 0.5 \times 0.003$ m aluminium plate with $\eta = 0.1$): —modal radiation efficiency; — average radiation efficiency.

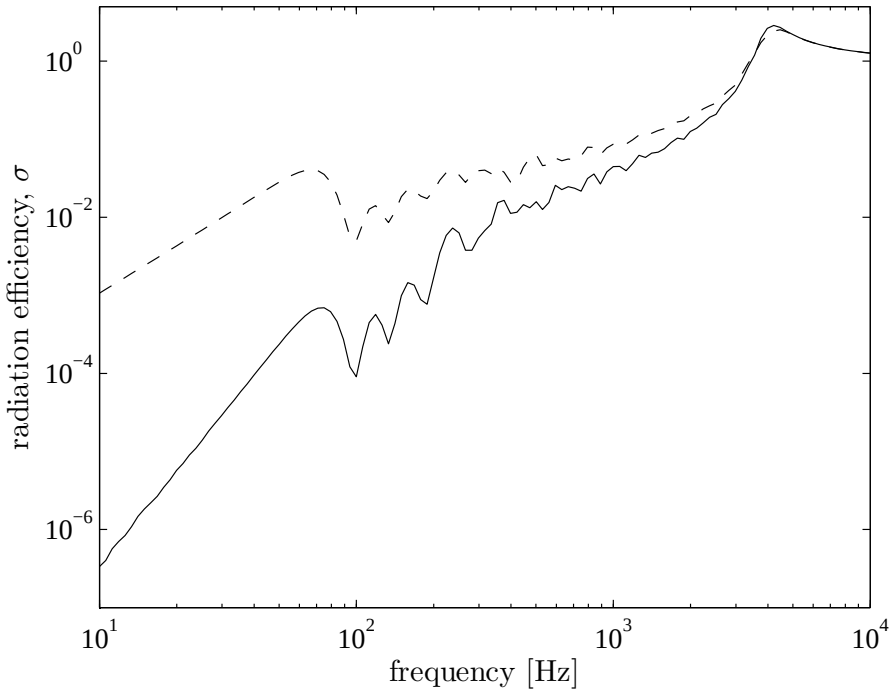


FIGURE 3.6: Comparison of average radiation efficiency between unbaffled (—) and baffled (−−) plates ($0.65 \times 0.5 \times 0.003$ m aluminium plate with $\eta = 0.1$).

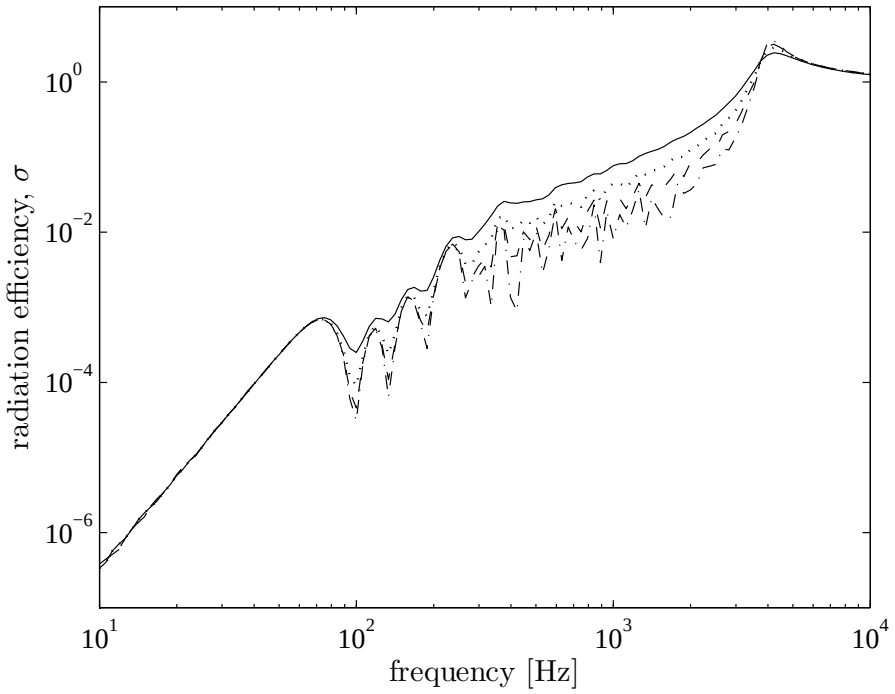


FIGURE 3.7: The average radiation efficiency of an unbaffled plate with different damping loss factor: —, 0.2; $\cdots$, 0.1; $--$, 0.05; $-\cdot-$, 0.01 ($0.65 \times 0.5 \times 0.003$ m, aluminium plate).

for the baffled plate (Section 2.4.4) with $K = 1$, $dk_x = 2\pi a/dn$ and $dk_y = 2\pi b/dn$ for $dn = 40$, the calculation of the averaged radiation efficiency takes approximately 4 hours.

With different values of damping loss factor, Figure 3.7 again shows the same phenomenon as that for the baffled plate (Figure 2.12), where the radiation efficiency increases as the damping increases in the corner and edge mode regions. As explained in section 2.4, with high damping the contributions of individual modes become less important and consequently the curves become smoother. Moreover the near-field in the vicinity of the driving force has a greater effect. The average mean-square velocity is reduced and hence the radiation efficiency is increased.

The ratios of the radiation efficiency of unbaffled and baffled plates are shown in Figure 3.8 for various damping factors and plate dimensions. With different damping loss factors, as seen in Figure 3.8(a), the ratio starts with a 20 dB/decade slope in the fundamental mode region until 100 Hz. In the corner mode region (100−400 Hz), the slope changes to roughly 10−15 dB/decade. As many ripples exist in this region, it is difficult to determine a precise value. However, in the edge mode region, the ratio

starts with a slope of 4.7 dB/decade from 400 Hz up to about 3 kHz. Each curve then has a different slope as it rises up to the critical frequency (4 kHz) depending on the damping loss factor. It can also be seen that at the critical frequency, the ratio is more than 0 dB. It means that the peak at the critical frequency is higher for an unbaffled plate than for a baffled plate (see also Figure 3.6).

With constant plate damping and different plate dimensions, a roughly constant slope can be seen in the results in the edge mode region, see Figure 3.8(b). Above the critical frequency, the baffled and unbaffled results are identical.

## 3.4 Empirical formulae for radiation efficiency of an unbaffled plate

The average radiation efficiency of an unbaffled plate obtained with a summation over individual modes, presented in the previous section, is not efficient from a practical point of view, considering the calculation time required. One solution is to develop an empirical formula for the region below the critical frequency, based on the results of the ratio of the radiation efficiencies of unbaffled and baffled plates. Considering different frequency regions, as for the baffled plate, the empirical formulae for a simply supported unbaffled plate are therefore derived below. In the proposed formula, $\sigma_b$ equals the radiation efficiency of a baffled plate in Eq.(2.71) in the corresponding frequency region.

1. Below the fundamental mode, the monopole radiation in the baffled plate case now becomes dipole radiation in the unbaffled plate case. By analogy with a sphere of radius $a$, where a monopole has $\sigma = (ka)^2$ and a dipole has $\sigma = (ka)^4/4$ [73], the formula can be expressed as

$$\sigma_{ub} = \frac{4S^2 f^4}{c^4} = \sigma_b \frac{f^2 S}{c^2}, \qquad f < f_{1,1} \tag{3.52}$$

2. In the corner mode region, the radiation efficiency of the unbaffled plate is found to increase with approximately 20 dB/decade, see Figure 3.6. The second term

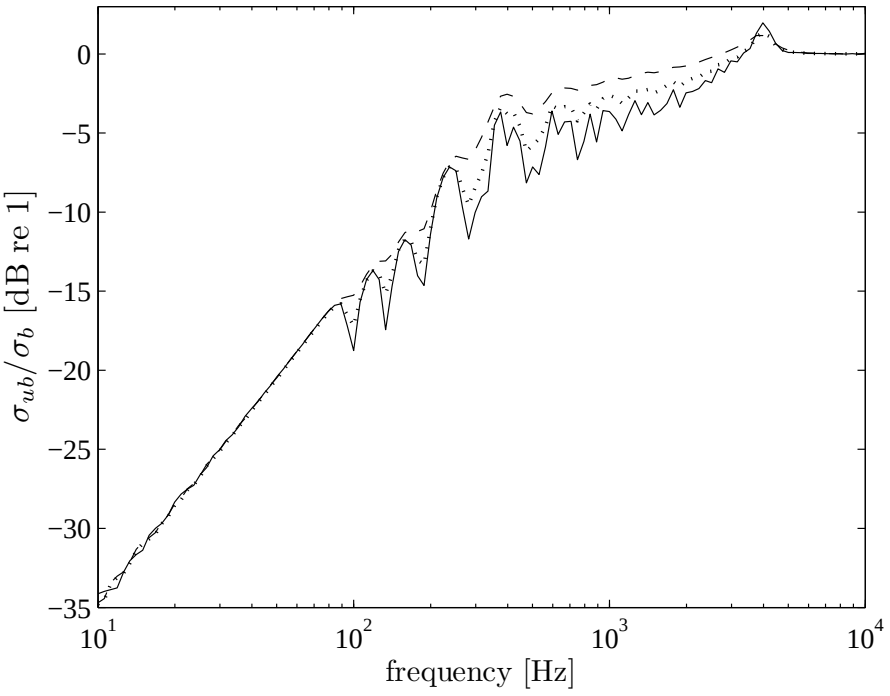


(a)

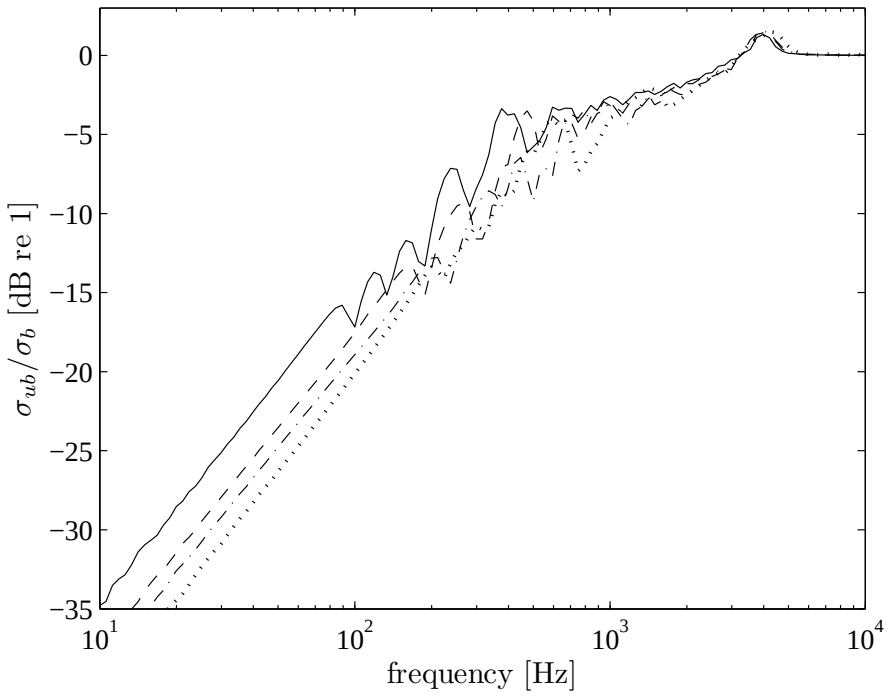


(b)

FIGURE 3.8: Ratio between radiation efficiency of simply supported unbaffled and baffled plates: (a) $0.65 \times 0.5 \times 0.003$ m; —$\eta = 0.05$, $\cdots \eta = 0.1$, $--\eta = 0.2$ and (b) $\eta = 0.1$; —$0.65 \times 0.5 \times 0.003$ m, $--0.325 \times 0.5 \times 0.003$ m, $- \cdot -0.25 \times 0.5 \times 0.003$ m, $\cdots 0.9 \times 0.2 \times 0.003$ m.

in Eq.(2.68) can then be replaced with one having a dependency on $f^2$. The following formula is found to fit the results

$$\sigma_{ub} = \frac{4\pi^2}{c^4}\frac{B}{m}f^2 = \left(\frac{f}{f_c}\right)^2, \qquad f_{1,1} < f < f_e \tag{3.53}$$

Note that this can be written as $\sigma_{ub} = \sigma_b \frac{f^2 S}{c^2}$, similar to Eq.(3.52).

3. The 4.7 dB/decade slope found from the ratio of unbaffled and baffled radiation efficiency in the edge mode region can be used here as a correction for the baffled plate formula to obtain a reasonably good estimation for the unbaffled plate. Having corrected the radiation efficiency formula for the baffled plate by also including the near field effect, the formula can be defined as

$$\sigma_{ub} = \sigma_b \times 10^{c_r}, \qquad f_e < f < f_c \tag{3.54}$$

where $c_r = 0.466 \times \log_{10}(\alpha^2) - 0.266 \times \log_{10}(\eta) - 0.286$ and $\alpha = \sqrt{f/f_c}$.

The second and the third terms of $c_r$ are derived to adjust the correction depending on the damping loss factor.

4. Above the critical frequency, the radiation efficiency of the unbaffled plate is identical with that of the baffled plate

$$\sigma_{ub} = \sigma_b = \left(1 - \frac{f_c}{f}\right)^{-1/2}, \qquad f > f_c \tag{3.55}$$

Figure 3.9 presents a comparison of average radiation efficiency with various damping loss factors from Eqs.(3.52), (3.53), (3.54) and from the method by Laulagnet described in Section 3.2. In the latter case, the average radiation efficiency is obtained from the summation over individual modes. The results show good agreement over the frequency range. However in the corner mode region between 200 and 400 Hz, the empirical results overestimate the analytical calculation because the formula does not include the effect of damping in this region. The agreement is improved as the damping increases. Figure 3.10 plots the comparison for different plate dimensions and thicknesses with the damping loss factor $\eta = 0.1$. This also shows good agreement.

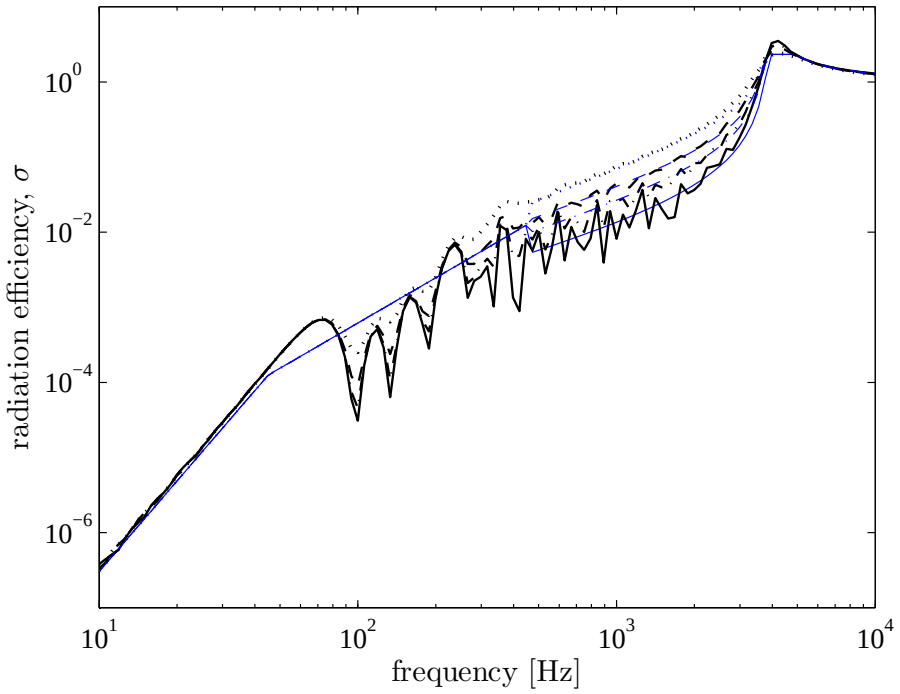


FIGURE 3.9: The average radiation efficiency of a simply supported unbaffled plate from Eqs. (3.52), (3.53), (3.54) (thin line, blue) and the method by Laulagnet (thick line) ($0.65 \times 0.5 \times 0.003$ m: —$\eta = 0.01$, $-\cdot-\eta = 0.05$, $--$ $\eta = 0.1$ and $\cdots\eta = 0.2$).

For the purpose of presentation, for all the plotted graphs here, Maidanik's formula is used at the critical frequency.

## 3.5 Summary

Williams' and Lauglagnet's models for the sound radiation from an unbaffled rectangular plate have been implemented and assessed. It has been shown that Williams' iterative scheme has problems with convergence at low frequency. The model fails to converge when a small sample spacing (finer resolution) is used. However such a spacing would be required in order to calculate the radiation from higher order modes of vibration. Therefore, this model is not considered suitable to calculate the radiation efficiency of an unbaffled plate, especially for the multi-modal response.

Laulagnet's model gives a good result for radiation efficiency even up to very high frequency. The most important finding concerns a comparison of these results with the radiation efficiency of a baffled plate up to the critical frequency. It has been shown that below the critical frequency, due to the partial cancellation of the sound

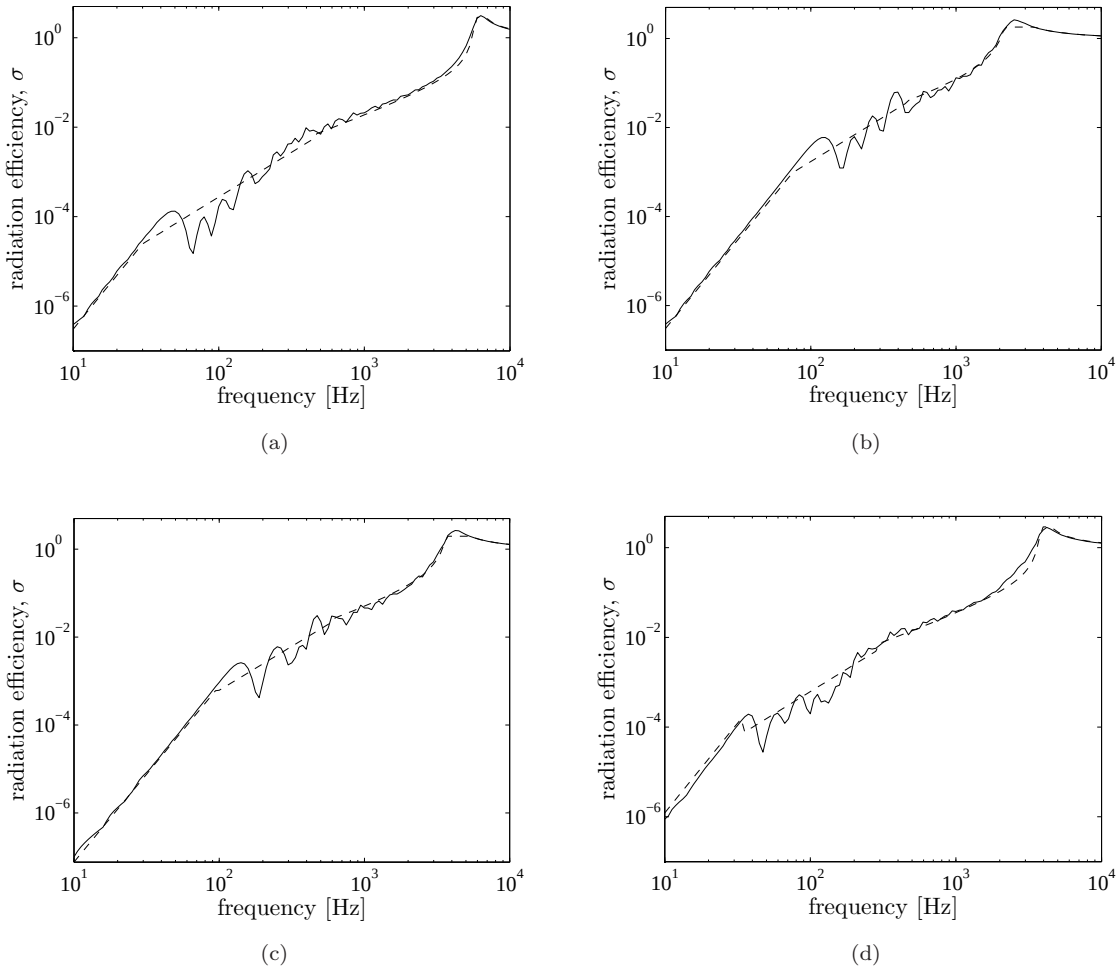


FIGURE 3.10: The average radiation efficiency of a simply supported unbaffled plate from Eqs. (3.52), (3.53), (3.54) (−−) and the method by Laulagnet (—), $\eta = 0.01$: (a) $0.65 \times 0.5 \times 0.002$ m, (b) $0.65 \times 0.5 \times 0.005$ m, (c) $0.325 \times 0.5 \times 0.003$ m and (d) $1.3 \times 0.5 \times 0.003$ m.

field between the two sides of the plate, the unbaffled plate radiates less sound than the baffled plate. The difference is greater as the frequency reduces. Above the critical frequency, there is no difference between the radiation from baffled and unbaffled plates.

From the ratio between the radiation efficiency of baffled and unbaffled plates, empirical formulae have been developed which have been shown to give good agreement for the whole frequency range. The proposed empirical formulae are summarised as follows.

$$\sigma_{ub} = \begin{cases} \dfrac{4S^2}{c^4} f^4 , & f < f_{1,1}, \\ & f_{1,1} = \dfrac{\pi}{2}\sqrt{\dfrac{B}{\rho_p t_p}}\left(\dfrac{1}{a^2}+\dfrac{1}{b^2}\right) \\ \left(\dfrac{f}{f_c}\right)^2 , & f_{1,1} < f < f_e,\ f_e = \dfrac{3c}{P_s} \\ \sigma_b \times 10^{c_r} , & f_e < f < f_c,\ \alpha = \sqrt{\dfrac{f}{f_c}} \\ c_r = 0.466\ \log_{10}(\alpha^2) - 0.266\ \log_{10}(\eta) - 0.286 & \\ \left(1 - \dfrac{f_c}{f}\right)^{-1/2} , & f > f_c \end{cases} \tag{3.56}$$

# Chapter 4

# Radiation efficiency of a guided-guided plate

## 4.1 Introduction

In Chapters 2 and 3 results have been presented for simply supported plate boundaries. It has been noted in Chapter 1 that some authors [15, 16, 17] suggest that 3 dB should be added to the radiation efficiency for clamped boundaries. In this chapter, the effect of changing boundary conditions is studied. However, rather than consider a clamped (or free) edge for which the plate modes are more complicated [18] a guided boundary is introduced. While a simply supported boundary has zero displacement but unconstrained rotation, the guided boundary has zero rotation and unconstrained displacement.

Thus the mode shapes consist of cosine functions given by

$$\varphi_{mn}(x,y) = \cos\left(\frac{m\pi x}{a}\right)\cos\left(\frac{n\pi y}{b}\right) \tag{4.1}$$

The corresponding modal natural frequency is given by

$$\omega_{mn} = \left(\frac{B}{\rho_p t_p}\right)^{1/2}\left[\left(\frac{m\pi}{a}\right)^2 + \left(\frac{n\pi}{b}\right)^2\right] \tag{4.2}$$

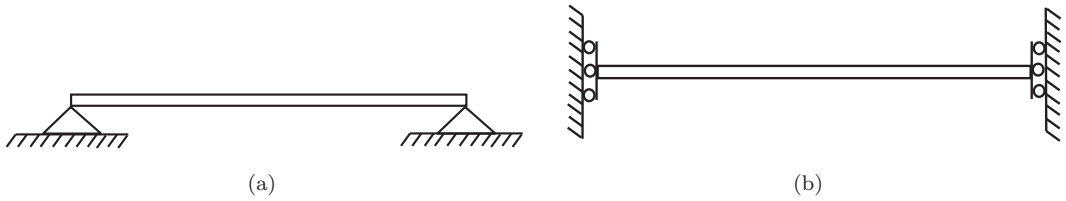


FIGURE 4.1: Edge conditions: (a) Simply supported and (b) guided-guided.

as for the simply supported plate (Eq.(2.7)). However, modes also exist with $m = 0$ or $n = 0$.

Figure 4.1 illustrates both simply supported and guided-guided boundary conditions.

The aim of this chapter is to determine the effect of these boundary conditions on the radiation efficiency, particularly for multi-modal responses, both for baffled and unbaffled plates.

## 4.2 Baffled plate

The wavenumber decomposition approach as in Section 2.2 can be used to calculate the radiation efficiency for the baffled plate case. For a guided-guided plate having dimensions $a \times b$, the spatial Fourier transform of the velocity distribution of mode $(m, n)$ in terms of the non-dimensional wavenumber $\alpha = k_x/k$ and $\beta = k_y/k$, as in Eq.(2.45), yields

$$\widetilde{V}_{g-g}(\alpha, \beta) = u_{mn}\Lambda_{g-g}k^{-2}(\varepsilon + j\vartheta)(\gamma + j\varsigma) \tag{4.3}$$

where

$$\Lambda_{g-g} = \frac{\alpha\beta}{\left[\alpha^2 - \left(\frac{m\pi}{ka}\right)^2\right]\left[\beta^2 - \left(\frac{n\pi}{kb}\right)^2\right]}$$

and $\varepsilon$, $\vartheta$, $\gamma$ and $\varsigma$ are the same as in Section 2.2.

A further configuration can be considered in which the boundaries along the $x$-axes of the plate are simply supported and those along the $y$-axes are guided. In this case, the mode shape is

$$\varphi_{mn}(x, y) = \sin\left(\frac{m\pi x}{a}\right)\cos\left(\frac{n\pi y}{b}\right) \tag{4.4}$$

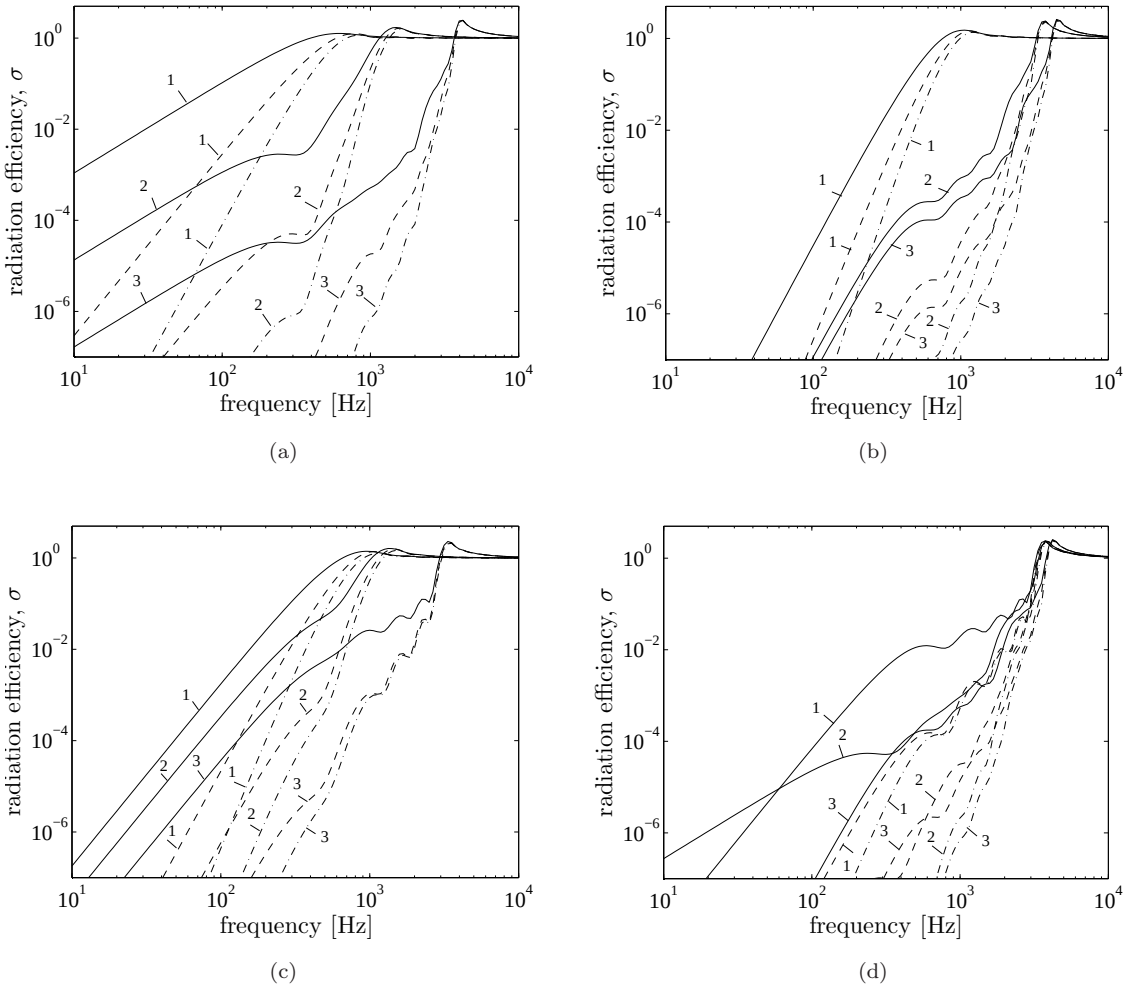


FIGURE 4.2: Modal radiation efficiencies of baffled plates. (a). 1:(1,1), 2:(3,3), 3:(9,9); (b). 1:(2,2), 2:(8,8), 3:(10,10); (c). 1:(1,2), 2:(2,3), 3:(2,9); (d). 1:(1,10), 2:(7,9), 3:(8,10) ($0.65 \times 0.5 \times 0.003$ m aluminium plate). —(ss−ss), −−(ss−g), − · −(g−g).

and the Fourier transform of the velocity in mode $(m, n)$ is

$$\widetilde{V}_{ss-g}(\alpha, \beta) = u_{mn} \Lambda_{ss-g} k^{-2} (\varepsilon + j\vartheta)(\gamma + j\varsigma) \tag{4.5}$$

where

$$\Lambda_{ss-g} = \frac{j\beta \left(\frac{m\pi}{ka}\right)}{\left[\alpha^2 - \left(\frac{m\pi}{ka}\right)^2\right] \left[\beta^2 - \left(\frac{n\pi}{kb}\right)^2\right]}$$

Results for several modes are presented in Figure 4.2, some of which have also been produced by Gompert [19]. It is shown that the guided-guided (g−g) plate has a lower radiation efficiency than those from the simply supported-guided (ss−g) and simply supported (ss−ss) plates for a given mode order. However, equal radiation

efficiency is obtained for all three cases at and above the modal coincidence frequency, i.e. $f_{mn} = (c/2\pi)\sqrt{(m\pi/a)^2 + (n\pi/b)^2}$.

The g−g plate also has a (0,0) mode i.e. a rigid body motion where all the plate surface moves in the same phase (piston). In addition it has modes $(m, 0)$ and $(n, 0)$ while the ss−g plate also has modes of zero index, i.e. $(m, 0)$. For the rigid body motion, the Fourier transform of the velocity is

$$\widetilde{V}_{00}(\alpha, \beta) = u_{mn}\Lambda_{00}k^{-2}(\varepsilon_o + j\vartheta_o)(\gamma_o + j\varsigma_o) \tag{4.6}$$

where

$$\Lambda_{00} = \frac{1}{\alpha\beta}$$

$$\varepsilon_o = \cos(\alpha ka) - 1,\ \vartheta_o = \sin(\alpha ka)$$

$$\gamma_o = \cos(\beta kb) - 1,\ \varsigma_o = \sin(\beta kb)$$

Similar expressions can be found for $(m, 0)$ and $(0, n)$ modes.

Recalling Eq.(3.19) for the modal mass

$$M_{mn} = \int_{S_p} m_p\, \varphi_{mn}^2\, dS_p \tag{4.7}$$

the modal mass for the guided-guided plate is given by

$$M_{mn} = \begin{cases} m_p S_p = M, & m = 0;\ n = 0 \\ m_p \dfrac{S_p}{2} = \dfrac{M}{2}, & m = 0;\ n \neq 0 \ \text{ and } \ m \neq 0;\ n = 0 \\ m_p \dfrac{S_p}{4} = \dfrac{M}{4}, & m \neq 0;\ n \neq 0 \end{cases} \tag{4.8}$$

where $S_p$ is the plate area, $m_p$ is the mass per unit area and $M$ is the plate mass. For the simply supported-guided boundary conditions, the modal mass $M_{mn}$ is similar to Eq.(4.8) for $m \neq 0,\ n = 0$ and $m \neq 0,\ n \neq 0$. The remaining procedures to calculate the radiation efficiency are the same as in Section 3.2.2.

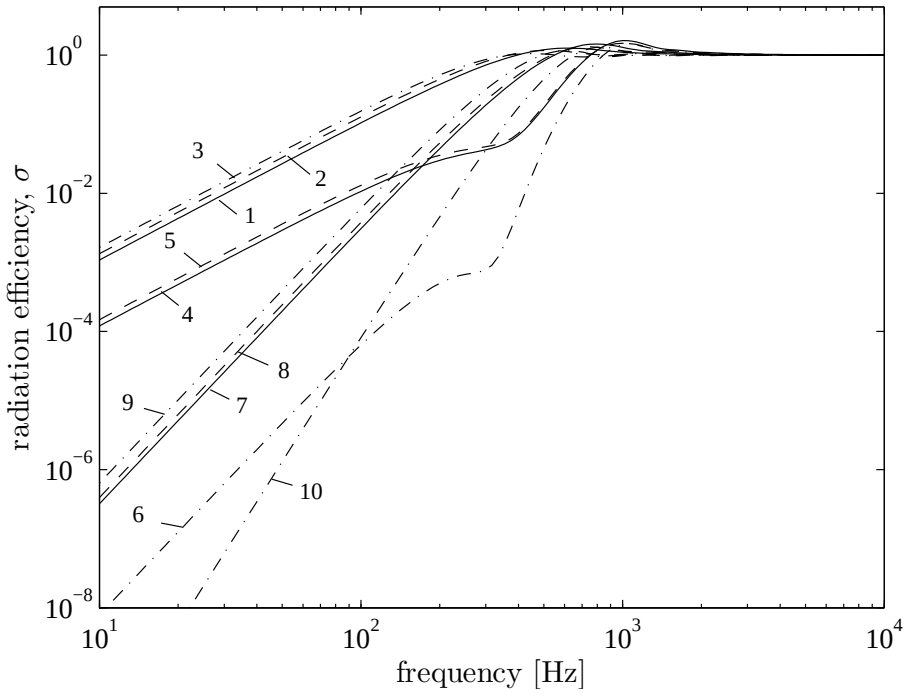


FIGURE 4.3: Modal radiation efficiencies of baffled plates. 1:(1,1), 2 and 9:(1,0), 3:(0,0), 4:(3,1), 5-6:(3,0), 7:(2,1), 8 and 10:(2,0) (0.65×0.5×0.003 m aluminium plate). —(ss−ss), −−(ss−g), − · −(g−g).

Results for some of the low modes are shown in Figure 4.3. This shows that the rigid body motion is the most effective radiator dominating the sound radiation, with a similar characteristic to the (1,1) mode of the ss−ss plate and mode (1,0) for the ss−g plate. Additionally it is found that modes (1,0) of a g−g plate, (2,0) of a ss−g plate and (2,1) of a ss−ss plate all have similar radiation characteristics.

TABLE 4.1: Mode order and its type of radiation

| simply supported | | |
|---|---|---|
| mode | order | radiation type |
| (odd,odd) | 1 | monopole |
| (odd,even) or (even,odd) | 2 | dipole |
| (even,even) | 3 | quadrupole |
| guided-guided | | |
| mode | order | radiation type |
| (0,0) | 1 | monopole |
| (0,odd) or (odd,0) | 2 | dipole |
| (0,even), (even,0) or (odd,odd) | 3 | quadrupole |
| (odd,even) or (even,odd) | 4 | 2×quadrupole |
| (even,even) | 5 | 4×quadrupole |

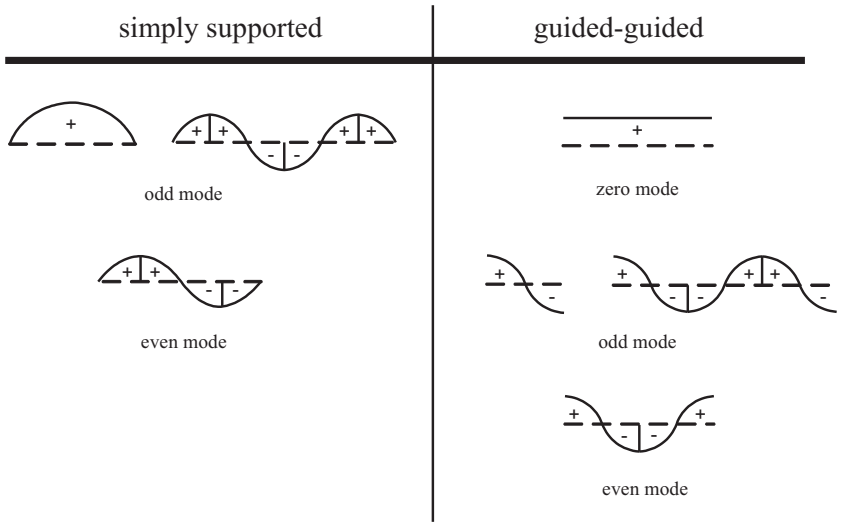


FIGURE 4.4: Illustration of positive and negative inter-cells for vibrating simply supported and guided-guided plates (−−steady state condition).

Table 4.1 lists the mode order corresponding to its type of radiation for baffled plates. The slope of the radiation efficiency at low frequency is proportional to $f^q$ where $q$ is the order listed. For example from Figure 4.3, mode (2,1) for the ss−ss plate has the slope of 40 dB/decade ($10\log_{10} f^4$) and mode (2,0) for the g−g plate has 60 dB/decade ($10\log_{10} f^6$). It can be seen that apart from the zero order modes, the g−g plate produces a higher order type of radiation. This is a very much less effective radiator than a quadrupole source, as seen in Figure 4.2.

For the g−g plate, other than its fundamental mode, all modes have no net volume velocity, that is the positive and negative regions are equal in area. For the ss−ss plate this is only the case for even-even modes as illustrated in Figure 4.4. This makes the g-g plate radiate less sound than the ss-ss plate except at very low frequency where the (0,0) mode is dominant. This can be clearly observed in the multimodal responses.

For that reason, it is also interesting to consider the effect of multimodal radiation due to force excitation. Calculating the averaged radiation efficiencies for $20 \times 20$ modes (frequency resolution of 40 points per decade spaced logarithmically), Figure 4.5 shows the radiation index ($10\log_{10}\sigma$) of a 3 mm thick plate with dimensions of $0.65 \times 0.5$m. It can be seen that the g-g plate has the lowest radiation efficiency, particularly in corner and edge mode regions. In this frequency range, the ss−g plate has a radiation efficiency between that of the ss−ss and g−g plates. At very low frequencies, in this case $< 10$ Hz, the g−g plate has the largest radiation efficiency due to the rigid body

motion. At $< 40$ Hz, the ss−g plate has a higher radiation efficiency than that of the ss−ss plate due to the first zero index mode (1,0).

The first non-rigid mode of the g−g plate, mode (1,0), occurs at 17 Hz as seen in Figure 4.6 which shows the modal mean square velocity. This is responsible for the dip in the radiation efficiency between 10 Hz and 20 Hz. The subsequent modes also correspond to the dips appearing in the radiation efficiency result, for example at 29 Hz and 47 Hz.

The radiation efficiency of the g−g plate is around 10 dB lower than that of the ss−ss plate in the corner mode region between 100 and 400 Hz. This discrepancy reduces as the frequency increases. The radiation efficiencies for the three boundary conditions are similar above the critical frequency (4 kHz).

Figure 4.7 shows the averaged radiation efficiency for a rectangular plate having different dimensions, i.e. $0.4 \times 0.3 \times 0.0015$ m. Similar phenomena can be seen as in Figure 4.5. From these results, it can be concluded that for a baffled plate, the edge conditions have a significant effect on the radiation efficiency.

Figure 4.8 shows the results for lower damping loss factors for only ss−ss and g−g plates, plotted in $\frac{1}{3}$ octave bands for clarity. It can be seen that the difference between the radiation efficiency of ss−ss and g−g plates for damping loss factor $\eta = 0.05$ increases by around 1 dB and by roughly by 2 dB for $\eta = 0.01$ in corner and edge mode regions compared to the results for $\eta = 0.1$ in Figure 4.5. This indicates that the nearfield has more effect in increasing the radiation efficiency for the g−g plate than for the ss−ss plate. For the guided-guided boundary conditions, the plate edges can move freely compared to the simply supported edges. As the damping decreases, the mean-square velocity around the guided plate edges increases more than that of the simply supported plate. For the same radiated sound power for different damping loss factors, this therefore also reduces the radiation efficiency in a greater amount for a guided-guided plate than for a simply supported plate.

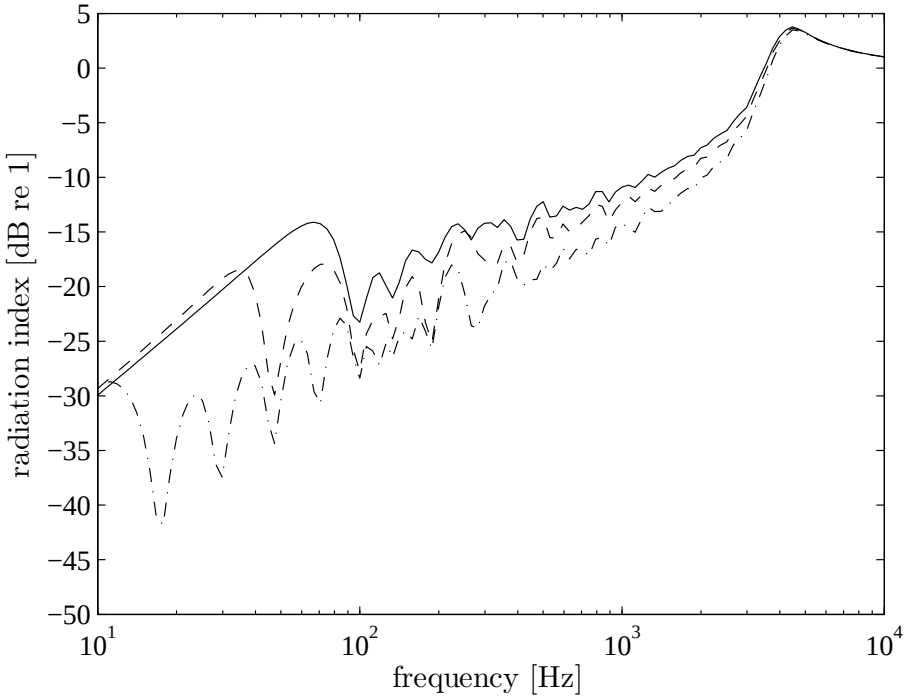


FIGURE 4.5: Average radiation efficiencies of baffled plates for different boundary conditions: —(ss−ss), −−(ss−g), − · −(g−g) ($0.65 \times 0.5 \times 0.003$ m aluminium plate with $\eta = 0.1$).

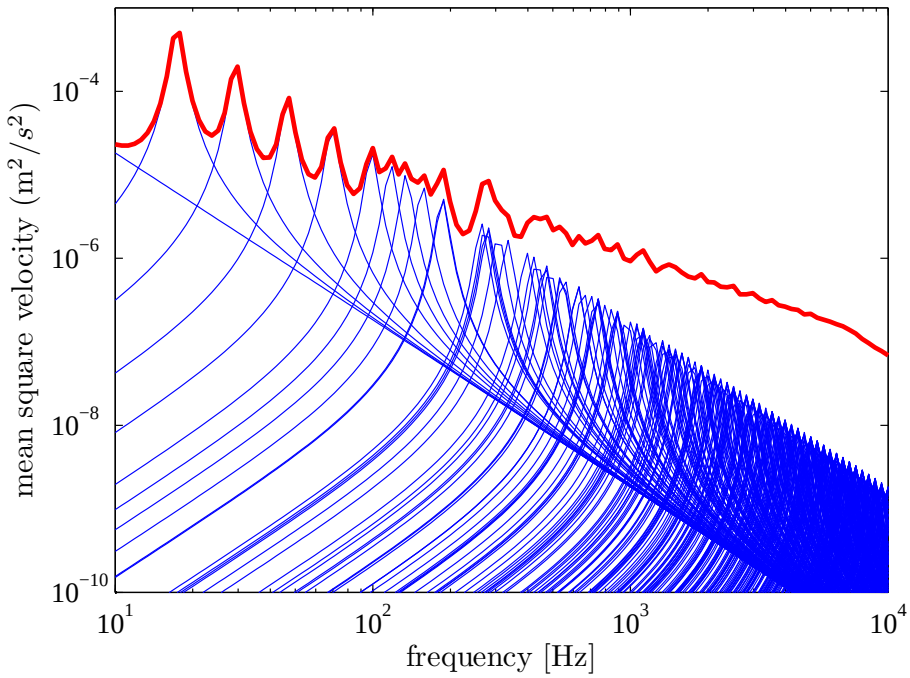


FIGURE 4.6: Contibution of modal mean square velocity (—) to total mean square velocity (—) of a rectangular guided-guided plate ($0.65 \times 0.5 \times 0.003$ m aluminium plate with $\eta = 0.1$).

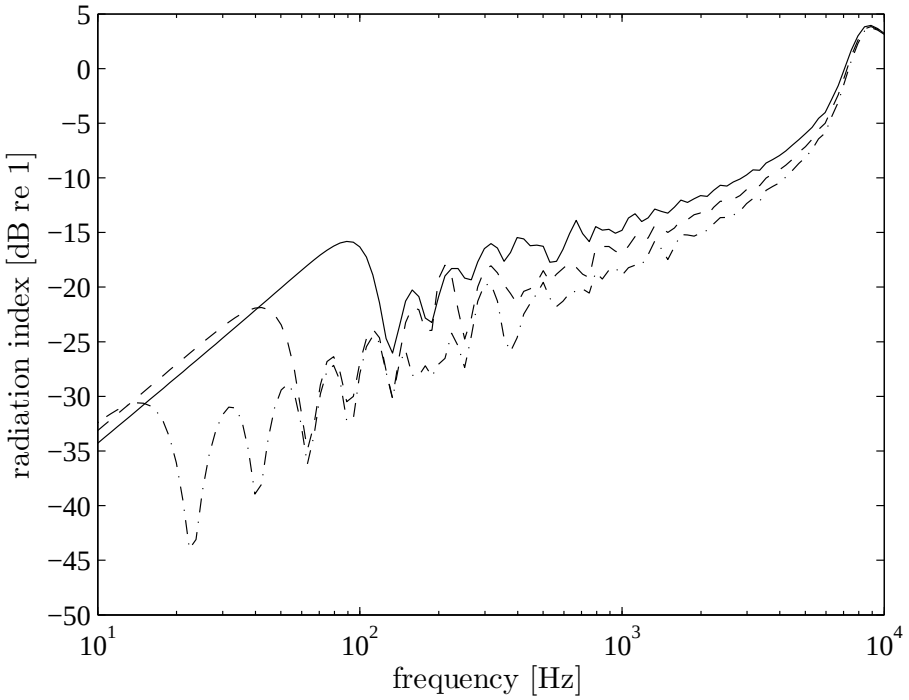


FIGURE 4.7: Average radiation efficiencies of baffled plates for different boundary conditions: —(ss−ss), −−(ss−g), − · −(g−g) ($0.4 \times 0.3 \times 0.0015$ m aluminium plate with $\eta = 0.1$).

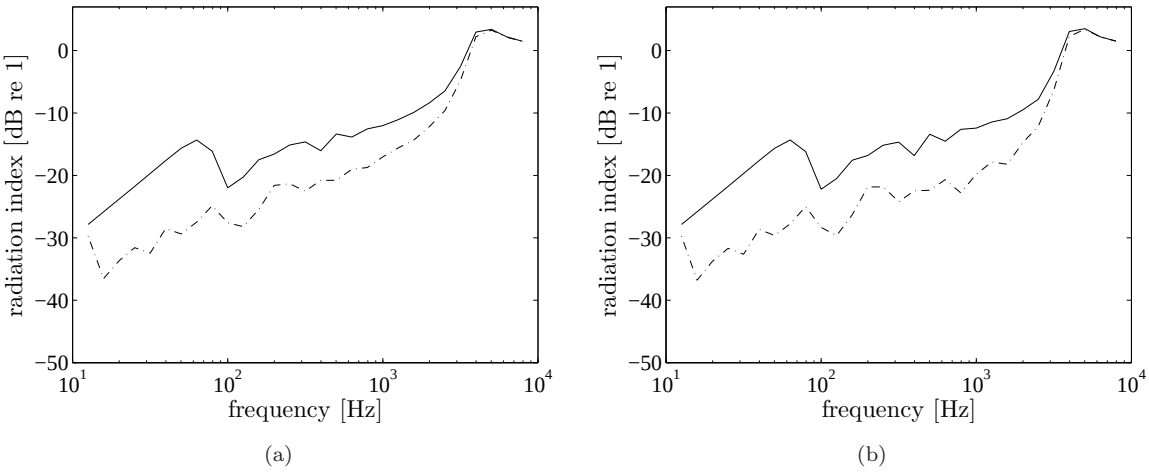


FIGURE 4.8: Average radiation efficiencies of baffled plates for different boundary conditions: —(ss−ss), − · −(g−g) ($0.65 \times 0.5 \times 0.003$ m aluminium plate with (a) $\eta = 0.05$ and (b) $\eta = 0.01$).

## 4.3 Unbaffled plate

As in the baffled plate case, the radiation efficiency of an unbaffled guided-guided plate and of a simply supported-guided plate can be easily investigated by performing the Fourier transform of the appropriate mode shape function.

Recalling Eq.(3.26), the Fourier transform of the mode shape function is given by

$$\widetilde{\varphi}_{mn}(k_x, k_y) = \int_0^a \int_0^b \varphi_{mn}(x, y) e^{-j(k_x x + k_y y)}\, dx\, dy \tag{4.9}$$

For the guided-guided unbaffled plate, by substituting Eq.(4.1) into Eq.(4.9) yields

$$\widetilde{\varphi}_{pq}(k_x, k_y) = -\mu\chi \frac{ab}{\pi^4 p^2 q^2} \left[\frac{(-1)^p e^{-j\mu} - 1}{(\mu/(p\pi))^2 - 1}\right] \left[\frac{(-1)^q e^{-j\chi} - 1}{(\chi/(q\pi))^2 - 1}\right] \tag{4.10}$$

where $\mu = k_x a$ and $\chi = k_y b$. The derivation can be found in Appendix C.

For the rigid body motion, Eq.(4.9) is written as

$$\begin{aligned}
\widetilde{\varphi}_{00}(k_x, k_y) &= \int_0^a \int_0^b e^{-j(k_x x + k_y y)}\, dx\, dy \\
&= \int_0^a e^{-jk_x x}\, dx \int_0^b e^{-jk_y y}\, dy \\
&= -\frac{1}{k_x k_y}(e^{-jk_x a} - 1)(e^{-jk_y b} - 1) \\
&= -\frac{ab}{\mu\chi}(e^{-j\mu} - 1)(e^{-j\chi} - 1)
\end{aligned} \tag{4.11}$$

As in Chapter 3, the radiation efficiency is calculated only for the self-modal radiation, i.e. taking only the diagonal terms of the acoustic cross-modal coupling ($C_{pqpq}$). Eq.(3.25) is now written as

$$C_{pqpq} = \frac{j}{8\pi^2} \int_{-\infty}^{\infty} \int_{-\infty}^{\infty} k_z\, \widetilde{\varphi}^*_{pq}(k_x, k_y) \widetilde{\varphi}_{pq}(k_x, k_y)\, dk_x\, dk_y \tag{4.12}$$

where $k_z = \sqrt{k^2 - k_x^2 - k_y^2}$.

Due to the presence of the zero mode index in the guided boundary condition, i.e. $(0, q)$ or $(p, 0)$, $C_{pqpq}$ is given separately for four conditions

$$C_{pqpq} = \begin{cases} \dfrac{j}{8\pi^2}\displaystyle\int_0^\infty\int_0^\infty k_z \left(\frac{ab}{\mu\chi}\right)^2 \left[\sin^2\left(\frac{\mu}{2}\right)\right]\left[\sin^2\left(\frac{\chi}{2}\right)\right]\, dk_x\, dk_y, \\ \qquad\qquad\qquad\qquad\qquad\qquad\qquad\qquad p=0;\ q=0 \\ \dfrac{j2b^4}{q^4\pi^6}\displaystyle\int_0^\infty\int_0^\infty k_z \left(\frac{a\chi}{b\mu}\right)^2 \frac{[1-\cos\mu]\,[1-(-1)^q\cos\chi]}{\left[\left(\frac{\chi}{q\pi}\right)^2-1\right]^2}\, dk_x\, dk_y, \\ \qquad\qquad\qquad\qquad\qquad\qquad\qquad\qquad p=0;\ q\neq 0 \\ \dfrac{j2a^4}{p^4\pi^6}\displaystyle\int_0^\infty\int_0^\infty k_z \left(\frac{b\mu}{a\chi}\right)^2 \frac{[1-\cos\chi]\,[1-(-1)^p\cos\mu]}{\left[\left(\frac{\mu}{p\pi}\right)^2-1\right]^2}\, dk_x\, dk_y, \\ \qquad\qquad\qquad\qquad\qquad\qquad\qquad\qquad p\neq 0;\ q=0 \\ \dfrac{2ja^4b^4}{p^4q^4\pi^{10}}\displaystyle\int_0^\infty\int_0^\infty k_z \left(\frac{\mu\chi}{ab}\right)^2 \frac{[1-(-1)^p\cos\mu]\,[1-(-1)^q\cos\chi]}{\left[\left(\frac{\mu}{p\pi}\right)^2-1\right]\left[\left(\frac{\chi}{q\pi}\right)^2-1\right]}\, dk_x\, dk_y, \\ \qquad\qquad\qquad\qquad\qquad\qquad\qquad\qquad p\neq 0;\ q\neq 0 \end{cases} \tag{4.13}$$

For the case of simply supported boundary conditions along the edges $x = 0, a$ and guided boundary conditions along the edges $y = 0, b$ the modal coupling $C_{pqpq}$ is given by

$$C_{pqpq} = \begin{cases} \dfrac{j2a^2}{p^2\pi^4}\displaystyle\int_0^\infty\int_0^\infty k_z \left(\frac{b}{\chi}\right)^2 \frac{[1-(-1)^p\cos\mu]\,[1-\cos\chi]}{\left[\left(\frac{\mu}{p\pi}\right)^2-1\right]^2}\, dk_x\, dk_y, \\ \qquad\qquad\qquad\qquad\qquad\qquad\qquad\qquad p\neq 0;\ q=0 \\ \dfrac{2ja^2b^2}{p^2q^4\pi^8}\displaystyle\int_0^\infty\int_0^\infty \chi^2 \frac{[1-(-1)^p\cos\mu]\,[1-(-1)^q\cos\chi]}{\left[\left(\frac{\mu}{p\pi}\right)^2-1\right]\left[\left(\frac{\chi}{q\pi}\right)^2-1\right]}\, dk_x\, dk_y, \\ \qquad\qquad\qquad\qquad\qquad\qquad\qquad\qquad p\neq 0;\ q\neq 0 \end{cases} \tag{4.14}$$

The Fourier transform of the sinusoidal component is the same as in Section 2.2, see also Appendix C. The modal mass is the same as in Eq.(4.8).

Figure 4.9 presents the radiation efficiencies for various modes of vibration. The results show the same pattern as those for the baffled plate in Figure 4.2, although the present curves have a steeper slope. Figure 4.10 shows the radiation efficiency for some low order modes of vibration. As for the baffled plate, mode (0,0) of the g−g plate has a similar characteristic to mode (1,1) of the ss−ss plate. Compared with the baffled plate, the unbaffled plate becomes a less effective radiator. The slope of the radiation efficiency at low frequency for the unbaffled case is now proportional to $f^{2q+2}$, where $q$ is the order listed in Table 4.1. The corresponding radiation characteristics are increased, for example, the rigid mode (0,0) of the g−g unbaffled plate now exhibits a dipole rather than a monopole radiation.

Figure 4.11 shows the radiation index for a 3 mm thick plate determined from the multimodal responses (400 modes) averaged over forcing points. This reveals an interesting phenomenon. Although the modal radiation efficiencies for the non-rigid modes show large differences for the simply supported and guided boundary conditions (see Figure 4.9), the radiation efficiencies are very similar in the corner and edge mode regions above 100 Hz. Whereas for the baffled plate case, there were large differences. The difference here between the simply supported plate and the guided-guided plate is less than 2 dB. Figure 4.12 presents equivalent results for a 1.5 mm thick plate showing the same phenomenon.

As for the baffled plate, Figure 4.13 shows the results for lower damping loss factors for ss−ss and g−g plates. It can also be seen that the difference between the radiation efficiency of ss−ss and g−g plates for damping loss factor for $\eta = 0.01$ increases to be up to 3−4 dB on average in the edge mode region. In the corner mode regions, the radiation efficiency for both edge conditions is still similar. The same as the baffled plate, the nearfield at the plate edges has more effect in increasing the radiation efficiency for the g−g plate.

However, the difference is still not significant compared with that for the baffled plate. Figure 4.9 shows that the modal radiation efficiencies of the ss−ss plate are closer to those of the ss−g and g−g plates compared to the baffled plate in Figure 4.2 in the same frequency range. Compare for example Figure 4.9(b), (d) and Figure 4.2(b),

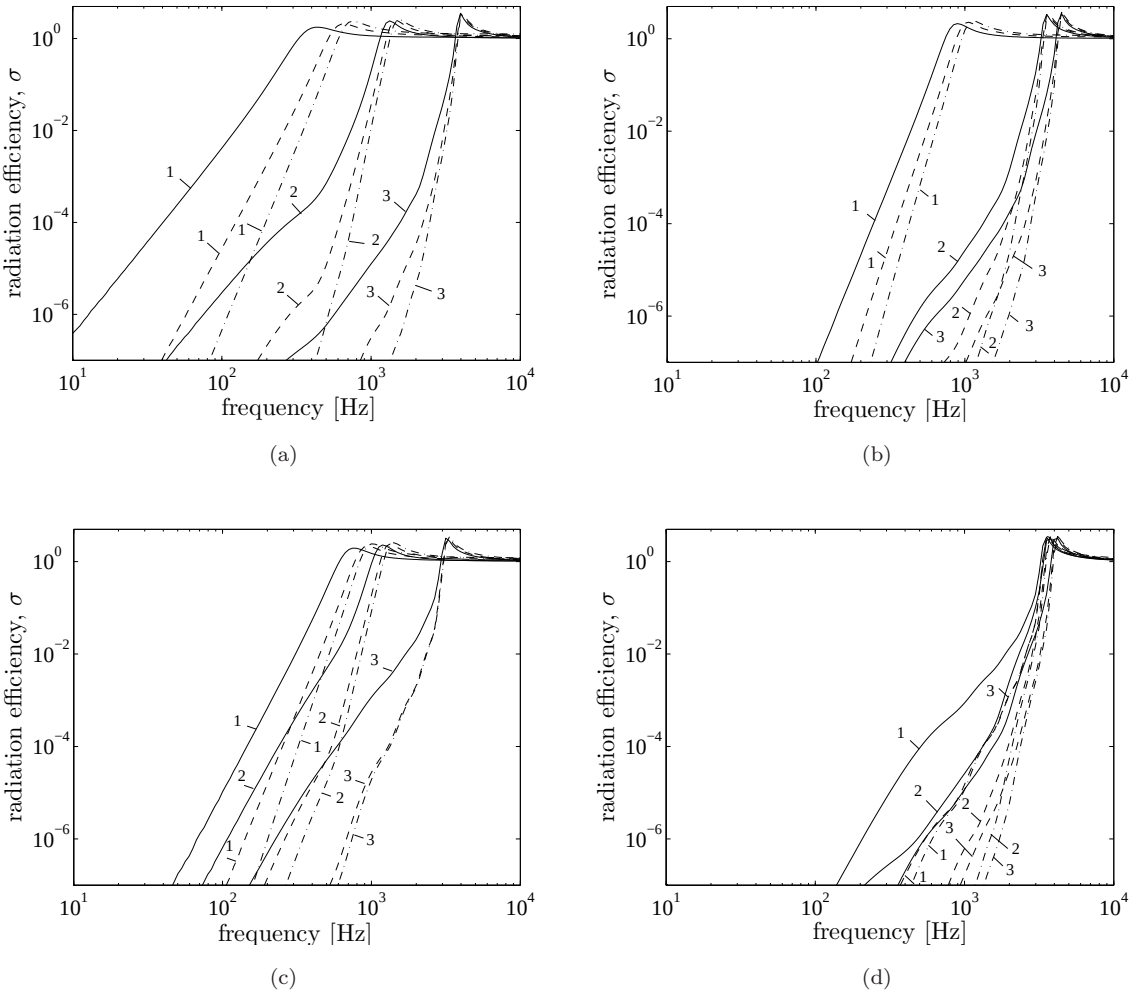


FIGURE 4.9: Modal radiation efficiencies of unbaffled plates. (a). 1:(1,1), 2:(3,3), 3:(9,9); (b). 1:(2,2), 2:(8,8), 3:(10,10); (c). 1:(1,2), 2:(2,3), 3:(2,9); (d). 1:(1,10), 2:(7,9), 3:(8,10) ($0.65 \times 0.5 \times 0.03$ m aluminium plate). —(ss−ss), −−(ss−g), − · −(g−g).

(d). The unbaffled plate results will have the same difference with the baffled plate at lower frequency. The same phenomena can also be observed for the zero mode orders in Figure 4.10 and Figure 4.3. Furthermore, the zero mode orders of the ss−g and g−g plates have higher radiation efficiencies than the identical non-rigid modes of the ss−ss plate which then increase their radiation efficiencies in the multimodal responses.

As already mentioned in Chapter 3, due to the absence of the baffle, the cancellation of sound radiation from the two sides of the plate around the plate edges reduces the radiated sound significantly at low frequencies compared with that from the baffled plate. It appears that this cancellation is less sensitive to the edge conditions of the plate modes for the unbaffled plate. On the other hand for the baffled plate case, the baffle appears to have an effect of increasing the sound radiation.

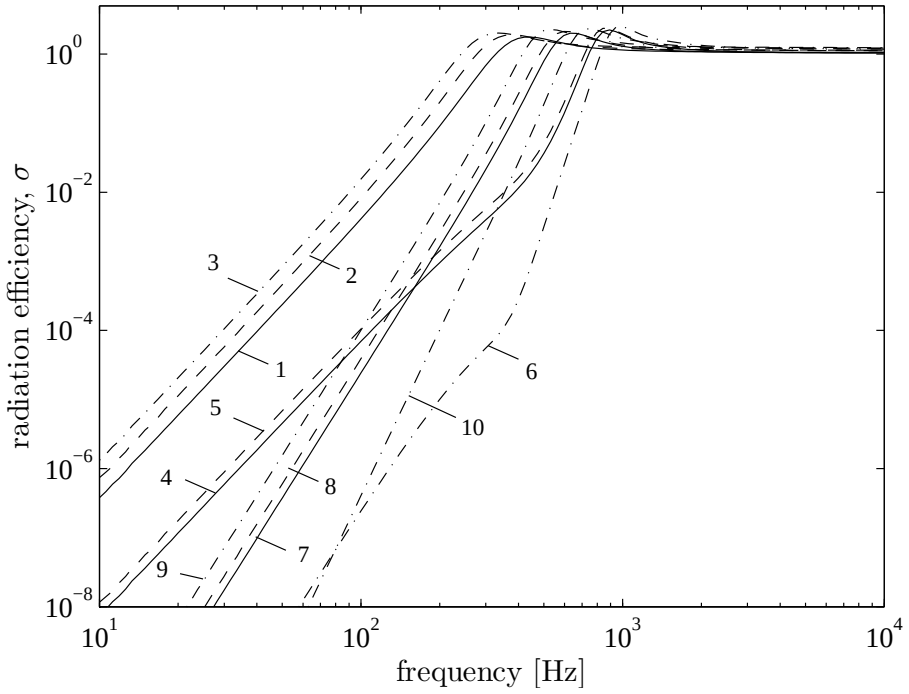


FIGURE 4.10: Modal radiation efficiencies of unbaffled plates. 1:(1,1), 2 and 9:(1,0), 3:(0,0), 4:(3,1), 5-6:(3,0), 7:(2,1), 8 and 10:(2,0) ($0.65 \times 0.5 \times 0.003$ m aluminium plate). —(ss−ss), −−(ss−g), −·−(g−g).

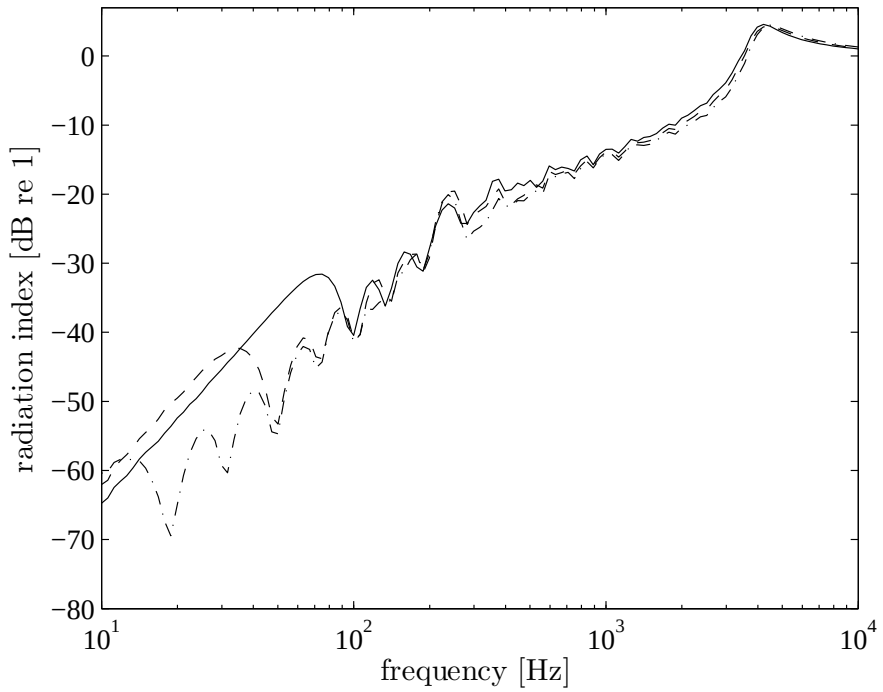


FIGURE 4.11: Average radiation efficiencies of unbaffled plates for different boundary conditions: —(ss−ss), −−(ss−g), −·−(g−g) ($0.65 \times 0.5 \times 0.003$ m aluminium plate with $\eta = 0.1$).

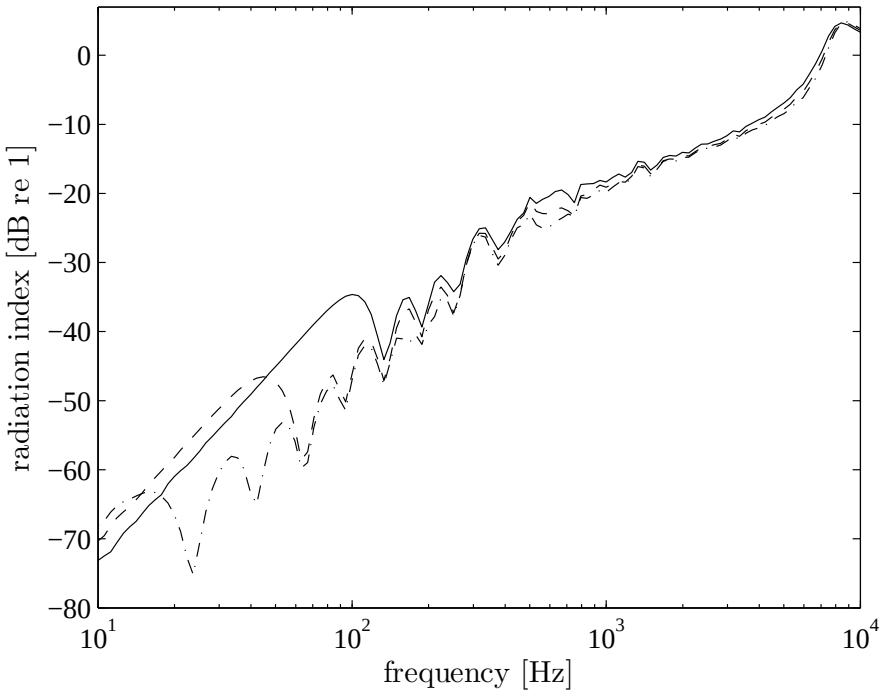


FIGURE 4.12: Average radiation efficiencies of unbaffled plates for different boundary conditions: —(ss−ss), −−(ss−g), −·−(g−g) ($0.4 \times 0.3 \times 0.0015$ m aluminium plate with $\eta = 0.1$).

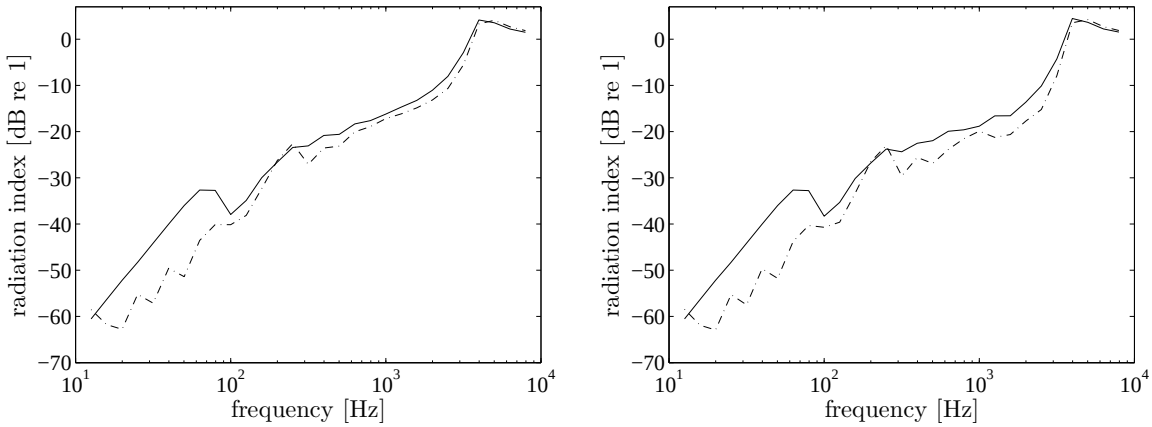


FIGURE 4.13: Average radiation efficiencies of unbaffled plates for different boundary conditions: —(ss−ss), −·−(g−g) ($0.65 \times 0.5 \times 0.003$ m aluminium plate with (a) $\eta = 0.05$ and (b) $\eta = 0.01$).

## 4.4 Summary

The radiation efficiency of a plate with the guided-guided boundary conditions and also a combination of the simply supported and guided edges has been calculated for baffled and unbaffled cases. It has been shown that the guided-guided plate gives less sound radiation for the baffled case. However, it is found that the boundary condition does not have a significant effect on the radiation efficiency for the unbaffled case.

# Chapter 5

# Radiation efficiency of a perforated plate

The radiation efficiency of solid plates, both for baffled and unbaffled conditions has been discussed in the previous chapters. However, although the applications of a perforated plate to reduce the sound radiation are frequently found in practice, models to calculate its radiated sound are lacking. This chapter now focuses on the radiation efficiency of perforated plates. After derivation of the acoustic impedance associated with perforation, two approaches are used. The first follows Fahy and Thompson [37] in studying a perforated plate in a perforated baffle. The second extends the model of Laulagnet [33] to include perforation for an unbaffled plate.

## 5.1 Acoustic impedance of the perforated plate

One of the most important parameters of a perforated plate is the perforation ratio. The perforation ratio $\tau$ is defined as the ratio of the total area of the holes to the total area of the plate $S$ (including the holes), i.e.

$$\tau = \frac{N_o \pi r_o^2}{S} \tag{5.1}$$

where $r_o$ is the radius of each hole (assumed circular) and $N_o$ is the number of holes.

As a result of a pressure difference between the two sides of the plate when the plate is vibrating, the fluid in the hole is forced to move in the opposite direction relative to the plate motion. The fluid driven through the holes reduces the strength of the volume velocity sources, which then causes a reduction in the sound radiation. Therefore, the amplitude of the fluid motion in the holes will play an important role. This is related to its physical property, namely its impedance.

For a circular hole in a plate of finite thickness $t_p$, its acoustic impedance (ratio between pressure and velocity) can be approximated by that of a static (non-moving) short tube ($kt_p \ll 1$). The specific acoustic impedance of a short tube has been studied by various authors [9], [74], [75]. Maa [61] gives the following approximate formula

$$Z_h = Z_{h,R} + Z_{h,I} = \frac{\Delta p}{v_f} \tag{5.2}$$

where

$$Z_{h,R} = \frac{32\nu_a t_p}{d_o^2}\left[\left(1+\frac{X_o^2}{32}\right)^{1/2} + \frac{\sqrt{2}}{32}X_o\frac{d_o}{t_p}\right]$$

$$Z_{h,I} = j\rho\omega t_p\left[1+\left(9+\frac{X_o^2}{2}\right)^{-1/2} + \left(\frac{8}{3\pi}\right)\frac{d_o}{t_p}\right]$$

$$X_o = \frac{d_o}{2}\sqrt{\frac{\omega\rho}{\nu_a}}$$

$\Delta p$ is the sound pressure difference between the two sides of the plate, $v_f$ is the fluid velocity in the tube, $\rho$ is the density of the fluid, $d_o$ is the hole diameter and $\nu_a$ is the viscosity, which for air is $1.8 \times 10^{-5}$ N.s/m$^2$.

The real part $Z_{h,R}$ is called the acoustic resistance and is associated with energy radiation and viscous losses. It includes the distortion of the acoustic flow around the hole edges at the plate surface. The imaginary part is termed the acoustic reactance which is inertial in nature [4]. It corresponds to the mass of the air moving inside the hole, including a part beyond the plate thickness (end correction). This is shown in the diagram in Figure 5.1 [76]. The combination of reactive and resistive motion comprises a region of uniform motion on the centre of the hole, and a boundary layer close to the edges, which reduces in size as frequency increases.

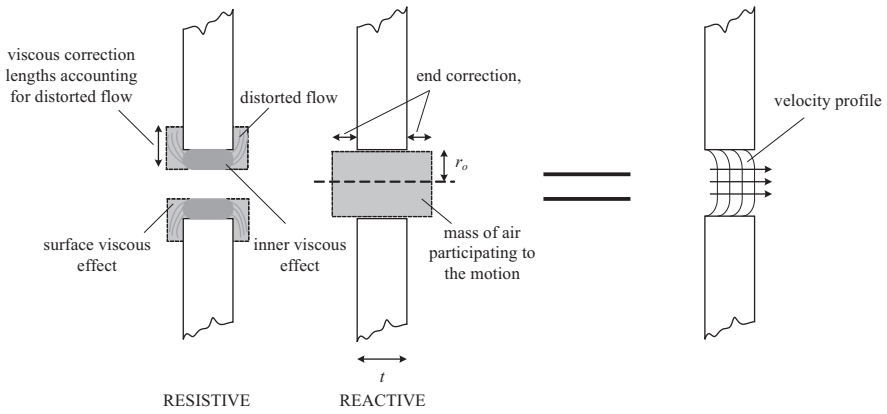


FIGURE 5.1: Physical explanation for the resistive and reactive parts of impedance (re-drawn from [76]).

The above formula was developed for use in the case of a micro-perforated plate (MPP) for an acoustic absorber. For effective absorption, it is suggested that the MPP should have a hole diameter $d_o$ between 0.05 and 1 mm and a perforation ratio $\tau$ between 0.5 and 1.5% [57], [61], [77]. In order to use the formula for larger perforations, as here, some of the terms can be neglected, as will be discussed below.

### 5.1.1 The effect of fluid viscosity and end correction

The effect of the fluid viscosity $\nu$ must be taken into account in modelling microperforations. $X_o$ in Eq.(5.2) is called the perforation constant [61] that includes the effect of friction between the air and the plate interface in the hole due to the viscosity.

Figure 5.2 plots the real and imaginary parts of the acoustic impedance of a 3 mm tube length for certain frequencies as a function of hole diameter. This shows that, for a small hole diameter, the reactance component is almost independent of $d_o$. For $d_o < 0.1$ mm, the resistive component has a higher contribution to the acoustic impedance. However, the resistive component contribution decreases as the hole diameter increases. For a larger hole diameter ($d_o > 1$ mm), the contribution of the reactive component becomes more significant than that of the resistive component. Moreover, its contribution becomes more important as the frequency increases. Therefore for the purpose of the present study, where the hole diameters are generally larger than 1 mm, it can be assumed that the fluid reaction in the holes is purely inertial (behaves like a mass). Hence the resistive component $Z_{h,R}$ will be neglected, leaving only the reactive component $Z_{h,I}$.

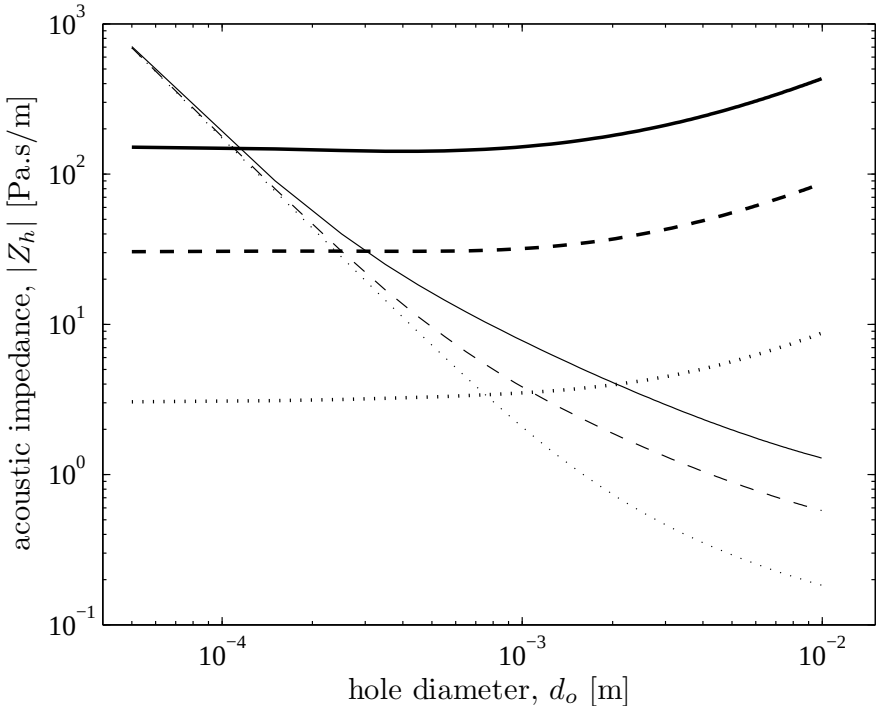


FIGURE 5.2: The magnitude of the real (thin line) and imaginary (thick line) part of the acoustic impedance of a circular hole for particular frequencies ($\cdots$ 100 Hz, $--$1 kHz and —5 kHz; 3 mm tube length).

As $\nu$ for air is small, for larger $d_o$ the term $()^{-1/2}$ in the reactive component is also small. It becomes much smaller than unity as the frequency increases. Hence it can also be omitted from the equation and Eq.(5.2) reduces to

$$Z_h = j\rho\omega t_p \left[1 + \frac{2\epsilon_e}{t_p}\right] \tag{5.3}$$

This corresponds to the impedance of the mass of the fluid in the hole plus an end correction (correction length) $\epsilon_e$ for each end of the tube. For a hole in a thin plate where $t_p \ll r_o$; where $r_o$ is the radius of the hole ($d_o/2$) and $t_p$ is the plate thickness, Rayleigh [9] proposed the end corrections to be between $(\pi/4)r_o$ and $(8/3\pi)r_o$. The first term is proportional to an added mass that corresponds to the excess kinetic energy of fluid motion due to the open end of the hole [73]. In Eq.(5.2), Maa used $(8/3\pi)r_o$. This end correction is proportional to an added mass in the proximity of a moving rigid piston [4, 73]. This can be used assuming that the velocity in the hole is uniform. Another end correction has also been proposed by King [78] i.e. $0.82r_o$. However, quantitatively these values are very similar ($0.79r_o$, $0.85r_o$ and $0.82r_o$ respectively). In the remainder of this thesis the form $(\pi/4)r_o$ will be used as in [9].

Atalla and Sgard [76] applied an equivalent, effective tortuosity following the Johnson-Allard [79] approach for the case of rigid porous media. This effective tortuosity was shown to depend on the end correction due to radiation from the fluid at the end of the hole and also the dynamic tortuosity of the media interfacing with it. Tortuosity is a geometrical parameter related to the kinetic energy of an ideal incompressible potential fluid flow through the material [80]. The end correction used was $\epsilon_e = \epsilon_o(1 - 1.14\sqrt{\tau})$ for $\sqrt{\tau} < 0.4$, where $\epsilon_o = 0.85r_o$ from Rayleigh's end correction [9]. Here, the presence of $\tau$ indicates the effect of adjacent holes on the end correction and hence on the individual impedance of the hole.

An incident sound pressure causes a jet flow through holes and also a grazing flow can reduce the air mass oscillating in the holes and hence change the hole impedance. From this, for low sound pressure levels and no grazing flow, Mechel and Vér [81] proposed a rather similar end correction derived from empirical data i.e. $\epsilon_e = \epsilon_o(1 - 1.47\sqrt{\tau} + 0.47\sqrt{\tau^3})$; $\epsilon_o = 0.85r_o$.

Figure 5.3 compares the hole impedance using three different end correction models, from Rayleigh [9], Atalla and Sgard [76] and Mechel and Vér [81], against the perforation ratio $\tau$. It can be seen that the impedance is similar for all the models at very low perforation ($\tau < 0.4\%$) as expected. The Rayleigh model does not completely converge with the other two models as it uses $\epsilon_e = (\pi/4)r_o$ rather than $0.85r_o$. The impedance from the Mechel-Vér model is lower than the Atalla-Sgard model and both decrease as the perforation ratio increases. At 40% perforation the impedance is likely to be reduced by roughly by 30−40% relative to the simple model. However, both Atalla and Sgard [76] and Mechel and Vér [81] models are for the case of a sound field impinging on a perforated panel. This could differ from the case of sound radiation from a vibrating perforated plate. It is unclear whether these end correction models can be used in the different context. Further discussion will be presented in the next section.

### 5.1.2 The effect of interaction between holes

In order to see whether the model of the hole impedance proposed (Rayleigh's end correction) for sound radiation from a perforated plate is valid, one consideration is to

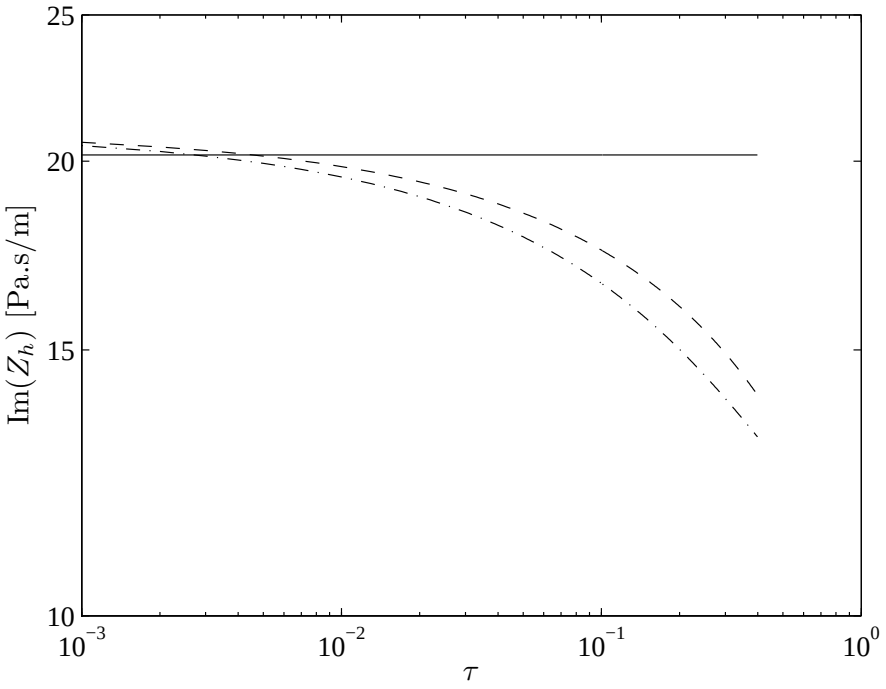


FIGURE 5.3: The magnitude of the acoustic impedance of a circular hole against the perforation ratio $\tau$ at 100 Hz for different models (—Rayleigh, −−Atalla-Sgard and $-\cdot-$Mechel-Vér; $d_o = 15$ mm, $t = 1.5$ mm).

assess the effect of the acoustic field from one hole on the adjacent holes. From this it should be possible to say whether the acoustic impedance of an array of holes can be derived simply from that of a single hole.

The idea is to calculate the acoustic pressure on the surface of the plate as a function of distance from the centre of the hole and to compare it with the acoustic pressure at the centre of the hole. It is assumed that if the hole is large enough to ignore viscous effects at the edges, but small compared with the acoustic wavelength, the motion of fluid inside the holes can be treated as uniform across the hole area. The fluid motion at the hole can then be represented by a piston mounted in an infinite rigid baffle, see Figure 5.4. Assuming a piston of radius $r_o$ moves harmonically with a uniform velocity amplitude $U_o$, the acoustic pressure $p$ can be obtained by using the Rayleigh integral [9]

$$p(R,\phi,\theta) = \frac{jk\rho cU_o}{2\pi}\int_S \frac{e^{-jkR'}}{R'}dS \tag{5.4}$$

where $R'$ is the distance between the point $(r,\theta)$ on the piston and the field point $(R,\phi,\theta)$.

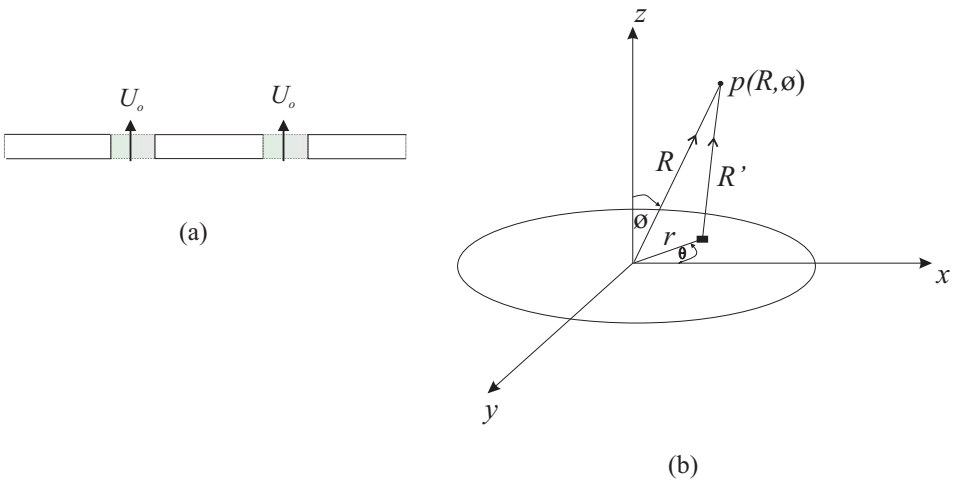


FIGURE 5.4: (a) Fluid motion inside the holes acting like a moving piston with velocity $U_o$ and (b) co-ordinate system of a flat piston.

Following Kinsler and Frey [82], along the $z$ axis ($\phi = 0$), the pressure can be written as

$$p(R,\phi)\Big|_{\phi=0} = \frac{jk\rho c U_o}{2\pi}\int_0^{r_o}\frac{e^{-jk\sqrt{R^2+r^2}}}{\sqrt{R^2+r^2}}2\pi r dr \tag{5.5}$$

The integral can be solved readily since

$$\frac{r}{\sqrt{R^2+r^2}}e^{-jk\sqrt{R^2+r^2}} = -\frac{d}{dr}\left(\frac{e^{-jk\sqrt{R^2+r^2}}}{jk}\right)$$

Then the complex acoustic pressure is

$$p(R,\phi)\Big|_{\phi=0} = \rho c U_o\left[e^{-jkR} - e^{-jk\sqrt{R^2+r_o^2}}\right] \tag{5.6}$$

The pressure at the centre $p_c$ of the piston ($R = 0$) is thus

$$p_c = p(R,\phi)\Big|_{R=0,\phi=0} = \rho c U_o\left(1 - e^{-jkr_o}\right) = \rho c U_o e^{-jkr_o/2}\left(e^{jkr_o/2} - e^{-jkr_o/2}\right) \tag{5.7}$$

This has magnitude

$$|p_c| = 2\rho c U_o\left|\sin\left(\frac{kr_o}{2}\right)\right| \tag{5.8}$$

For a point in the plane of the piston at distance $R$ from the centre, see Figure 5.5, the distance $R'$ from the small element $dS$ of the piston to the observer point can be

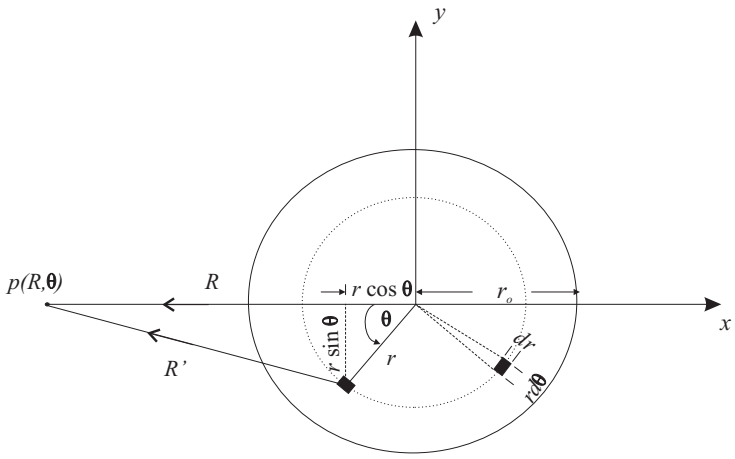


FIGURE 5.5: Co-ordinate system of a piston in $xy$ axes plane.

written as

$$R' = \sqrt{(R - r\cos\theta)^2 + (r\sin\theta)^2} = \sqrt{R^2 - 2Rr\cos\theta + r^2} \tag{5.9}$$

Eq.(5.4) can now be written as

$$p(R,\phi,\theta)\Big|_{\phi=\pi/2} = \frac{jk\rho c U_o}{2\pi}\int_0^{2\pi}\int_0^{r_o}\frac{e^{-jk\sqrt{R^2-2Rr\cos\theta+r^2}}}{\sqrt{R^2-2Rr\cos\theta+r^2}}\, r\, dr\, d\theta \tag{5.10}$$

The double integral in Eq.(5.10) is more difficult to solve analytically so a numerical calculation has been used.

Figure 5.6 plots the ratio of the acoustic pressure on the plate surface to the pressure at the centre of the piston for $kr_o \ll 1$. This is found to be independent of the frequency. The pressure falls very steeply around $R = r_o$. For values of $R > 2r_o$, the pressure ratio becomes less than 0.25 corresponding to a significant sound pressure level (SPL) difference ($10\log_{10} p_1^2/p_2^2$) of more than 12 dB. The SPL difference increases as the distance increases. Relating this to an array of holes, if $R = 2r_o$, $R$ corresponds to the centre of a second hole whose edge is just touching the first, which is quite an extreme form of perforation. Thus for practical situations where $R \gg 2r_o$, the pressure due to one hole can be ignored at the next. Therefore, it can be concluded that the acoustic field of one hole does not have a significant effect on the pressure at the adjacent holes.

Considering a perforated plate with a rectangular array of circular holes, the perforation ratio can be expressed as

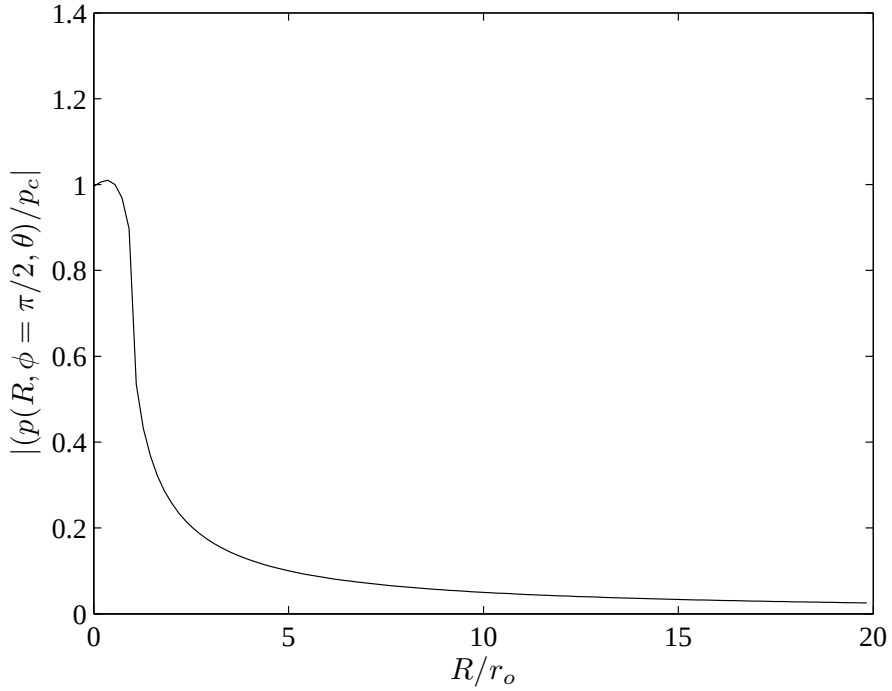


FIGURE 5.6: Pressure on plate surface due to a circular piston of radius $r_o$ relative to the pressure at the centre of the piston ($kr_o \ll 1$).

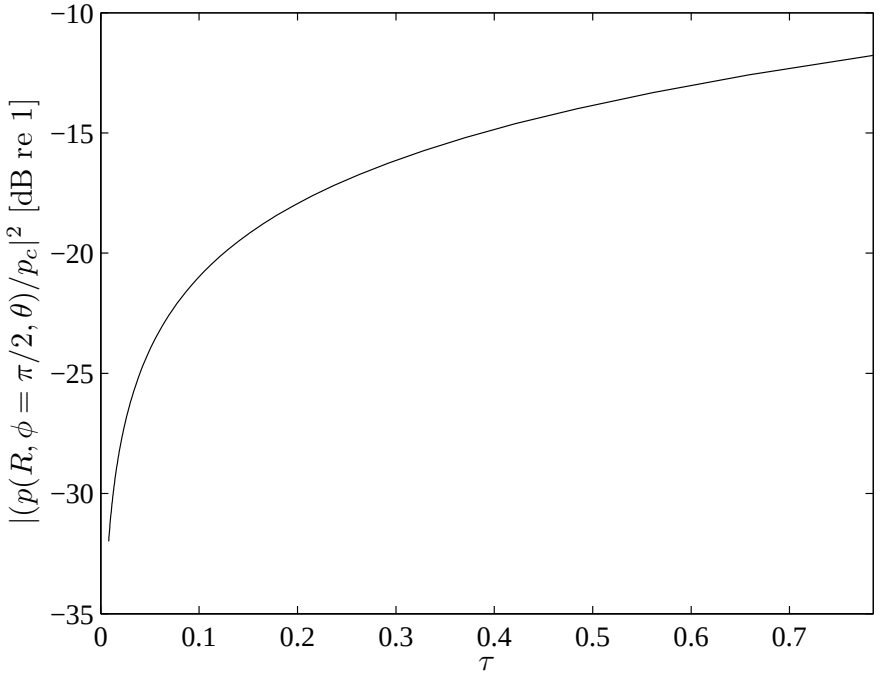


FIGURE 5.7: Pressure on plate surface due to a circular piston of radius $r_o$ relative to the pressure at the centre of the piston plotted against the perforation ratio ($kr_o \ll 1$).

$$\tau = \frac{\pi r_o^2}{R^2} \tag{5.11}$$

where $R$ is the distance between adjacent hole centres.

Figure 5.7 presents the pressure ratio on a dB scale ($10\log_{10}|p/p_c|^2$) for $p$ at the centre of an adjacent hole, plotted against perforation ratio. This shows that a plate can have a very high perforation ratio yet still the influence of one hole on another is small. Even for the maximum theoretical perforation of $\pi/4$, the pressure difference is more than 10 dB.

### 5.1.3 Condition for use of uniform acoustic impedance

Another factor that has to be considered to have a simple model of the sound radiation from a perforated plate is the assumption that the array of holes can be replaced by a uniform distributed acoustic impedance at the surface of the plate. For this to be valid, the distance between the holes must be small enough compared with the acoustic wavelength.

Figure 5.8(a) presents the real part of the ratio between the pressure at some distance $R$ and the pressure at the piston centre. The real part is plotted as this corresponds to radiated part of the sound field. Results are shown for different frequencies. It can be seen that the curves intersect roughly around $kR = \pi/2$. Figure 5.8(b) also shows that at $kR = \pi/2$ the phase is $-90^o$. This suggests that the distance between holes to achieve a uniform acoustic impedance must satisfy

$$R < \frac{\pi}{2k} = \frac{\lambda}{4} \tag{5.12}$$

where $\lambda$ is the acoustic wavelength. However this condition will be considered in more detail in Chapter 6 using a different approach.

### 5.1.4 Uniform acoustic impedance

Consider a plate with a uniform array of holes as shown in Figure 5.9. If the hole distance $b_o$ is much smaller than the acoustic wavelength such that $kb_o \ll 1$, the

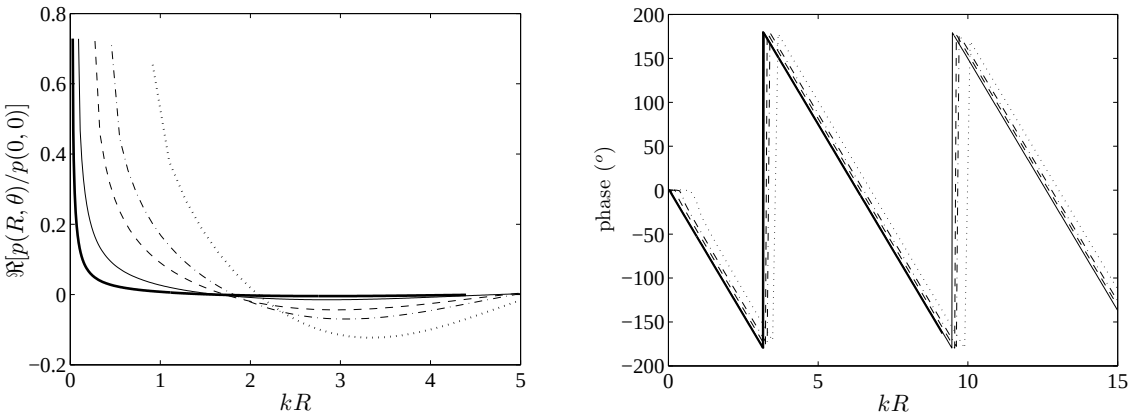


(a) (b)

FIGURE 5.8: (a) The real part of the ratio between the pressure at a distance from and at the centre of the piston and (b) the phase of the pressure ratio (— 500 Hz, —1 kHz, −−3 kHz, − · −5 kHz, · · · 10 kHz).

resulting local pressure difference $\Delta p$ at the mouth of the hole can be distributed over an area $S_a$. From this, the individual hole interaction to the sound field (the local impedance) is of interest and the array of holes can be defined as an equivalent layer of uniform impedance on the plate surface [81]

$$z_h = \frac{\langle \Delta p \rangle}{\langle v_f \rangle} = \frac{\Delta p}{v_f}\frac{S_a}{S_o} = Z_h \frac{S_a}{S_o} = \frac{Z_h}{\tau} \tag{5.13}$$

where $\tau$ is the perforation ratio and $z_h$ is termed an equivalent, continuously distributed specific acoustic impedance.

Using Rayleigh's end correction in Eq.(5.3), $\epsilon_e = (\pi/4)\, r_o$, the continuously distributed specific acoustic impedance is given by

$$z_h = \frac{Z_h}{\tau} = \frac{j\rho\omega t_p}{\tau}\left[1 + \left(\frac{\pi}{4}\right)\frac{d_o}{t_p}\right] \tag{5.14}$$

Using $k = \omega/c$, this can be expressed as

$$z_h = j\rho c\left[\frac{kt_p}{\tau}\left(1 + \frac{\pi d_o}{4t_p}\right)\right] = j\rho c h \tag{5.15}$$

where $h$ is the non-dimensional specific acoustic reactance, which can be written as

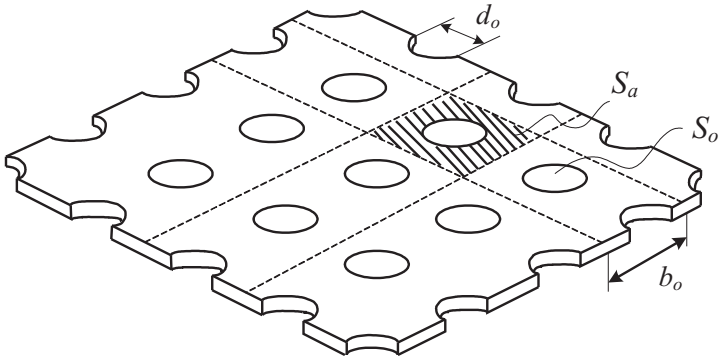


FIGURE 5.9: An array of holes in a plate.

$$h = \frac{k}{\tau}\left(t_p + \frac{\pi d_o}{4}\right) \tag{5.16}$$

In Chapter 6, the plate and the holes are modelled with discrete sources, i.e. an array of monopole sources that contribute to the sound radiation. This allows the frequency limit of the uniform acoustic impedance to be verified in terms of distance between holes.

All the results throughout the remainder of this thesis will be based on using the impedance as in Eq.(5.15).

## 5.2 Radiation by modes of a perforated plate in a perforated baffle

### 5.2.1 Wave in an infinite plate

For a plane, harmonic, bending wave of frequency $\omega$ and wavenumber $k_x$ propagating in the $x$-direction in an infinite plate (see Figure 2.3), the specific acoustic impedance presented to the upper surface of the plate by the fluid ($z > 0$), $z_a(k_x)$, is given by [4]

$$z_a(k_x) = \frac{\widetilde{P}(k_x)}{\widetilde{V}(k_x)} = \frac{\omega\rho}{(k^2 - k_x^2)^{1/2}}, \qquad k_x < k \tag{5.17}$$

where $\widetilde{P}(k_x)$ and $\widetilde{V}(k_x)$ are the complex acoustic pressure and the plate velocity amplitudes respectively (see Eq.(2.32)). For $k_x > k$, $z_a(k_x)$ is imaginary (reactive). Only

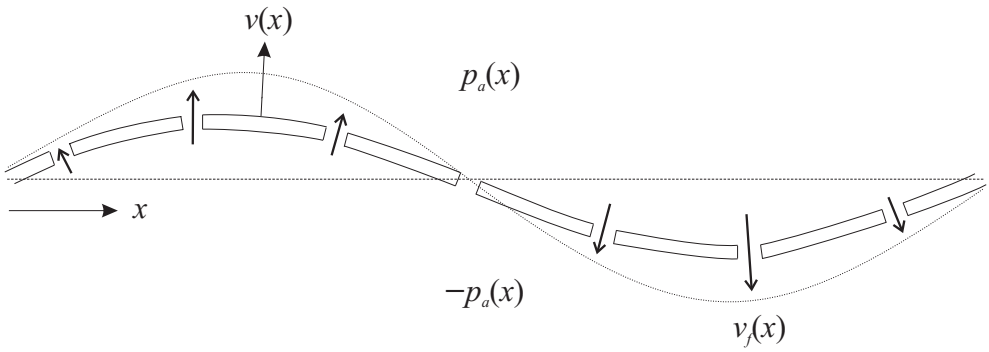


FIGURE 5.10: Analytical model of a perforated plate

the real part of $z_a(k_x)$ is required here to calculate the propagating waves producing sound radiation. The imaginary part produces a near field.

In the case of a perforated plate, as shown in Figure 5.10, following the method of [37] the difference between the local pressures on the upper and lower surfaces of the plate drives fluid through the individual holes. In turn, these pressures are modified by the flow through the holes. Considering the holes as a continuous distribution, an equivalent fluid particle velocity $v_f(x)$, due to the flow through the holes *relative* to the plate, can be given by

$$v_f(x) = \frac{-2p_a(x)}{z_h} \tag{5.18}$$

where $p_a$ is the upper surface pressure (the pressure on the lower surface is $-p_a$) resulting from the combination of the plate velocity $v(x)$ and the equivalent continuously distributed fluid velocity through the holes $v_f(x)$ and $z_h$ is the distributed hole impedance given by Eq.(5.15) (the actual flow through the holes is $v_f/\tau$). Therefore for the perforated plate, the net particle velocity $v_p$ formed by the combination of the normal velocity of plate $v$ and the continuously distributed average fluid motion $v_f$ is given by

$$v_p(x) = v(x) + v_f(x) = v(x) - \frac{2p_a(x)}{z_h} \tag{5.19}$$

Since the plate is assumed infinite and the bending wave has a unique wavenumber $k_x$, the plate and the equivalent fluid particle velocity also have the same unique wavenumber in the $x$ direction. Eq.(5.19) can be expressed as

$$\widetilde{V}_p(k_x) = \widetilde{V}(k_x) + \widetilde{V}_f(k_x) = \widetilde{V}(k_x) - \frac{2\widetilde{P}_a(k_x)}{z_h} \tag{5.20}$$

From Eq.(5.17), this generates the pressure $\widetilde{P}_a$

$$\widetilde{P}_a(k_x) = \widetilde{V}_p(k_x) z_a(k_x) = \left( \widetilde{V}(k_x) - \frac{2\widetilde{P}_a(k_x)}{z_h} \right) z_a(k_x) \tag{5.21}$$

Rearranging yields

$$\widetilde{P}_a(k_x) = \frac{z_h \, z_a(k_x)}{z_h + 2z_a(k_x)} \widetilde{V}(k_x) \tag{5.22}$$

Finally substituting Eq.(5.22) into Eq.(5.20) yields the ratio of the complex amplitudes of the combined normal velocity of plate and fluid flow through the holes to that of the plate alone

$$\frac{\widetilde{V}_p(k_x)}{\widetilde{V}(k_x)} = \frac{1}{1 + 2z_a(k_x)/z_h} \tag{5.23}$$

Eq.(5.23) confirms that the sound radiation from the plate is reduced by introducing perforation to the plate. As $|z_a(k_x)/z_h| \to \infty$, i.e. open area condition (absence of the plate), the ratio tends to zero so that flow through the holes completely compensates the plate motion, while as $z_a(k_x)/z_h \to 0$, i.e. the unperforated plate (absence of the holes), the ratio tends to unity.

The sound power radiated per unit area of the perforated plate can be calculated from

$$W_p(k_x) = \frac{1}{2} \Re \left\{ \widetilde{P}(k_x) \widetilde{V}_p^*(k_x) \right\} \tag{5.24}$$

By using the relation from Eq.(5.17)

$$W_p(k_x) = \frac{1}{2} \Re \left\{ z_a(k_x) \widetilde{V}_p(k_x) \widetilde{V}_p^*(k_x) \right\} = \frac{1}{2} \left| \widetilde{V}_p(k_x) \right|^2 \Re \left\{ z_a(k_x) \right\} \tag{5.25}$$

The ratio of sound power per unit area of the perforated plate to that of the unperforated plate is therefore given by

$$\frac{W_p(k_x)}{W(k_x)} = \left| \frac{\widetilde{V}_p(k_x)}{\widetilde{V}(k_x)} \right|^2 = \frac{1}{1 + 4(z_a(k_x)/\left|z_h\right|)^2} \,, \qquad k_x < k \tag{5.26}$$

since $z_h$ is imaginary and $z_a$ is real.

In terms of the non-dimensional specific acoustic reactance $h$, the ratio $z_a(k_x)/|z_h|$ can be expressed as

$$\frac{z_a(k_x)}{|z_h|} = \frac{1}{h(1-k_x^2/k^2)^{1/2}} = \frac{1}{h(1-\alpha^2)^{1/2}}, \qquad \alpha < 1 \tag{5.27}$$

where $\alpha = k_x/k$.

For a plane wave travelling with components in the $x$ and $y$ directions, $k_x^2$ can be replaced by the square of the resultant $k_x^2 + k_y^2$. It follows that Eq.(5.27) can be written as

$$\frac{z_a(k_x, k_y)}{|z_h|} = \frac{1}{h(1-\alpha^2-\beta^2)^{1/2}}, \qquad \alpha^2 + \beta^2 < 1 \tag{5.28}$$

where $\beta = k_y/k$.

### 5.2.2 Finite plate in a perforated baffle

From the infinite plate case, the situation can be extended to the case of modes of vibration in a finite baffled plate which can be decomposed into a spectrum of travelling waves.

Consider a rectangular plate set in an infinite baffle. For convenience at this stage, the baffle is assumed to be similarly perforated to the plate so that the previous analysis can be used, i.e. the plate and the equivalent fluid particle velocity through the holes share the same wavenumber. If the baffle is rigid, a mixed boundary impedance would exist and Eq.(5.20) would not be valid and would have to be modified.

Suppose the plate is vibrating in mode $(m, n)$. The plate vibration can be defined by its non-dimensional wavenumber spectrum over $(\alpha, \beta)$. From Eq.(5.26), the ratio of the squared amplitudes of the total normal velocity of plate and fluid flow through the holes to that of the unperforated plate velocity, for the mode $(m,n)$ at non-dimensional wavenumber $(\alpha, \beta)$ is given by

$$|X(\alpha,\beta)|^2 = \left|\frac{\widetilde{V}_{p,mn}(\alpha,\beta)}{\widetilde{V}_{mn}(\alpha,\beta)}\right|^2 = \frac{h^2(1-\alpha^2-\beta^2)}{4+h^2(1-\alpha^2-\beta^2)}, \qquad \alpha^2+\beta^2 < 1 \tag{5.29}$$

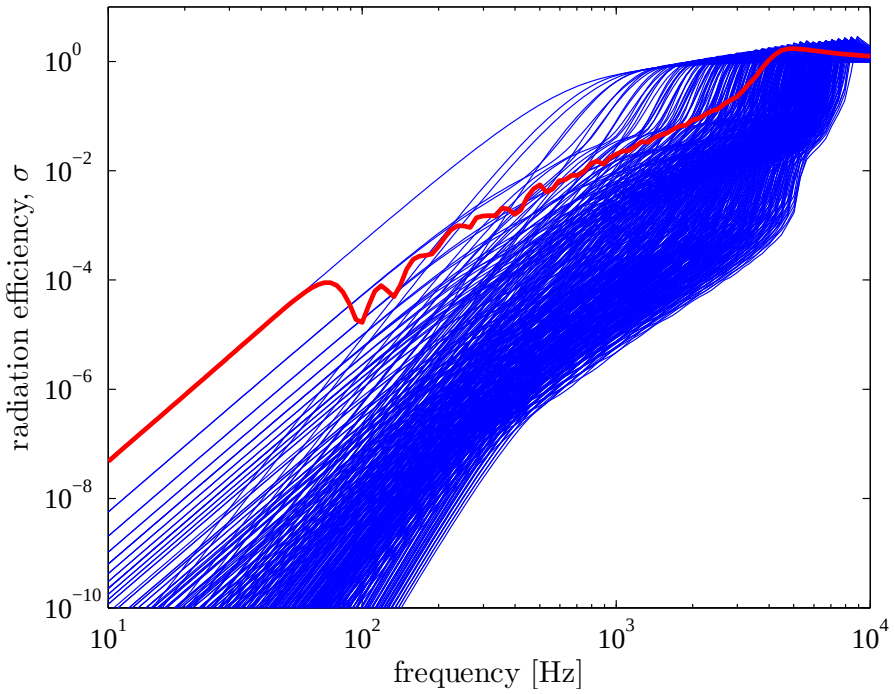


FIGURE 5.11: Modal and average radiation efficiency of a simply supported rectangular perforated plate in an infinite perforated baffle ($0.65 \times 0.5 \times 0.003$ m aluminium plate with $\eta = 0.1$; $d_o = 5$ mm, $\tau = 5\%$):—modal radiation efficiency; — average radiation efficiency.

Therefore to calculate the sound power radiated by a mode of a perforated plate, $|X(\alpha,\beta)|^2$ can be inserted into Eq.(2.49) in the wavenumber domain approach in Section 2.2. This equation now becomes

$$\overline{W}_{p,mn} = \frac{\rho c \overline{|u_{mn}|^2}}{2\pi^2 k^2} \int_0^1 \int_0^{\sqrt{1-\alpha^2}} |X(\alpha,\beta)|^2 \, \Lambda^2 \frac{(\Gamma^2 + \Pi^2)}{(1-\alpha^2-\beta^2)^{1/2}} \, d\beta \, d\alpha \tag{5.30}$$

The radiation efficiency of the perforated plate is then given by

$$\sigma_{mn} = \frac{4}{\pi^2 (ka)(kb)} \int_0^1 \int_0^{\sqrt{1-\alpha^2}} |X(\alpha,\beta)|^2 \, \Lambda^2 \frac{(\Gamma^2 + \Pi^2)}{(1-\alpha^2-\beta^2)^{1/2}} \, d\beta \, d\alpha \tag{5.31}$$

where the normalisation is based on the whole area of the plate including the perforation.

### 5.2.3 Results

With the same plate dimensions and properties as in the previous chapters, Figure 5.11 shows the results of the modal and average radiation efficiencies of an example plate having a 5% perforation ratio with 5 mm diameter holes. As seen from the figure, at very low frequencies, at the fundamental mode ($< 70$ Hz), instead of increasing at 20 dB/decade as the unperforated plate does, the slope of the average radiation efficiency of the perforated plate now becomes 40 dB/decade, where the additional 20 dB/decade is due to the effect of the holes. The motion of the fluid in the holes is in the opposite direction to that of the plate, i.e. 180° out of phase. The field produced by the surface sources of the plate in the vicinity of the holes is largely suppressed by the opposite fluid motion through the holes. Hence below the natural frequency of the fundamental mode, the motion of the plate and the fluid in the holes can be associated with the motion of two monopole sources acting in opposite directions which now constitute a dipole source. In the region from 100 Hz to 1 kHz, the average radiation efficiency has a frequency dependence of approximately 20 dB/decade.

Figure 5.12 plots the average radiation efficiencies obtained with various perforation ratios $\tau$ and constant hole diameter $d_o$ and also the radiation efficiency of the unperforated plate for comparison. It can be seen that, as the perforation ratio increases, the radiation efficiency is simply reduced by an amount that is approximately constant over the frequency range.

In order to show the effect of the perforation on the sound radiation, the results are presented in terms of the sound radiation of a perforated plate relative to that of the equivalent unperforated plate. The effect of perforation (EoP) is defined in decibels (dB) by

$$\text{EoP} = 10 \log_{10} \left( \frac{W_p}{W} \right) \tag{5.32}$$

where $W_p$ and $W$ are the overall radiated power of the perforated and unperforated plates respectively. This is related to the insertion loss (IL) commonly used in noise control where EoP $= -$IL. As the perforation is assumed to have no effect on the average mean square velocity of the plate $\overline{\langle v^2 \rangle}$, the $EoP$ can also be written as

$$\text{EoP} = 10 \log_{10} \left( \frac{\sigma_p}{\sigma} \right) \tag{5.33}$$

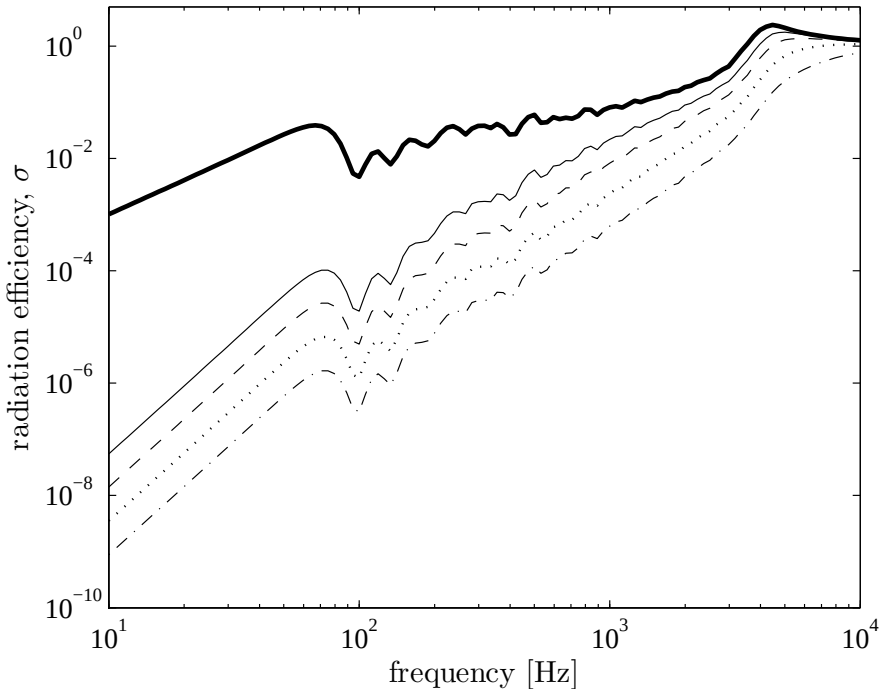


FIGURE 5.12: Average radiation efficiency of a simply supported rectangular perforated plate in an infinite perforated baffle ($0.65 \times 0.5 \times 0.003$ m aluminium plate with $\eta = 0.1$; $d_o = 5$ mm: — unperforated, $\tau$= — 5%, −− 10%, $\cdots$ 20% and $-\cdot-$ 40%).

where $\sigma_p$ is the radiation efficiency of the perforated plate and $\sigma$ is for the unperforated plate. However, the validity of this assumption will be considered in Section 5.5.

Figure 5.13 plots the effect of perforation (EoP) for a constant hole diameter of 10 mm and varying perforation ratio. It can be seen the EoP has a trend of 20 dB/decade slope before converging to 0 dB at high frequency. The 0 dB value in the EoP curve means that the perforation no longer has an effect on the radiated sound. A slight dip occurs at the critical frequency (4 kHz).

Figure 5.14 show results with a constant perforation ratio and various hole diameters. This shows that the sound radiation can be further reduced by reducing the hole diameter, i.e. increasing the number of holes per unit area of the plate (hole density) for a given perforation ratio. From Eq.(5.16), for a thin plate where the plate thickness is much smaller than the hole radius, $t_p \ll d_o$, the non-dimensional specific acoustic reactance is dominated by the end correction and can be expressed as $h = k\pi d_o/(4\tau)$. Consequently, the effect of perforation is controlled by a factor of $d_o/\tau$. As seen from Figure 5.13 and Figure 5.14, with the same values of $d_o/\tau$, the effect of the perforation is almost equal. For example $d_o = 10$ mm, $\tau = 10\%$ and $d_o = 20$ mm, $\tau = 20\%$ give

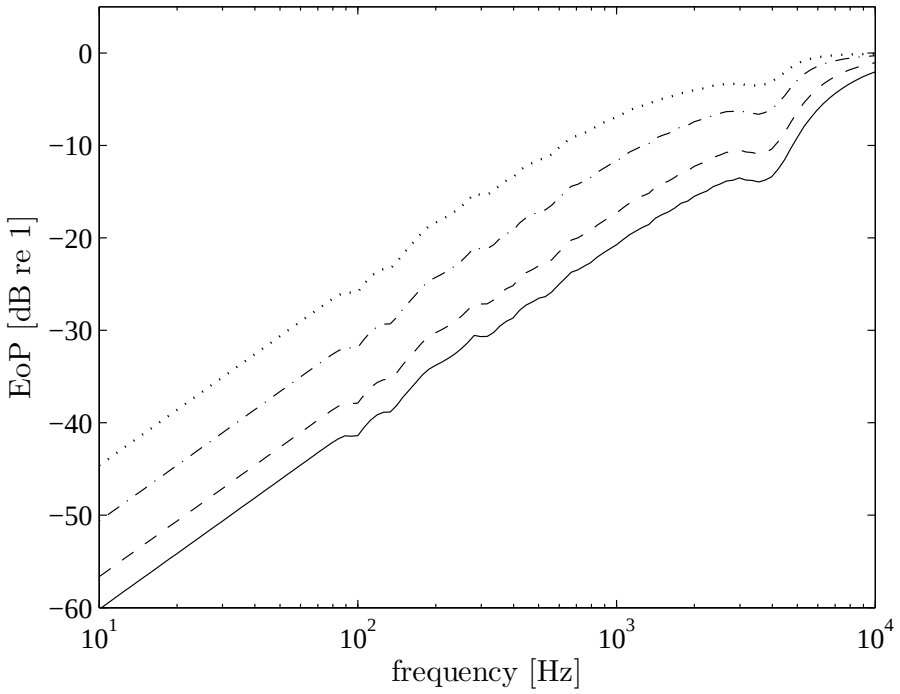


FIGURE 5.13: Effect of perforation (EoP) on sound power radiation of a simply supported rectangular perforated plate in an infinite perforated baffle ($0.65 \times 0.5 \times 0.003$ m aluminium plate, $\eta = 0.1$, $d_o = 10$ mm; $\cdots \tau = 10\%$, $- \cdot - \tau = 20\%$, $-- \tau = 40\%$, $\text{—} \tau = 60\%$).

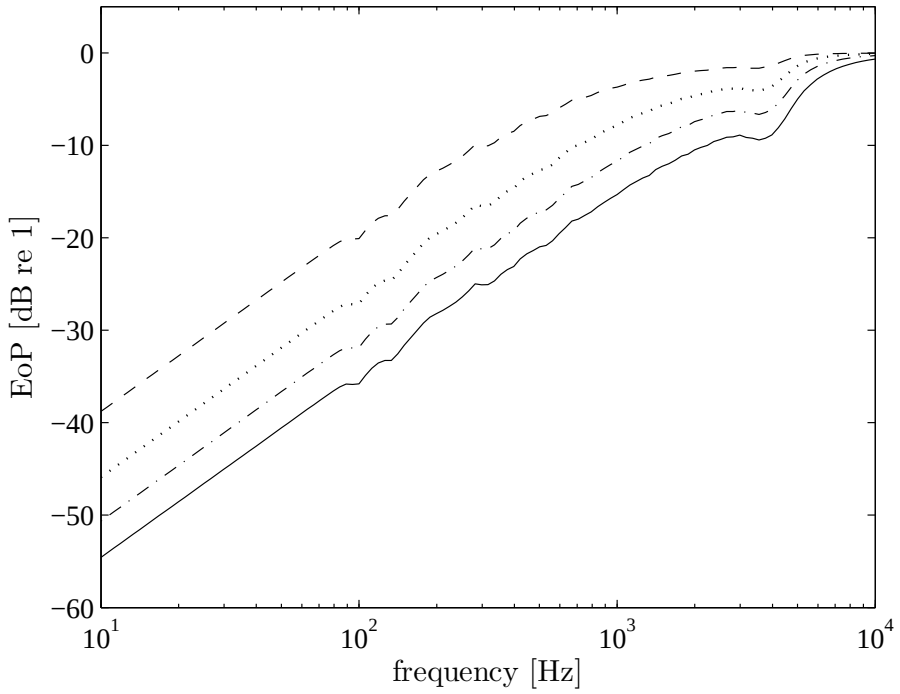


FIGURE 5.14: Effect of perforation (EoP) on sound power radiation of a simply supported rectangular perforated plate in an infinite perforated baffle ($0.65 \times 0.5 \times 0.003$ m aluminium plate, $\eta = 0.1$, $\tau = 20\%$; $\text{—} d_o = 5$ mm, $- \cdot - d_o = 10$ mm, $\cdots d_o = 20$ mm, $-- \; d_o = 50$ mm).

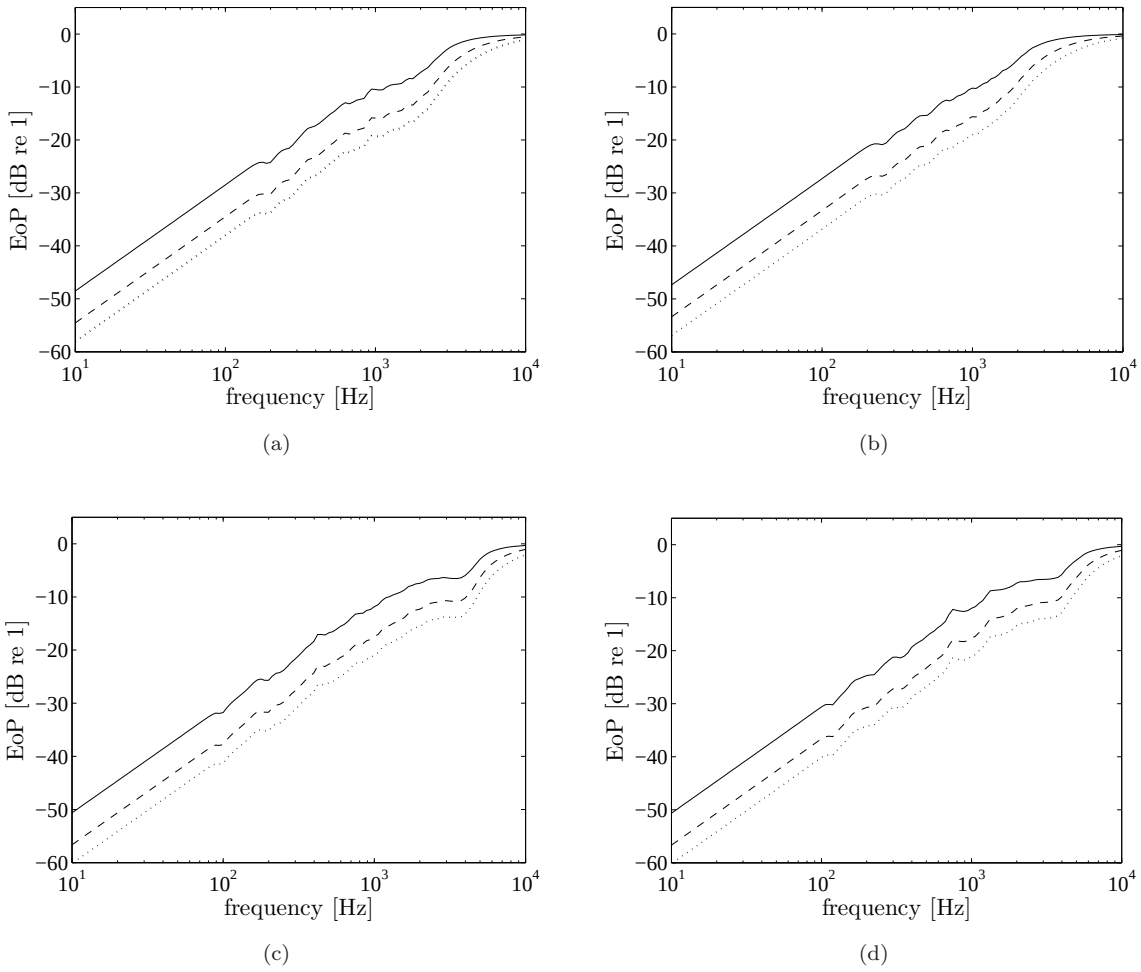


FIGURE 5.15: Effect of perforation (EoP) on sound power radiation of a simply supported rectangular perforated plate in a perforated baffle for different thicknesses; (a) $0.65 \times 0.5 \times 0.006$ m, (b) $0.65 \times 0.5 \times 0.008$ m and dimensions; (c) $0.75 \times 0.4 \times 0.003$ m, (d) $0.9 \times 0.3 \times 0.003$ m (aluminium plate, $\eta = 0.1$; $d_o = 10$ mm, $\tau =$ — 20%, $--$ 40%, $\cdots$ 60%).

very similar results.

Figure 5.15 presents the results for different thicknesses and dimensions of the plate. For different thicknesses, Figure 5.15(a) and (b) show similar results apart from the region of the critical frequency (2 kHz for 6 mm and 1.5 kHz for 8 mm thickness). The thickness also has an effect on $h$ (Eq.(5.16)).

Figure 5.15(c) and Figure 5.15(d) show clearly that, for this model, the effect of perforation does not depend on the plate dimensions, see also Figure 5.13. The effect of perforation is affected only by the perforation ratio and the hole size (see Eq.(5.16)) and to a lesser extent by the plate thickness.

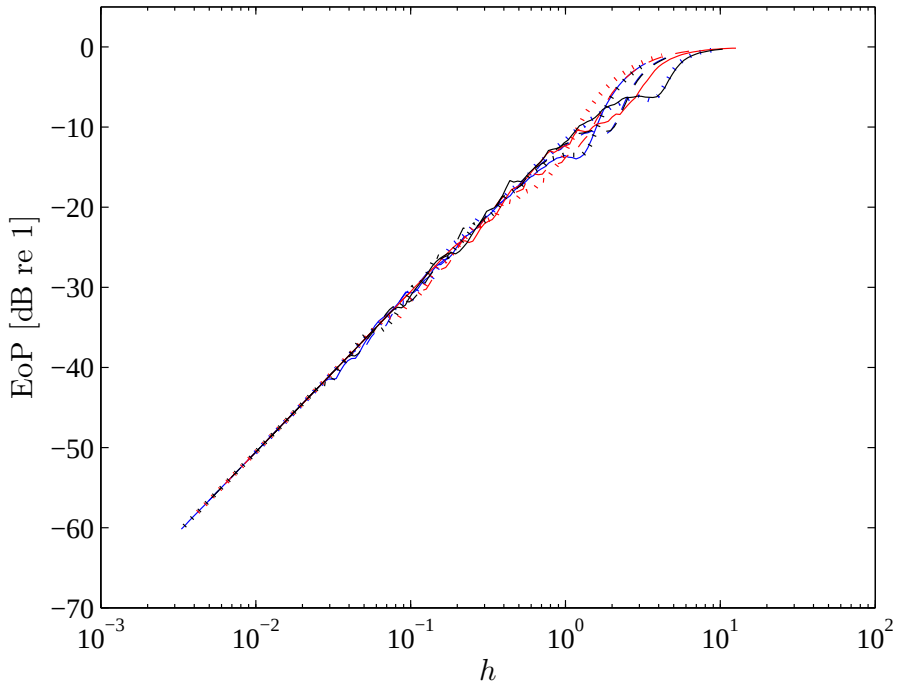


FIGURE 5.16: Effect of perforation (EoP) on sound power radiation of a simply supported rectangular perforated plate in an infinite perforated baffle plotted against non-dimensional reactance $h$ ($0.65 \times 0.5 \times 0.003$ m (blue line), $0.65 \times 0.5 \times 0.006$ m (red line) and $0.75 \times 0.4 \times 0.003$ m (black line); aluminium plate with $\eta = 0.1$, $d_o = 10$ mm; $\tau =$ — 20%, −− 40%, $\cdots$ 60%).

The results can also be plotted against the non-dimensional acoustic reactance $h$. It can be seen from Figure 5.16 that for different dimensions and thicknesses, all the results collapse to a single line apart from small differences among the results that occur close to the critical frequency. Because the effect of perforation is independent of the plate dimensions, the curves are identical for similar plate thickness (see blue and black curves).

### 5.2.4 Approximate formula for EoP

The differences in the effect of perforation at high frequencies are due to the results around and above the critical frequency as each curve converges to 0 dB. Neglecting this, an approximation can be made, at least up to the edge mode region of the sound radiation by fitting a straight line to the results in Figure 5.16. The approximate formula for the effect of perforation for a perforated plate in an infinite perforated

baffle can be written as

$$\mathrm{EoP}_{\mathrm{aprx}} = 20\log_{10}(h) - 10.5\,, \qquad f < f_c/2 \tag{5.34}$$

Figure 5.17 plots the results comparing the analytical (EoP) and approximated ($\mathrm{EoP}_{\mathrm{aprx}}$) effect of perforation. Good agreement is found between the results up to $h_c/2$, where $h_c$ is the non-dimensional acoustic reactance at the critical frequency, $f_c$.

## 5.3 Radiation by modes of a perforated, unbaffled plate

Although mathematically convenient, a perforated plate set in a similarly perforated baffle is not of direct practical relevance, as such a situation is rarely found in practice. The more interesting case is where the baffle has a different acoustic impedance, such as a perforated plate mounted in a rigid baffle or an unbaffled perforated plate. The latter especially is frequently found in real applications and is discussed in this section.

### 5.3.1 Extended equations

The method of Laulagnet [33] for the sound radiation of an unbaffled plate discussed in Section 3.2 can be extended to introduce perforation on the plate.

Recalling Eq.(3.5), the flexural wave equation of a perforated plate excited by a point force is written as

$$B\nabla^4 w(x,y) - m_p\omega^2 w(x,y) = F(x,y) + (1-\tau)\Delta p(x,y) \tag{5.35}$$

where $\tau$ is the perforation ratio.

The motion of the fluid inside the holes depends on the pressure difference $\Delta p(x,y)$ between the two sides of the plate surface as in Eq.(3.4) (positive for larger pressure at $z<0$ than at $z>0$). The specific acoustic impedance of the distribution of holes can then be expressed as

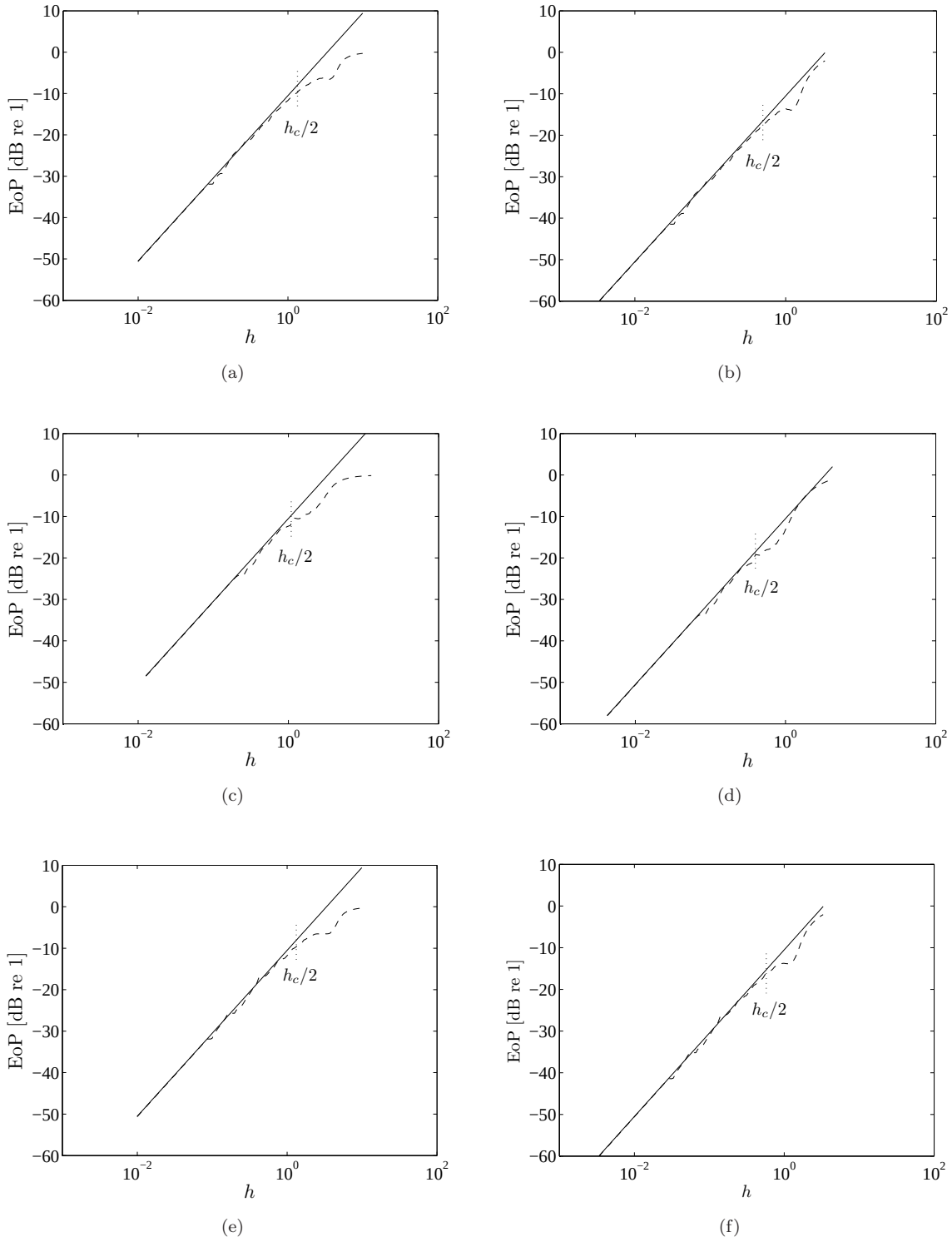


FIGURE 5.17: Comparison of exact (−−) and approximated (—) effect of perforation (EoP) of a simply supported plate in an infinite perforated baffle.(a) and (b) $0.65 \times 0.5 \times 0.003$ m, (c) and (d) $0.65 \times 0.5 \times 0.006$ m, (e) and (f) $0.75 \times 0.4 \times 0.003$ m; (a),(c), (e): $\tau = 20\%$ and (b),(d), (f): $\tau = 60\%$ (aluminium plate with $\eta = 0.1$; $d_o = 10$ mm).

$$z_h = \frac{\Delta p(x,y)}{v_f(x,y)} \tag{5.36}$$

where $v_f(x,y)$ is the velocity of the fluid.

With the same coordinate system of the plate as in Figure 3.2 in Chapter 3, by using Eq.(3.8) on the plate surface at $z = 0$ and substituting Eq.(5.36), the pressure gradient at the plate surface can be written as

$$\begin{aligned}\frac{\partial p}{\partial z}(M)|_{z=0} &= \rho\,\omega^2(w(M) - w_f(M)) = \rho\,\omega^2 w(M) + j\rho\,\omega\,v_f(M) \\ &= \rho\,\omega^2 w(M) + \frac{j\rho\omega}{z_h}\Delta p(M)\end{aligned} \tag{5.37}$$

where $M$ is a point in the medium above the plate, $w_f$ is the fluid displacement relative to the plane $z = 0$ and $v_f = j\omega w_f$.

Substituting for $\Delta p$ from Eq.(5.35) gives

$$\frac{\partial p}{\partial z}(M)|_{z=0} = \rho\,\omega^2 w(M) + \frac{j\rho\omega}{z_h}(B\nabla^4 w(M) - m_p\omega^2 w(M) - F(M))\frac{1}{(1-\tau)} \tag{5.38}$$

Following the same procedure as in Section 3.2, this is inserted into the Kirchhoff-Helmholtz integral of Eq.(3.13) to give

$$\begin{aligned}&(1-\tau)\rho\,\omega^2 w(M) + \frac{j\rho\omega}{z_h}(B\nabla^4 w(M) - m_p\omega^2 w(M) - F(M)) \\ &\qquad = -\int_{S_p}(B\nabla^4 w(Q) - m_p\omega^2 w(Q) - F(Q))\,\frac{\partial^2 G(Q,M)}{\partial z_Q \partial z_M}\,dS_p\end{aligned} \tag{5.39}$$

where $Q$ is a point on the plate surface. Compared with Eq.(3.15) the second term on the left-hand side has been added by the perforation.

Writing the displacement $w$ (Eq.(3.16)) and the excitation force $F$ (Eq.(3.17)) in terms of modal series gives

$$
\begin{aligned}
&(1-\tau)\rho\,\omega^2 \sum_{m=1}^{\infty}\sum_{n=1}^{\infty} d_{mn}\varphi_{mn}(x_0,y_0) \\
&\quad + \frac{j\rho\omega}{z_h}\sum_{m=1}^{\infty}\sum_{n=1}^{\infty}(Bd_{mn}\nabla^4\varphi_{mn}(x_0,y_0) - m_p\omega^2 d_{mn}\varphi_{mn}(x_0,y_0) - F_{mn}\varphi_{mn}(x_0,y_0)) \\
&\quad = -\int_{S_p}(Bd_{mn}\nabla^4\varphi_{mn}(x,y) - m_p\omega^2 d_{mn}\varphi_{mn}(x,y) - F_{mn}\varphi_{mn}(x,y))\,\frac{\partial^2 G(Q,M)}{\partial z_Q \partial z_M}\,dS_p
\end{aligned}
\tag{5.40}
$$

where $d_{mn}$ is the modal complex displacement amplitude and $F_{mn}$ is the generalized force density.

Substituting Eq.(3.22) to eliminate the terms $\nabla^4\varphi_{mn}$ yields

$$
\begin{aligned}
&(1-\tau)\rho\,\omega^2 \sum_{m=1}^{\infty}\sum_{n=1}^{\infty} d_{mn}\varphi_{mn}(x_0,y_0) + \frac{j\rho\omega}{z_h}\sum_{m=1}^{\infty}\sum_{n=1}^{\infty}(m_p(\omega_{mn}^2-\omega^2)d_{mn} - F_{mn})\varphi_{mn}(x_0,y_0) \\
&\quad = -\int_{S_p}\sum_{m=1}^{\infty}\sum_{n=1}^{\infty}(m_p(\omega_{mn}^2-\omega^2)d_{mn} - F_{mn})\varphi_{mn}(x,y)\,\frac{\partial^2 G(Q,M)}{\partial z_Q \partial z_M}\,dS_p
\end{aligned}
\tag{5.41}
$$

Multiplying by $\varphi_{pq}$ and integrating over the plate area gives

$$
\begin{aligned}
&(1-\tau)\frac{\rho\,\omega^2}{m_p}d_{pq}M_{pq} + \frac{j\rho\omega}{z_h m_p}(m_p(\omega_{pq}^2-\omega^2)d_{pq} - F_{pq})M_{pq} \\
&\quad = \sum_{m=1}^{\infty}\sum_{n=1}^{\infty}(F_{mn} - m_p(\omega_{mn}^2-\omega^2)d_{mn})\,C_{pqmn}
\end{aligned}
\tag{5.42}
$$

where $C_{pqmn} = C_{mnpq}$ are the acoustical cross-modal coupling terms as defined in Eq.(3.24).

For the case of a simply supported plate, using the modal mass as in Eq.(3.27) yields

$$
\begin{aligned}
&(1-\tau)\rho\omega^2\frac{S_p}{4}d_{pq} + \frac{j\omega\rho}{z_h}\frac{S_p}{4}(m_p(\omega_{pq}^2-\omega^2)d_{pq} - F_{pq}) \\
&\quad = \sum_{m=1}^{\infty}\sum_{n=1}^{\infty}(F_{mn} - m_p(\omega_{mn}^2-\omega^2)d_{mn})C_{pqmn}
\end{aligned}
\tag{5.43}
$$

To include the effect of damping into the sound radiation calculation, the plate natural frequency $\omega_{mn}^2$ is replaced by $\omega_{mn}^2(1+j\eta)$.

After re-arranging Eq.(5.43), its solution can be written in terms of vectors and matrices as

$$[C_{mnpq}]\{m_p(\omega_{mn}^2-\omega^2)d_{mn}\}+(1-\tau)\rho\omega^2\frac{S_p}{4}[I]\{d_{mn}\}+\frac{j\omega\rho}{z_h}\frac{S_p}{4}[I]\{m_p(\omega_{mn}^2-\omega^2)d_{mn}\} \tag{5.44}$$
$$=[C_{mnpq}]\{F_{mn}\}+[I]\frac{j\omega\rho}{z_h}\frac{S_p}{4}\{F_{mn}\}$$

where $[I]$ is the $mn\times mn$ identity matrix and $\{\}$ denotes a column vector.

Multiplying by $[C_{mnpq}]^{-1}$ yields

$$\begin{aligned}&[I]\{m_p(\omega_{mn}^2-\omega^2)d_{mn}\}+\\&+\rho\omega^2\frac{S_p}{4}[C_{mnpq}]^{-1}\left((1-\tau)[I]\{d_{mn}\}+\frac{jm_p}{\omega z_h}[I]\{(\omega_{mn}^2-\omega^2)d_{mn}\}\right)\\&=\left([I]+\frac{j\omega\rho}{z_h}\frac{S_p}{4}[C_{pqmn}]^{-1}\right)\{F_{mn}\}\end{aligned} \tag{5.45}$$

By neglecting the cross-modal coupling contributions in the sound radiation as in Chapter 3 ([33]) i.e. only the self-modal coupling terms are considered, this can be approximated by

$$M_{pq}(\omega_{pq}^2-\omega^2)d_{pq}+\rho\omega^2\left(\frac{S_p}{4}\right)^2\frac{1}{C_{pqpq}}\left(1-\tau+\frac{4jM_{pq}}{S_p\omega z_h}(\omega_{pq}^2-\omega^2)\right)d_{pq} \tag{5.46}$$
$$=\left(1+\frac{j\omega\rho}{z_h}\frac{S_p}{4}\frac{1}{C_{pqpq}}\right)\hat{F}_{pq}$$

where $M_{pq}=m_p(S_p/4)$ and $\hat{F}_{pq}=F_{pq}(S_p/4)$ are the generalized mass and the generalized force respectively for the simply supported plate. The case of the unperforated, unbaffled plate (Eq.(3.34)) can be recovered by introducing very large $z_h$ and setting $\tau=0$.

The remaining procedure to calculate the sound power $W$ is similar to that for the unperforated unbaffled plate in Chapter 3.

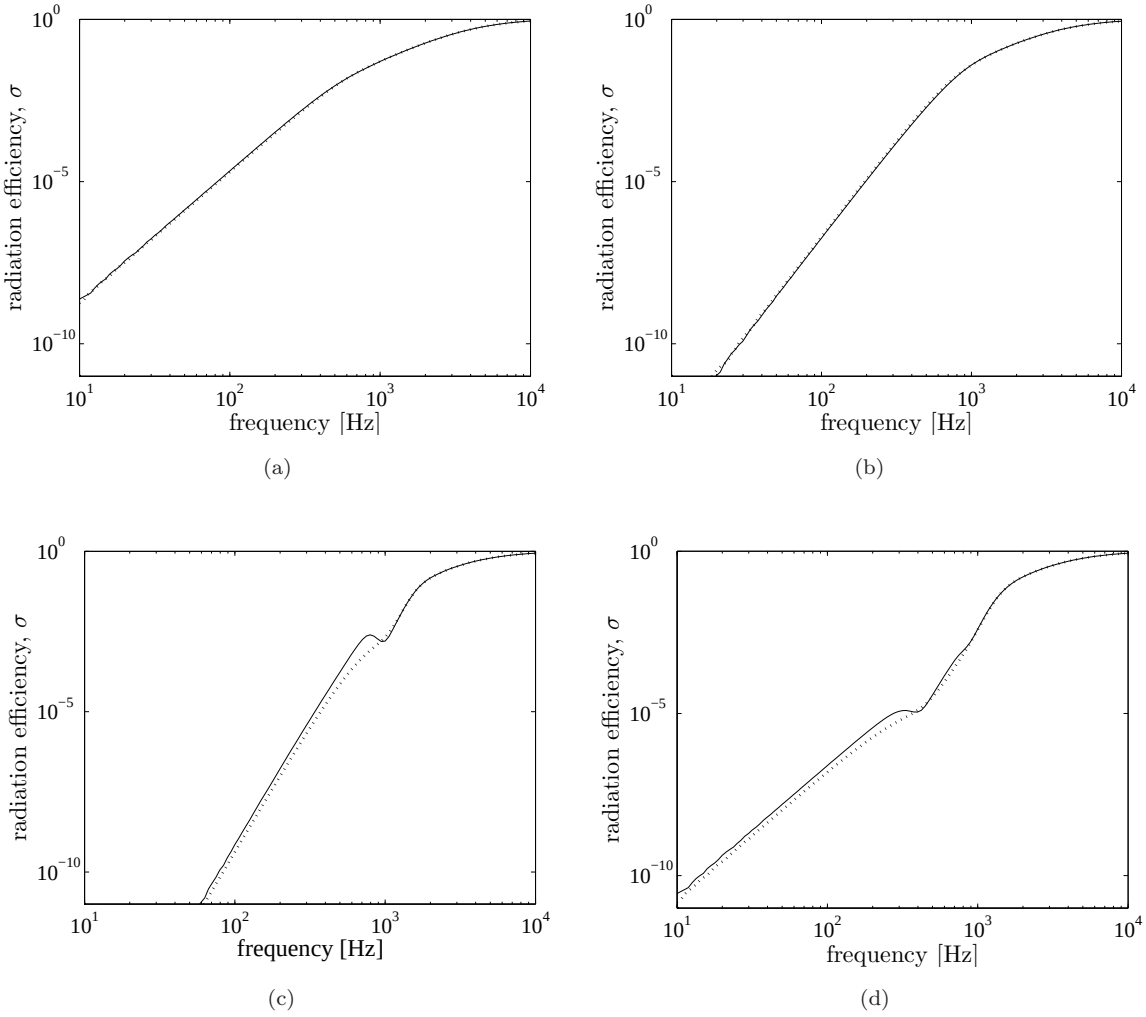


FIGURE 5.18: Comparison of modal radiation efficiency including the cross-modal terms (—) and only the self-modal terms (· · · ): (a) mode (1,1), (b) mode (1,2), (c) mode (2,4) and (d) mode (3,3) ($0.65 \times 0.5 \times 0.003$ m aluminium plate with $\eta = 0.1$; $d_o = 10$ mm, $\tau = 40\%$).

### 5.3.2 Results

Figure 5.18 shows a comparison between the calculation of the radiation efficiency for modes (1,1),(1,2),(2,4) and (3,3) using Eq.(5.45) involving the full matrix $[C_{pqmn}]$ and the one using Eq.(5.46), based on neglecting cross-modal terms. For calculating the results using the full matrix of $C_{pqmn}$ (Eq.(5.45)), a total of $49 \times 49$ modes are included in each calculation. In each case only modes of the same parity are included as other terms are zero.

For modes (1,1) and (1,2), both results appear to have a perfect agreement. Differences occur for modes (2,4) and (3,3) below the modal coincidence frequency of each mode.

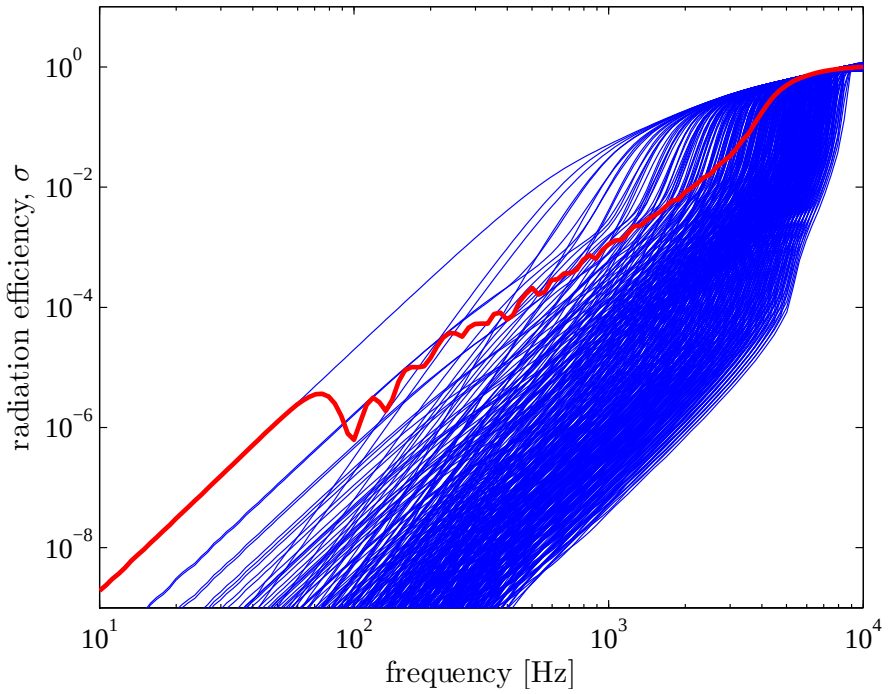


FIGURE 5.19: Modal and average radiation efficiency of a simply supported rectangular unbaffled perforated plate ($0.65 \times 0.5 \times 0.003$ m aluminium plate, $\eta = 0.1$; $d_o = 10$ mm, $\tau = 40\%$): —modal radiation efficiency; — average radiation efficiency.

This is the effect of the cross-modal coupling which is greater in the higher modes. In the unbaffled plate case, the cross-modal terms do not completely converge to zero as they do for the baffled plate case, even though all possible force positions have been averaged. However, the self-modal radiation is still considered to give quite good agreement with the result where the cross-modal terms are included, especially when the full modal summation is considered. Over the whole frequency range, the average differences are less than 1 dB, which thus can be neglected, except at certain frequencies where the discrepancy is a bit higher. For example at 700 Hz for mode (2,4) in Figure 5.18(c) the difference is around 4−5 dB. Therefore, in the remainder of this section, the calculation of the radiation efficiency is carried out by using Eq.(5.46), i.e. neglecting the cross-modal coupling distribution.

Figure 5.19 presents the results of the modal and average radiation efficiencies of an unbaffled perforated plate with 40% perforation ratio and 10 mm diameter holes. The results show a curve which has the same trend of slope as obtained from the case of a perforated plate in an infinite perforated baffle, see Figure 5.11, particularly for the region below the first mode (40 dB/decade) and the corner mode region (about 20 dB/decade). However, the unbaffled plate has a lower radiation efficiency than

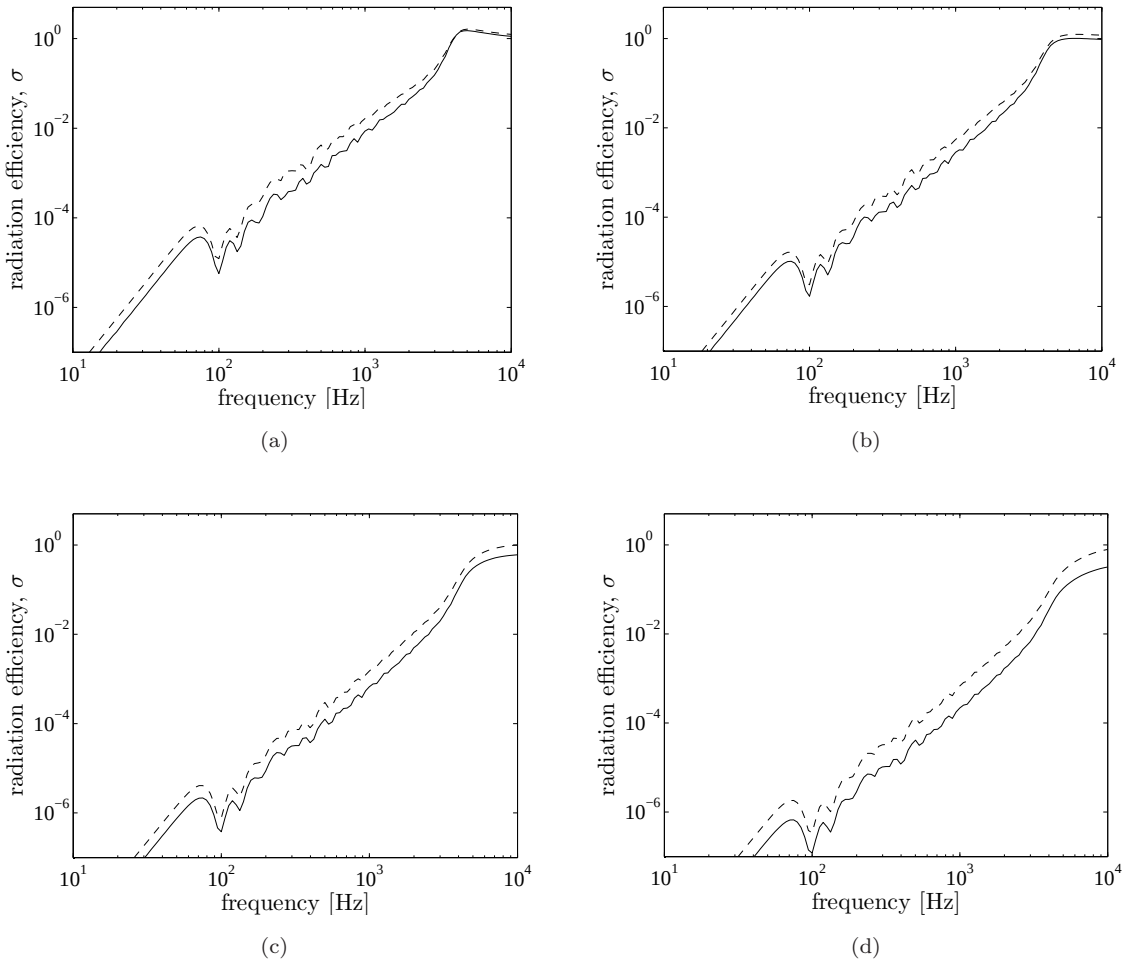


FIGURE 5.20: Average radiation efficiency of simply supported rectangular perforated plates in a perforated baffle (−−) and unbaffled (—) ($0.65 \times 0.5 \times 0.003$ m aluminium plate with $\eta = 0.1$; $d_o = 10$ mm): (a) $\tau = 10\%$, (b) $\tau = 20\%$, (c) $\tau = 40\%$ mm, (d) $\tau = 60\%$.

that of the plate in the perforated baffle for most of the frequency range as shown in Figure 5.20.

It can be seen that the difference is almost constant for the increasing perforation ratio from 10% to 40%. For very high perforation at 60%, the difference increases in about 1-2 dB. This can be seen clearly in Figure 5.21 which shows the differences of the radiation efficiencies $\Delta\sigma$ for no baffle and with a perforated baffle on a dB scale. It is found that there is no consistent trend on the difference level between both cases that can be related to the perforation ratio.

Figure 5.22 compares the results with those for the unperforated unbaffled plate from Section 3.2. Perforation yields a constant reduction at low frequencies including the corner mode region (up to 450 Hz in this case). The effect then reduces as frequency

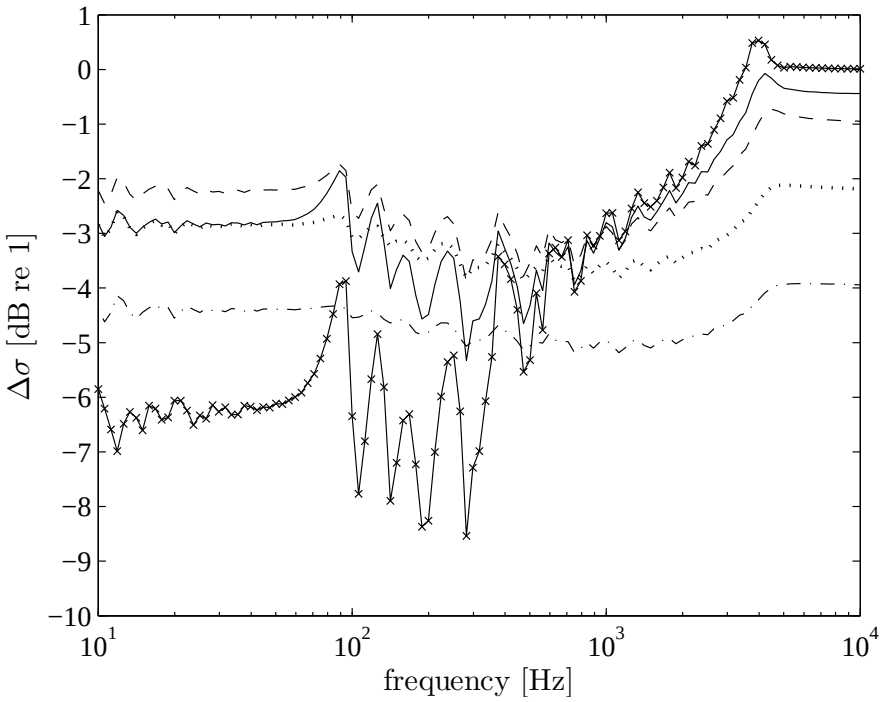


FIGURE 5.21: Radiation efficiency difference of a perforated plate in a perforated baffle and an unbaffled plate) ($0.65 \times 0.5 \times 0.003$ m aluminium plate, $\eta = 0.1$; $d_o = 10$ mm): $\times$—$\tau = 3\%$, —$\tau = 10\%$, $--\tau = 20\%$, $\cdots\tau = 40\%$ mm, $-\cdot-\tau = 60\%$.

increases. This can be explained as the impedance of the hole is proportional to frequency. Therefore at high frequency, the fluid in the holes has very high mass-like impedance. This mass does not move sufficiently to compensate for the volume sources adjacent to the hole. The cancellation of radiated sound thus becomes ineffective.

As in the previous section, the level difference between the perforated and unperforated results can be expressed as the 'effect of perforation', EoP, see Eq.(5.32). Figure 5.23 and Figure 5.24 present the effect of perforation for a constant hole diameter and a constant perforation ratio, respectively. These show that, for the case of the unbaffled perforated plate, the effect of perforation is almost independent of frequency at low frequencies and the effect reduces in the edge mode region as the frequency increases. Results for different thicknesses and dimensions are presented in Figure 5.25. Unlike the case of a perforated baffle (Fig.5.15), the results show that the effect of perforation in the unbaffled case depends on both the plate thickness (see Figure 5.25(a), 5.25(b)) and on the plate dimensions (see Figure 5.25(c), 5.25(d)).

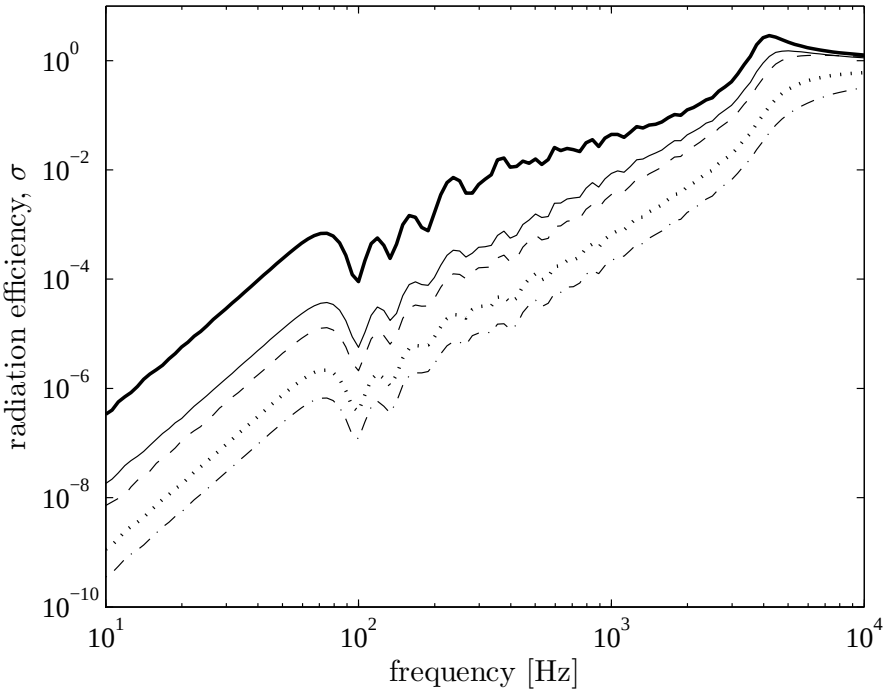


FIGURE 5.22: Average radiation efficiency of a simply supported rectangular unbaffled perforated plate ($0.65 \times 0.5 \times 0.003$ m aluminium plate, $\eta = 0.1$, $d_o = 10$ mm; — unperforated, —$\tau = 10\%$, −−$\tau = 20\%$, $\cdots\,\tau = 40\%$ mm, $-\cdot-\tau = 60\%$).

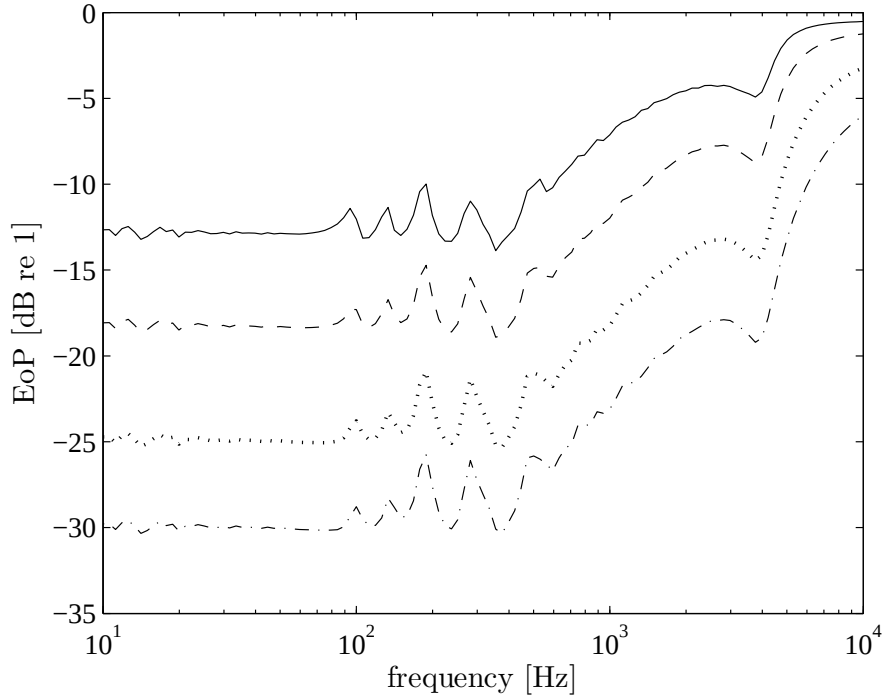


FIGURE 5.23: Effect of perforation (EoP) on sound power radiation of a simply supported rectangular perforated unbaffled plate ($0.65 \times 0.5 \times 0.003$ m aluminium plate with $\eta = 0.1$, $d_o = 10$ mm; —$\tau = 10\%$, −−$\tau = 20\%$, $\cdots\,\tau = 40\%$ mm, $-\cdot-\tau = 60\%$).

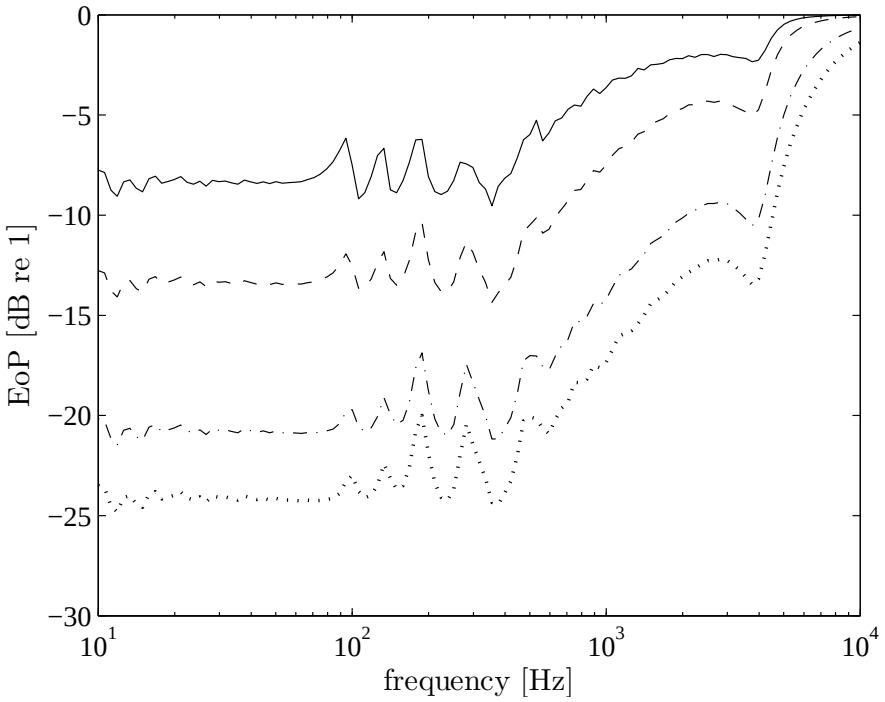


FIGURE 5.24: Effect of perforation (EoP) on sound power radiation of a simply supported rectangular perforated unbaffled plate ($0.65 \times 0.5 \times 0.003$ m aluminium plate with $\eta = 0.1$; $\tau = 20\%$: $d_o =$ — 50 mm, −− 20 mm, $-\cdot-$ 5 mm, $\cdots$ 2 mm).

### 5.3.3 Approximate formula for EoP

Figure 5.26 plots the effect of perforation against non-dimensional specific acoustic reactance $h$ for different plate thicknesses. It can be seen that the curves collapse together with the same slope of 15 dB/decade in the edge mode region. Below the edge mode region, the results are independent of $h$ but vary with plate dimensions and perforation ratio.

In the edge mode region, up to half the critical frequency ($f_c/2$), the effect of perforation (EoP) can be written as

$$\mathrm{EoP}_{\mathrm{ub,edge}} = 15 \log_{10} [h(1-\tau)] - 11, \qquad f_e < f < f_c/2 \tag{5.47}$$

where $f_e$ is as in Eq.(2.68).

As the effect of perforation ratio for the unbaffled perforated plate shows constant values at low frequency, at least up to end of the corner mode region, an approximate formula can be developed to determine the EoP ratio in this frequency range.

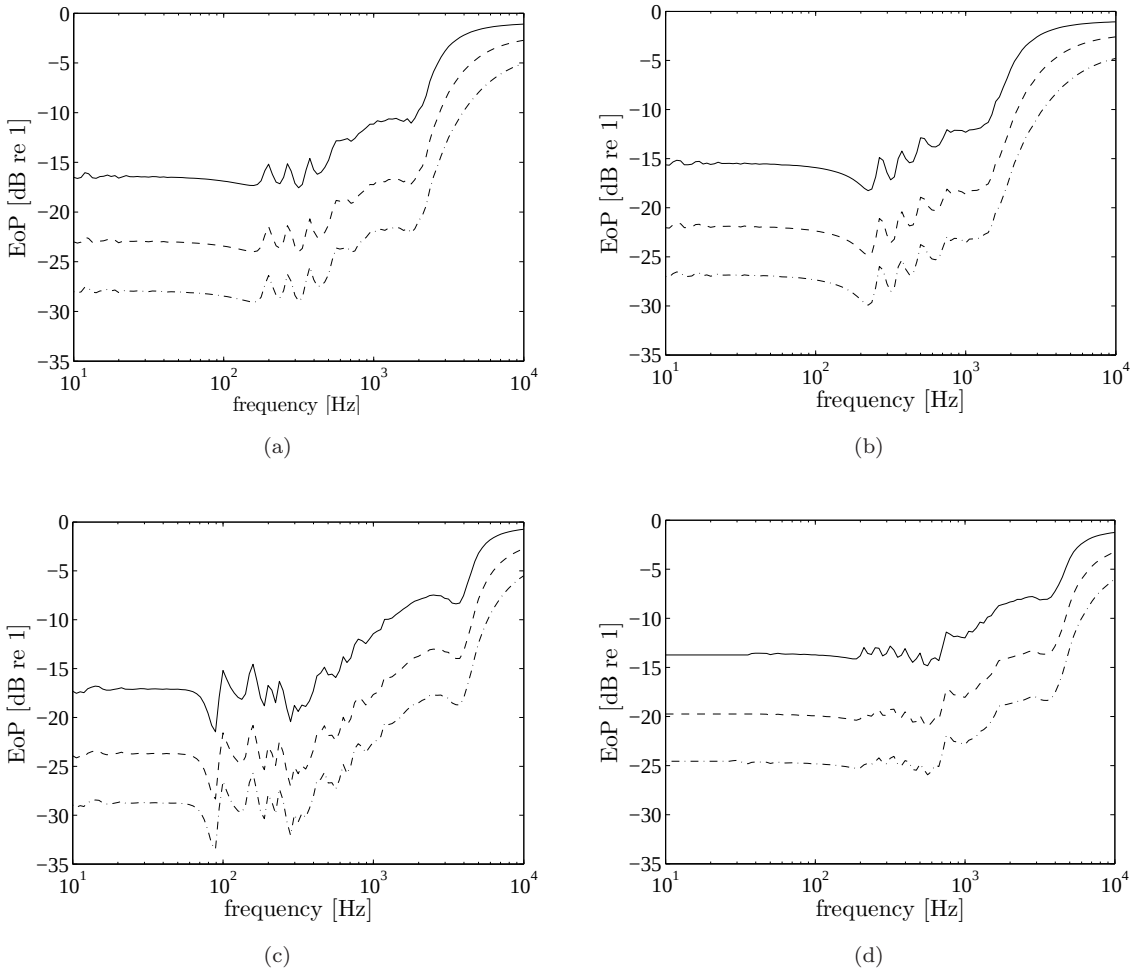


FIGURE 5.25: Effect of perforation (EoP) on sound power radiation of a simply supported rectangular perforated unbaffled plate for different thicknesses; (a) $0.65 \times 0.5 \times 0.006$ m, (b) $0.65 \times 0.5 \times 0.008$ m and different dimensions; (c) $0.8 \times 0.4 \times 0.003$ m, (d) $0.9 \times 0.2 \times 0.003$ m (aluminium plate with $\eta = 0.1$; $d_o = 10$ mm, $\tau =$ — 20%, $--$ 40%, $-\cdot-$ 60%).

Figure 5.27 plots the effect of perforation at low frequency for plates with the same dimensions but different thickness and perforation ratio to show the increment in the EoP curve as the plate thickness increases. This is plotted against $h(1-\tau)/k$ which is independent of frequency. The constant values over the corner mode region are taken from the average value between 30 Hz and 60 Hz.

It is seen that the perforation of thinner plates has a greater effect of reducing the sound radiation. The result also shows that the trend has a dependency of 15 dB/decade. Therefore a simple curve fit can be obtained as a function of the non-dimensional acoustic reactance $h$

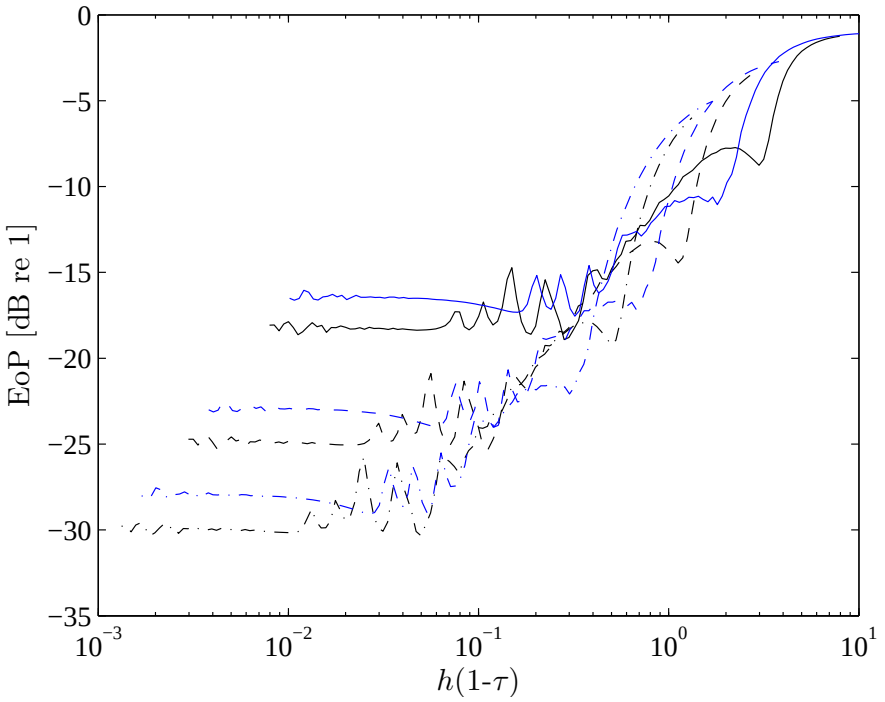


FIGURE 5.26: Effect of perforation (EoP) on sound power radiation of a simply supported rectangular perforated, unbaffled plate plotted against $h$ ($0.65 \times 0.5 \times 0.003$ m (black line), $0.65 \times 0.5 \times 0.006$ m (blue line) ); aluminium plate, $\eta = 0.1$, $d_o = 10$ mm; $\tau =$ — 20%, −− 40%, − · − 60%).

$$\mathrm{EoP}_{\mathrm{ubf,corner}} = 15 \log_{10} \left[ \frac{h(1-\tau)}{k} \right] + 2.3, \qquad f < f_e \tag{5.48}$$

where $\mathrm{EoP}_{\mathrm{ub,corner}}$ is the effect of perforation of the unbaffled perforated plate at very low frequency, i.e. in the dipole and the corner mode regions, as a function of $h$ (which include thickness, perforation ratio and hole diameter).

The EoP at low frequency for different dimensions with the same plate thickness is shown in Figure 5.28 for perforation ratios of 20% and 40%. For the 20% perforation ratio, the dependence on the plate dimensions $a$ and $b$ can be written as

$$\mathrm{EoP}_{\mathrm{ub},a\times b} = -8.46 \log_{10} \left( \frac{1}{1/a^2 + 1/b^2 + 1/2ab} \right) - 25, \qquad f < f_e \tag{5.49}$$

where $a \times b$ is the plate area[1] and the unit length should be in metre (m). The EoP in Fig. 5.28 is calculated for different plate areas and plate ratios. It can be seen that the 40% perforation has similar gradient to that of the 20%.

[1]The results were also plotted against $ab$, $a/b$, $ab/(a+b)$ and $a+b$ but these did not yield a consistent relationship as here.

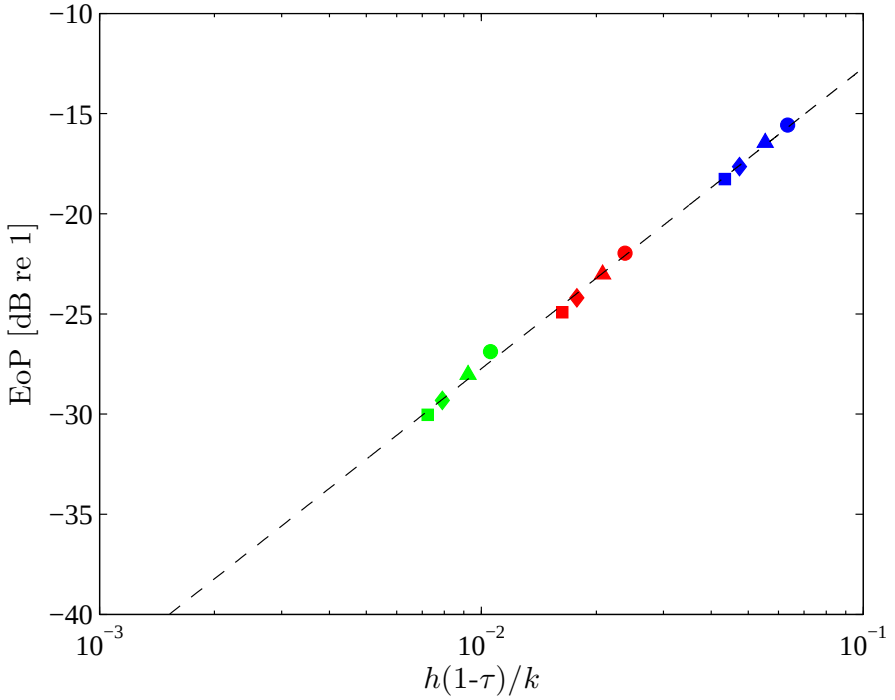


FIGURE 5.27: Effect of perforation (EoP) on sound power radiation of a simply supported rectangular perforated unbaffled plate at low frequency asymptote for different thickness (□: $0.65 \times 0.5 \times 0.003$ m, ◊: $0.65 \times 0.5 \times 0.004$ m, △: $0.65 \times 0.5 \times 0.006$ m, ○: $0.65 \times 0.5 \times 0.008$ m aluminium plate with $\eta = 0.1$; $\tau = 20\%$ (blue), $\tau = 40\%$ (red), $\tau = 60\%$ (green)).

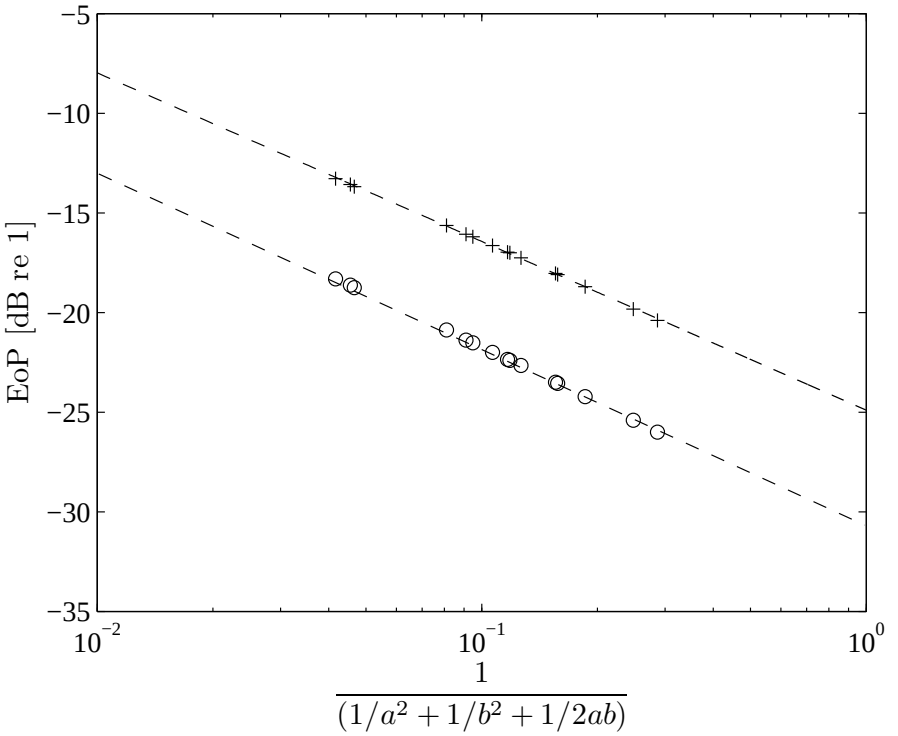


FIGURE 5.28: Effect of perforation (EoP) on sound power radiation of a simply supported rectangular perforated unbaffled plate at low frequency asymptote for various plate dimensions ($t = 3$ mm, aluminium plate with $\eta = 0.1$; +=20%, ○=40%).

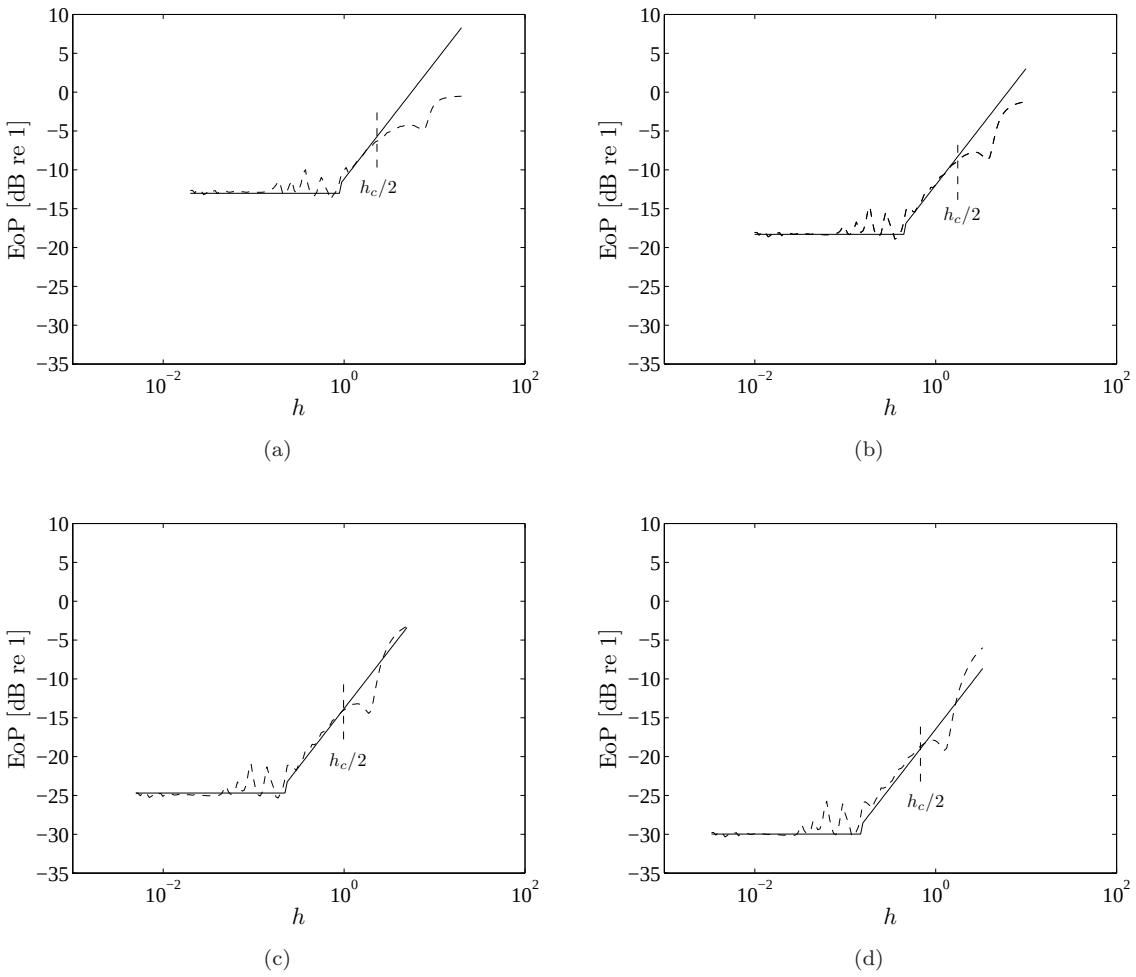


FIGURE 5.29: Comparison of exact (−−) and approximated (—) effect of perforation (EoP) on sound power radiation of a simply supported rectangular perforated unbaffled plate: $0.65 \times 0.5 \times 0.003$ m; (a) $\tau = 10\%$, (b) $\tau = 20\%$, (c) $\tau = 40\%$, (d) $\tau = 60\%$ (aluminium plate with $\eta = 0.1$, $d_o = 10$ mm).

These two equations (Eq.(5.48) and Eq.(5.49)) can be combined to give a general equation for the effect of perforation at low frequency. For the sake of clarity, the coefficients are rounded to give the form

$$\mathrm{EoP_{ub}} = -8.5 \log_{10}\left(\frac{1}{1/a^2 + 1/b^2 + 1/2ab}\right) + 15 \log_{10}\left[\frac{h(1-\tau)}{k}\right] - 5.5, \qquad f < f_e \tag{5.50}$$

Figures 5.29 and 5.30 show a comparison of the effect of perforation to test the validity of Eq.(5.50) and Eq.(5.47) for different perforation ratios, plate dimensions and thicknesses. The results show good agreement over the frequency range up to half the critical frequency. However in the corner mode region, the approximate model does not give such a good estimation. This is due to high fluctuations in this region both

from the radiation efficiency of the perforated plate and that of the solid plate, which then also lead to high fluctuations in the effect of perforation curve. Nevertheless the differences in this region are only 2−4 dB at most.

## 5.4 Perforated plate near a rigid surface

Another consideration for sound radiation from a plate is its radiation characteristic when it is placed near a reflecting, rigid surface. Such an application can be found, for example, when a plate is used as a dynamic vibration absorber [56]. The vibration of the structure under treatment is suppressed while its vibration energy is transfered to the absorber. This plate absorber will then radiate sound into the air.

This section will first evaluate the radiation efficiency of a solid unbaffled plate located close to an infinite rigid surface before considering the effect due to perforation.

### 5.4.1 Modifying the Green's function

Consider the situation in Figure 5.31 where an unbaffled plate is located at a distance $D$ above an infinite rigid, reflecting surface lying in the $xy$-plane. The boundary condition on the rigid surface is that the normal fluid velocity is zero, or from Eq.(3.8) that the normal gradient of the pressure is zero. This boundary condition is equivalent to the situation in which an imaginary plate, vibrating in the opposite direction, is located at a distance $2D$ below the real vibrating plate, in the absence of the infinite reflecting surface. The sound field below the rigid surface, of course, has no physical meaning. However, the corresponding sound field above the rigid surface ($z \geq 0$) includes the reflected wave from this surface.

The Green's function can now be modified to include the contribution of the image source $Q'$ at $(x, y, -z)$ to the pressure at the observation point $M$ at $(x_0, y_0, z_0)$. The appropriate Green's function is given by

$$G(Q, M) = \frac{e^{-jkR}}{4\pi R} + \frac{e^{-jkR'}}{4\pi R'} \tag{5.51}$$

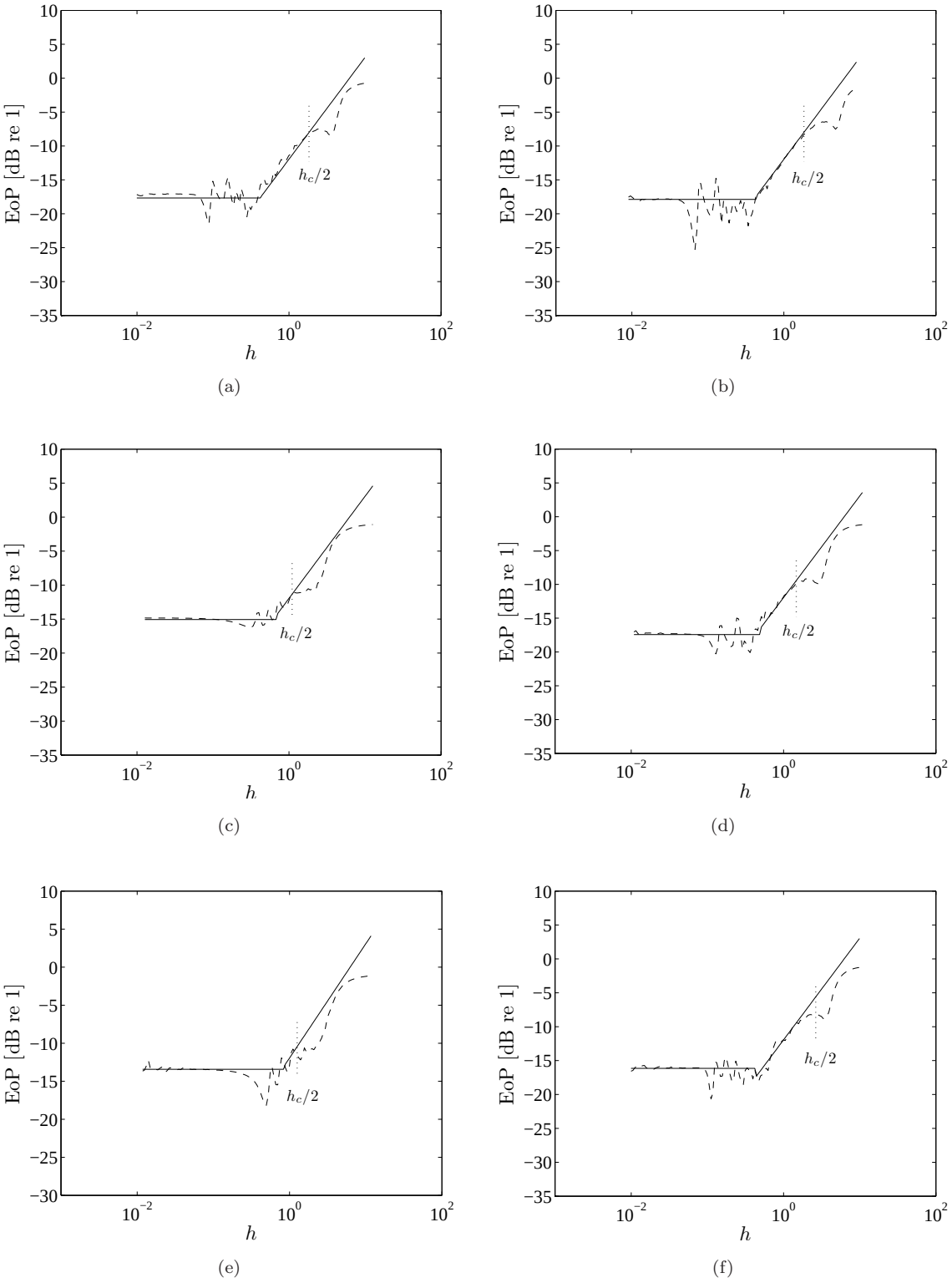


FIGURE 5.30: Comparison of exact (−−) and approximated (—) effect of perforation (EoP) on sound power radiation of a simply supported rectangular perforated unbaffled plate: $\tau = 20\%$; (a) $0.8 \times 0.4 \times 0.003$ m, (b) $0.65 \times 0.4 \times 0.002$ m, (c) $0.52 \times 0.4 \times 0.006$ m, (d) $0.7 \times 0.45 \times 0.004$ m, (e) $0.39 \times 0.3 \times 0.005$ m and (f) $0.9 \times 0.3 \times 0.003$ m (aluminium plate with $\eta = 0.1$, $d_o = 10$ mm).

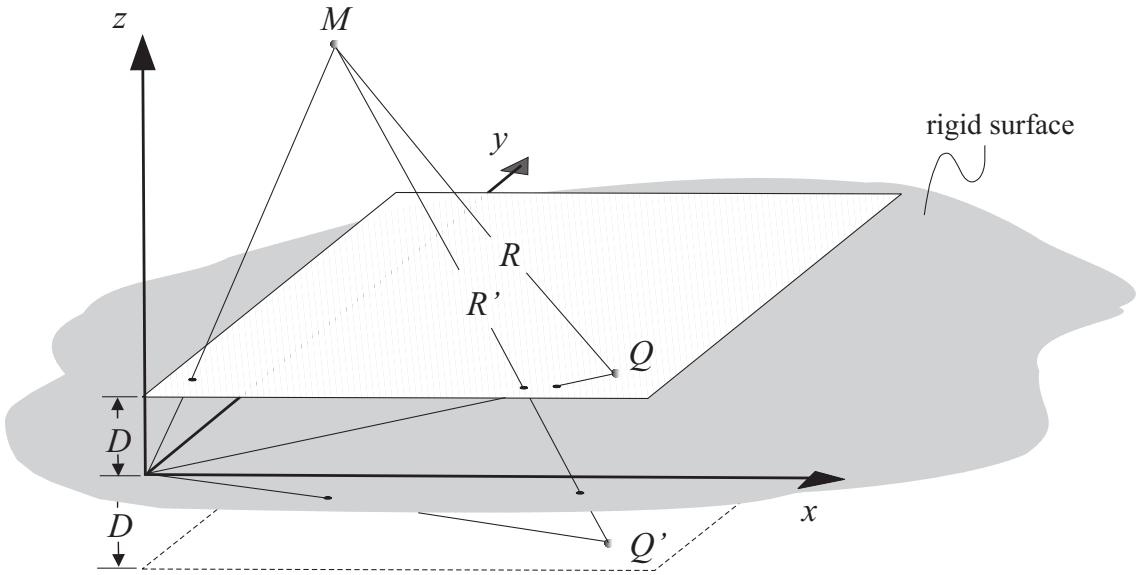


FIGURE 5.31: Perforated, unbaffled plate near a reflecting rigid surface

where

$$R = \sqrt{(x_0 - x)^2 + (y_0 - y)^2 + (z_0 - z)^2}$$

$$R' = \sqrt{(x_0 - x)^2 + (y_0 - y)^2 + (z_0 + z)^2}$$

As in Eq.(3.9), the Green's function must now satisfy

$$\nabla^2 G(Q, M) + k^2 G(Q, M) = \delta(x_0 - x)\delta(y_0 - y)\delta(z_0 - z) \; + \; \delta(x_0 - x)\delta(y_0 - y)\delta(z_0 + z) \tag{5.52}$$

Taking the two dimensional Fourier transform of Eq.(5.52), the Green's function can be expressed as [72]

$$G = \frac{j}{8\pi^2} \int_{-\infty}^{\infty} \int_{-\infty}^{\infty} \frac{1}{k_z} \left\{ e^{jk_z|z-z_0|} + e^{jk_z(z+z_0)} \right\} e^{jk_x(x-x_0)} e^{jk_y(y-y_0)} \, dk_x \, dk_y \tag{5.53}$$

where $k_z = \sqrt{k^2 - k_x^2 - k_y^2}$.

The additional term in the bracket (compare Eq.(3.10)) is the image source contribution.

For $z_0 \geq z$, the term in the bracket can be expressed as

$$e^{jk_z(z_0 - z)} + e^{jk_z(z+z_0)} = e^{jk_z z_0}(e^{-jk_z z} + e^{jk_z z}) = 2e^{jk_z z_0} \cos(k_z z)$$

For $z_0 \leq z$ the terms in $z_0$ and $z$ should be exchanged.

Following the method of Laulagnet [33] in Section 3.2, the acoustical cross-modal coupling terms in Eq.(3.25) thus become

$$\begin{aligned} C_{pqmn} &= \frac{1}{4\pi^2} \int_{-\infty}^{\infty} \int_{-\infty}^{\infty} k_z \, e^{jk_z z_0} \, \sin(k_z z) \, \widetilde{\varphi}^*_{pq}(k_x, k_y) \widetilde{\varphi}_{mn}(k_x, k_y) \, dk_x \, dk_y \\ &= \frac{1}{\pi^2} \int_{0}^{\infty} \int_{0}^{\infty} k_z \, e^{jk_z z_0} \, \sin(k_z z) \, \widetilde{\varphi}^*_{pq}(k_x, k_y) \widetilde{\varphi}_{mn}(k_x, k_y) \, dk_x \, dk_y \end{aligned} \tag{5.54}$$

For $z = z_0 = D$, Eq.(3.32) becomes

$$C_{pqmn} = C_{mnpq} = \frac{4}{pqmn} \left( \frac{ab}{\pi^3} \right)^2 \int_{0}^{\infty} \int_{0}^{\infty} k_z \, e^{jk_z D} \, \sin(k_z D) \, \Upsilon \, \Omega \, dk_x \, dk_y \tag{5.55}$$

The remaining steps to obtain the radiation efficiency are the same as in Section 3.2 for a solid plate or in Section 5.3 for perforated plate.

### 5.4.2 Results for solid plates

Figure 5.32 plots the modal radiation efficiencies and the average radiation efficiency for the unbaffled plate (dimensions as before) located 2 and 4 cm above the rigid surface. At very low frequency ($<$ 100 Hz), the average radiation efficiency has a frequency dependence of 60 dB/decade. This shows that the vibrating plate behaves like a quadrupole source, a very inefficient radiator. At very low frequency the unbaffled plate itself behaves like a dipole source; the rigid surface provides its image with opposite phase hence constructing a quadrupole source. However, this requires that the distance from the rigid surface is much smaller than the acoustic wavelength ($kD \ll 1$).

For each mode the modal radiation efficiency has a sharp peak which occurs around a frequency when $k^2 = (m\pi/a)^2 + (n\pi/b)^2$, i.e. the modal coincidence frequency. Figure 5.33 shows the modal radiation efficiencies for modes (1,1) and (6,6) together with those for the plate without the rigid surface. The peak can be seen to occur at the same frequency for different values of $D$. This sharp peak is due to the standing

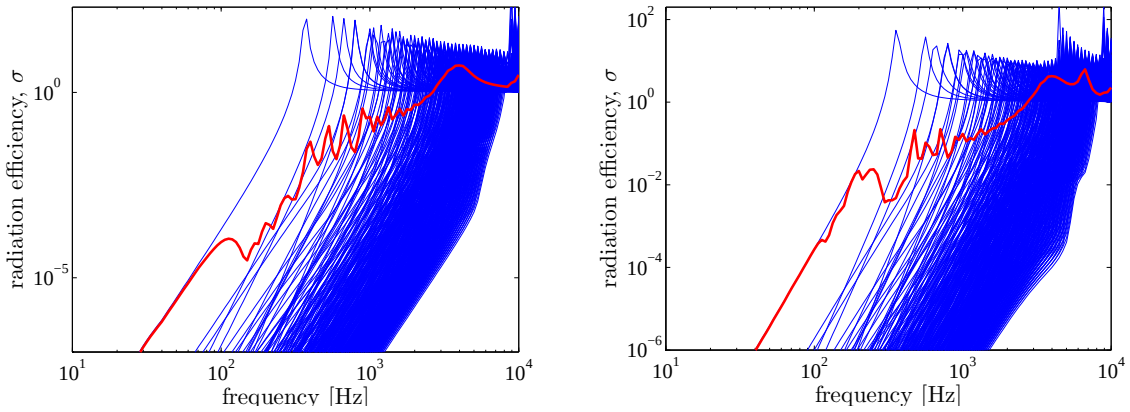


FIGURE 5.32: —Modal radiation efficiency and —average radiation efficiency of an unbaffled plate near rigid surface: (a) $D = 0.02$ m and (b) $D = 0.04$ m (aluminium plate, $0.65 \times 0.5 \times 0.003$ m, $\eta = 0.1$).

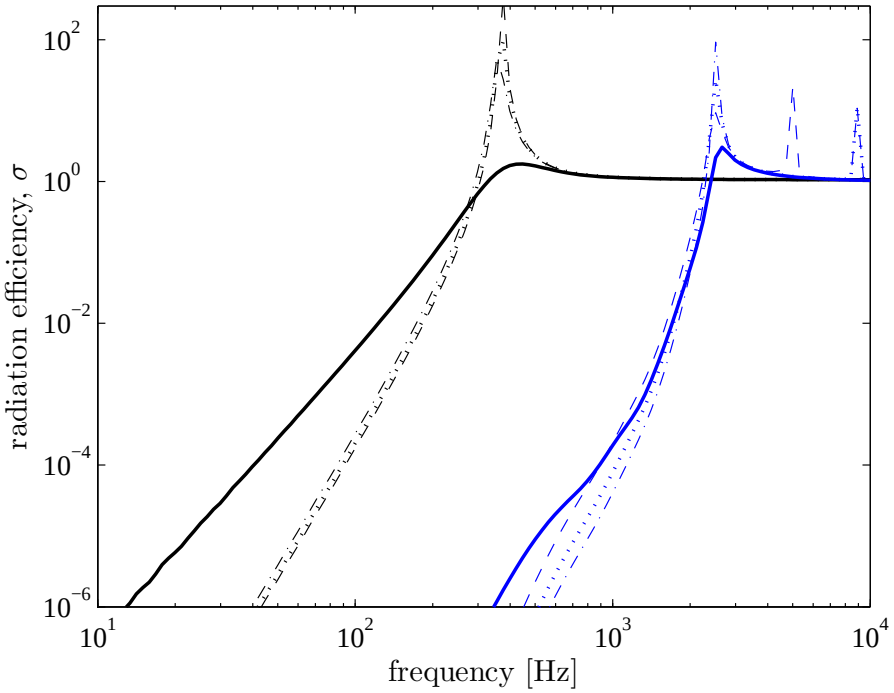


FIGURE 5.33: Radiation efficiency of an unbaffled plate near rigid surface for mode (1,1)(black) and mode (6,6)(blue): —absence of rigid surface, $--D = 0.04$ m, $\cdots D = 0.02$ m, $-\cdot-D = 0.01$ m ($0.65 \times 0.5 \times 0.003$ m, $\eta = 0.1$).

wave between the plate and the rigid surface. At higher frequencies for higher modes, peaks are built up above the modal coincidence frequency as seen in mode (6,6).

In Figure 5.32, very high peaks also can be seen at high frequencies. This causes the average radiation efficiency to increase instead of converging to unity. This appears to be due to an interference effect of the incident and reflected waves when the plate

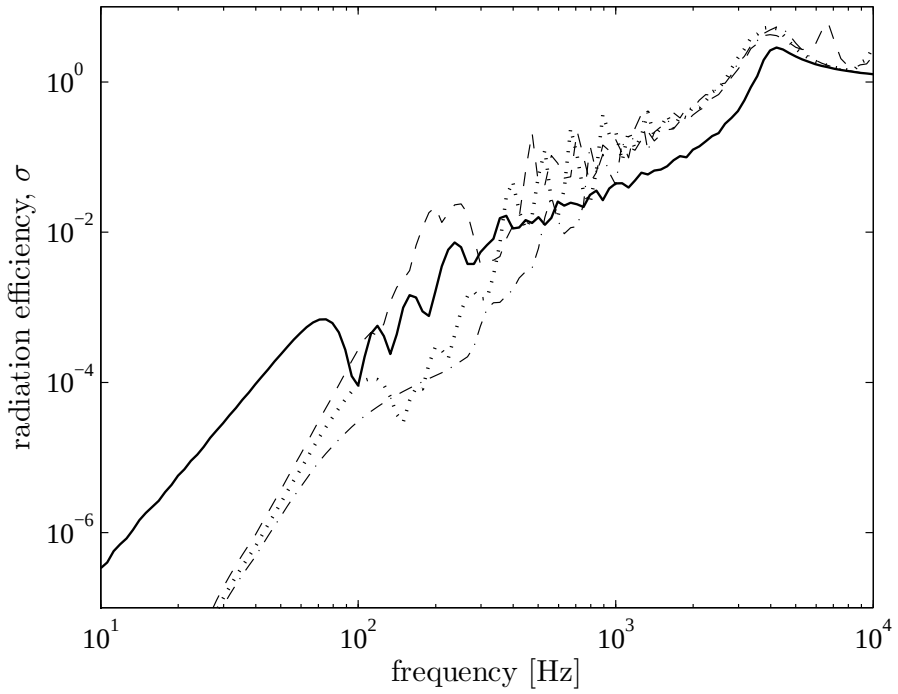


FIGURE 5.34: Radiation efficiency of an unbaffled plate near rigid, reflecting surface: — absence of rigid surface, $--D = 0.04$ m, $\cdots D = 0.02$ m, $-\cdot-D = 0.01$ m ($0.65 \times 0.5 \times 0.003$ m, $\eta = 0.1$).

distance above the rigid surface is a multiple of half of the acoustic wavelength ($kD = n\pi$, $n$ =interger). Thus it can be seen from Figure 5.32 the very high peak starts at 8.5 kHz for $D = 2$ cm and at 4.2 kHz for $D = 4$ cm and is repeated at 8.5 kHz.

Figure 5.34 shows the average results for the unperforated unbaffled plate located at various distances from a reflecting rigid surface compared with the result without a rigid surface. This shows that, as the plate is placed closer to the rigid surface, the point at which the radiation efficiency intersects that of the plate without the rigid surface shifts to a higher frequency. Above this intersection frequency, the radiation efficiency in the presence of the rigid surface becomes larger than that without the rigid surface. The sound radiation reflected from the rigid surface contributes to and increases the radiated sound above the vibrating plate. It appears that it is independent of the distance $D$ particularly in the edge mode region just before the critical frequency (above 1 kHz in the given case). Figure 5.35 shows similar phenomena in the corner and edge mode regions for a plate with different dimensions and thickness.

Figure 5.36 shows the effect of the presence of a rigid surface on the radiated sound power from the plate in Figure 5.34. This is also the same as the insertion loss (IL) of

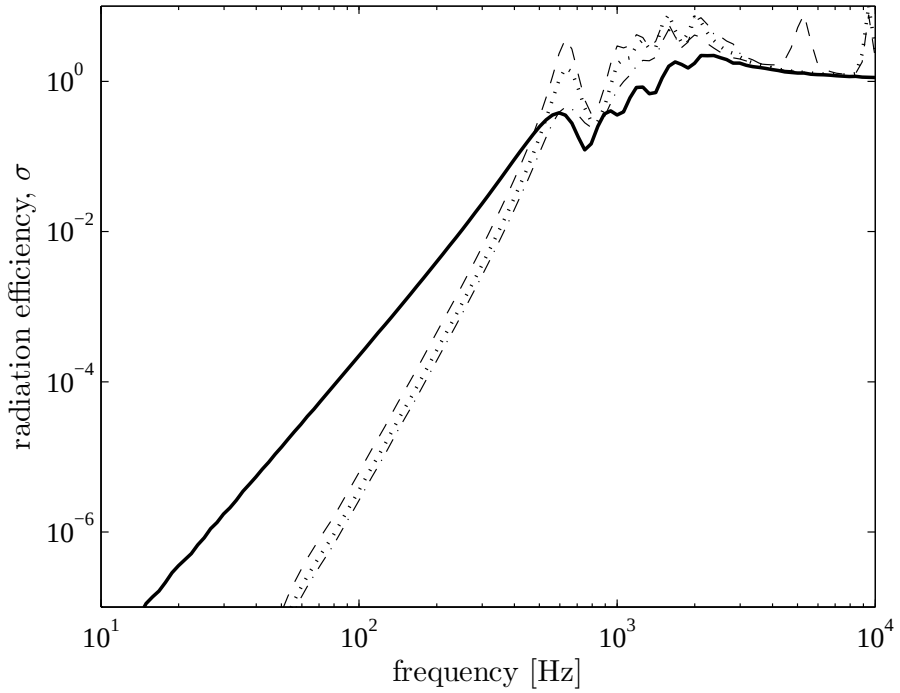


FIGURE 5.35: Radiation efficiency of an unbaffled plate near rigid, reflecting surface ($0.325 \times 0.25 \times 0.006$ m, $\eta = 0.1$): — absence of rigid surface, $--D = 0.04$ m, $\cdots D = 0.02$ m, $-\cdot-D = 0.01$ m.

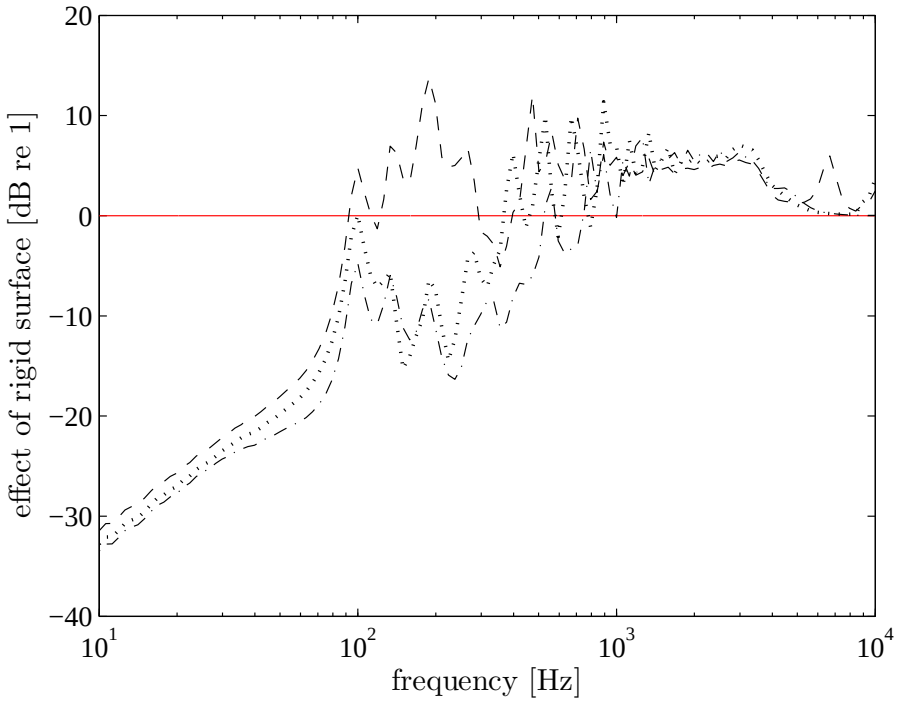


FIGURE 5.36: The effect of rigid surface on sound radiation of an unbaffled plate ($0.65 \times 0.5 \times 0.003$ m, $\eta = 0.1$): $--D = 0.04$ m, $\cdots D = 0.02$ m, $-\cdot-D = 0.01$ m.

a rigid surface. However, in this thesis, this is presented as -IL, i.e. the ratio between sound radiation with the presence of a rigid surface and with no rigid surface in place.

### 5.4.3 Results for perforated plates

Figure 5.37 plots the modal radiation efficiencies and the average radiation efficiency for a perforated unbaffled plate having hole diameter of 10 mm and 10% perforation ratio. The plate is located 2 or 4 cm above the rigid surface. As in the previous result for the unperforated plate in Figure 5.32, the interference effect also appears at high frequency ($>$ 4.2 kHz) when the plate distance $D$ is more than half of the acoustic wavelength. The sharp peak for each mode, as seen in Figure 5.32 around 400 Hz and above, vanishes as there is no longer a standing wave between the vibrating plate and the rigid surface because the sound can now easily 'escape' through the holes.

Figure 5.38 presents the average results for the same perforated plate but at various distances above the rigid surface. It shows similar phenomenon as for the unperforated plate except that the radiation efficiency of the plate close to the rigid surface is much lower in this case and does not very much exceed that of the perforated plate without the rigid surface even in the edge mode region (1$-$4 kHz). Figure 5.39 plots the effect of the rigid surface on the sound radiation from the perforated plate. It can be seen that as the vibrating perforated plate is brought closer to the rigid wall, a sound reduction is obtained over a broader frequency range.

Figure 5.40 compares results for perforated and unperforated plates at various distances from the rigid surface. It can be seen here that peaks in corner and edge mode regions occurring for the solid plate vanish in the radiation efficiency of the perforated plate. Results are also included for another plate dimensions i.e. $0.325 \times 0.25 \times 0.006$ m. In both cases the reduction due to perforation is effective over a wide range of frequency, up to the critical frequency (4 kHz and 2 kHz respectively).

The effect of perforation (EoP) is plotted in Figures 5.41 and 5.42 for both plates including the case with no rigid surface. In the fundamental mode and edge mode regions, the effect of perforation becomes greater as the plate is located closer to the rigid surface. However, in the corner mode region, there is no consistent effect in terms of the plate distance from the surface. The effect of perforation is greater than for

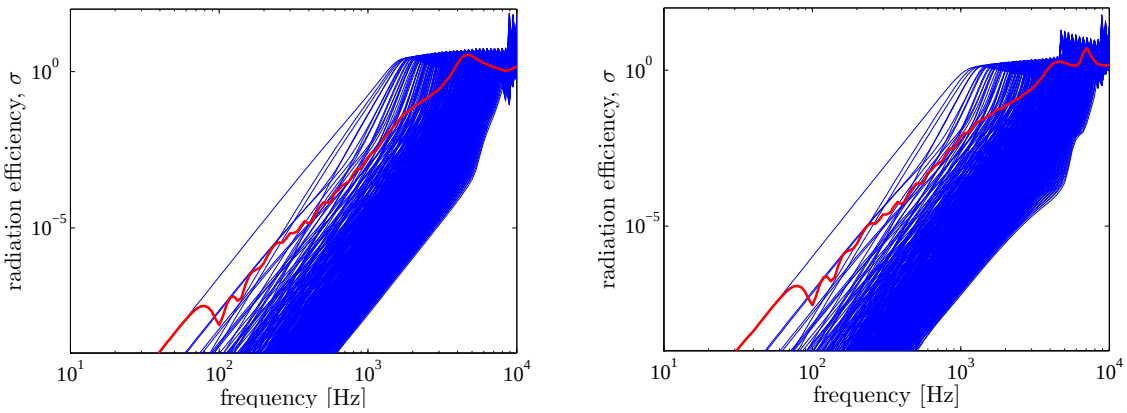


FIGURE 5.37: —Modal radiation efficiency and —average radiation efficiency of a perforated unbaffled plate near rigid surface: (a) $D = 0.02$ m and (b) $D = 0.04$ m (aluminium plate, $0.65 \times 0.5 \times 0.003$ m, $\eta = 0.1$, $d_o = 0.01$ m, $\tau = 10\%$).

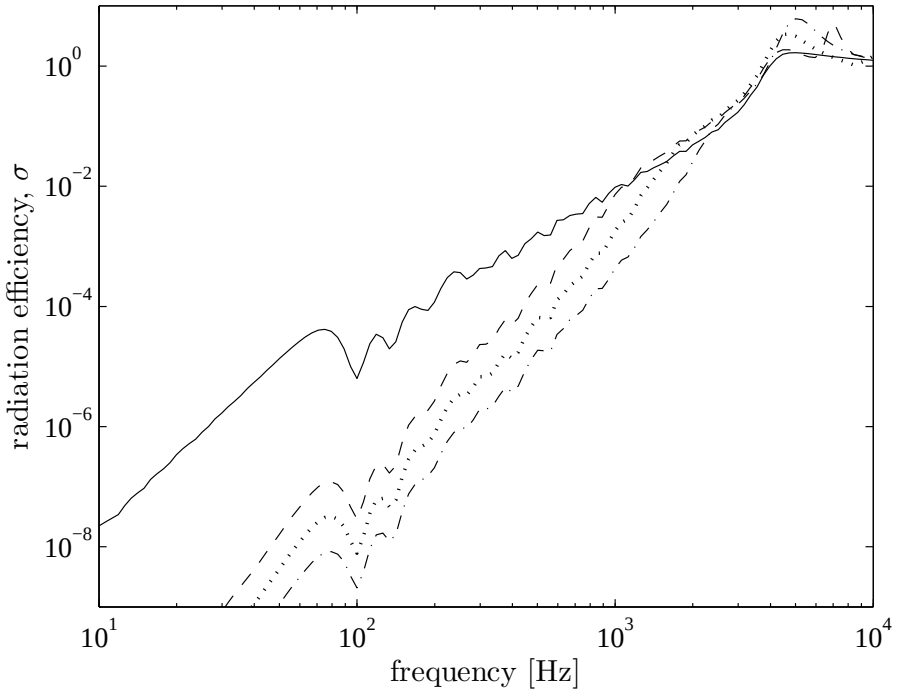


FIGURE 5.38: Radiation efficiency of perforated unbaffled plate near rigid, reflecting surface: —absence of rigid surface, $--D = 0.04$ m, $\cdots D = 0.02$ m, $-\cdot-D = 0.01$ m (aluminium plate, $0.65 \times 0.5 \times 0.003$ m, $\eta = 0.1$, $d_o = 0.01$ m, $\tau = 10\%$).

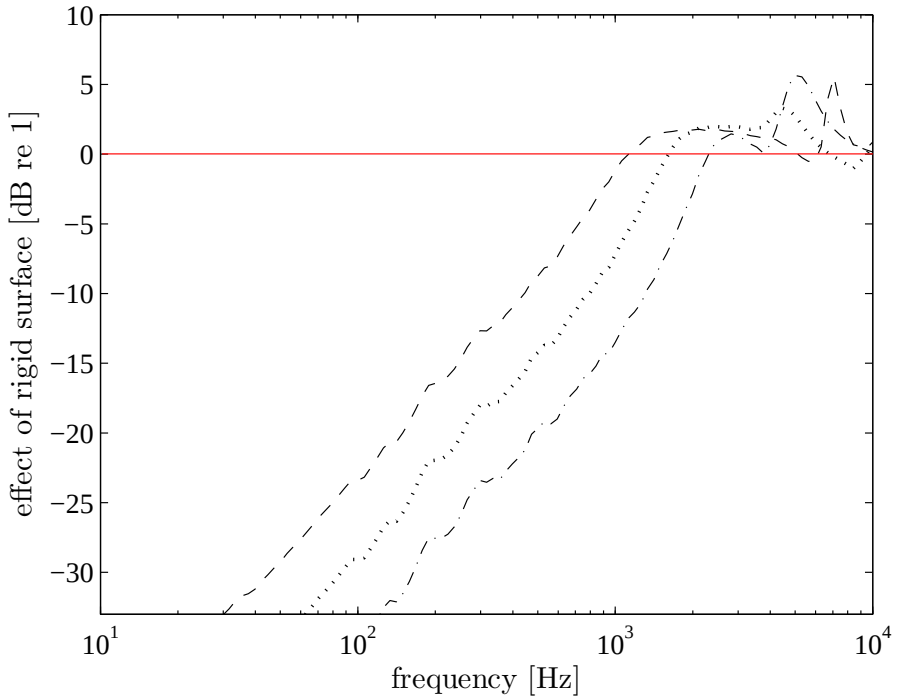


FIGURE 5.39: The effect of rigid surface on sound radiation of a perforated unbaffled plate: $--D = 0.04$ m, $\cdots D = 0.02$ m, $-\cdot-D = 0.01$ m ($0.65 \times 0.5 \times 0.003$ m aluminium plate, $\eta = 0.1$, $d_o = 0.01$ m, $\tau = 10\%$).

the plate without the rigid surface in all cases below the critical frequency, as in all previous results.

Figures 5.43 and 5.44 shows the EoP for a fixed plate distance with varying perforation ratio. The effect of perforation is almost constant with frequency in each case in the corner mode region. The effect of perforation is increased as the perforation increases.

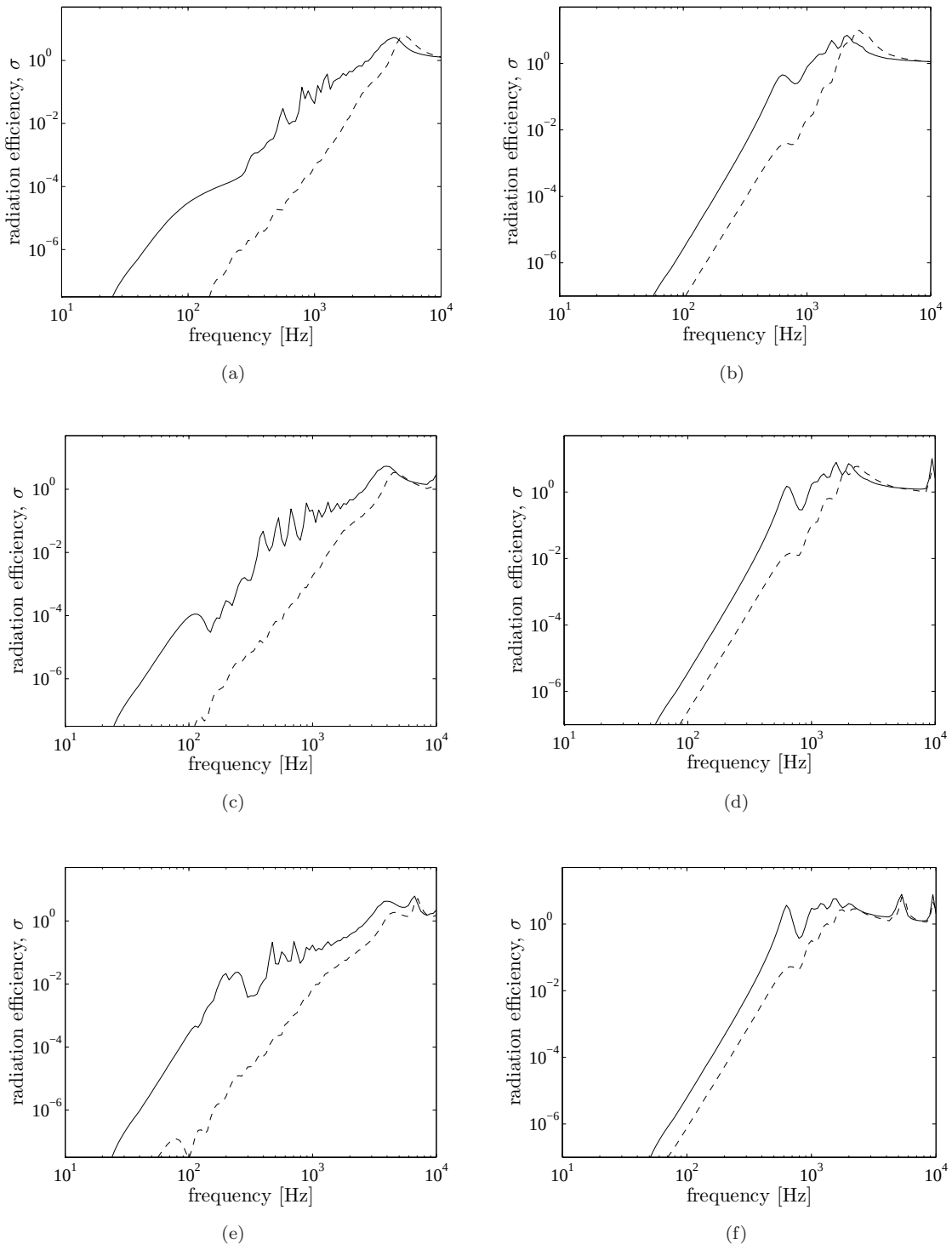


FIGURE 5.40: Radiation efficiency of a perforated unbaffled plate near a reflecting rigid surface: —unperforated, −−perforated; (a)-(b) $D = 0.01$ m, (c)-(d) $D = 0.02$ m and (e)-(f) $D = 0.04$ m ($d_o = 0.01$ m, $\tau = 10\%$, $\eta = 0.1$; first column: $0.65 \times 0.5 \times 0.003$ m, second column: $0.325 \times 0.25 \times 0.006$ m).

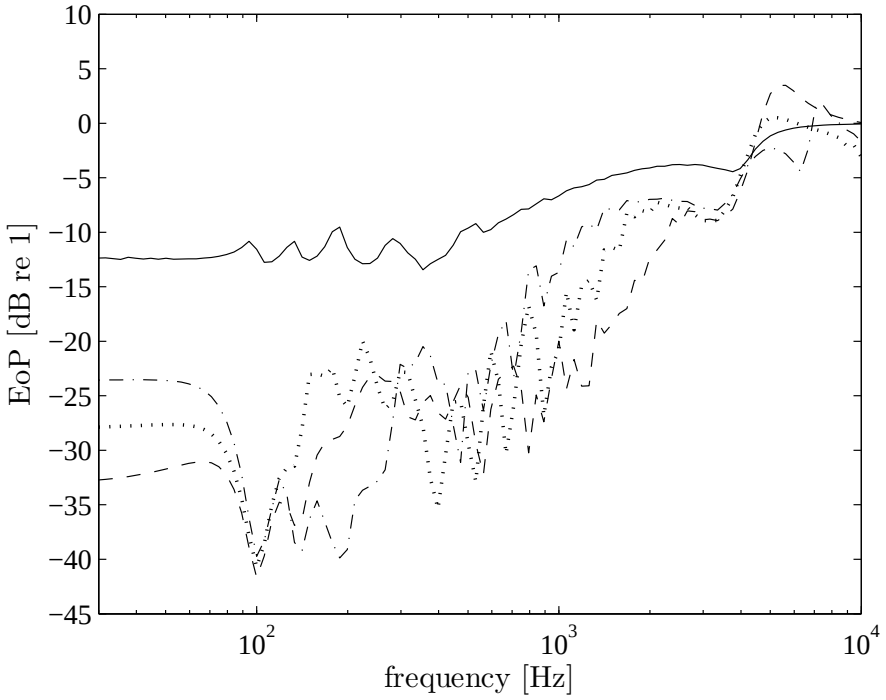


FIGURE 5.41: The effect of perforation on sound radiation of a perforated unbaffled plate near a reflecting rigid surface: —absence of rigid surface, $\tau = 10\%$: $--D = 0.01$ m, $\cdots D = 0.02$ m, $-\cdot-D = 0.04$ m ($0.65 \times 0.5 \times 0.003$ m; $\eta = 0.1$, $d_o = 0.01$ m).

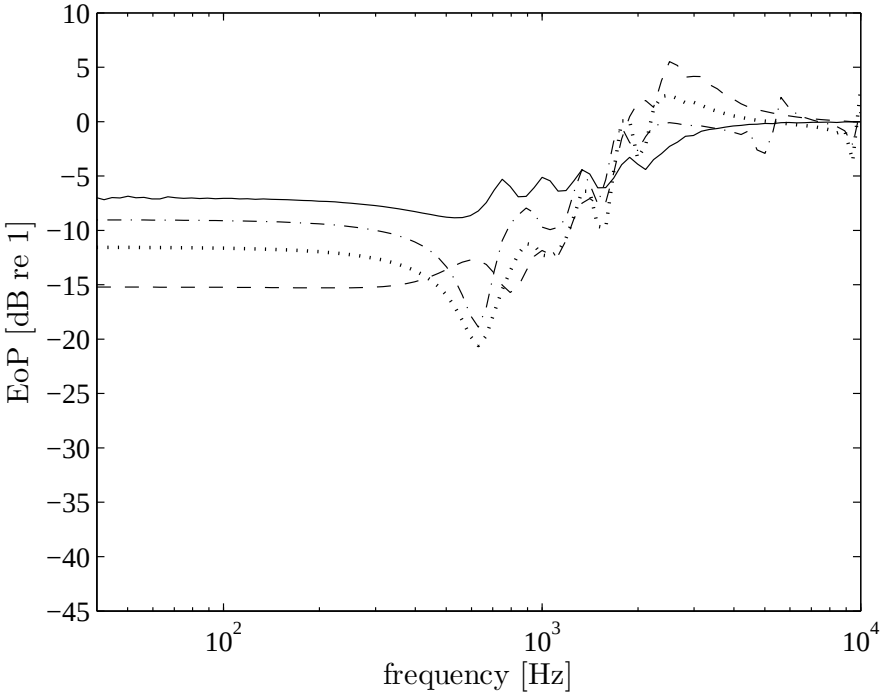


FIGURE 5.42: The effect of perforation on sound radiation of a perforated unbaffled plate near a rigid surface: —absence of rigid surface, $\tau = 10\%$: $--D = 0.01$ m, $\cdots D = 0.02$ m, $-\cdot-D = 0.04$ m ($0.325 \times 0.25 \times 0.006$ m; $\eta = 0.1$, $d_o = 0.01$ m).

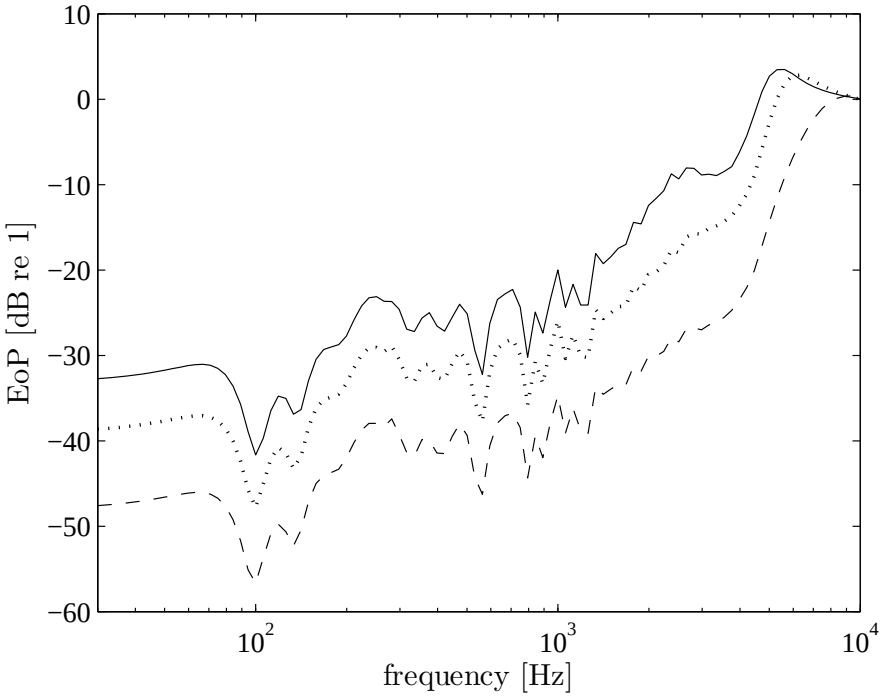


FIGURE 5.43: The effect of perforation of a perforated unbaffled plate near a rigid surface, $D = 0.01$ m: —$\tau = 10\%$, $\cdots\tau = 20\%$, $--\tau = 40\%$ ($0.65 \times 0.5 \times 0.003$ m; $\eta = 0.1$, $d_o = 0.01$ m).

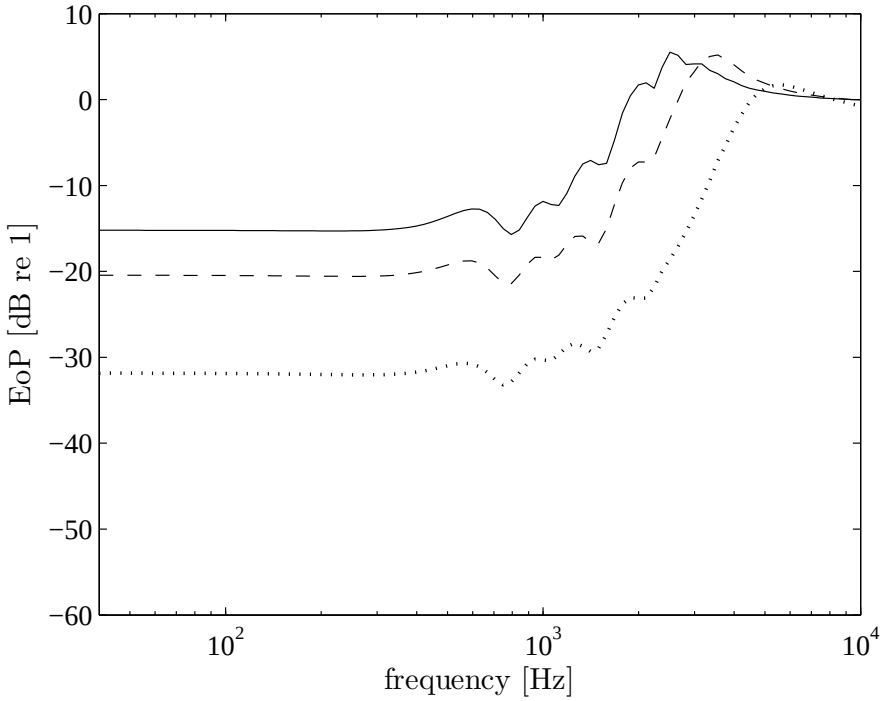


FIGURE 5.44: The effect of perforation of a perforated unbaffled plate near a rigid surface, $D = 0.01$ m: —$\tau = 10\%$, $\cdots\tau = 20\%$, $--\tau = 40\%$ ($0.325 \times 0.25 \times 0.006$ m; $\eta = 0.1$, $d_o = 0.01$ m).

## 5.5 Effect of perforation on plate dynamic properties

### 5.5.1 Effect on bending stiffness and mass

In the results in this chapter the effect of perforation on the dynamic properties of the plate have been neglected. However in practice perforation will reduce both bending stiffness and mass of a plate. This effect is discussed in this section.

The investigation of the effect of perforation on dynamic properties of plates began in the early 1960s in order to determine an accurate stress analysis of perforated panels used to support the tubes in a heat exchanger [83, 84, 85]. To obtain an equivalence with the actual properties corresponding to a solid plate, the effective material properties were defined, namely the effective Young's modulus ($E^*$), Poisson's ratio ($\nu^*$) and density ($\rho_p^*$).

To allow different spacing between holes in an array of perforation, Forskitt *et al.* [65] introduced a perpendicular and parallel ligament efficiency given by

$$\text{XLE} = \frac{b_x - 2d_o}{b_x}, \qquad \text{YLE} = \frac{b_y - 2d_o}{b_y} \tag{5.56}$$

where $b_x$ is perpendicular pitch and $b_y$ is parallel pitch as shown in Figure 5.45 for a triangular or rectangular array of perforation. Forskitt *et al.* [65] then used a Finite Element Method (FEM) to determine $E^*$ and $\nu^*$ for a perforation plate with circular holes.

Perforation also reduces the mass of a plate. Based on the solid plate, this effect is quantified by introducing the effective density $\rho_p^*$. The effective density $\rho_p^*$ according to [65] can be obtained based on the fraction of the solid plate i.e.

$$\frac{\rho_p^*}{\rho_p} = 1 - \left[\frac{\pi}{8}(1 - \text{XLE})(1 - \text{YLE})\right] \tag{5.57}$$

This is only for a regular triangular array of holes. For a rectangular array, it can be written as

$$\frac{\rho_p^*}{\rho_p} = 1 - \left[\frac{\pi}{16}(1 - \text{XLE})(1 - \text{YLE})\right] \tag{5.58}$$

In terms of perforation ratio $\tau$, both Eq.(5.57) and Eq.(5.58) are equivalent to $1 - \tau$.

It was then proposed that the effective resonance frequency of a simply supported plate is given as in Eq.(2.7), but introducing the effective material properties

$$\omega_{mn}^* = \left(\frac{E^* t_p^2}{12\rho_p^*(1 - \nu^{*2})}\right)^{\frac{1}{2}} \left[\left(\frac{m\pi}{a}\right)^2 + \left(\frac{n\pi}{b}\right)^2\right] \tag{5.59}$$

According to Burgemeister and Hansen [64], this equation does not provide correct resonance frequencies when using the effective material properties. The FEM was then implemented to model the modal response of range of plates with varying perforation geometries. From this, the resonance frequency $f^*$ was compared with that from the FEM model for the solid plate $f$. The results of these comparisons ($f^*/f$) were then fitted to a cubic expression as a general equation for other perforation geometries in terms of XLE and YLE which is independent of the mode order ($m$,$n$). The cubic function is given by

$$\begin{aligned}\frac{f^*}{f} = a_c \times \text{XLE}^3 + b_c \times \text{XLE}^2 + c_c \times \text{XLE} + \ldots \\ + d_c \times \text{YLE}^3 + e_c \times \text{YLE}^2 + f_c \times \text{YLE} + g_c\end{aligned} \tag{5.60}$$

where the coefficients are listed in Table 5.1.

This formula was validated by comparison with the measured resonance frequencies of two perforated plates. The results using Eq.(5.59) (with the material properties data from [65]) underestimated the measured results. However, the experimental validation was carried out on plates having similar geometries from among the models which gave a good agreement. It should also be made with different plate dimensions, thicknesses and hole geometries to ensure a stronger validation of the proposed formula.

Figure 5.46 shows a comparison between the results of the resonance frequency ratio $f^*/f$ from [64] with those using the effective material properties obtained from [65]. A large difference can be seen, particularly for small XLE and YLE (large $\tau$). Figure 5.46(a) is obviously non-linear. In [64], the graph was constructed from available

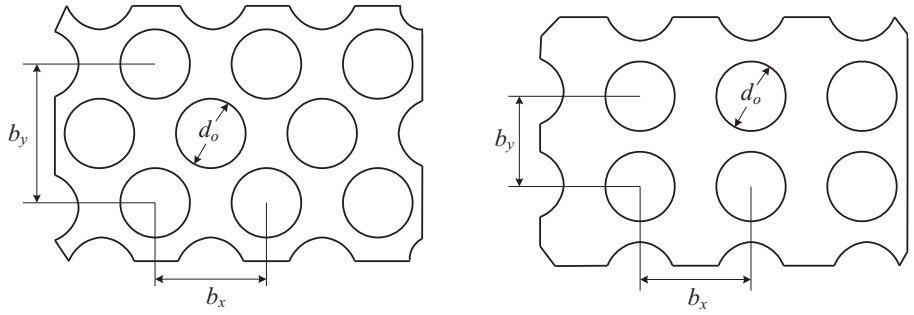


FIGURE 5.45: Array of holes: (a) triangular and (b) rectangular.

TABLE 5.1: Coefficient for the cubic function in Eq.(5.60)

| Coefficient | Value |
|---|---|
| $a_c$ | 0.0399 |
| $b_c$ | −0.0727 |
| $c_c$ | 0.1161 |
| $d_c$ | −0.1295 |
| $e_c$ | 0.1013 |
| $f_c$ | 0.1096 |
| $g_c$ | 0.8395 |

data in [65]. The graph is only applicable for XLE $> 0$, YLE $> 0$. Meanwhile Figure 5.46(b) produces almost a smooth plane surface. The graph can also be expanded to include XLE $< 0$ and or YLE $< 0$.

Patil *et al.* [86] also used a curve fitting technique to develop an effective resonance frequency formula from simulation data of resonance frequencies for five perforated plates using FEM. The formula was a function of the so-called mass remnant ratio (MR) i.e. the ratio of surface area of a perforated plate to that of the solid plate for the same dimension. This is equivalent to $1-\tau$. The formula was then expressed as a seventh order polynomial function of MR. However, the formula was applicable only for the first three modes of vibration.

Soler and Hill [87] proposed a formula for calculating the effective bending stiffness $B^*$. For a regular array of circular holes in a very thin plate ($t_p \ll b_x$) where XLE $\approx$ YLE, the effective modal resonance frequency is given by

$$\omega^*_{mn} = \left(\frac{B^*}{\rho_p t_p}\right)^{\frac{1}{2}} \left[\left(\frac{m\pi}{a}\right)^2 + \left(\frac{n\pi}{b}\right)^2\right] \tag{5.61}$$

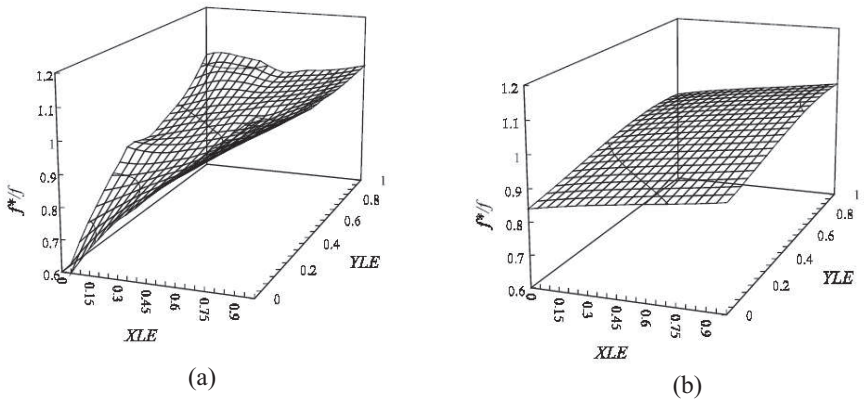


FIGURE 5.46: The ratio of the effective resonance frequency of a perforated plate to the resonance frequency of a solid plate: (a) using effective material properties data from [65] and (b) using FEM [64].

where

$$B^* = \frac{B}{(1-\pi d_o^2/\sqrt{3}b_x^2)}\left(1-\frac{\pi}{2\sqrt{3}}\left(1-\frac{b_x-d_o}{b_x}\right)^2\right)^{(2b_x-d_o)/0.8b_x}$$

and $B = Et_p^3/12(1-\nu^2)$. The true density $\rho_p$ is used in this equation because the correction factor has been implicitly included in the effective bending stiffness $B^*$. It was shown that this formula agrees well with the results from Figure 5.46(a) [65].

Table 5.2 lists the changes in resonance frequency predicted for different perforation geometries and plate thicknesses considered in the experiments in Chapter 7. Results are given for the ratio $f^*/f$ using Eq.(5.60) and Eq.(5.61). The hole distance is made similar ($b_x = b_y$) to be able to apply Eq.(5.61). Using Eq.(5.60) for 1.5 mm plate thickness, it can be seen the ratio $f^*/f$ is reduced as the hole diameter is increased. The reduced resonance frequency is due to a reduction in the bending stiffness of the plate due to the perforation, which basically makes the plate more flexible. For the 3 mm thick plate, all the plates with 20% perforation ratio give the same effective resonance frequency ratio. This is because the hole diameter and the hole separation distance increase with the same factor.

The results using Eq.(5.61) give a frequency ratio which is sometimes greater than unity. This is due to the plate thicknesses given which is not small enough to apply this equation. Eq.(5.61) also has another limitation. It can be observed from the formula that in order to avoid a negative bending stiffness, it requires that $d_o^2 < (\sqrt{3}/\pi)b_x^2$. In other words, the holes cannot be very closely spaced. The results in Table 5.2, i.e. for

1.5 mm plates with 19% and 44% and 3 mm plates for 20% perforation ratios, suggest that Eq.(5.61) is being used outside its range of validity.

TABLE 5.2: Comparison of effective resonance frequencies

| Dimensions (m) | $d_o$ (m) | $b_x$ (m) | $\tau$ (%) | $f^*/f$ | |
|---|---|---|---|---|---|
| | | | | Eq.(5.60) | Eq.(5.61) |
| $0.4 \times 0.3 \times 0.0015$ | 0.005 | 0.027 | 5 | 0.9706 | 0.9963 |
| | 0.008 | 0.027 | 12 | 0.9301 | 0.9984 |
| | 0.010 | 0.027 | 19 | 0.8984 | 1.0078 |
| | 0.015 | 0.027 | 44 | 0.8149 | 1.1206 |
| $0.4 \times 0.3 \times 0.003$ | 0.005 | 0.010 | 20 | 0.8395 | 1.0629 |
| | 0.010 | 0.020 | 20 | 0.8395 | 1.0629 |
| | 0.015 | 0.050 | 7 | 0.9286 | 0.9986 |
| | 0.025 | 0.050 | 20 | 0.8395 | 1.0629 |

As Eq.(5.61) is limited in its perforation geometry and plate thickness, therefore for the purpose of this study, only Eq.(5.60) will be implemented.

The critical frequency will also be altered. In this case a reduction in bending stiffness leads to an increase in critical frequency

$$\frac{f_c^*}{f_c} = \frac{f}{f^*} \tag{5.62}$$

## 5.6 Summary

The sound radiation from a perforated plate set in an equally infinite perforated baffle has been calculated using an approach from Fahy and Thompson [37]. It has been shown that the radiation efficiency of a baffled plate is reduced drastically at low frequency because of the perforation in the plate and the baffle. The effect of perforation (EoP) curve also shows that the reduction follows a 20 dB/decade trend against the frequency. From this, an approximate formula for determining the EoP has been proposed that gives a good agreement up to half the critical frequency. It is also found that the EoP is independent of the plate dimensions, depending only on the non-dimensional reactance of the perforation, $h$.

A model for sound radiation from an unbaffled plate has been developed by modifying Laulagnet's model for the radiation efficiency of an unbaffled solid plate [33]. For

the thin plates ($t_p \ll d_o$), similar to the case of a perforated plate set in an infinite perforated baffle, the EoP is proportional to $\tau/d_o$. The EoP increases as the perforation ratio increases and as the hole size reduces for a given perforation ratio. However, unlike the former case, the EoP for an unbaffled plate depends on the plate thickness and dimensions. An approximate formula has also been proposed for this case which gives a good agreement up to half the critical frequency.

The model has then been extended to consider a plate located near a rigid, reflecting surface. Depending on the distance between the plate and the rigid surface, the radiation efficiency is considerably reduced at low frequencies. More sound reduction can be gained by introducing perforation to the plate. However, at higher frequencies, the radiation efficiency is similar than or greater than that for the plate in absence of the rigid surface.

It has also been shown that the perforation changes the bending stiffness of the plate which causes a slight reduction of the resonance frequencies and corresponding increase in the critical frequency.

The proposed approximate formulae for the EoP can be used as an engineering design guide for noise control measures. The results show that for only 10% perforation ratio, the sound radiation can be reduced by $10 - 15$ dB at low frequencies which shows the effectiveness of perforation as a noise control measure. However, it should be remembered that in certain structures, the stiffness reduction due to perforation also has to be considered. In other words, the structural strength must be taken into account when the perforation is introduced. Consequently, a trade-off may be required between reducing the sound radiation and maintaining the strength of the structure.

# Chapter 6

# Sound Radiation from a Plate Modelled by Discrete Sources

In Chapter 5, the assumption was made that the array of holes can be replaced by a uniform acoustic impedance at the suface of the plate. For this to be valid, the distance between the holes must be short enough compared with the acoustic wavelength. However, the effect is not obvious in the models because the perforation ratio is a parameter defined without necessarily knowing the hole position or the distance between holes. As already mentioned in Section 5.1.3, a frequency limit should exist where the continuous impedance assumption is breached when the hole distance is large compared with the acoustic wavelength.

In this chapter, a discrete source approach is taken. A continuous baffled source can be modelled by replacing it with an array of point sources. In the same way a perforated plate can also be modelled by an array of sources, some representing the plate and others the holes. The acoustic pressure at each source due to the motion of the other sources is calculated numerically. This discrete source model is attractive as the hole configuration can be set arbitrarily and the hole distance is known. This approach also provides a model for the case of a perforated plate set in an infinite rigid baffle which has not been covered in Chapter 5. In principle, the concept is similar to the models of Vitiello *et al.* [25], Cunefare and Koopman [26], Elliott and Johnson [27] and Gardonio *et al.* [28] which used discrete elementary radiators to replace a continuous

radiator. However, as will be shown later, the self-radiation impedance used in the proposed model is slightly different.

## 6.1 Discrete version of Rayleigh integral

The well-known Rayleigh integral [9] can be used to calculate the sound pressure at any point of observation due to a vibrating plate set in an infinite rigid baffle. The equation can be written as

$$p(\mathbf{x}) = -2 \int_s G(\mathbf{x}|\mathbf{x}_o) \left( \frac{\partial p(\mathbf{x})}{\partial n} \right)_S dS \tag{6.1}$$

where $\mathbf{x} = (x, y, z)$ and $S$ denotes the surface area of the plate (assumed to lie in the $xy$-plane). The first term of the integrand is the free-field Green's function, which is the sound pressure contribution at $\mathbf{x}$ due to the radiation from a unit point monopole source at $\mathbf{x}_o$. Since $\partial p/\partial n = -j\rho ck\, U_p$ and $G = e^{-jkR}/4\pi R$, this equation can be written as

$$p(\mathbf{x}) = \frac{j\rho ck}{2\pi} \int_s U_p(\mathbf{x}_o) \frac{e^{-jkR}}{R} dS \tag{6.2}$$

where $R = |\mathbf{x} - \mathbf{x}_o|$ and $U_p$ is the normal velocity amplitude of the plate.

The Rayleigh integral requires that the normal velocity $U_p$ is known over the whole plate surface area. For the simple case of a moving piston, the normal velocity is uniform across the surface

$$U_p(\mathbf{x}_o) = U_n \tag{6.3}$$

where $U_n$ is constant. For bending of a rectangular plate with dimensions $a \times b$ and assuming simply supported edges, the velocity can be written as the sum of modal contributions given by

$$U_p(\mathbf{x}_s) = \sum_{m=1}^{\infty} \sum_{n=1}^{\infty} u_{mn} \sin\left(\frac{m\pi x}{a}\right) \sin\left(\frac{n\pi y}{b}\right) \tag{6.4}$$

where $u_{mn}$ is the complex velocity amplitude of mode $(m,n)$. For a point force excitation at $(x_0, y_0)$, it can be defined as in Eq.(2.5)

$$u_{mn} = \frac{4j\omega F}{[\omega_{mn}^2(1+j\eta) - \omega^2]M} \sin\left(\frac{m\pi x_0}{a}\right) \sin\left(\frac{n\pi y_0}{b}\right) \tag{6.5}$$

where $F$ is the force amplitude, $\omega_{mn}$ is the natural frequency, $\eta$ is the damping loss factor and $M$ is the plate mass.

The Rayleigh integral can next be written in discrete form as a sum over discrete source regions. For a rectangular plate in the $xy$ coordinate plane, the sources are defined by dividing the plate into a set of grid points. The spacings between points are $dx$ in the $x$ direction and $dy$ in the $y$ direction. The small element of the plate $dS = dxdy$ thus becomes a discrete monopole source. This requires that the size of the elemental source must be much smaller than the acoustic wavelength $(k\,dx \ll 1, k\,dy \ll 1)$.

Discretizing the Rayleigh integral yields

$$p(\mathbf{x}) = \frac{j\rho ck}{2\pi} \sum_s U_p(\mathbf{x}_s) \frac{e^{-jkR}}{R} dxdy \tag{6.6}$$

where $R = |\mathbf{x} - \mathbf{x}_s|$. However for positions $\mathbf{x}$ on the surface $(\mathbf{x} = \mathbf{x}_r)$ the integrand is singular for $r = s$. To solve the integral for element $r$, another approximation corresponding to the pressure distribution on the plate surface is needed. Morse and Ingard [75] give the total force per unit area (pressure) acting on a rectangular (almost square) piston moving with uniform velocity $U_n$. For a plate of dimensions $a \times b$, where $b \cong a$, the radiation impedance is given by

$$\frac{p}{U_n} = \frac{\rho ck^2}{16}(a^2 + b^2) + \frac{j8\rho ck}{9\pi}\left(\frac{a^2 + ab + b^2}{a + b}\right), \qquad ka \ll 1 \tag{6.7}$$

Applying this to the elemental source $dS$ and assuming a square piston, i.e. $a = dx = b = dy$, this reduces to

$$\frac{p}{U_n} = \rho c\left(\frac{k^2 dx^2}{8} + \frac{j4k\,dx}{3\pi}\right), \qquad k\,dx \ll 1 \tag{6.8}$$

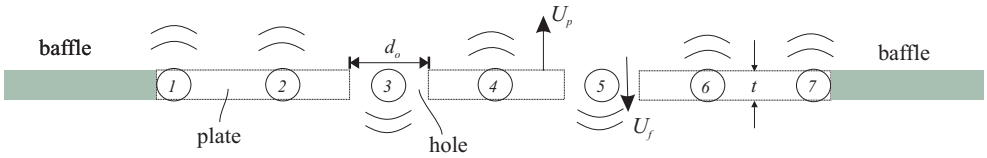


FIGURE 6.1: Analytical model of an array of discrete (monopole) sources for calculating the sound radiation of a perforated plate

Therefore the Rayleigh integral can be written in the form

$$\{p_r\} = \mathbf{M}_{rs}\{U_s\} \tag{6.9}$$

where

$$\mathbf{M}_{rs} = \begin{cases} \dfrac{j\rho ck}{2\pi}\left(\dfrac{e^{-jkR_{rs}}}{R_{rs}}\right)dx^2, & r \neq s \\ \\ \rho c\left(\dfrac{k^2dx^2}{8} + \dfrac{j4k\,dx}{3\pi}\right), & r = s \end{cases} \tag{6.10}$$

The matrix $\mathbf{M}$ is actually an impedance matrix since the acoustic impedance expresses the ratio of complex pressure to the associated particle velocity. In the models of Elliott and Johnson [27] and Gardonio *et al.* [28], the impedance of the elementary radiator is defined by

$$\Re\left(\mathbf{M}_{rs}\right) = \frac{\rho ck^2d_x^2}{2\pi}\left(\frac{\sin kR_{rs}}{kR_{rs}}\right) \tag{6.11}$$

where $\dfrac{\sin kR_{rs}}{kR_{rs}} = 1$ for $kR_{rs} \to 0$.

For the real part of the self-radiation impedance ($\mathbf{M}_{rr}$), the difference between the two models is 27%.

## 6.2 Impedance matrix including perforation

Consider an array of circular holes on a plate, as shown in Figure 6.1. Each hole can be considered to be an acoustic source with volume velocity $\pi d_o^2U_h/4$ where $U_h$ is the fluid velocity in the hole and $d_o$ is the diameter of the hole.

The pressure at any point on the plate surface can be written as a sum of the pressure contributions from all sources representing the plate and the holes. The pressure at source position $r$ due to source $s$ can be written as

$$p_r = \sum_s M_{rs} U_s \tag{6.12}$$

where $U_s$ is the velocity of source $s$ which may represent the plate surface or the holes. Using the example in Figure 6.1, $M_{rs}$ can be written as a matrix, for example

$$\mathbf{M}_{rs} = \left(\begin{array}{cc:c:cc:cc} M_{11} & \cdot & M_{13} & \cdot & M_{15} & \cdot & M_{17} \\ \cdot & \cdot & M_{23} & \cdot & M_{25} & \cdot & \cdot \\ \hdashline M_{31} & M_{32} & M_{33} & M_{34} & M_{35} & M_{36} & M_{37} \\ \hdashline \cdot & \cdot & M_{43} & \cdot & M_{45} & \cdot & \cdot \\ \hdashline M_{51} & M_{52} & M_{53} & M_{54} & M_{55} & M_{56} & M_{57} \\ \hdashline \cdot & \cdot & M_{63} & \cdot & M_{65} & \cdot & \cdot \\ M_{71} & \cdot & M_{73} & \cdot & M_{75} & \cdot & M_{77} \end{array}\right) \tag{6.13}$$

In the present example, sources 3 and 5 correspond to the holes. The elements inside the dashed lines correspond to the pressure at the hole locations due to the sources at the plate or the holes; or the pressure at the plate location due to the holes. The matrix $\mathbf{M}_{rs}$ can be partitioned to give

$$\mathbf{M} = \left(\begin{array}{c:c} \mathbf{M}_{p-p} & \mathbf{M}_{p-h} \\ \hdashline \mathbf{M}_{h-p} & \mathbf{M}_{h-h} \end{array}\right) \tag{6.14}$$

where $p-p$ refers to the pressure at a plate location due to plate sources, $p-h$ refers to the pressure at plate locations due to hole sources, etc.

The pressure and velocity can be partitioned into components corresponding to the plate and the holes giving

$$\left\{\begin{array}{c} p_p \\ \hdashline p_h \end{array}\right\} = \mathbf{M} \left\{\begin{array}{c} U_p \\ \hdashline U_h \end{array}\right\} \tag{6.15}$$

where $\{\}$ denotes a column vector.

The fluid velocity in the hole is defined from the acoustic impedance of the hole $Z_h$

$$U_f = -\frac{2p_h}{Z_h} \tag{6.16}$$

where $Z_h = \tau z_h$ is given in Eq (5.14) and $2p_h$ is the difference between the pressure on both sides of the plate.

The model is developed for discrete, independent holes on the plate. Therefore, the acoustic impedance is no longer treated as a uniform specific acoustic impedance $z_h$ across the plate surface.

As the fluid velocity in each hole may be represented by $n_e$ monopole sources, where $n_e$ may be greater than one, the fluid velocity through the hole area must be averaged to the corresponding element area $dS$ of the monopole sources to maintain the correct source strength. Thus

$$U_{fa} = U_f c_f \tag{6.17}$$

where $U_{fa}$ is the corrected fluid velocity and $c_f$ is the correction factor given by

$$c_f = \frac{1}{n_e dS}\left(\frac{\pi d_o^2}{4}\right) \tag{6.18}$$

Since $U_f$ represents the motion of the fluid relative to the plate, the source velocity from the hole $U_h$ is the combination of the velocity of the plate and the fluid. It can be expressed as

$$U_h = U'_p + U_{fa} = U'_p - \frac{2p_h}{Z_h} c_f \tag{6.19}$$

where $U'_p$ is the (interpolated) plate velocity for a solid plate at the hole locations.[1]

The pressure at the plate location and at the holes can then be written as

$$\{p_p\} = [M_{p-p}]\{U_p\} + [M_{p-h}]\{U_h\} \tag{6.20}$$

[1]Without any viscous effect, the impedance of the hole is inertial. It may be appropriate for the absolute velocity in the hole to depend on the pressure difference rather than the relative velocity as given. However, this has not been investigated here.

$$\{p_h\} = [M_{h-p}]\{U_p\} + [M_{h-h}]\{U_h\} \tag{6.21}$$

Substituting Eq.(6.19) into Eq.(6.21) and rearranging yields

$$\left[I + \frac{2M_{h-h}\, c_f}{Z_h}\right]\{p_h\} = ([M_{h-p} \;\; M_{h-h}])\{\bar{U}_p\} \tag{6.22}$$

where $\{\bar{U}_p\}$ is a vector containing the plate velocity at all locations including the plate ($U_p$) and the holes ($U_p'$) and $I$ is the identity matrix of dimension equal to the number of holes.

Inverting the matrix on the left-hand side of Eq.(6.22) gives

$$\{p_h\} = \left[I + \frac{2M_{h-h}\, c_f}{Z_h}\right]^{-1}([M_{h-p} \;\; M_{h-h}])\{\bar{U}_p\} \tag{6.23}$$

The pressure at the plate locations $p_p$ can be obtained by substituting Eq.(6.23) into Eq.(6.19) to give $U_h$ and then substituting into Eq.(6.20).

The total sound power radiated by the plate can be expressed as the summation over the power contributions from all discrete sources. The sound power can thus be given by

$$W = \frac{1}{2}\Re\left(\sum p_p U_p^* + \sum p_h U_h^*\right) dS \tag{6.24}$$

where $dS$ is the elemental source area.

Finally, recalling Eq.(1.2), the radiation efficiency of the perforated plate can be written as

$$\sigma = \frac{W}{\frac{1}{2}\rho c a b \left\langle \left|\bar{U}_p^2\right| \right\rangle} \tag{6.25}$$

where $\left\langle \left|\bar{U}_p^2\right| \right\rangle$ is the spatially averaged squared surface velocity of the plate.

## 6.3 Results

### 6.3.1 Radiation by a vibrating piston

The model is examined first for a uniform plate velocity or vibrating piston. The sound radiated by a perforated vibrating piston is calculated by using Eq.(6.3) to represent the plate velocity. The accuracy of the results depends on the source spacing $dx$. Figure 6.2 shows the results for different source spacings. It can be seen that the smaller the spacing, i.e. the larger the number of sources, the better the result converges. The blue curve is plotted as a reference and calculated analytically using Rayleigh's integral from Eq.(2.1) where the velocity $v$ is set to be unity. The results show that the spacing must be less than 0.01 m to ensure that the result (black, solid line) converges to unity up to at least 4 kHz. However, as $dx$ is reduced the calculation time becomes more intensive and the impedance matrices representing this number of sources become large requiring greater computer memory. With the elemental source spacing of $dx = dy = 0.01$ m, the number of elemental sources is 3250. As from 1 kHz the radiation efficiency for a vibrating piston is close to unity, the remaining calculations in this section are performed only up to 3 kHz and using $dx = 0.01$ m.

The calculation is carried out for the same plate dimensions $0.65 \times 0.5 \times 0.003$ m and parameters as in previous chapters. For a rigid piston the thickness is only relevant for the definition of the hole impedance. Figure 6.3 shows the plate with the grid points and the locations of the holes for one example in which, 20 holes are chosen with each hole represent by 16 monopole sources. The hole distance in the $x$ or $y$ directions is 0.13 m.

Figure 6.4 plots the results for the rectangular piston with various perforation ratios (different numbers of holes) with the hole diameter $d_o = 4$ cm. It can be seen that the radiation efficiency reduces as the perforation ratio increases. The curves all have a 20 dB/decade slope until they converge to unity. This proportionality to $f^2$ shows the characteristic of a monopole source radiation. For the present case, the calculation of radiation efficiency up to 3 kHz (frequency resolution of 20 points per decade, spaced logarithmically) using MATLAB takes about 11 minutes. See Table 2.1 for the computer specification.

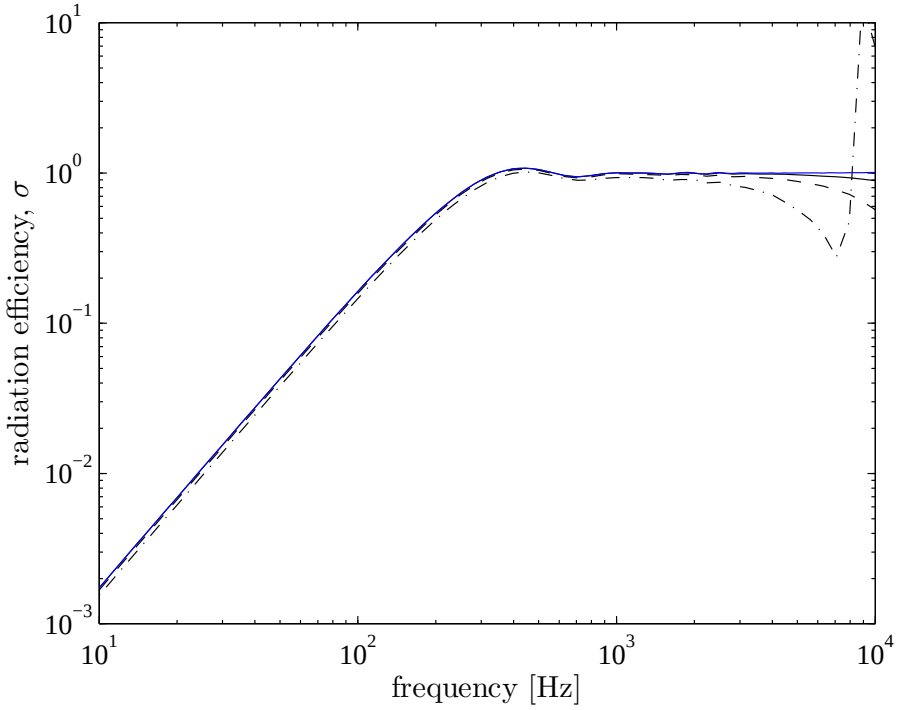


FIGURE 6.2: Radiation efficiency of a solid baffled plate (rectangular piston) from discrete monopole sources: $0.65 \times 0.5 \times 0.003$ m (— analytical, $- \cdot -dx = 0.04$ m, $--dx = 0.02$ m and $—dx = 0.01$ m).

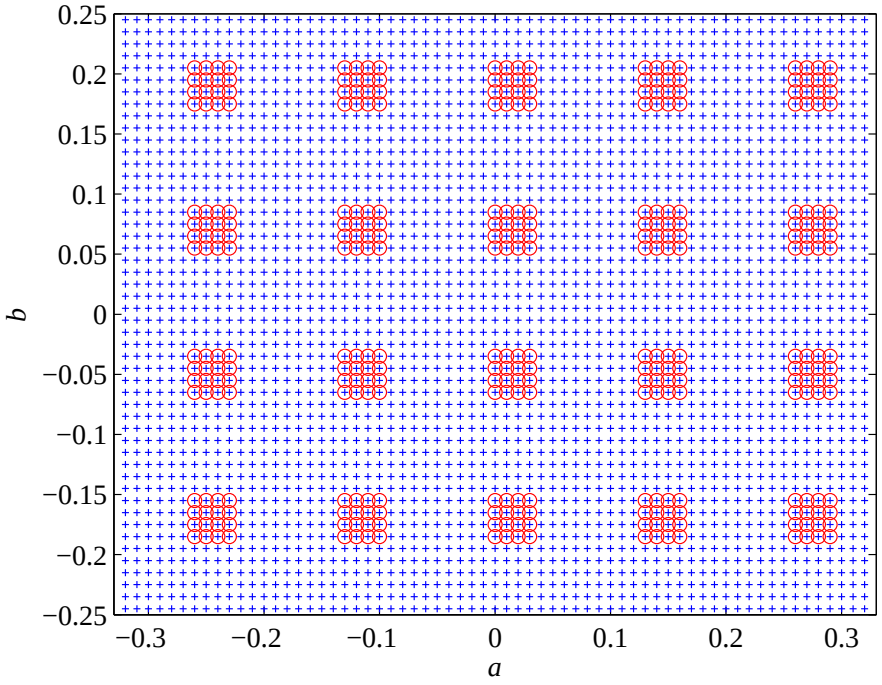


FIGURE 6.3: Example of the grid points (+) and the locations of $5 \times 4$ holes from groups of monopole sources (○) on the plate ($0.65 \times 0.5$ m).

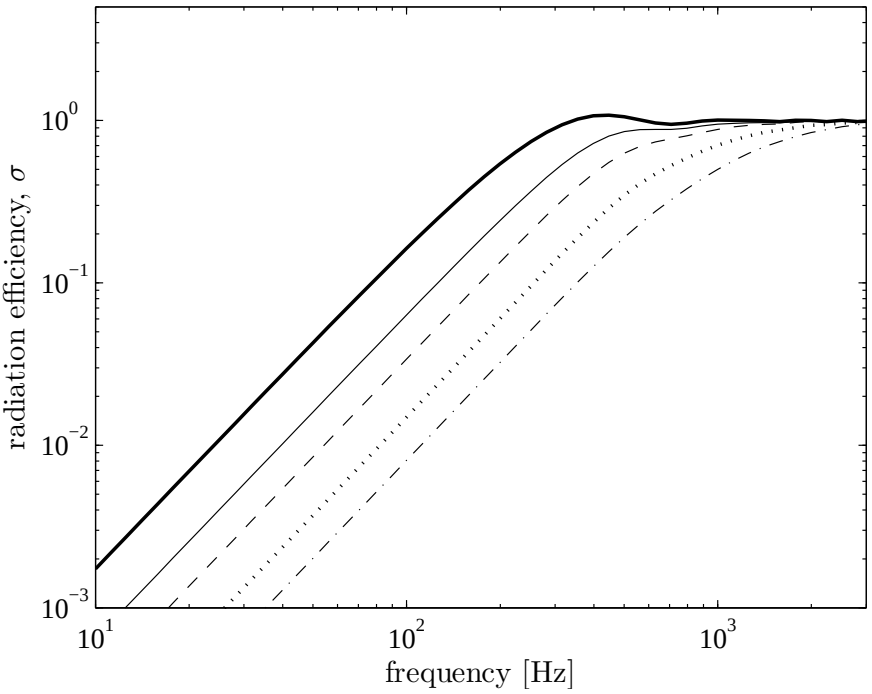


FIGURE 6.4: Radiation efficiency of a perforated baffled plate (rectangular piston) from discrete monopole sources: $0.65 \times 0.5 \times 0.003$ m, $d_o = 0.04$ m, $dx = 0.01$ m (— unperforated, —$\tau = 6\%$, −−$\tau = 12\%$, $\cdots\tau = 22\%$, $-\cdot-\tau = 31\%$ ).

As the spacing between holes is also defined by the elemental sources, the perforation ratio (number of holes and their diameter) thus affects the number of sources required, particularly for the plate with a large number of holes. For example consider a perforated plate of similar dimensions having $40 \times 30$ holes with 5 mm diameter ($\tau = 20\%$). Assuming in each direction, one monopole source is set to represent the hole and the plate parts, the number of sources required is $81 \times 61 = 4941$. Consequently, the larger the number of holes, the more sources are required and the more intensive the calculation time. This limits the capability of the model to calculate the radiation efficiency of a perforated plate only for a moderate number of holes.

Figure 6.5 plots the results for various hole diameters with constant perforation ratio. It can be seen that the radiation efficiency can be further reduced by reducing the hole size, as also seen for the case of a perforated plate set in a perforated baffle and a perforated unbaffled plate (see Section 5.2.3).

Figure 6.6 plots the effect of perforation (EoP) corresponding to the results in Figure 6.4. It shows that the trend is similar to that for the perforated unbaffled case (see Figure 5.23) where the EoP curve is constant at low frequencies until it rises toward

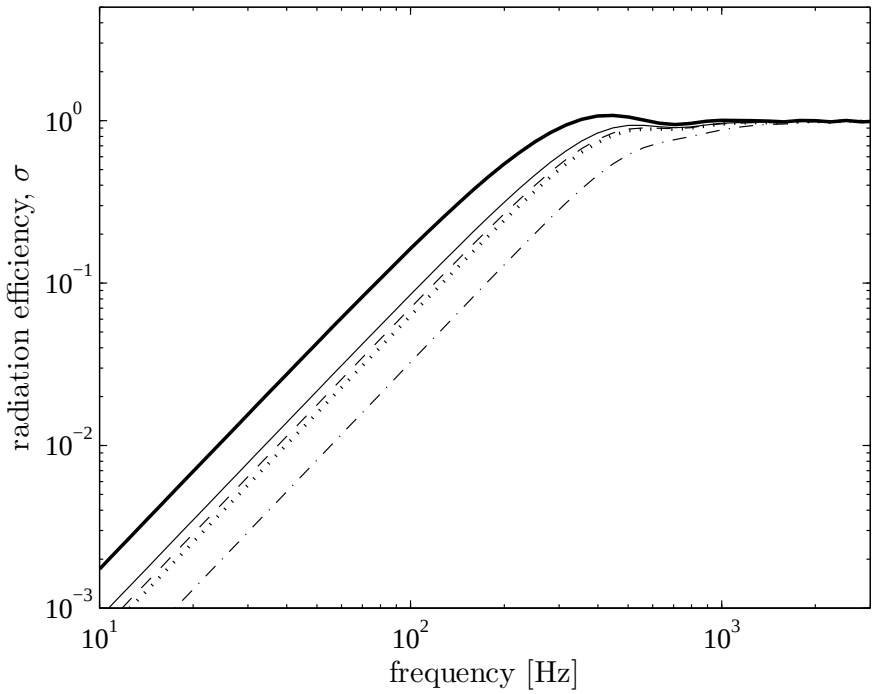


FIGURE 6.5: Radiation efficiency of a perforated baffled plate (rectangular piston) from discrete monopole sources: $0.65 \times 0.5 \times 0.003$ m, $\tau = 4\%$, $dx = 0.01$ m (— unperforated, —$d_o = 43$, −−$d_o = 33$, $\cdots d_o = 26$, $-\cdot-d_o = 13$ mm ).

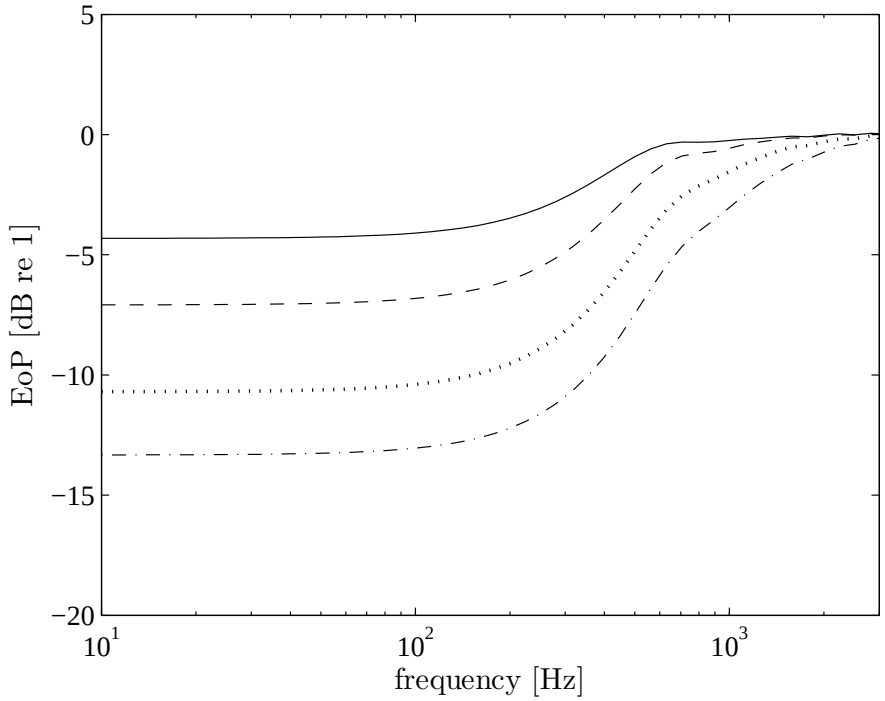


FIGURE 6.6: Effect of perforation (EoP) on sound power radiation of a perforated baffled plate (rectangular piston) from discrete monopole sources: $0.65 \times 0.5 \times 0.003$ m, $d_o = 0.04$ m, $dx = 0.01$ m (—$\tau = 6\%$, −−$\tau = 12\%$, $\cdots \tau = 22\%$, $-\cdot-\tau = 31\%$ ).

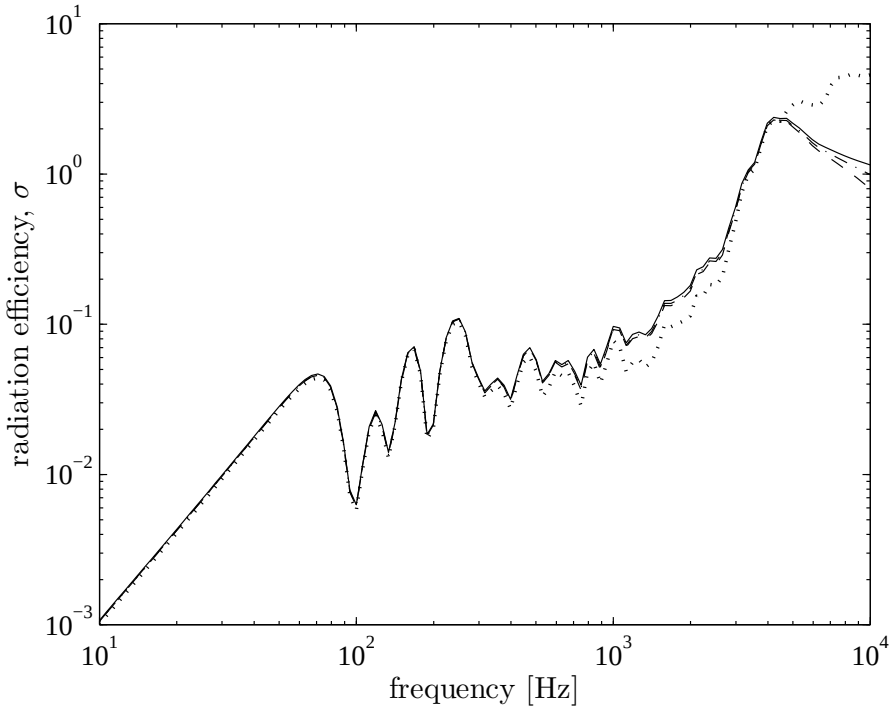


FIGURE 6.7: Radiation efficiency from modal response of a perforated baffled plate from discrete monopole sources: $0.65 \times 0.5 \times 0.003$ m with $\eta = 0.1$ ($\cdots dx = 0.04$ m, $--dx = 0.02$ m, $-\cdot-dx = 0.015$ m and —$dx = 0.01$ m).

0 dB.

### 6.3.2 Radiation by bending vibration

The model is next applied to calculate the sound radiation due to the forced vibration of a simply supported, perforated baffled plate. Eq.(6.4) is now implemented for the plate vibration.

Figure 6.7 plots the radiation efficiency for the same plate specifications as in the previous section. The force is applied at $(-0.13a, -0.1b)$ where the origin (0,0) is at the plate centre as in Figure 6.3. The results are presented for different source spacings $dx$. As also expected from Figure 6.2, the choice of $dx$ defines the discrepancy at high frequency. It can be seen that the convergence of the curves to the true value of radiation efficiency needs a small value of $dx$. For $20 \times 20$ modes and $dx = 0.01$ m, which involves 3250 sources for the present case, the calculation time is 38 minutes. The frequency resolution is 40 points per decade (spaced logarithmically) to ensure 3 points within the half-power bandwith of resonances.

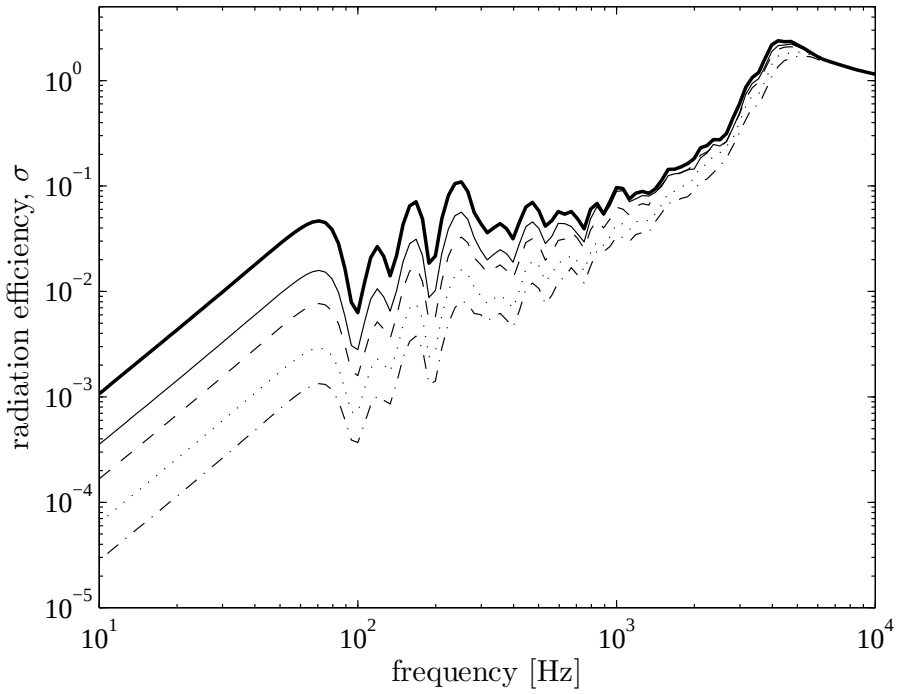


FIGURE 6.8: Radiation efficiency from bending vibration of a perforated baffled plate from discrete monopole sources: $0.65 \times 0.5 \times 0.003$ m, $d_o = 0.04$ m, $dx = 0.01$ m, $\eta = 0.1$ ( — unperforated, —$\tau = 6\%$, −−$\tau = 12\%$, $\cdots \tau = 22\%$, $- \cdot -\tau = 31\%$ ).

Figure 6.8 plots the radiation efficiency of a perforated baffled plate for constant hole diameter of 4 cm with different perforation ratios. The radiation efficiency reduces as the perforation ratio increases. The effect of hole density (number of holes per unit area) on the radiation efficiency is shown in Figure 6.9. For the same perforation ratio, the sound radiation can again be seen to be reduced by increasing the hole density (reducing the size).

The effect of perforation (EoP) corresponding to the results in Figure 6.8 is shown in Figure 6.10. This shows that the sound reduction due to perforation is constant at the fundamental mode ($< 70$ Hz). The effect is also almost constant in the edge mode region up to the critical frequency, i.e. between 1.5 kHz and 4 kHz.

Figure 6.11 compares these results with the EoP for the baffled piston from Section 6.3.1 and also for an unbaffled perforated plate from Chapter 5. It can be seen that these three sets of results diverge as the perforation ratio increases. In the fundamental mode region, the perforated baffled plate has the greatest effect (−EoP), while in the edge mode region between 400 Hz and 4 kHz, the perforated unbaffled plate has the largest effect. However, in the corner mode region between 100 Hz and 400 Hz, the

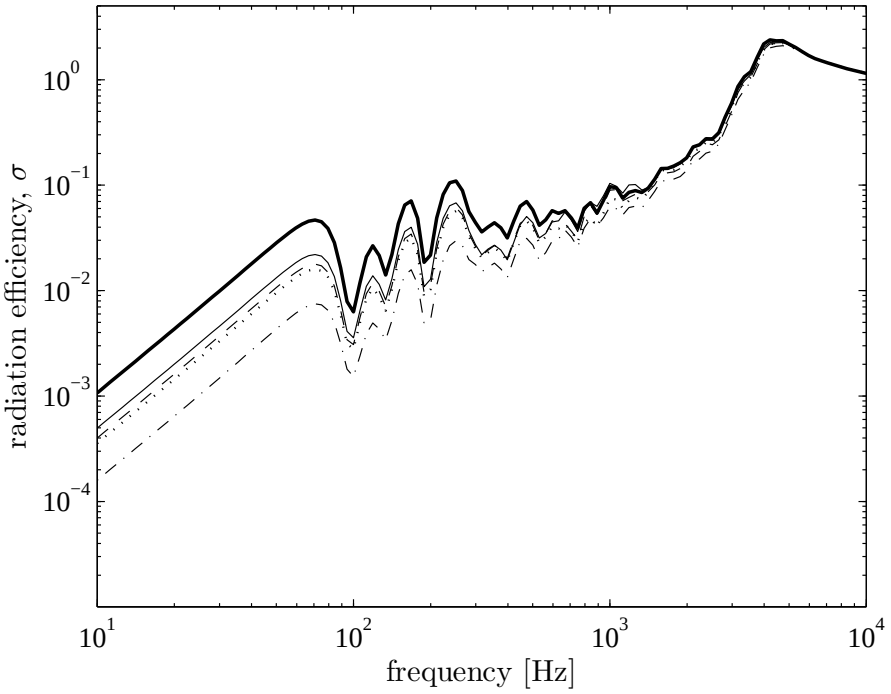


FIGURE 6.9: Radiation efficiency from bending vibration of a perforated baffled plate from discrete monopole sources: $0.65 \times 0.5 \times 0.003$ m, $\tau = 4\%$, $dx = 0.01$ m ( — unperforated, —$d_o = 43$, $--d_o = 33$, $\cdots d_o = 26$, $-\cdot-d_o = 13$ mm ).

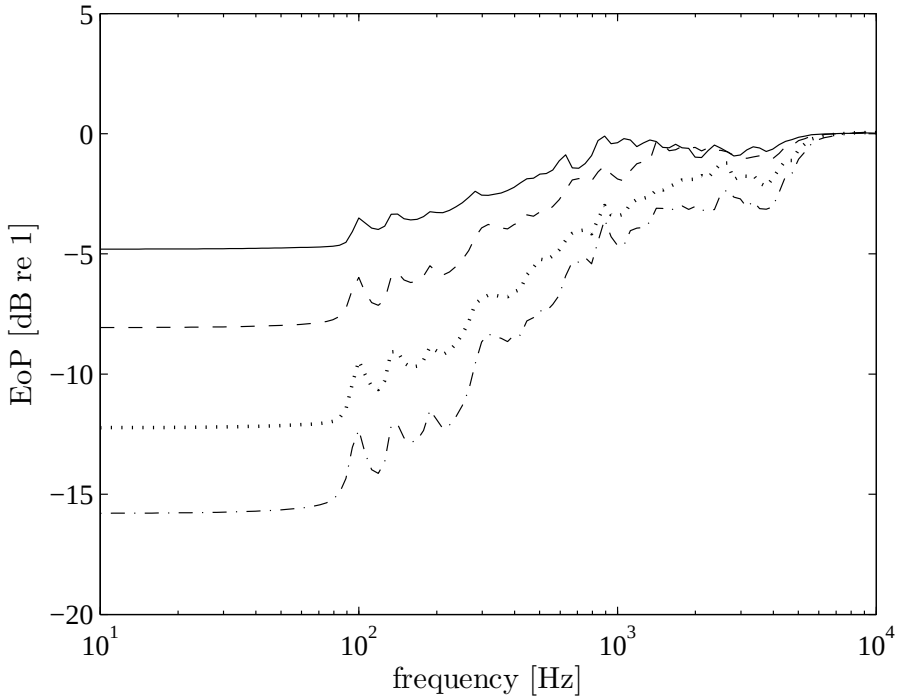


FIGURE 6.10: Effect of perforation (EoP) on sound power radiation of a perforated baffled plate in bending vibration from discrete monopole sources: $0.65 \times 0.5 \times 0.003$ m, $d_o = 0.04$ m, $dx = 0.01$ m (—$\tau = 6\%$, $--\tau = 12\%$, $\cdots \tau = 22\%$, $-\cdot-\tau = 31\%$ ).

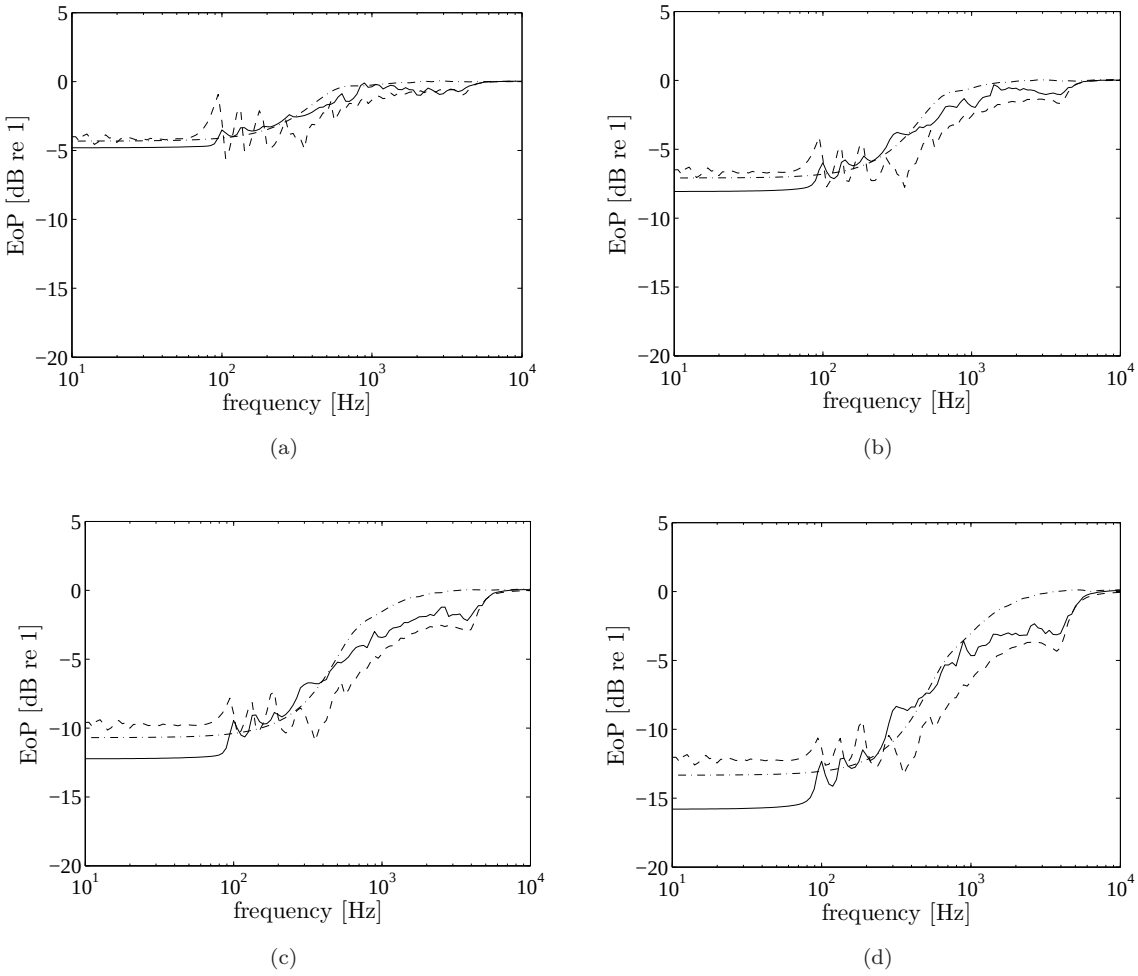


FIGURE 6.11: Comparison of the effect of perforation (EoP) on sound power radiation: perforated baffled plate (—), perforated unbaffled plate (−−) and baffled piston (−·−); $0.65 \times 0.5 \times 0.003$ m, $d_o = 0.04$ m, $dx = 0.02$ m, $\eta = 0.1$; (a) $\tau = 6\%$, (b) $\tau = 12\%$, (c) $\tau = 22\%$, (d) $\tau = 31\%$.

three results are similar.

## 6.4 Frequency limit of continuous impedance

All the models developed in Chapter 5 are based on the assumption that the distribution of holes can be represented by a continuous impedance on the plate surface. This implies that the hole distance must be much smaller than the acoustic wavelength. The effect of perforation is expected to be limited in frequency depending on the distance between holes. However, the models cannot predict the frequency limit because the perforation ratio is defined only as a function of hole size and number, not as a

TABLE 6.1: Distance between holes.

| No. | number of holes, $N_o$ | distance (m) |
|---|---|---|
| 1 | $5 \times 5$ | 0.12 |
| 2 | $3 \times 3$ | 0.20 |
| 3 | $2 \times 2$ | 0.32 |

function of hole distance. This section investigates the frequency limit above which the sound reduction no longer occurs due to the excessive hole distance.

### 6.4.1 Frequency limit for vibrating piston

Figure 6.12 presents the the radiation efficiency of a perforated plate having a uniform velocity (rectangular piston) with a small number of holes in order to have a large hole separation. The hole distances are listed in Table 6.1.

An interesting phenomenon is found at a certain frequency where the radiation efficiency from the perforated plates exceeds or becomes similar to that of the unperforated plate. This is marked in Figure 6.12 at 1100, 1700 and 2700 Hz for Figure 6.12(a), (b) and (c), respectively. If these intersection frequencies (limit frequencies) $f_l$ are examined for each case, it is found that the hole spacing equals one acoustic wavelength at $f_l$: $\lambda = c/1100 \approx 0.32$ m (Figure 6.12(a)), $\lambda = c/1700 = 0.20$ m (Figure 6.12(b)) and $\lambda = c/2700 \approx 0.12$ m (Figure 6.12(c)) where $\lambda$ is the acoustic wavelength and $c = 343$ m/s is the speed of sound.

The phenomenon is more obvious when the results are plotted in terms of the effect of perforation, as seen in Figure 6.13. The limit frequencies are denoted by $f_{l1}$, $f_{l2}$ and $f_{l3}$. It can be seen that above these limit frequencies, the perforation no longer reduces the sound radiation, i.e. EoP $\cong 0$ dB.

However, the case of a vibrating piston is rarely found in practice. A more practical problem is to observed this effect in the bending vibration case.

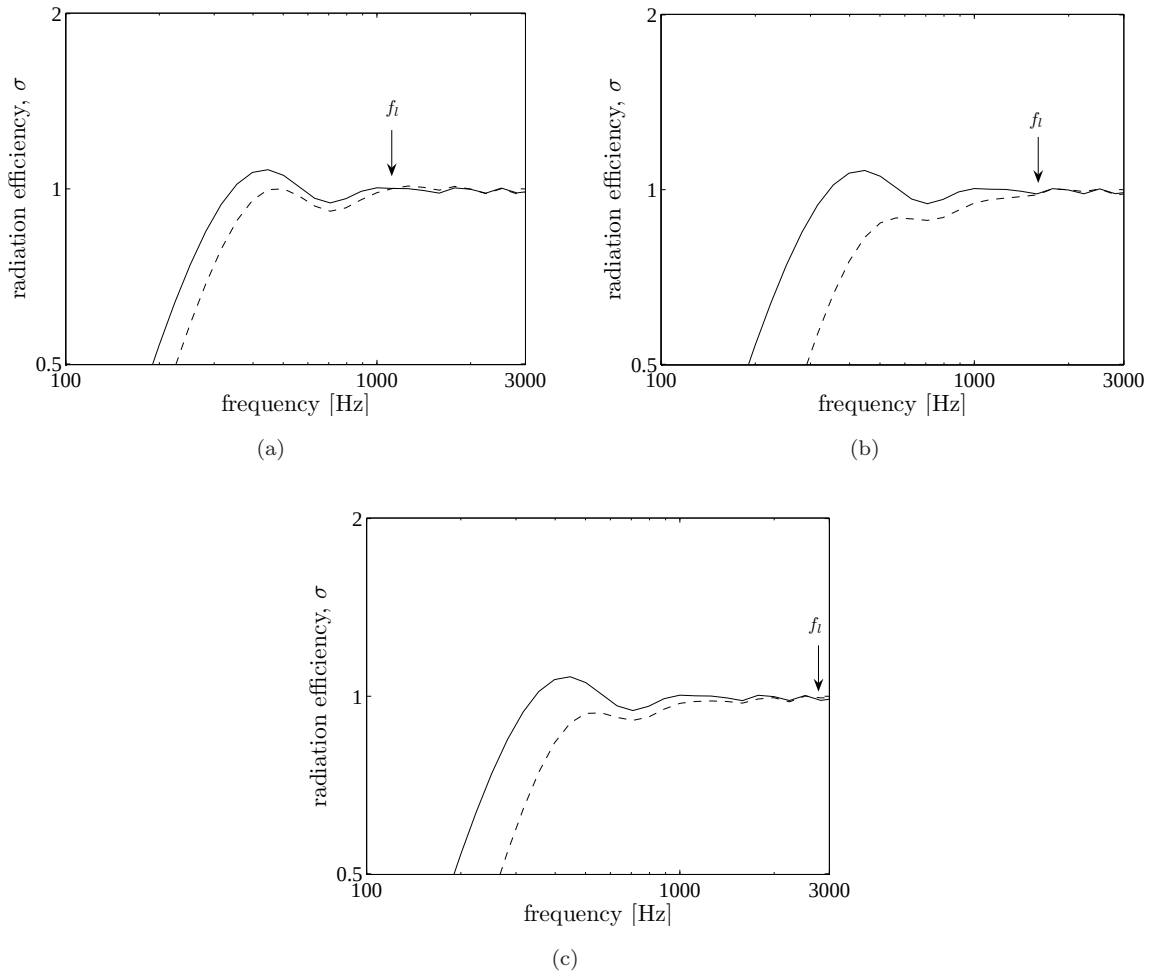


FIGURE 6.12: Radiation efficiency of a perforated baffled plate (rectangular piston) from discrete monopole sources showing the frequency limit of continuous impedance assumption: $0.65 \times 0.5 \times 0.003$ m, $dx = 0.01$ m (—unperforated, −−perforated; (a) $d_o = 0.05$ m: $N_o = 2 \times 2$, (b) $d_o = 0.06$ m: $N_o = 3 \times 3$ and (c) $d_o = 0.02$ m: $N_o = 5 \times 5$).

### 6.4.2 Frequency limit for bending vibration

Figure 6.14 plots the the radiation efficiency of perforated plates with similar number and distance of holes as in Table 6.1. The unit force is applied at $(-0.315a, -0.3b)$ from the origin $(0, 0)$ at the plate centre. It can be seen from Figure 6.14, that in this case, the intersection frequencies between the perforated and unperforated results are half those for the vibration piston. The frequencies are 530, 850 and 1400 Hz. At these frequencies, the hole distance is equal to half the acoustic wavelength. At these frequencies, well below $f_c$, the wavelength in the panel is much shorter than that in air, whereas for the piston the structural wavelength is effectively infinite.

Figure 6.15 plots the EoP for the same results which clearly shows the limit frequencies

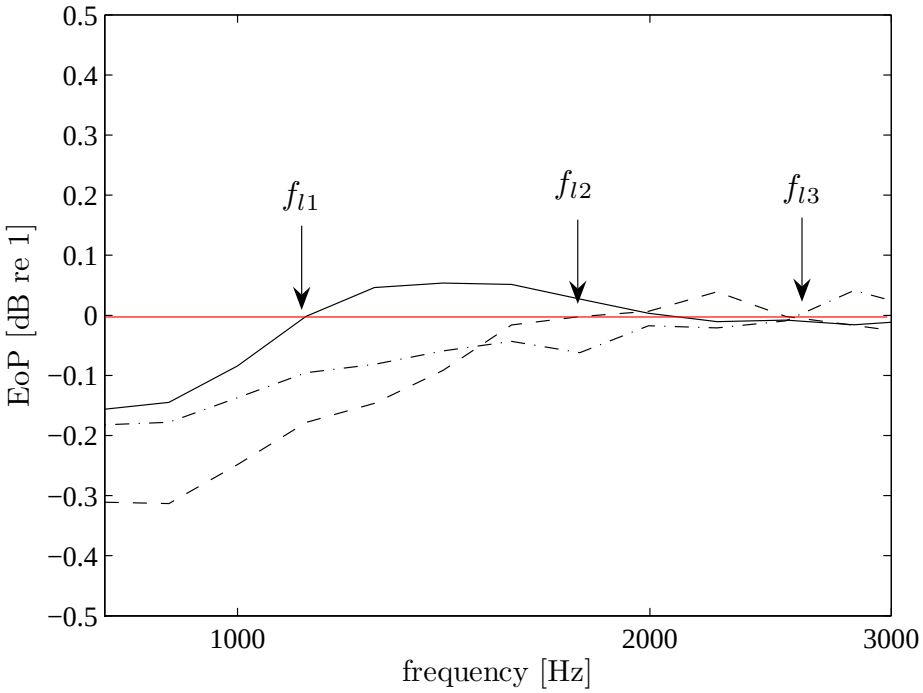


FIGURE 6.13: Effect of perforation (EoP) from a perforated baffled plate (rectangular piston) from discrete monopole sources showing the frequency limit of continuous impedance assumption: $0.65 \times 0.5 \times 0.003$ m, $dx = 0.01$ m ((a) —$d_o = 0.06$ m; $N_o = 2 \times 2$, (b) $--d_o = 0.075$ m; $N_o = 3 \times 3$ and (c) $-\cdot-d_o = 0.03$ m; $N_o = 5 \times 5$).

$f_l$. Figure 6.16 shows corresponding results for a different hole radius but with the same hole separation. This gives a similar result and confirms that the limit frequency $f_l$ depends only on the hole separation, regardless of the hole radius.

Therefore it has been shown that in order for the perforation of the vibrating plate still to have an effect in reducing the radiated sound, the distance between holes must be less than half the acoustic wavelength. If this condition is satisfied, the holes can effectively suppress part of the adjacent volume sources resulting in a reduction of the radiated sound. However when the the holes are further apart than half a wavelength, this process is no longer effective and the sound is radiated as from the solid plate.

## 6.5 Summary

A model of sound radiation from a perforated baffled plate has been proposed. The model is developed by dividing the plate and the holes into discrete monopole sources. The contribution of the sound sources to each other is assembled into an impedance matrix. The pressure due to the holes is obtained by inverting the impedance matrix.

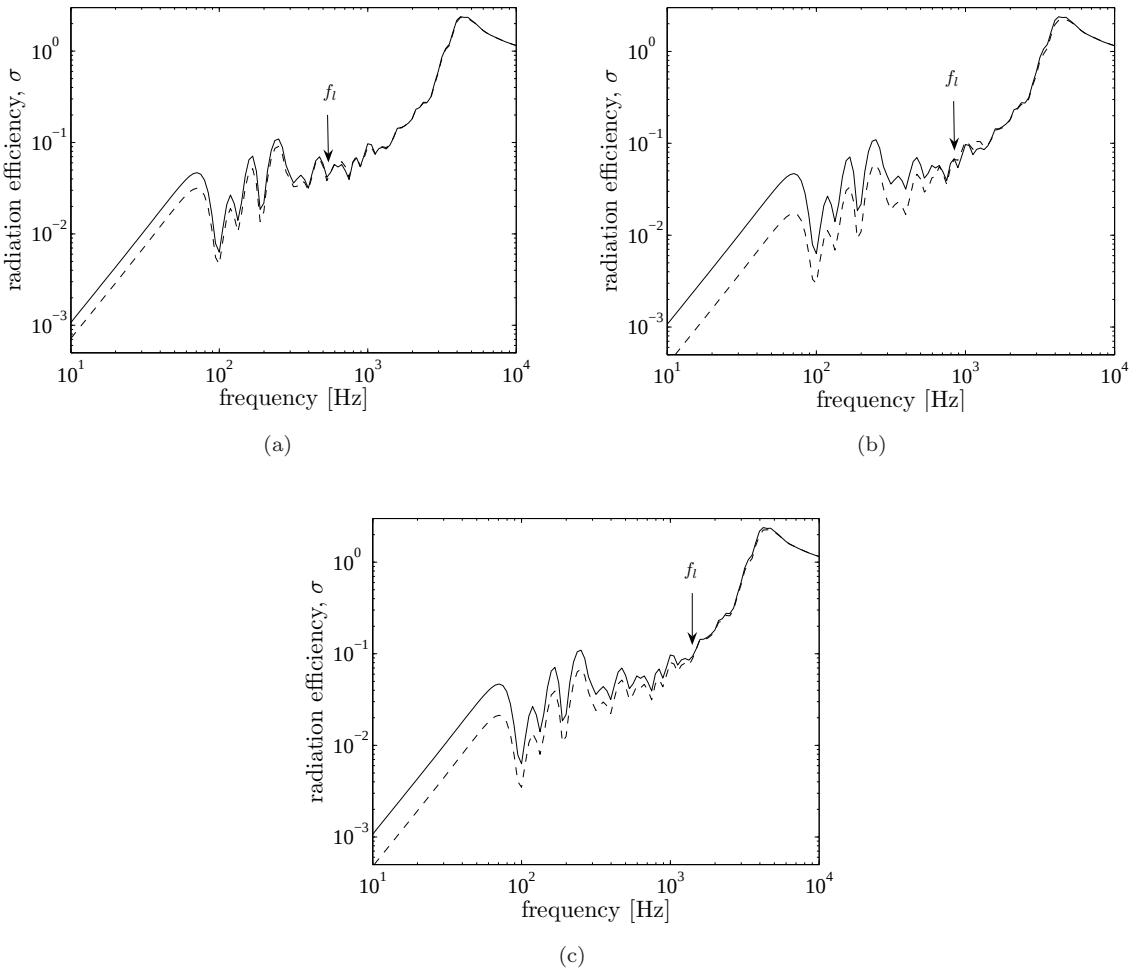


FIGURE 6.14: Radiation efficiency from bending vibration of a perforated baffled plate from discrete monopole sources showing the frequency limit of continuous impedance assumption: $0.65 \times 0.5 \times 0.003$ m, $dx = 0.01$ m, $\eta = 0.1$ (—unperforated, −−perforated; (a) $d_o = 0.05$ m: $N_o = 2 \times 2$, (b) $d_o = 0.06$ m: $N_o = 3 \times 3$ and (c) $d_o = 0.02$ m: $N_o = 5 \times 5$).

This avoids assuming a layer of continuous impedance (Section 5.1.4) as the interaction of the holes with the sound field is analysed individually. The holes are now arranged at a known separation distance. The major important finding from this model is that the holes can effectively suppress the adjacent volume sources which hence reduce the radiated sound from a plate surface, when the hole distance is less than an acoustic wavelength for a rectangular vibrating piston and less than half the acoustic wavelength for a rectangular plate in bending vibration below its critical frequency.

This frequency limit should be taken into account depending on the desired frequency range of noise reduction. Of course, the shorter the hole distance, the wider the frequency range of sound reduction. This means introducing large perforation to the

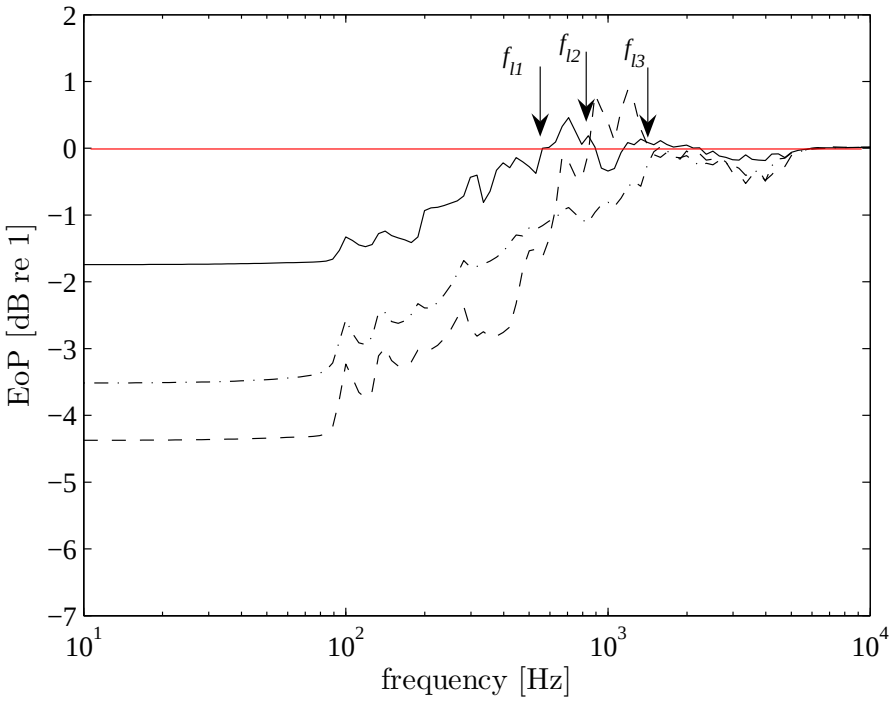


FIGURE 6.15: Effect of perforation (EoP) from bending vibration of a perforated baffled plate from discrete monopole sources showing the frequency limit of continuous impedance assumption: $0.65 \times 0.5 \times 0.003$ m, $dx = 0.01$ m, $\eta = 0.1$ ((a) —$d_o = 0.05$ m; $N_o = 2 \times 2$, (b) $--d_o = 0.06$ m; $N_o = 3 \times 3$ and (c) $- \cdot -d_o = 0.02$ m; $N_o = 5 \times 5$).

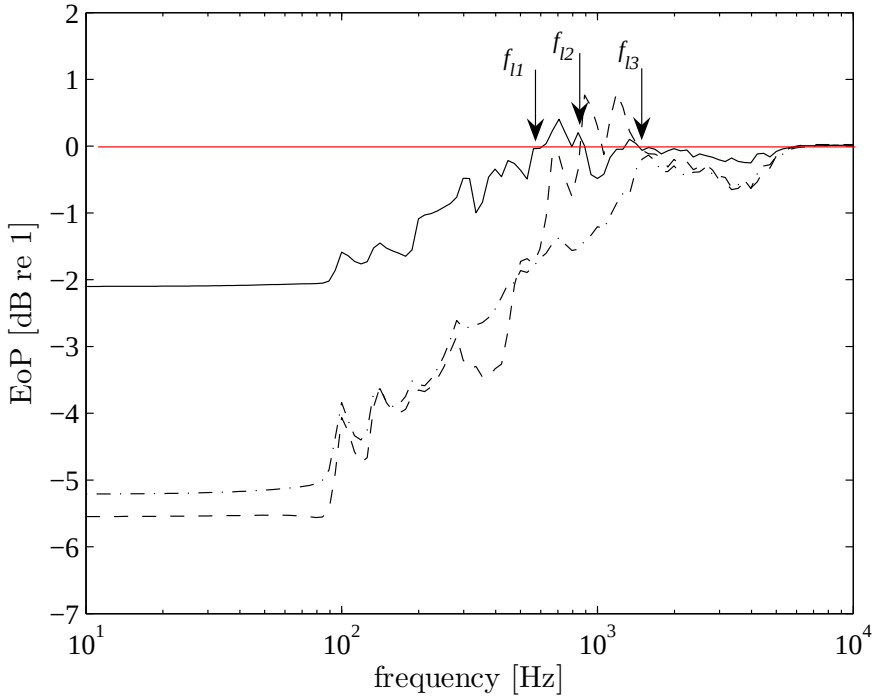


FIGURE 6.16: Effect of perforation (EoP) from bending vibration of a perforated baffled plate from discrete monopole sources showing the frequency limit of continuous impedance assumption: $0.65 \times 0.5 \times 0.003$ m, $dx = 0.01$ m, $\eta = 0.1$ ((a) —$d_o = 0.06$ m; $N_o = 2 \times 2$, (b) $--d_o = 0.075$ m; $N_o = 3 \times 3$ and (c) $- \cdot -d_o = 0.03$ m; $N_o = 5 \times 5$).

plate or increasing the number of holes. However, large perforation can reduce the stiffness of the plate which then increases the plate vibration, particularly for point force or rain on the roof excitations. This will be discussed in Chapter 7 in the context of experimental validation.

Unfortunately it was not possible to compare results from the discrete sources model with equivalent results from the previous chapter, based on a continuous impedance assumption, as the boundary conditions differ. In particular in the current chapter results are for a rigid baffle whereas the previous chapter has results for a perforated baffle and an unbaffled plate.

# Chapter 7

# Experimental Validation

In this chapter, measurements are presented of the radiation efficiency of a series of perforated plates. The experiments consist of separate measurements of the plate mobility and the radiated sound power. For each plate considered in the experiments, two types of boundary conditions are studied, namely simply supported and free-free. The simply supported boundary condition was applied as the theoretical predictions are calculated based on a simply supported plate. Meanwhile, the free-free boundary condition is chosen due to its practicality and to have additional and comparative data.

## 7.1 Plate parameters

In order to have sufficiently representative results, a series of plates was selected in which the various parameters were varied, i.e. the perforation ratio, hole size, hole density and plate thickness. All the plates are made of aluminium, with the various parameters listed in Table 7.1. The plate parameters were selected to provide a wide range of behaviours of perforated plates. The material properties assumed for the plates are listed in Table 7.2. In Figure 7.1 a diagram is given of a perforated plate, showing also a point force location $(x_o, y_o)$ in the $xy$ co-ordinates.

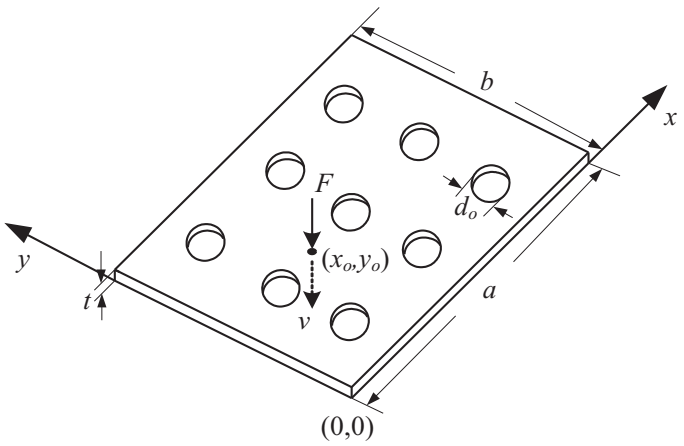


FIGURE 7.1: Co-ordinate system used for force location on the perforated plate.

TABLE 7.1: Parameters of the perforated plates used in the experiment

| No. | $d_o$ (mm) | $N_o/S$ (holes/m$^2$) | $\tau$ (%) | $a$ (mm) | $b$ (mm) | $t_p$ (mm) |
|---|---|---|---|---|---|---|
| 1 | - | - | 0 | 400 | 300 | 1.5 |
| 2 | 5 | 2500 | 5 | 400 | 300 | 1.5 |
| 3 | 8 | 2500 | 12.5 | 400 | 300 | 1.5 |
| 4 | 10 | 2500 | 20 | 400 | 300 | 1.5 |
| 5 | 15 | 2500 | 44 | 400 | 300 | 1.5 |
| 6 | - | - | 0 | 400 | 300 | 3 |
| 7 | 5 | 10000 | 20 | 400 | 300 | 3 |
| 8 | 10 | 2500 | 20 | 400 | 300 | 3 |
| 9 | 15 | 400 | 7 | 400 | 300 | 3 |
| 10 | 25 | 400 | 20 | 400 | 300 | 3 |
| 11 | - | - | 0 | 400 | 300 | 12 |
| 12 | 25 | 400 | 20 | 400 | 300 | 12 |

TABLE 7.2: Material properties assumed for the aluminium plates

| Property | Value |
|---|---|
| Young's modulus, $E$ (Nm$^{-2}$) | $7.1 \times 10^{10}$ |
| Density, $\rho_s$ (kgm$^{-3}$) | 2700 |
| Poisson's ratio, $\nu$ | 0.3 |

The plate dimensions $0.4 \times 0.3$ m were kept constant so that all plates could be supported in a single frame, constructed to represent the simply supported boundary condition. Plates 6−12 were already available from a previous undergraduate project [88] at ISVR. The configurations of plates 7, 8 and 10 were aimed to investigate the effect of the hole size on the radiated sound for constant perforation ratio. Plates 1−5 were obtained as commercial products to see the effect of the perforation area; plates 2−5 have a constant hole geometry but varying hole size. Three different thicknesses are included and should be sufficient to see the effect of the plate thickness. As the plates were very lightly damped, adhesive damping patches, made of a rubber material, were attached to parts of one side of the plates to increase their damping. The damping loss factors of the plates have been measured.

The perforated plates used in the experiment are shown in Figure 7.2. For the 1.5 mm thick plates (2−5), the hole configuration is triangular, while for the 3 mm thick plates (7−10) it is rectangular. The 12 mm perforated plate (plate 12) has the same configuration as plate 10 and is not shown in the figure.

## 7.2 Mobility measurements

Recalling Eq.(1.2)

$$\sigma = \frac{W}{\frac{1}{2}\rho c S \left\langle |v^2| \right\rangle} \tag{7.1}$$

determination of the radiation efficiency requires knowledge of the spatially averaged square surface velocity, $\langle |v^2| \rangle$, of the plate and also the radiated sound power $W$. These two unknown quantities can be normalised by the mean-square force $\overline{F^2} = \frac{1}{2}|F|^2$. Assuming that the system is linear, this normalisation allows a convenient comparison of different plates for which the input force spectrum may differ. For the normalised sound power, Eq.(7.1) then reads

$$\frac{W}{\overline{F^2}} = \rho c S \left\langle |Y_t|^2 \right\rangle \sigma \tag{7.2}$$

where $\langle |Y_t|^2 \rangle = \dfrac{\langle |v^2| \rangle}{|F^2|}$ is the spatially averaged squared transfer mobility.

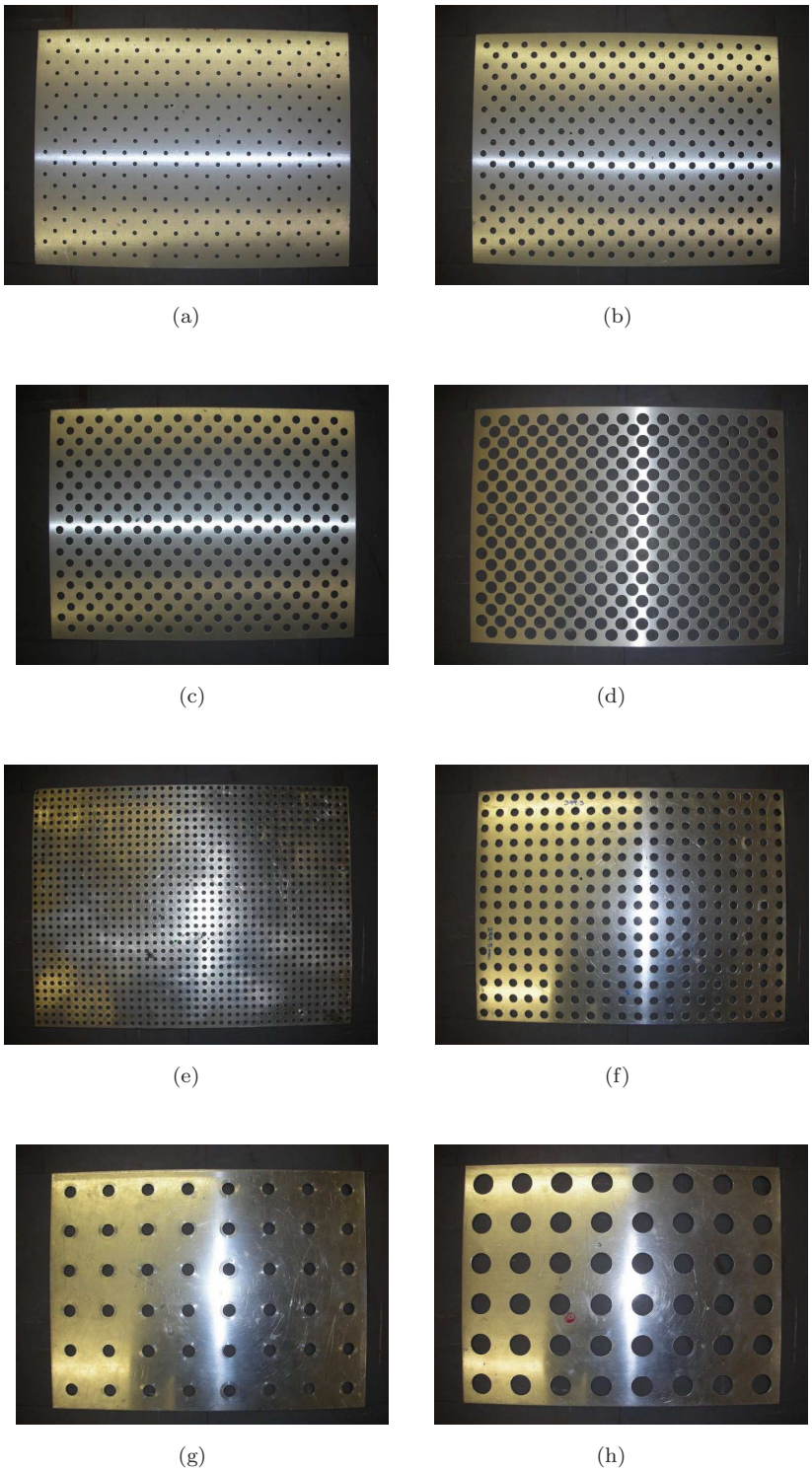

(a) (b) (c) (d) (e) (f) (g) (h)

FIGURE 7.2: Samples of perforated plates used in the experiment: (a) plate 2, (b) plate 3, (c) plate 4, (d) plate 5, (e) plate 7, (f) plate 8, (g) plate 9 and (h) plate 10.

It is important to note that, for the unbaffled plate, the sound is radiated from both sides of the plate. Therefore the surface area $S$ should equal $2ab$.

From now on, $Y_t$ and $Y_p$ are used to denote the transfer mobility and the point mobility respectively. The transfer mobility $Y_t$ is the response at one point due to an excitation at another point and the point mobility $Y_p$ is the response at the same location as that of the excitation. Comprehensive formulae for theoretical predictions of the mobility of a plate are summarised in [89].

### 7.2.1 Experimental setup and procedure

The experimental setup used for measuring the spatially averaged mobility is shown in Figure 7.3. The plate was excited by a broadband pseudo-random signal, using an LDS V201 shaker attached at a point. The point force locations on the plate $(x_o, y_o)$ are listed in Table 7.3 (see also Figure 7.1). The input force was measured by a PCB force gauge, type 208C01. A stud was tightly bolted on the transducer surface and then glued to the plate surface using an epoxy glue. To minimise the effect of moments transmitted from the shaker, a 25 mm long stinger was used to connect the force gauge and the shaker. Figure 7.4 shows the arrangement of the shaker and the force transducer attached to the plate, as used in the experiment. It also shows the damping patches attached on the plate surface. All other equipment used for the mobility measurements can be seen in Figure 7.5.

To improve the coherence of the input and output results, the excitation frequency range was divided into $0-3.2$ kHz and $3.2-6.4$ kHz. The division is aimed to concentrate the force within these frequency ranges and increase the frequency resolution. In processing the measured data, these two frequency ranges were combined using MATLAB. It was intended to include frequencies up to 10 kHz so that the measurements would cover the critical frequency of the 1.5 mm plate, i.e. 8 kHz. However it was found that the coherence was very poor for frequencies above 6.4 kHz. For the 12 mm plate, as its critical frequency is 1 kHz, only the lower frequency range of excitation (0−3.2 kHz) was used.

The plate surface velocity was measured by using a Polytec OFV 056 laser vibrometer. The vibrometer scanning head, in conjunction with the analyser through the PSV

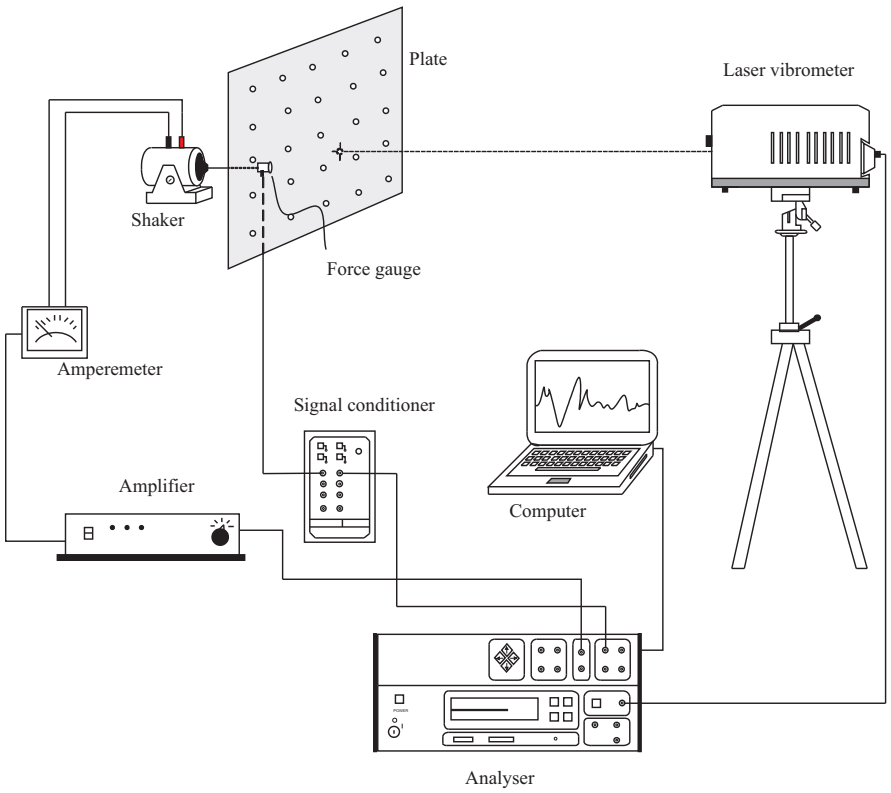


FIGURE 7.3: Experimental setup for mobility measurement using laser vibrometer.

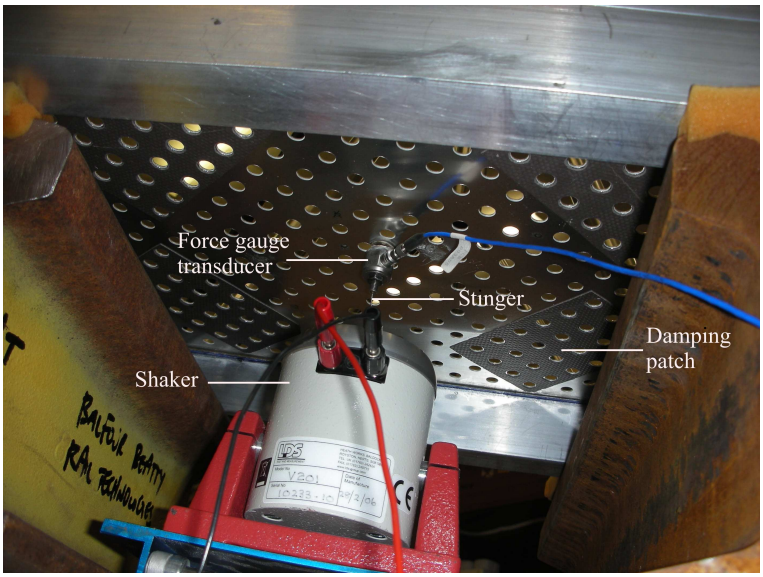


FIGURE 7.4: The shaker used to give random excitation and the force transducer attached to the plate.

TABLE 7.3: Force location on the plate

| $t_p$ (mm) | $d_o$ (mm) | $\tau$ (%) | $(x_o, y_o)$ | |
|---|---|---|---|---|
| | | | simply supported | free-free |
| 1.5 | 5 | 5 | $(0.47a, 0.37b)$ | $(0.32a, 0.46b)$ |
| | 8 | 12 | $(0.68a, 0.57b)$ | $(0.68a, 0.56b)$ |
| | 10 | 19 | $(0.61a, 0.38b)$ | $(0.71a, 0.52b)$ |
| | 15 | 44 | $(0.40a, 0.40b)$ | $(0.35a, 0.38b)$ |
| | - | 0 | $(0.60a, 0.48b)$ | $(0.61a, 0.47b)$ |
| 3 | 5 | 20 | $(0.50a, 0.40b)$ | $(0.60a, 0.60b)$ |
| | 10 | 20 | $(0.35a, 0.38b)$ | $(0.65a, 0.45b)$ |
| | 15 | 7 | $(0.33a, 0.62b)$ | $(0.63a, 0.67b)$ |
| | 25 | 20 | $(0.38a, 0.37b)$ | $(0.38a, 0.38b)$ |
| | - | 0 | $(0.38a, 0.57b)$ | $(0.38a, 0.57b)$ |
| 12 | 25 | 20 | | $(0.60a, 0.40b)$ |
| | - | 0 | | $(0.50a, 0.30b)$ |

software, was used to measure at 81 points on the plate surface to give a reliable surface average. It was ensured that the measurement points avoided the holes but also varied in location, e.g. at the plate corners and edges, between two holes, at the hole edge, etc. For free-free conditions the plate was hung vertically and the laser vibrometer positioned horizontally as indicated in Figure 7.3. For simply supported conditions the arrangement was as shown in Figure 7.5 with the laser pointing downwards. In each case, the scanning head was positioned at a distance of about 1.5 m perpendicular ($90^o$) to the plate surface. The scanning head then scanned each measurement point performing 30 FFT averages for each point. The results (mobility, coherence, etc) were calculated using the Polytec software. For all results it was ensured that the signal-to-noise ratio was sufficient (at least 10 dB).

The responses at all 81 measurement points were averaged to give the mean-square mobility of the plate $\langle |Y_t|^2 \rangle$. Using the laser vibrometer, the focus of the laser beam to the plate surface is critical to obtain a good coherence of the data. Therefore, in the measurement, some points resulted in poor coherence due to instability of the beam focus, particularly when the plate was vibrating. Roughly 20% of points were found to have poor coherence with values less than 0.5. These points were omitted from the calculation of spatially averaged mobility to ensure good measurement data. The remaining 80% of points still represent the spatial average of the plate surface vibration.

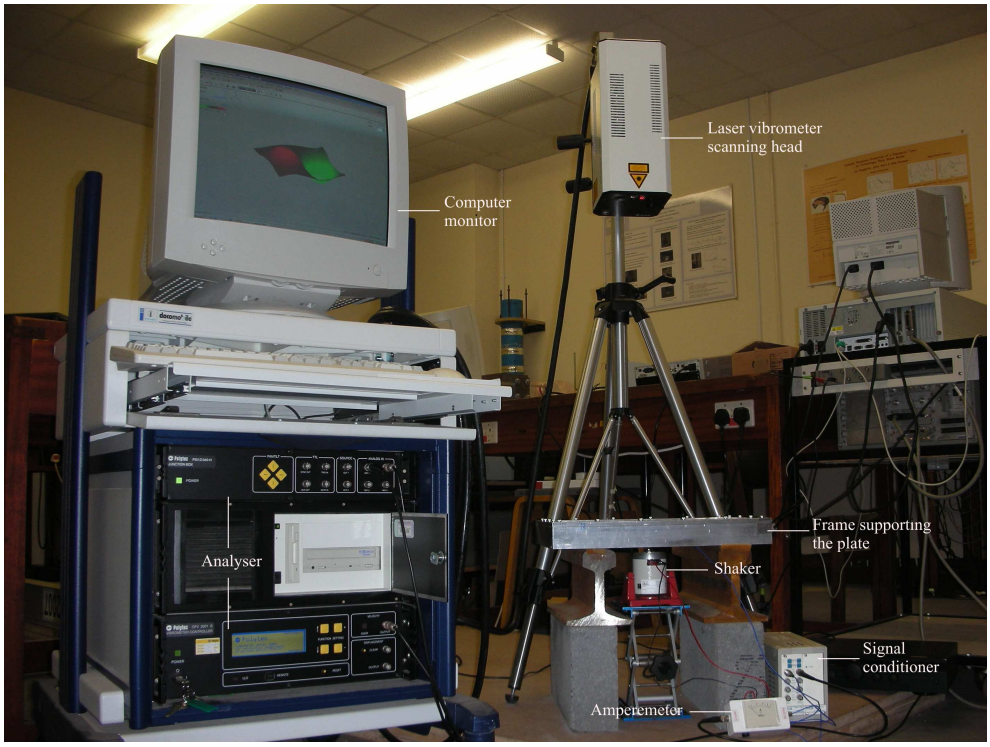


FIGURE 7.5: Equipment used for mobility measurement.

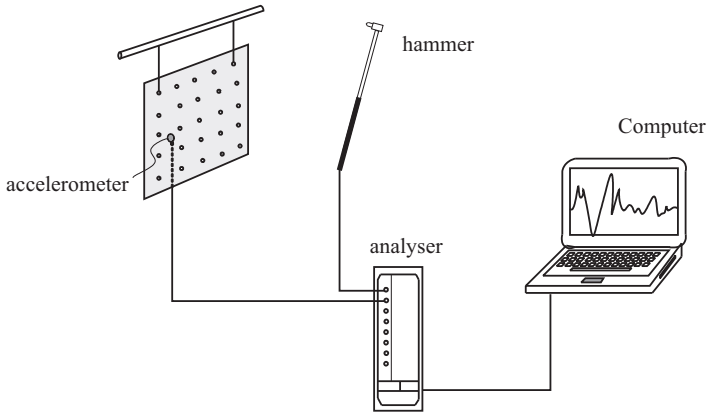


FIGURE 7.6: Experimental setup for mobility measurement using impact hammer.

For the 1.5 mm thick plates, mass loading occurred due to the force gauge used in the shaker excitation (as will be shown, for the thicker plates this had much less effect). Therefore measurements of the point mobility were also taken using impact excitation, as shown in Figure 7.6. A PCB 086D80 hammer was used to strike the plate at the same location as used with the shaker. At the same position on the other side of the plate, a PCB accelerometer was attached to the plate to measure the plate acceleration. The mobility and the coherence were then calculated using the analyser software (the Data Physics DP240 analyser was used).

### 7.2.2 Simply supported boundary condition

For an ideal simply supported boundary condition, the displacement is blocked at the plate edges but the rotation is free. Thus the realisation of such a boundary condition in practice is not easy. However, several attempts have been made in previous measurements involving this type of boundary condition [90, 91, 92]. Similar to the method used in [91], a 460 × 362 mm frame was constructed to support the plate. As shown in Figure 7.7, the frame was made with a very stiff aluminium section having a width of 31 mm. The frame height of 44 mm was designed to be greater than the width to minimise any transverse vibration induced by the vibrating plate. Furthermore, the mass was also large to prevent the frame moving together with the plate, particularly at low frequency (rigid body modes). The frame was then mounted on a rigid stand, using 1 cm thick pieces of soft foam between the frame corners and the stand to isolate the frame from the stand.

Along the plate perimeter, a 0.2 mm thick aluminium shim was glued in part under the plate and the other part was clamped by 3 mm thick aluminium beams using screws along the plate perimeter. A small gap was left between the plate and the frame to allow space for edge rotation. The frame used in the experiments is shown in Figure 7.8.

#### 7.2.2.1 Mobility results for 1.5 mm thick plates

Figure 7.9 plots the point mobility of various 1.5 mm thick plates, compared with the theoretical predictions for a solid plate, (see also [89]). The mobility formula for the simply supported plate is given in Appendix B. As already mentioned, the point mobilities were measured using an impact hammer. The results show that, in general, the measured mobilities have a good agreement with the predictions, even for the first four modes. This confirms that the realisation of the simply supported boundary condition has been very well achieved. By way of illustration, the first two mode shapes obtained from the Polytec software are also shown in Figure 7.10 for the 1.5 mm thick plate having 5 mm hole diameter.

The perforation of the plate also has an effect on the effective plate material properties, namely the Young's modulus ($E$), Poisson's ratio ($\nu$) and density ($\rho_p$) and hence

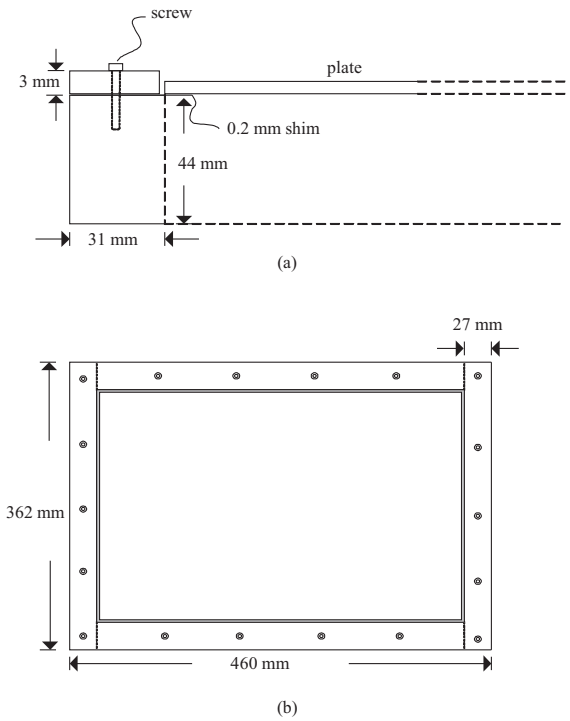


FIGURE 7.7: Diagram of frame for simply supported boundary condition: (a) side view and (b) top view.

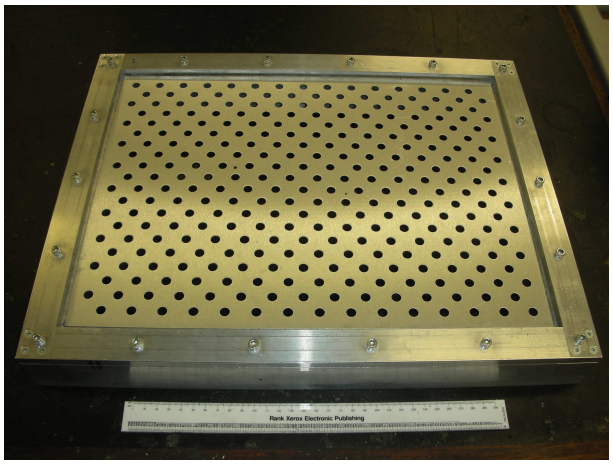

FIGURE 7.8: Specially constructed frame used for simply supported boundary condition.

changes the plate bending stiffness ($B$) and resonance frequencies as discussed in Section 5.5. For the same perforation, the effect becomes greater for thinner and lighter plates. As can be seen in Figure 7.9(e) for the 1.5 mm plate having the greatest perforation among the plate samples ($\tau = 44\%$), the measured mobility level is roughly 5 dB higher than the solid plate above 1 kHz.

Before presenting the mobilities measured using shaker excitation, Figure 7.11 shows examples of the coherence from one measurement point for the perforated 1.5 mm and

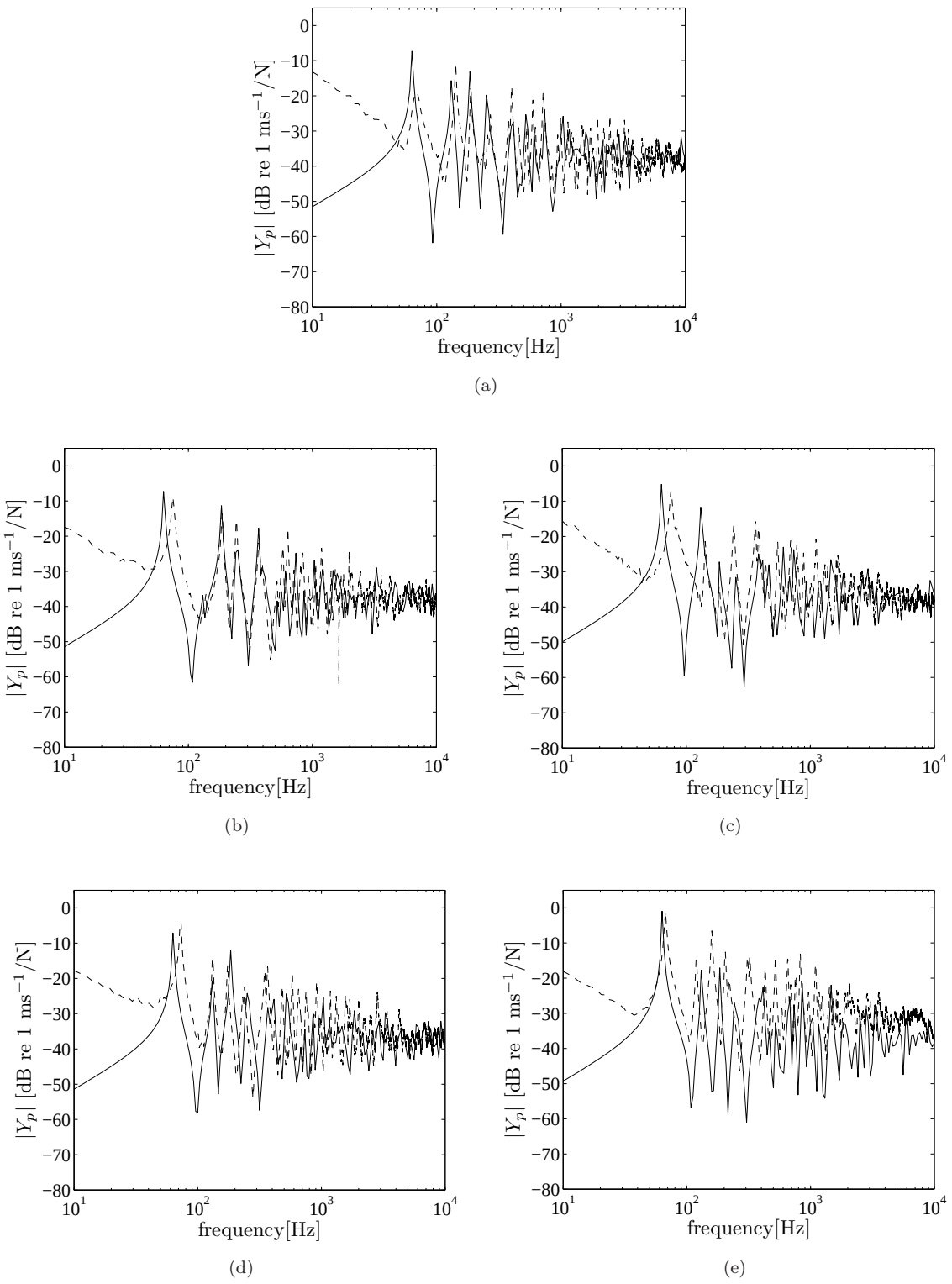


FIGURE 7.9: Comparison of measured point mobility and the theoretical prediction for 1.5 mm plates ($20\log_{10}|Y_p|$): −−experiment, —theoretical; (a) unperforated, (b) $d_o = 5$ mm, $\tau = 5\%$, (c) $d_o = 8$ mm, $\tau = 12\%$, (d) $d_o = 10$ mm, $\tau = 19\%$ and (e) $d_o = 15$ mm, $\tau = 44\%$.

(a) (b)

FIGURE 7.10: Diagram from scanning vibrometer software. Mode shape of simply supported plates from the experiment: (a) mode (1,1) and (b) mode (2,1).

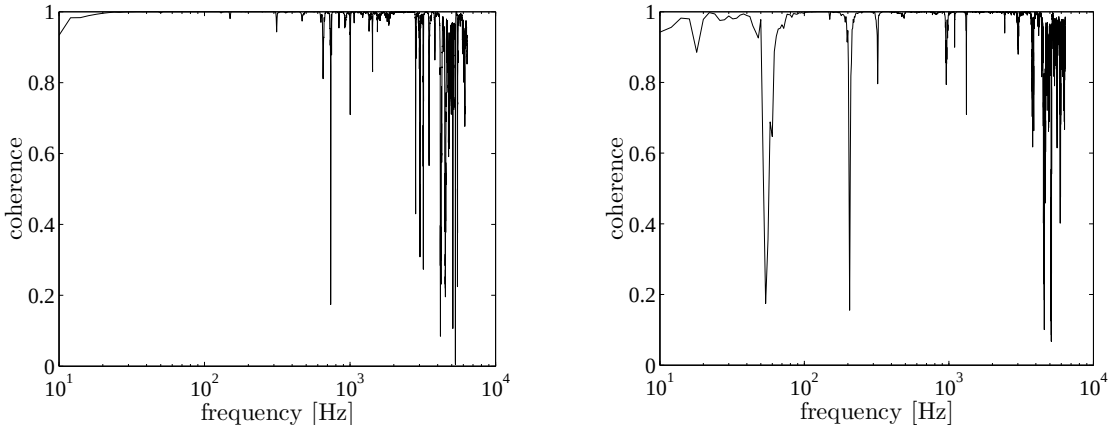


(a) (b)

FIGURE 7.11: Typical coherence for simply supported plates: (a) 1.5 mm and (b) 3 mm.

3 mm simply supported plates measured using shaker excitation. In an average sense, these are also typical of the coherence for all other plates including the solid plates. For the 1.5 mm plate, it is poor below 30 Hz but up to 4 kHz the coherence can be seen to be approximately unity apart from dips at anti resonances. Above 4 kHz, the coherence has a magnitude around 0.9. Thus for the whole frequency range, it can be judged to be acceptable. For the 3 mm plate, it can be seen that the coherence roughly has the same quality as that of the 1.5 mm plates. However, for the plate with 5 mm hole diameter, the coherence was very poor below 200 Hz where the coherence was less than 0.5. This was because this plate was not quite flat in one corner, so that the plate edge was not well attached to the shim on the frame. Its coherence is not presented here.

Figure 7.12 compares the point mobilities of the 1.5 mm plates obtained by using the

shaker and the force gauge transducer with the results obtained by impact excitation using the instrumented hammer. It is clear that the results obtained using the shaker roll off above 1 kHz, which indicates the effect of mass loading over that frequency range. The phase also tends to $-90^o$ above 1 kHz corresponding to a purely imaginary mobility (mass-like), i.e. $Y = -j/m\omega$. By comparing the mobilities from the shaker and impact hammer, it can be seen that the mass loading has started to take effect from around 600 Hz.

In order determine the loading effect of the transducer mass $m_t$ over the frequency range, the transducer mobility, i.e. $1/(jm_t\omega)$ is plotted together with the point mobility $Y_p$ of the plate. The active transducer mass itself was obtained by measuring the transfer function of its acceleration $a_t$ and the excitation force $F$ $(1/m_t = a_t/F)$. This was done by pointing the laser beam at the transducer surface (stud) without attaching the transducer to the plate. It was found that the active mass is 9.8 grams, see Figure 7.13(a), compared with a total mass of 25.5 grams. As the mean magnitude of the point mobility of a finite plate is equivalent to the point mobility of an infinite plate, given by $1/8\sqrt{B\rho_p t_p}$ [4], this can then be used to represent the point mobility of the finite plate. The graph is plotted in Figure 7.13(b).

For 1.5 mm plates, it can be confirmed again from Figure 7.13(b) that the mass loading effect ideally starts from around 1 kHz. Above the intersection, as the frequency increases, the impedance of the force transducer $Z = 1/Y$ seen by the shaker becomes greater than that of the plate. Hence the shaker no longer gives sufficient force to the plate. The effect starts below the intersection frequency as seen in the combined mobility curves.

Therefore the measured transfer mobility $Y_t$ for the 1.5 mm plates obtained with the shaker and the force transducer has to be corrected to eliminate the effect of mass loading. The correction factor can be derived using the point mobility measured using the saker $Y_{\text{shaker}}$ and that obtained using impact excitation $Y_{\text{impact}}$. The correction factor $C_Y$ for each frequency $\omega$ can be written as

$$C_Y(\omega) = \left| \frac{Y_{\text{impact}}(\omega)}{Y_{\text{shaker}}(\omega)} \right| \tag{7.3}$$

This correction factor represents the ratio of the total force to the force acting on the

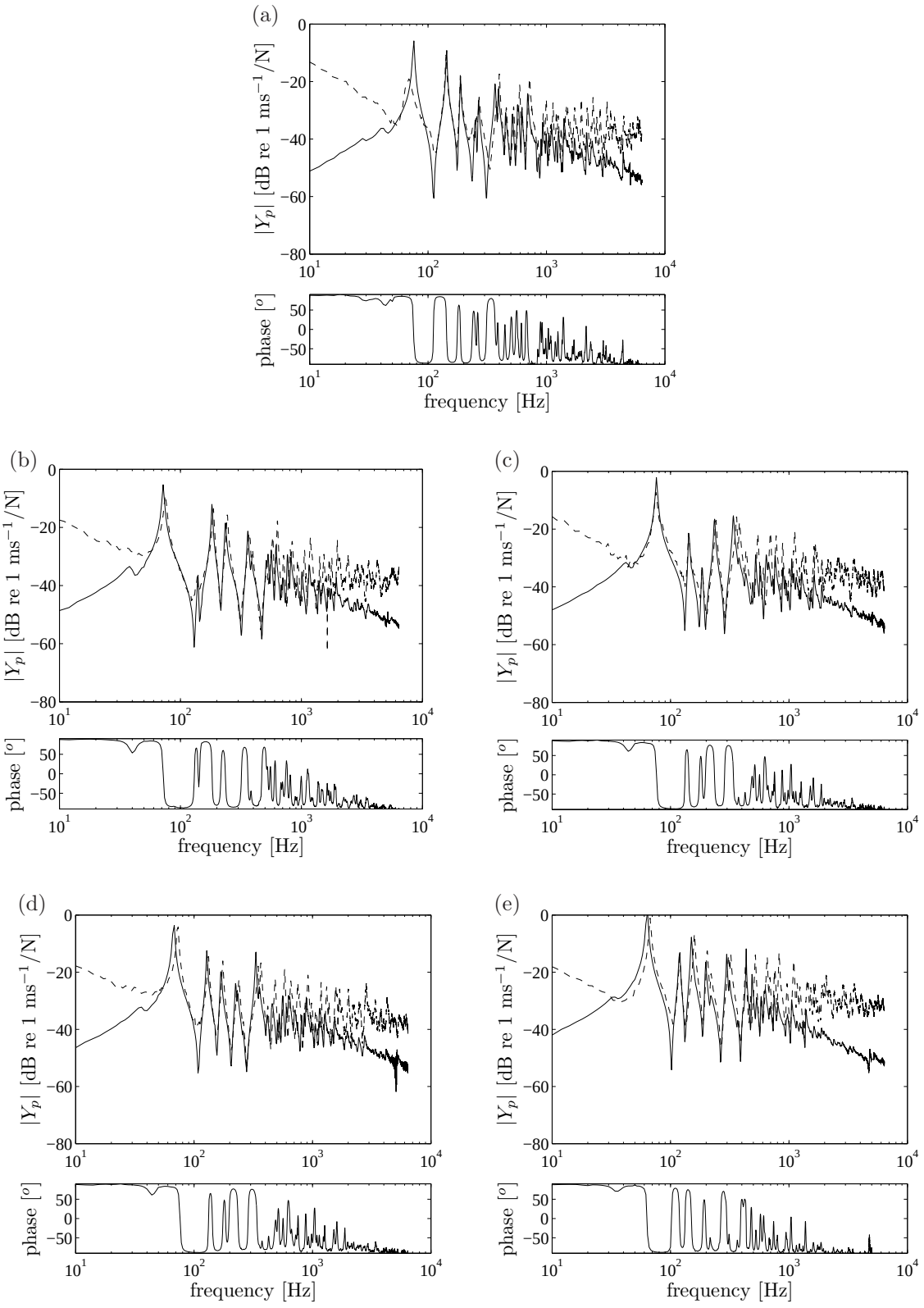


FIGURE 7.12: Measured point mobility and phase of 1.5 mm simply supported perforated plates ($20\log_{10}|Y_p|$): −−impact hammer, —shaker and force gauge transducer; (a) unperforated, (b) $d_o = 5$ mm, $\tau = 5\%$, (c) $d_o = 8$ mm, $\tau = 12\%$, (d) $d_o = 10$ mm, $\tau = 19\%$ and (e) $d_o = 15$ mm, $\tau = 44\%$.

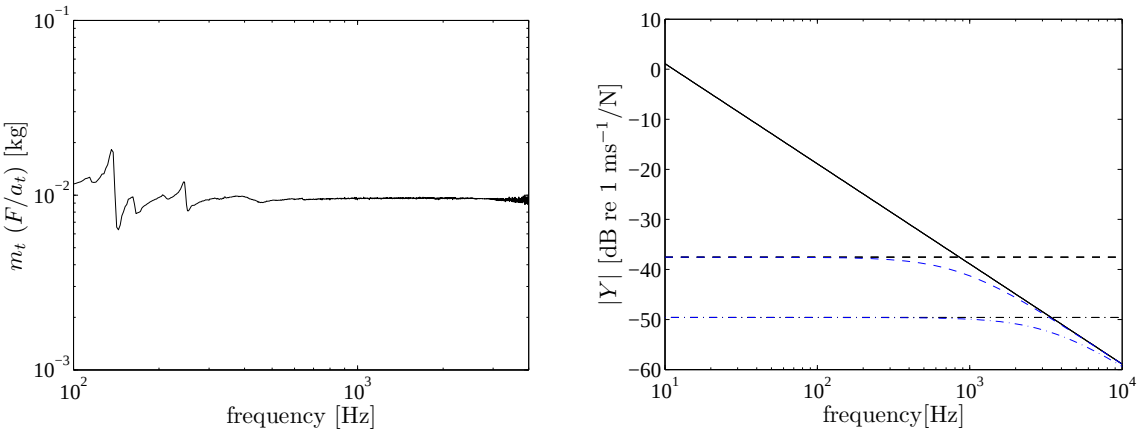


FIGURE 7.13: (a) Measured force gauge transducer mass and (b) Comparison of transducer mass mobility (—) with infinite plate mobilities of 1.5 mm (− −) and 3 mm (− · −) plates and combination between mobility of infinite plate and mass transducer (blue line) ($20\log_{10}|Y_i|$).

plate alone. Thus the corrected transfer mobility $Y_{ct}$ can be obtained by multiplying $Y_t$ by $C_Y$ for each response point, the excitation point being fixed. Since the phase of the transfer mobility is not required, it can be written as

$$|Y_{ct}| = |Y_t| \times C_Y \tag{7.4}$$

Based on the measurement results, the correction is applied from 600 Hz. Below 600 Hz, the correction is found to be unreliable as it is affected by the small shifting of individual resonances. However, from Figure 7.13(b) it is seen that no significant correction should be required below 600 Hz. The corrected spatially averaged squared-transfer mobilities $\langle|Y_{ct}|^2\rangle$ are shown in Figure 7.14 in $\frac{1}{3}$ octave bands along with the uncorrected results. It can be seen that the squared transfer mobilities can be reduced by up to roughly 15 dB at 5 kHz due to the mass loading effect.

#### 7.2.2.2 Mobility results for 3 mm thick plates

Figure 7.15 shows the measured point mobility for 3 mm plates along with the theoretical predictions for a simply supported solid plate. The results show good agreement with the predictions, although some resonance frequencies are found to be slightly shifted, as was the case for the 1.5 mm plates. A rigid body mode also appears at

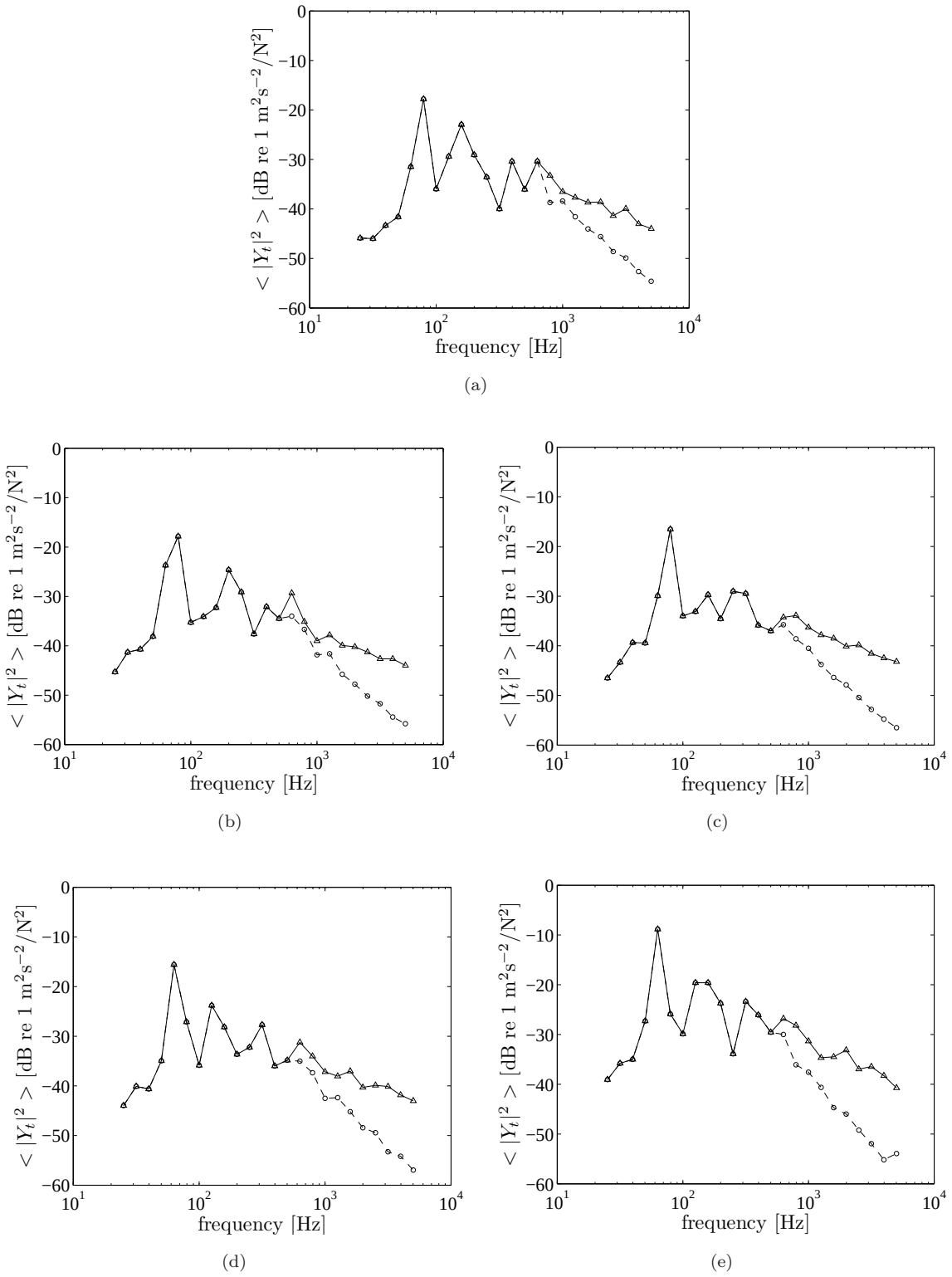


FIGURE 7.14: Experimental results of spatially averaged squared transfer mobilities of 1.5 mm simply supported perforated plates ($10 \log_{10} \langle |Y_t|^2 \rangle$): -o- before correction, -$\triangle$- corrected; (a) unperforated, (b) $d_o = 5$ mm, $\tau = 5\%$, (c) $d_o = 8$ mm, $\tau = 12\%$, (d) $d_o = 10$ mm, $\tau = 19\%$ and (e) $d_o = 15$ mm, $\tau = 44\%$.

very low frequency around 20 Hz. At this mode, the plate and the frame are coupled and hence move together in phase with each other. Noise from electrical interference is also found at 50 Hz as shown in Figure 7.15(b).

The point mobility for these 3 mm plates was measured using broadband noise excitation (using shaker and force transducer). From Figure 7.15, it is difficult to observe the mass loading effect as the results show the same average level of mobility between the measured data and the prediction at high frequencies. However, the phase shows a slight tendency to be biased towards $-90^o$ above 2.5 kHz. Therefore the mass loading correction has been applied from this frequency, seen from Figure 7.13(b).

The point mobility data from the hammer excitation is not available for the 3 mm plates. However, the mass loading correction can also be made by subtracting the mass loading effect from the measured point mobility data. Consider Figure 7.16 where a shaker gives a harmonic force excitation $F$ through a stinger connected to a force transducer attached to a plate. Assuming that the plate has an impedance $Z_p$, the net force on the transducer with mass $m_t$ can be given by

$$F - Z_p v_p = Z_{m_t} v_t = j\omega m_t v_t \tag{7.5}$$

The combined system (transducer and plate) 'seen through' the force is

$$Z_{m_t+p} = F/v \tag{7.6}$$

As the transducer is rigidly attached to the plate, both have identical velocity ($v_p = v_t$). Therefore

$$Z_{m_t+p} - Z_p = j\omega m_t \tag{7.7}$$

In terms of mobility ($Y = 1/Z$), Eq.(7.7) can written as

$$\frac{1}{Y_{m_t+p}} - \frac{1}{Y_p} = j\omega m_t \tag{7.8}$$

where $Y_{m_t+p}$ is the measured mobility having the mass loading effect and $Y_p$ the desired mobility. Therefore the corrected mobility can be obtained by

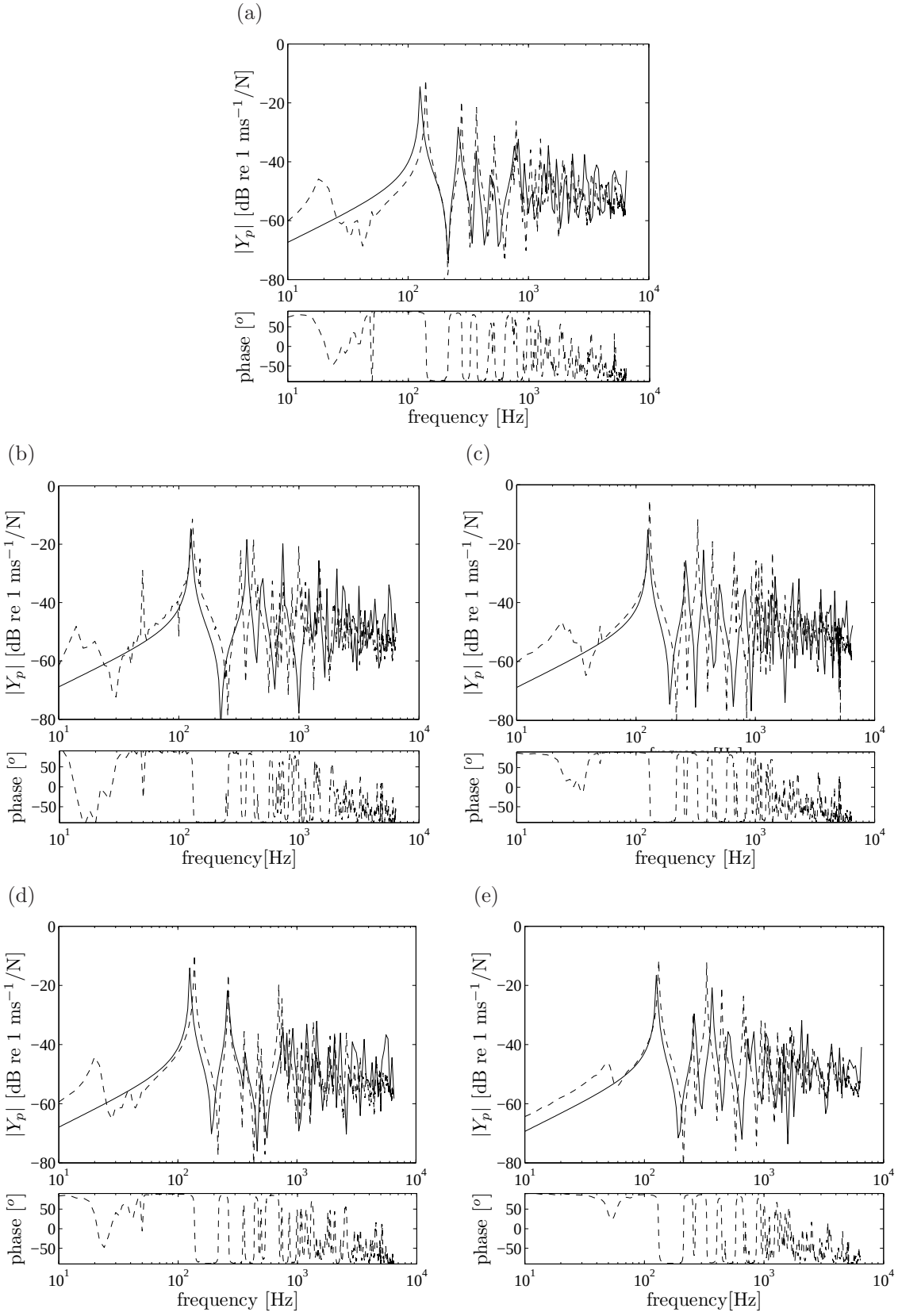


FIGURE 7.15: Comparison of measured point mobility and the theoretical prediction and phase for 3 mm simply supported plates ($20\log_{10}|Y_p|$): −−experiment, —theoretical; (a) unperforated, (b) $d_o = 5$ mm, $\tau = 20\%$, (c) $d_o = 10$ mm, $\tau = 20\%$, (d) $d_o = 15$ mm, $\tau = 7\%$ and (e) $d_o = 25$ mm, $\tau = 20\%$.

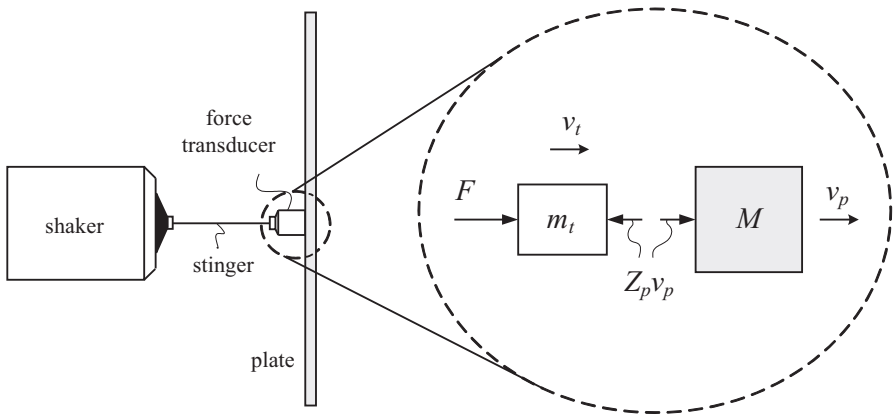


FIGURE 7.16: Digram of a dynamic force from a shaker acting between a transducer and a plate.

$$Y_p = \frac{1}{\dfrac{1}{Y_{m_t+p}} - j\omega m_t} \tag{7.9}$$

This correction can be applied provided that $\omega m_t$ is not much greater than $1/Y_{m_t+p}$. Eq.(7.9) is applied to the measured point mobility $Y_p$ for the 3 mm thick plates. The ratio between the corrected mobility $Y_p$ and the measured mobility $Y_{p+m_t}$ will be the correction factor $C_Y$ to the transfer mobility as in Eq.7.3, i.e.

$$C_Y(\omega) = \left| \frac{Y_p}{Y_{m_t+p}} \right| = \frac{1}{|1 - j\omega m_t Y_{m_t+p}|} \tag{7.10}$$

Figure 7.17 shows the measured and the corrected point mobilities in $\frac{1}{3}$ octave bands. The results show a correction by up to 5 dB from 2.5 kHz to 5 kHz. The spatially averaged squared transfer mobility for the 3 mm plates is shown in Figure 7.18.

For the 12 mm thick plates, it was difficult to mount them on the frame due to their heavy weight. Hence they were only measured under the free-free boundary conditions.

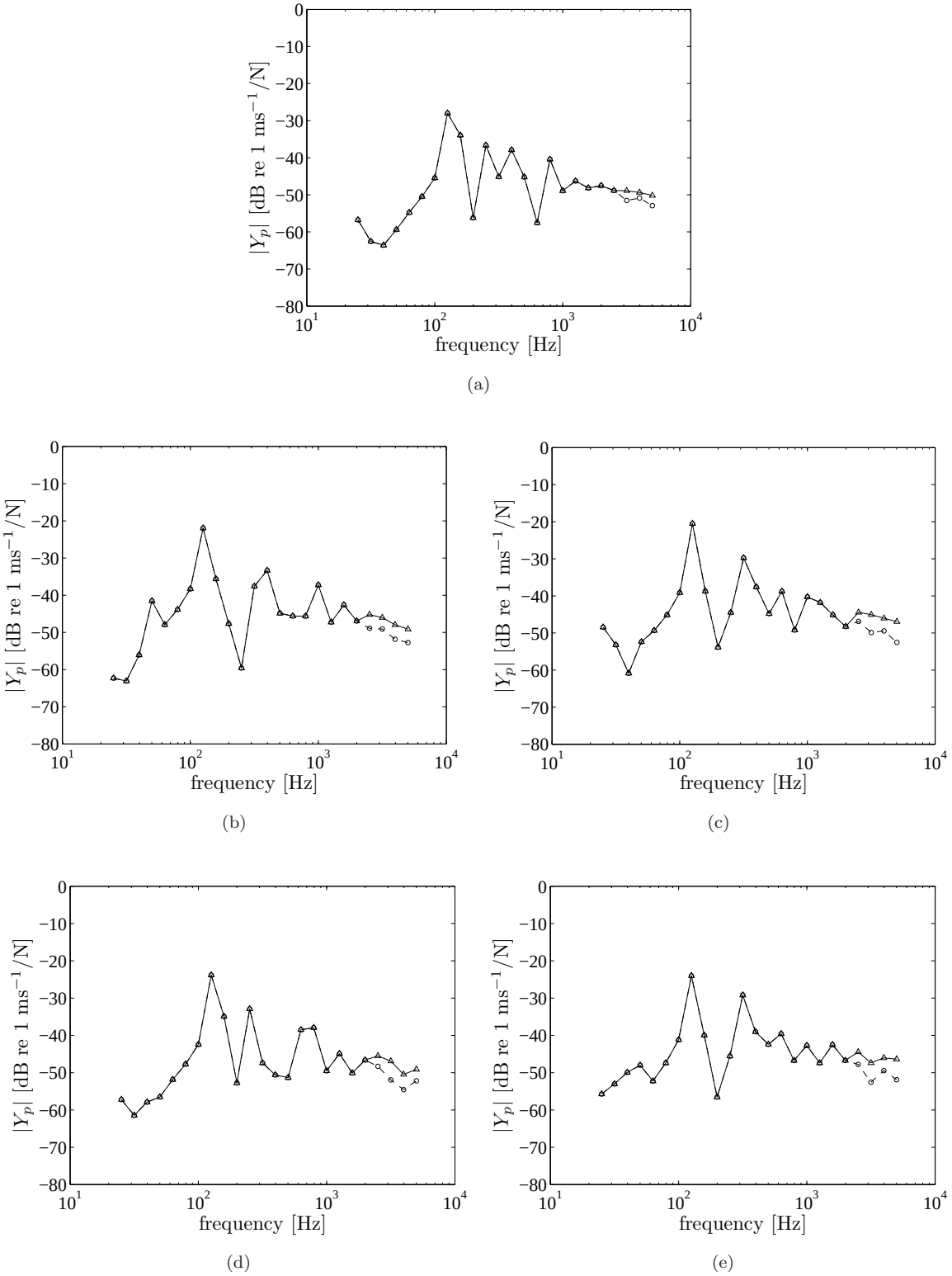


FIGURE 7.17: Experimental results of point mobility of 3 mm simply supported perforated plates ($20\log_{10}|Y_p|$) in $\frac{1}{3}$ octave bands: (a) unperforated, (b) $d_o = 5$ mm, $\tau = 20\%$, (c) $d_o = 10$ mm, $\tau = 20\%$, (d) $d_o = 15$ mm, $\tau = 7\%$, (e) $d_o = 25$ mm, $\tau = 20\%$ (-○-before correction, -△-corrected).

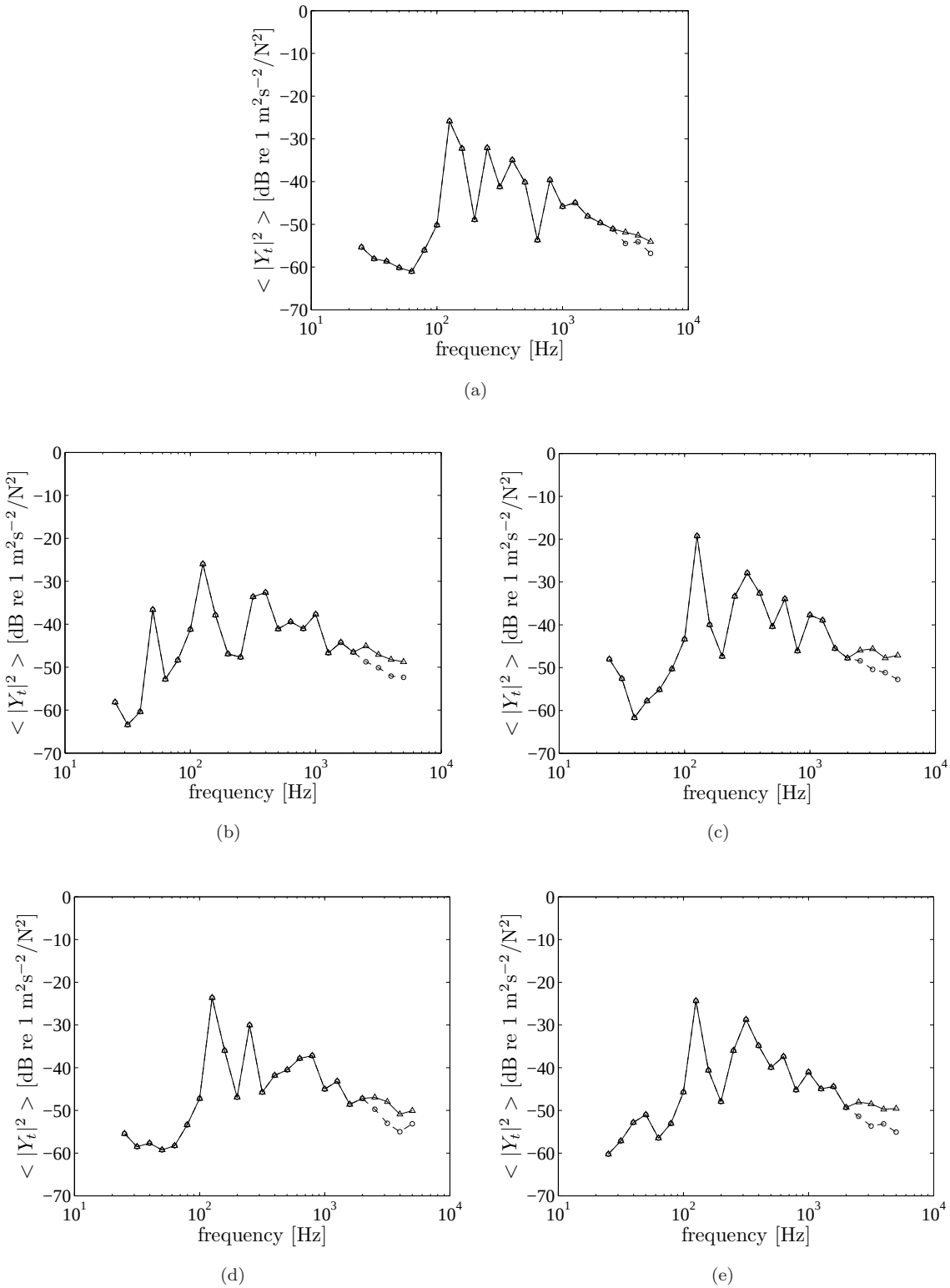


FIGURE 7.18: Experimental results of spatially averaged squared transfer mobility of 3 mm simply supported perforated plates ($10 \log_{10} \langle |Y_t|^2 \rangle$) in $\frac{1}{3}$ octave bands: (a) unperforated, (b) $d_o = 5$ mm, $\tau = 20\%$, (c) $d_o = 10$ mm, $\tau = 20\%$, (d) $d_o = 15$ mm, $\tau = 7\%$ and (e) $d_o = 25$ mm, $\tau = 20\%$ (-○-before correction, -△-corrected).

#### 7.2.2.3 Effect of perforation on mobility

The effect of perforation on the material dynamic properties of a plate has been discussed in Section 5.5. The perforation introduced to a plate reduces its bending stiffness $B$ and density $\rho_p$. It has also been shown that these effects, as a result, shift the resonance frequencies to a lower frequency. Since the mobility depends on the resonance frequencies and the plate density (mass), this section will discuss the effect of perforation on the plate mobility.

TABLE 7.4: Effective density and bending stiffness of perforated 1.5 mm and 3 mm simply supported plates.

| Dimensions (m) | $d_o$ (m) | $b_x$ (m) | $b_y$ (m) | $\tau$ (%) | $\rho_p^*/\rho_p$ | $B^*/B$ |
|---|---|---|---|---|---|---|
| $0.4 \times 0.3 \times 0.0015$ | 0.005 | 0.026 | 0.028 | 5 | 0.95 | 0.8959 |
| | 0.008 | 0.026 | 0.028 | 12 | 0.88 | 0.7579 |
| | 0.010 | 0.026 | 0.028 | 19 | 0.81 | 0.8020 |
| | 0.015 | 0.026 | 0.028 | 44 | 0.56 | 0.3685 |
| $0.4 \times 0.3 \times 0.003$ | 0.005 | 0.010 | 0.010 | 20 | 0.80 | 0.5638 |
| | 0.010 | 0.020 | 0.020 | 20 | 0.80 | 0.5638 |
| | 0.015 | 0.050 | 0.050 | 7 | 0.93 | 0.8020 |
| | 0.025 | 0.050 | 0.050 | 20 | 0.80 | 0.5638 |

Table 7.4 lists all the parameters for the plate samples as in Table 7.1 together with effective plate density $\rho_p^*$ and bending stiffness $B^*$. The hole arrays of all 1.5 mm plates are triangular and 3 mm plates are rectangular (see Figure 7.2). For 3 mm plates, the hole distances ($b_x$ and $b_y$) are similar for each plate, but the hole diameter varies. The effective plate density $\rho_p^*$ is calculated using Eq.(5.57) and Eq.(5.58). The effective bending stiffness $B^*$ can be calculated by $(f^*/f)^2(1-\tau)$, where $f^*/f$ is predicted using Eq.(5.60) for a common forcing point position. The results show that the density and the bending stiffness are reduced as the perforation ratio is increased.

Figure 7.19 shows the predicted plate point mobility $Y_p$ for the 1.5 mm simply supported plates based on the corrected bending stiffness and density. The results show that the level of the mobility increases as the perforation ratio increases as well as the natural frequencies being shifted to lower frequencies. Note that the average point mobility at high frequency is given by $1/8\sqrt{B\rho_p t_p}$. Hence as $\rho_p$ and $B$ are reduced due to perforation, the mobility increases. Based on an infinite plate, the average increase

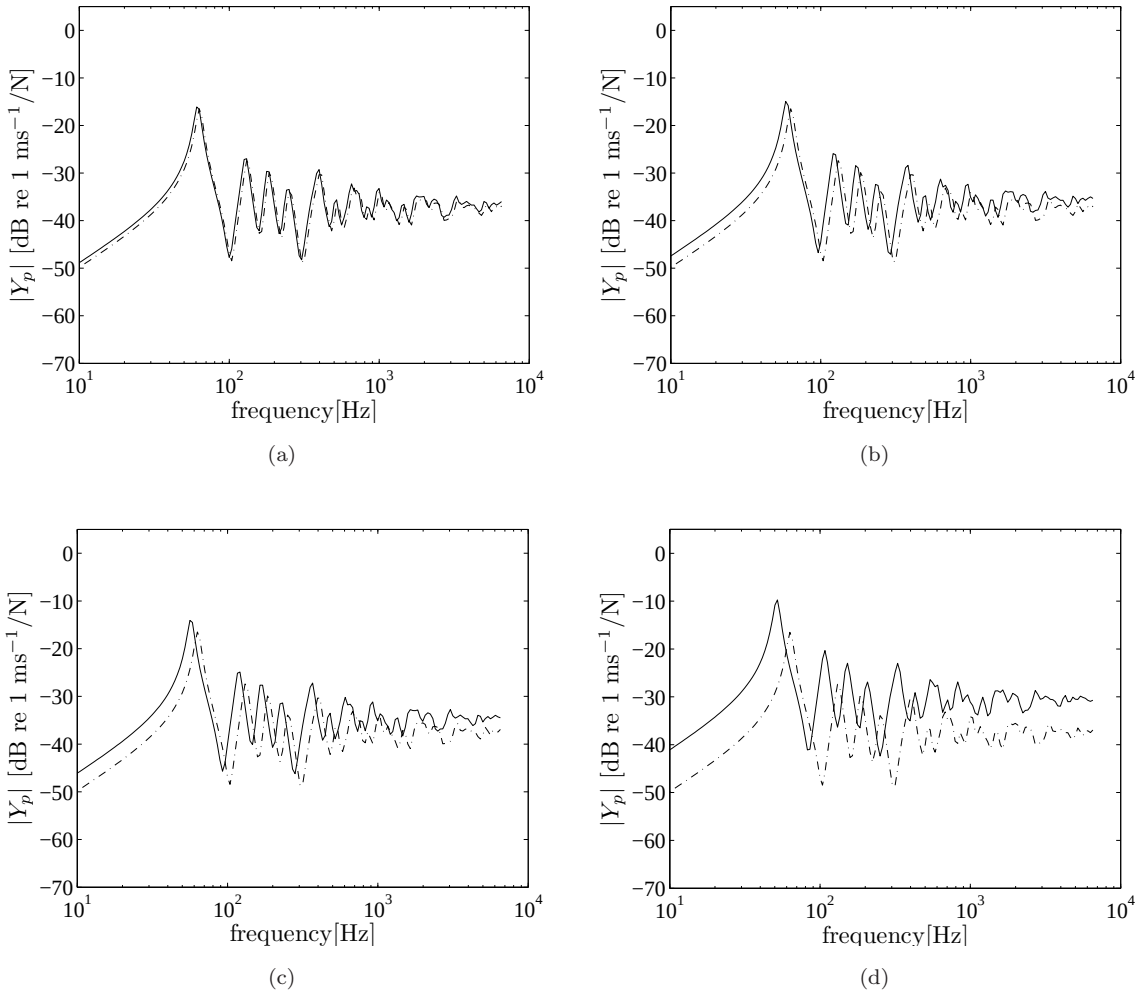


FIGURE 7.19: Calculated point mobility of simply supported perforated plates ($20\log_{10}|Y_p|$): —corrected bending stiffness due to perforation, $-\cdot-$solid plate; $t_p = 1.5$ mm, $b_x = 26$ mm, $b_y = 28$ mm: (a) $d_o = 5$ mm, $\tau = 5\%$, (b) $d_o = 8$ mm, $\tau = 12\%$, (c) $d_o = 10$ mm, $\tau = 19\%$, (d) $d_o = 15$ mm, $\tau = 44\%$ (forcing point at $(0.375a, 0.5b)$, $\eta = 0.1$).

of mobility (in dB) due to perforation can be defined by

$$\Delta Y = 20\log_{10}\sqrt{\frac{B^*}{B}\frac{\rho_p^*}{\rho_p}} \tag{7.11}$$

Figure 7.19(d) for 44% perforation ratio shows a mobility around almost 7 dB higher than that of the solid plate. Similar phenomena were also seen in the experimental results in Figure 7.9(e) when comparing the measured point mobility (without mass loading) and the theory.

The results for the 3 mm thick plate are given in Figure 7.20. These also show similar

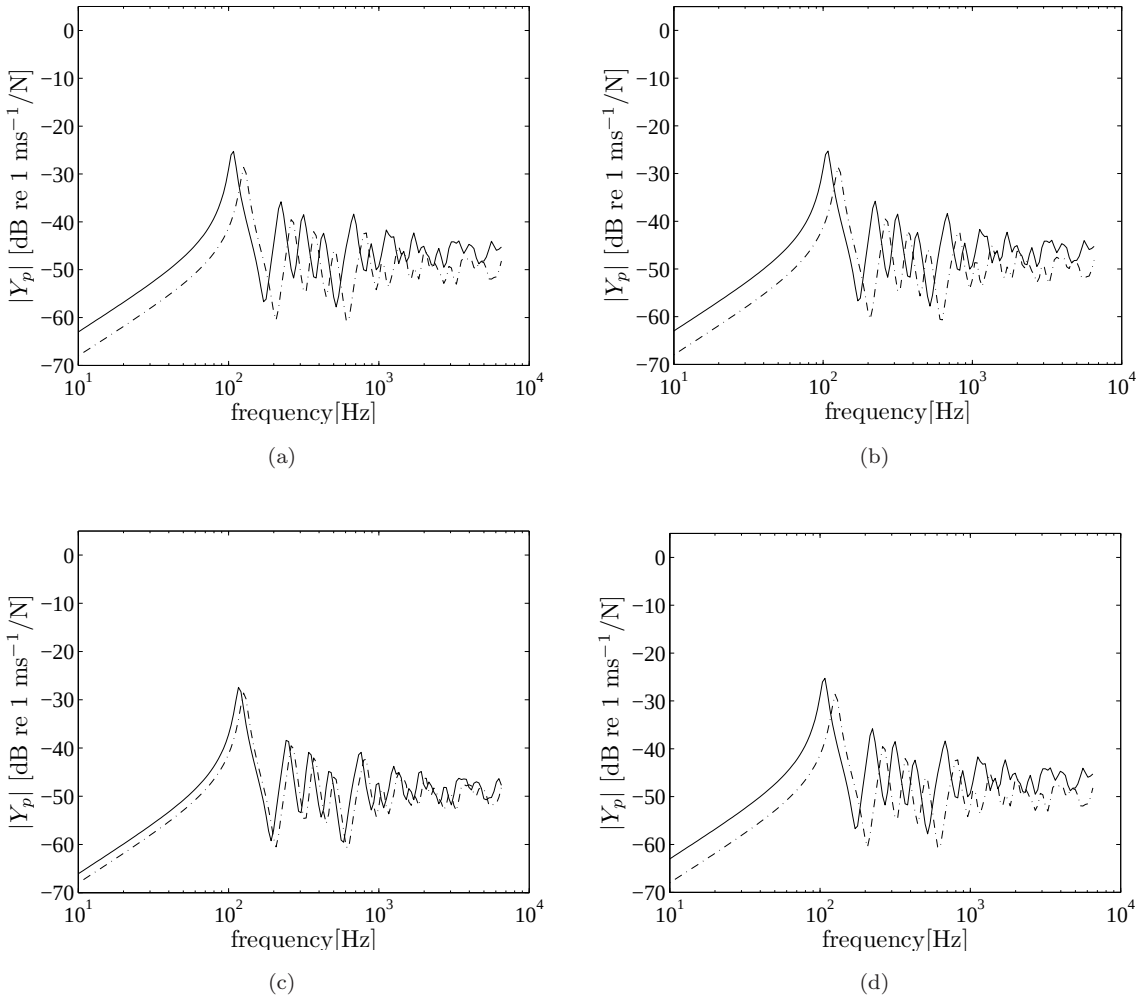


FIGURE 7.20: Calculated point mobility of simply supported perforated plates ($20\log_{10}|Y_p|$): —corrected bending stiffness due to perforation, $-\cdot-$solid plate; $t_p = 3$ mm: (a) $d_o = 5$ mm, $\tau = 20\%$, $b_x = b_y = 10$ mm, (b) $d_o = 10$ mm, $\tau = 20\%$, $b_x = b_y = 20$ mm, (c) $d_o = 15$ mm, $\tau = 7\%$, $b_x = b_y = 50$ mm, (d) $d_o = 25$ mm, $\tau = 20\%$, $b_x = b_y = 50$ mm (forcing point at $(0.375a, 0.5b)$, $\eta = 0.1$).

effects. These plate samples have a different hole distance $b_x$ for each plate and hence do not show an orderly increment of mobility level as for the 1.5 mm plate samples. Figure 7.20(a), (b) and (c) show similar results with 3.5 dB higher mobility level than that of the solid plate as they have equal perpendicular and parallel ligament efficiencies, i.e. XLE = YLE = 0.

For all the perforated plate samples given ($t_p = 1.5$ mm and 3 mm), it can be seen that the modal resonance frequencies, which are the peaks in the mobility, shift to lower frequencies, as also found in Section 5.5.

Figure 7.21 compares the point mobility of the 1.5 mm thick plates calculated using

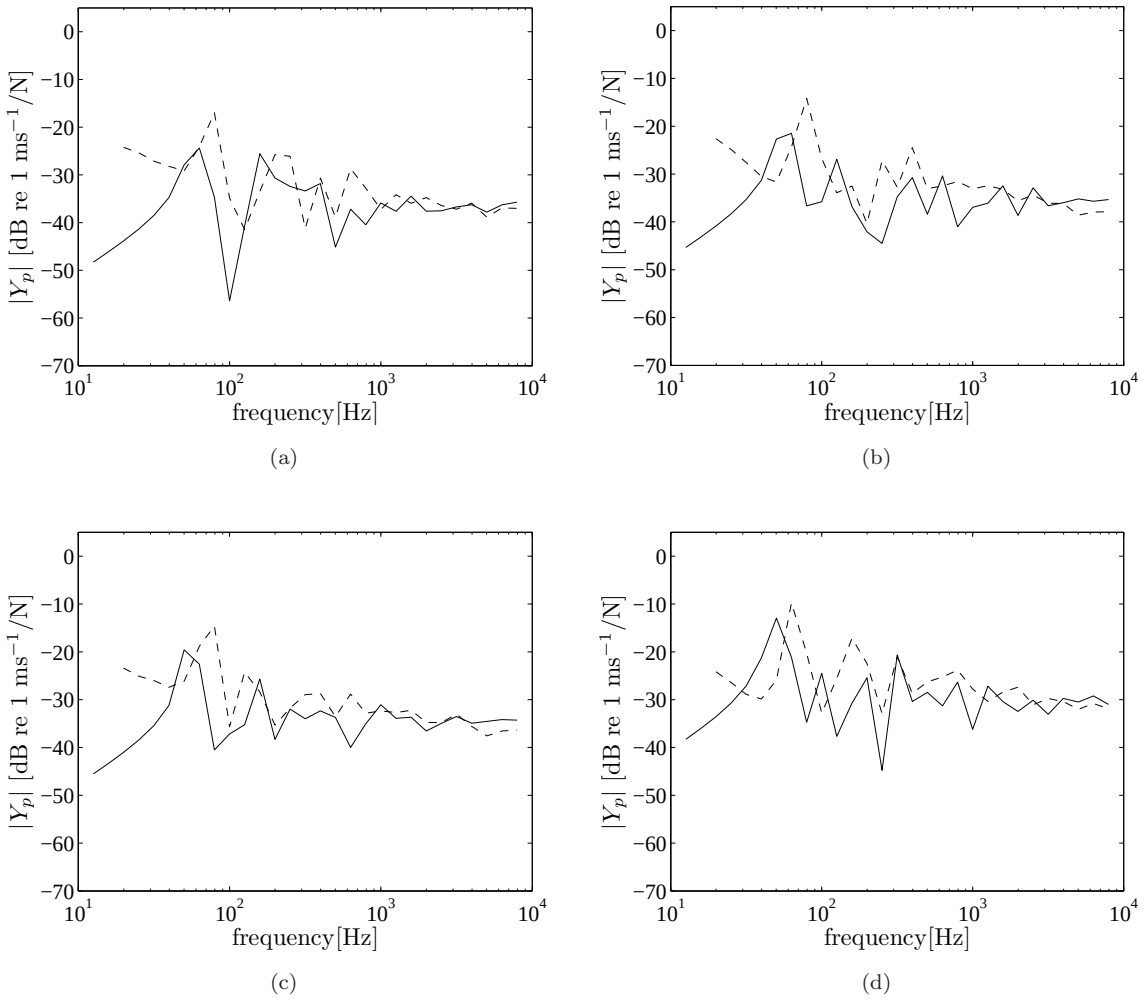


FIGURE 7.21: Point mobility of simply supported perforated plates ($20\log_{10}|Y_p|$): —corrected bending stiffness due to perforation, −−measurement; $t_p = 1.5$ mm, $p_x = 27$ mm: (a) $d_o = 5$ mm, $\tau = 5\%$, (b) $d_o = 8$ mm, $\tau = 12\%$, (c) $d_o = 10$ mm, $\tau = 19\%$, (d) $d_o = 15$ mm, $\tau = 44\%$.

the corrected plate bending stiffness and density with the measured data from hammer transducer (the point excitation is listed in Table 7.3 and the damping loss factor is in Table 7.7). The results are plotted in $\frac{1}{3}$ octave bands for clarity. Compared with the results of Figure 7.9 it can be seen that the mobility is closer to the measurement when the corrected bending stiffness and density is used, especially for frequencies above 1 kHz.

Figure 7.22 shows the corresponding results for the 3 mm plates. A good agreement is found between the corrected mobility level and the measured data in this case.

For the purpose of investigating the effect of material properties change due to perforation on the radiation efficiency, the focus is not paid in detail on the resonance

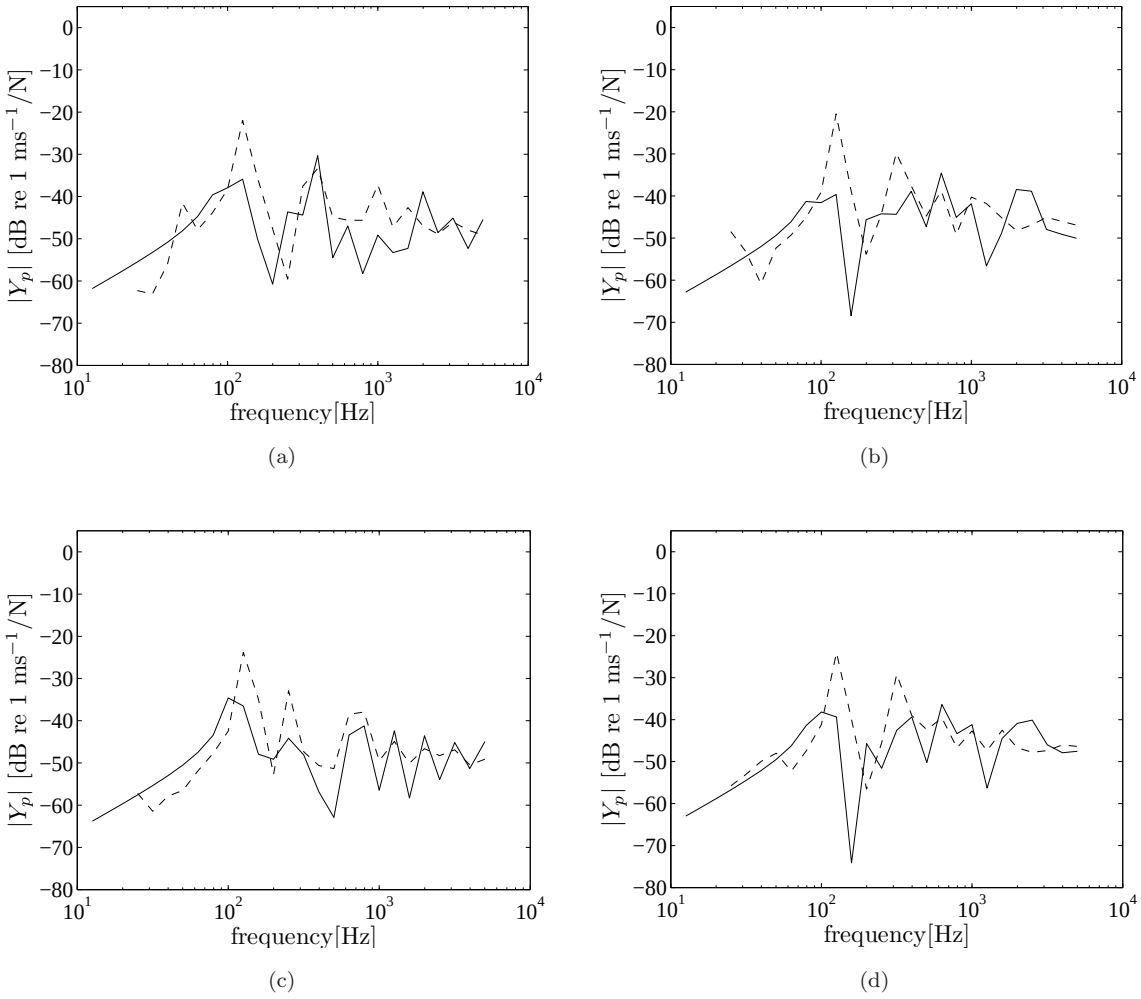


FIGURE 7.22: Point mobility of simply supported perforated plates ($20\log_{10}|Y_p|$): —corrected bending stiffness due to perforation, −−measurement; $t_p = 3$ mm: (a) $d_o = 5$ mm, $\tau = 20\%$, $p_x = 10$ mm, (b) $d_o = 10$ mm, $\tau = 20\%$, $p_x = 20$ mm, (c) $d_o = 15$ mm, $\tau = 7\%$, $p_x = 50$ mm, (d) $d_o = 25$ mm, $\tau = 20\%$, $p_x = 50$ mm.

frequencies, but to the level of mobility. Nevertheless, it can be seen from Figure 7.19 and Figure 7.20, that the resonance frequencies are reduced in the same way as in the measured data. Tables 7.5 and 7.6 compare the measured resonance frequencies for first four modes with those from the cubic function (Eq.(5.60)). It can be seen that the measured resonance frequency is reduced by perforation and has a reasonable agreement with the cubic function.

This investigation has only been made for the simply supported boundary conditions as the effective resonance frequency (Eq.5.60) applies to the simply supported plate. Moreover, the theoretical model of the radiation efficiency has only been implemented for the simply supported and guided boundary conditions.

TABLE 7.5: Measured effective resonance frequencies for 1.5 mm thick plates

| Mode | $f_{mn}$ (Hz) | $d_o = 8$ mm, $\tau = 12\%$ | | | $d_o = 10$ mm, $\tau = 19\%$ | | |
|---|---|---|---|---|---|---|---|
| | | $f^*_{mn}(Hz)$ | $f^*_{mn}/f_{mn}$ | Eq.(5.60) | $f^*_{mn}(Hz)$ | $f^*_{mn}/f_{mn}$ | Eq.(5.60) |
| (1,1) | 69 | 63 | 0.913 | 0.9311 | 67 | 0.971 | 0.8995 |
| (2,1) | 142 | 142 | 1.000 | 0.9311 | 119 | 0.838 | 0.8995 |
| (1,2) | 188 | 183 | 0.973 | 0.9311 | 159 | 0.846 | 0.8995 |
| (2,2) | 256 | 241 | 0.941 | 0.9311 | 203 | 0.793 | 0.8995 |

TABLE 7.6: Measured effective resonance frequencies for 3 mm thick plates

| Mode | $f_{mn}$ (Hz) | $d_o = 10$ mm, $\tau = 20\%$ | | | $d_o = 15$ mm, $\tau = 7\%$ | | |
|---|---|---|---|---|---|---|---|
| | | $f^*_{mn}$ (Hz) | $f^*_{mn}/f_{mn}$ | Eq.(5.60) | $f^*_{mn}$ (Hz) | $f^*_{mn}/f_{mn}$ | Eq.(5.60) |
| (1,1) | 140 | 131 | 0.936 | 0.8395 | 137 | 0.979 | 0.9286 |
| (2,1) | 279 | 254 | 0.910 | 0.8395 | 266 | 0.953 | 0.9286 |
| (1,2) | 372 | 329 | 0.884 | 0.8395 | 362 | 0.973 | 0.9286 |
| (2,2) | 495 | 438 | 0.885 | 0.8395 | 471 | 0.952 | 0.9286 |

### 7.2.3 Free-free boundary conditions

Although less common in practice, the free-free boundary condition is frequently used in experiments as it is easy to setup without special treatment of the plate edges. In order to measure the plates in free-free boundary conditions, they were hung from a frame with light ropes through the holes. The same measurement procedure was applied as in the simply supported boundary condition experiment.

Figure 7.23 shows typical examples of the coherence from one measurement point of 1.5 mm, 3 mm and 12 mm free-free plates. It can be seen that the coherence for the 1.5 mm plates is unity for the whole frequency range apart from some isolated frequencies above 1 kHz (anti resonances of the plate). For the 3 mm plates, the coherence is poor around 3.2 kHz. However generally, it can be judged to be satisfactory. For the 12 mm plate, the coherence is poor especially between 400 Hz and 1 kHz and above 3 kHz. This is because the plate thickness and its high stiffness made it difficult to obtain a good signal-to-noise ratio.

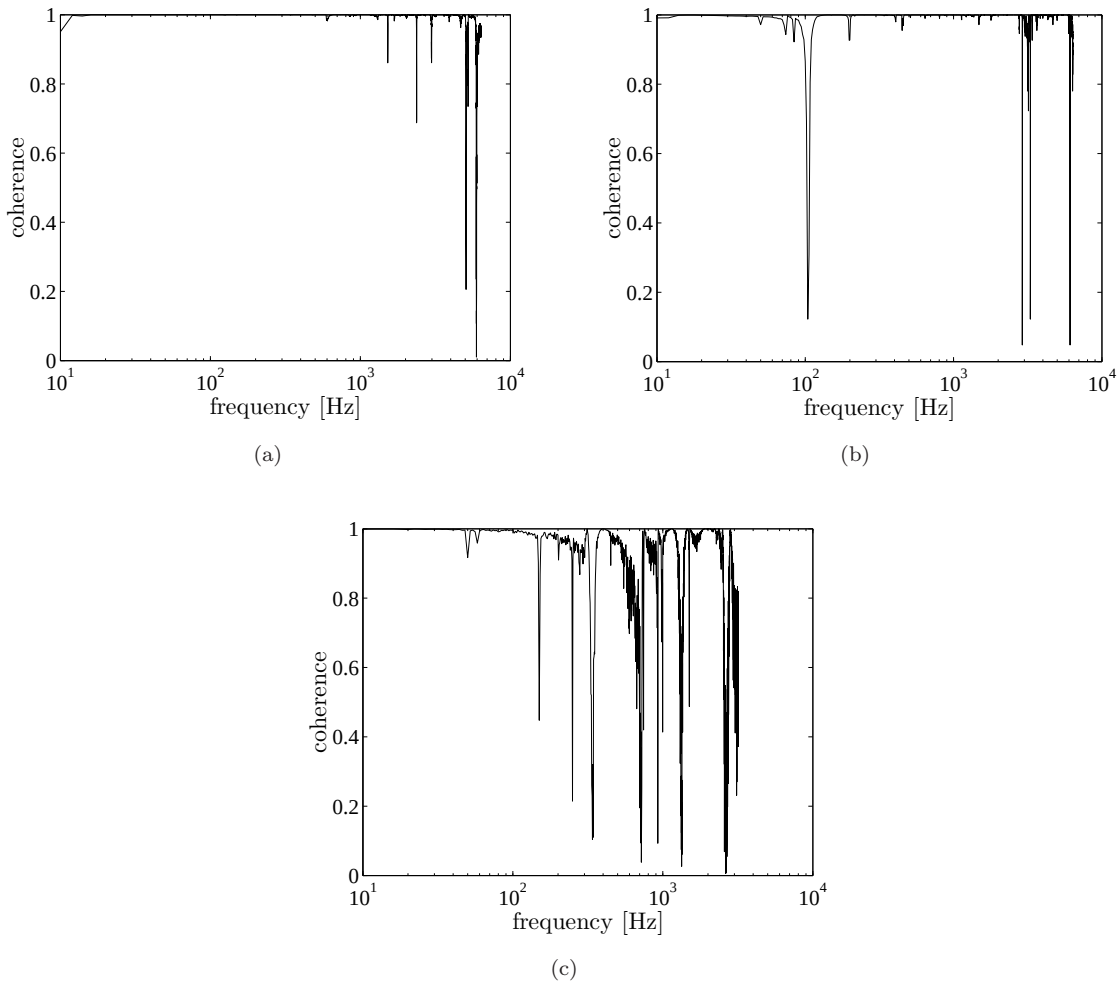


FIGURE 7.23: Typical coherence for free-free plates: (a) 1.5 mm, (b) 3 mm and (c) 12 mm

#### 7.2.3.1 Mobility results for 1.5 mm thick plates

Figure 7.24 shows the measured point mobility from both impact and shaker excitation for the 1.5 mm thick plates, which again shows the mass loading effect. As for the simply supported plate, the effect of mass loading begins at roughly 600 Hz. Also, as a result of this effect, it can be noted that the signal quality reduces at high frequencies as the plate responds less to the input force.

Using the same correction technique as in Section 7.2.2.1 for the 1.5 mm simply supported plate, Figure 7.25 shows corrected and uncorrected squared mobilities in $\frac{1}{3}$ octave bands. Similar to the simply supported plates, the difference between the curves, i.e. the effect of mass loading, becomes greater as the frequency increases.

The first two high peaks at 46 and 84 Hz seen in Figure 7.24(a), (b) and (c) are

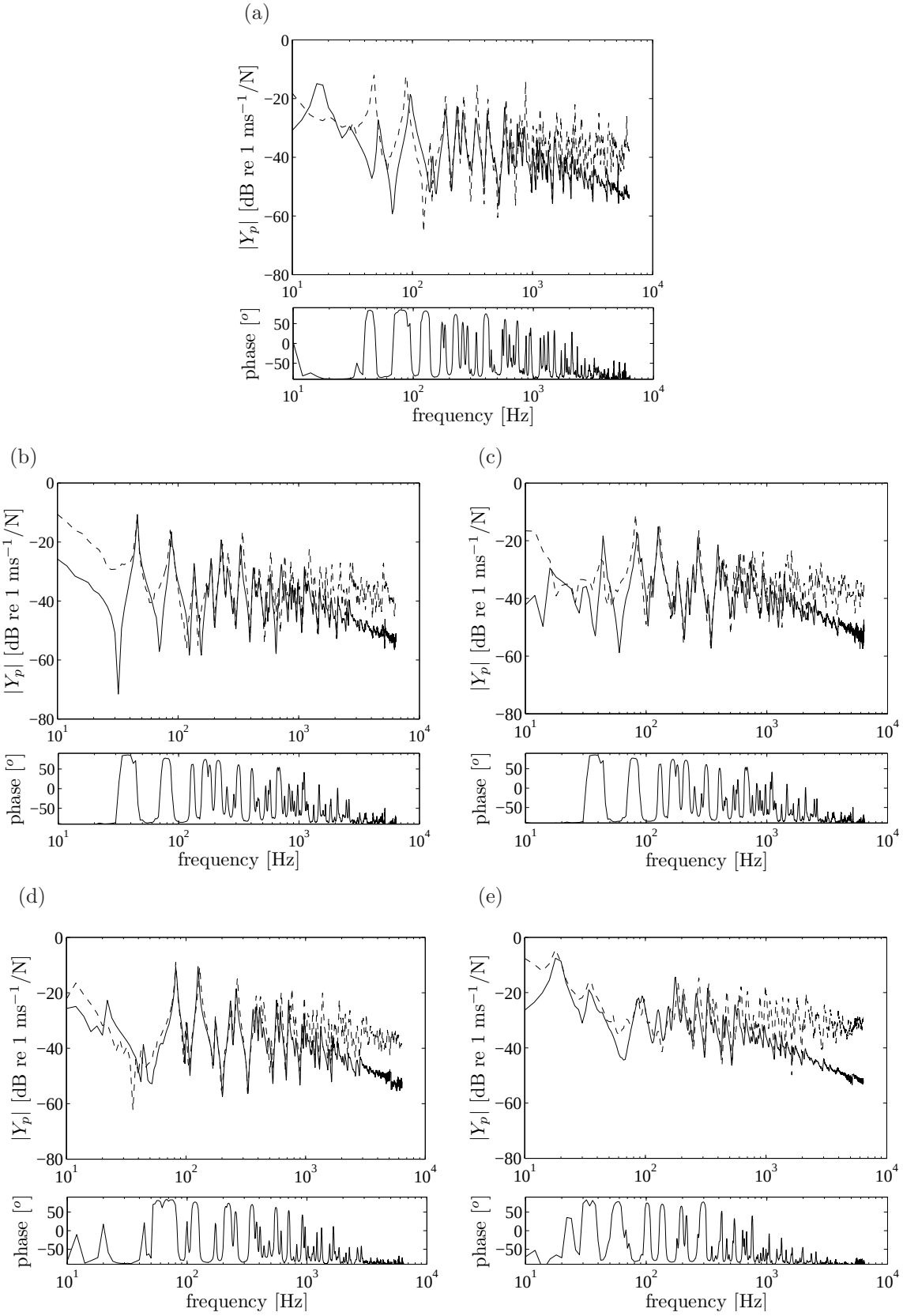


FIGURE 7.24: Measured point mobility and phase of 1.5 mm free-free perforated plates ($20\log_{10}|Y_p|$): −−impact hammer, —shaker and force gauge transducer; (a) unperforated, (b) $d_o = 5$ mm, $\tau = 5\%$, (b) $d_o = 8$ mm, $\tau = 12\%$, (c) $d_o = 10$ mm, $\tau = 19\%$, (d) $d_o = 15$ mm, $\tau = 44\%$.

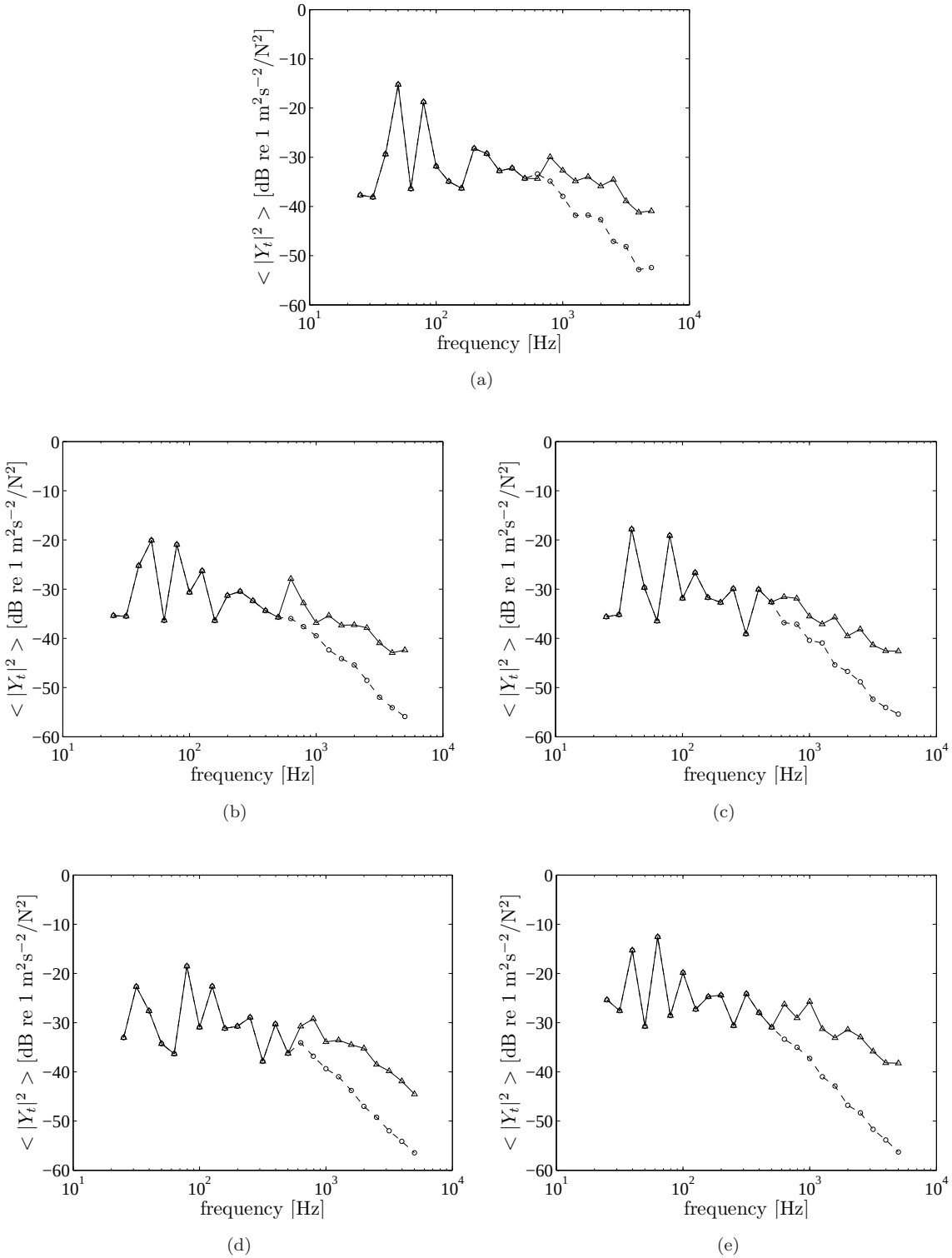


FIGURE 7.25: Experimental results of spatially average square-transfer mobilities of 1.5 mm free-free perforated plates ($10 \log_{10} \langle |Y_t|^2 \rangle$): (a) unperforated, (b) $d_o = 5$ mm, $\tau = 5\%$, (c) $d_o = 8$ mm, $\tau = 12\%$, (d) $d_o = 10$ mm, $\tau = 19\%$ and (d) $d_o = 15$ mm, $\tau = 44\%$ (-∘- before correction, -△-corrected).

(a) (b)

FIGURE 7.26: Operating deflections from scanning vibrometer software. Bending modes of 1.5 mm free-free plates from the experiment: (a) 46 Hz and (b) 84 Hz.

bending modes from the free-free boundary condition. These modes correspond to half a structural wavelength in one direction in the plate. The mode shapes calculated using the Polytec vibrometer software are illustrated in Figure 7.26.

#### 7.2.3.2 Mobility results for 3 mm thick plates

Figure 7.27 shows the point mobility for the 3 mm free-free plates in $\frac{1}{3}$ octave bands. The corrected point mobility is obtained by applying the same technique as for the 3 mm simply supported plates in Section 7.2.2.2, also from 3 kHz. It can be seen that the corrected mobility increases by roughly 5 dB. The corrected spatially averaged squared mobility is shown in Figure 7.28.

#### 7.2.3.3 Mobility results for 12 mm thick plates

The spatially averaged squared mobility for the 12 mm plates is plotted in Figure 7.29. It can be seen that it is dominated by a few individual modes especially below the critical frequency, i.e. 1 kHz.

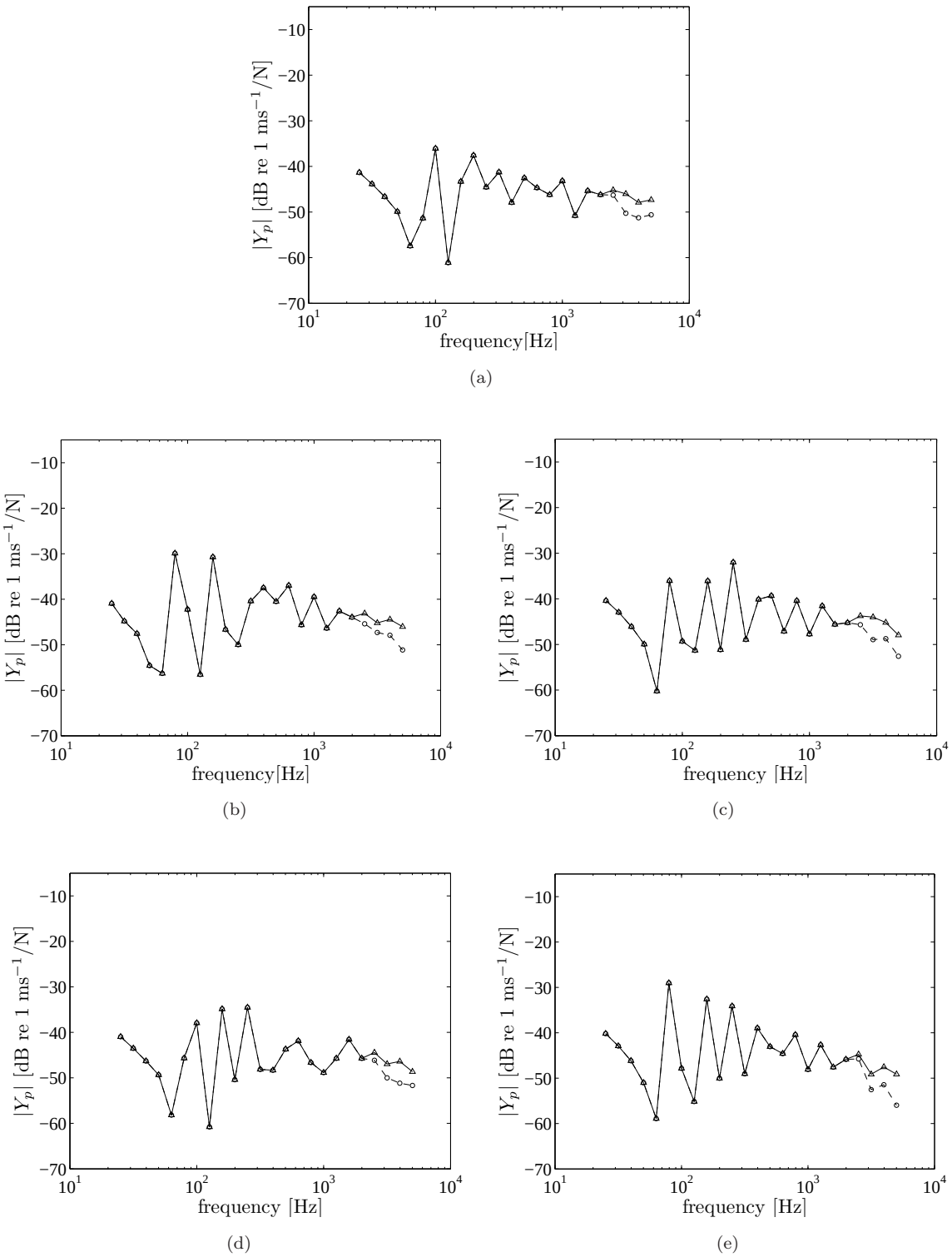


FIGURE 7.27: Experimental results of point mobility of 3 mm free-free plates ($20\log_{10}|Y_p|$) in $\frac{1}{3}$ octave bands: (a) unperforated, (b) $d_o = 5$ mm, $\tau = 20\%$, (c) $d_o = 10$ mm, $\tau = 20\%$, (d) $d_o = 15$ mm, $\tau = 7\%$, (e) $d_o = 25$ mm, $\tau = 20\%$ (-○- before correction, -△-corrected).

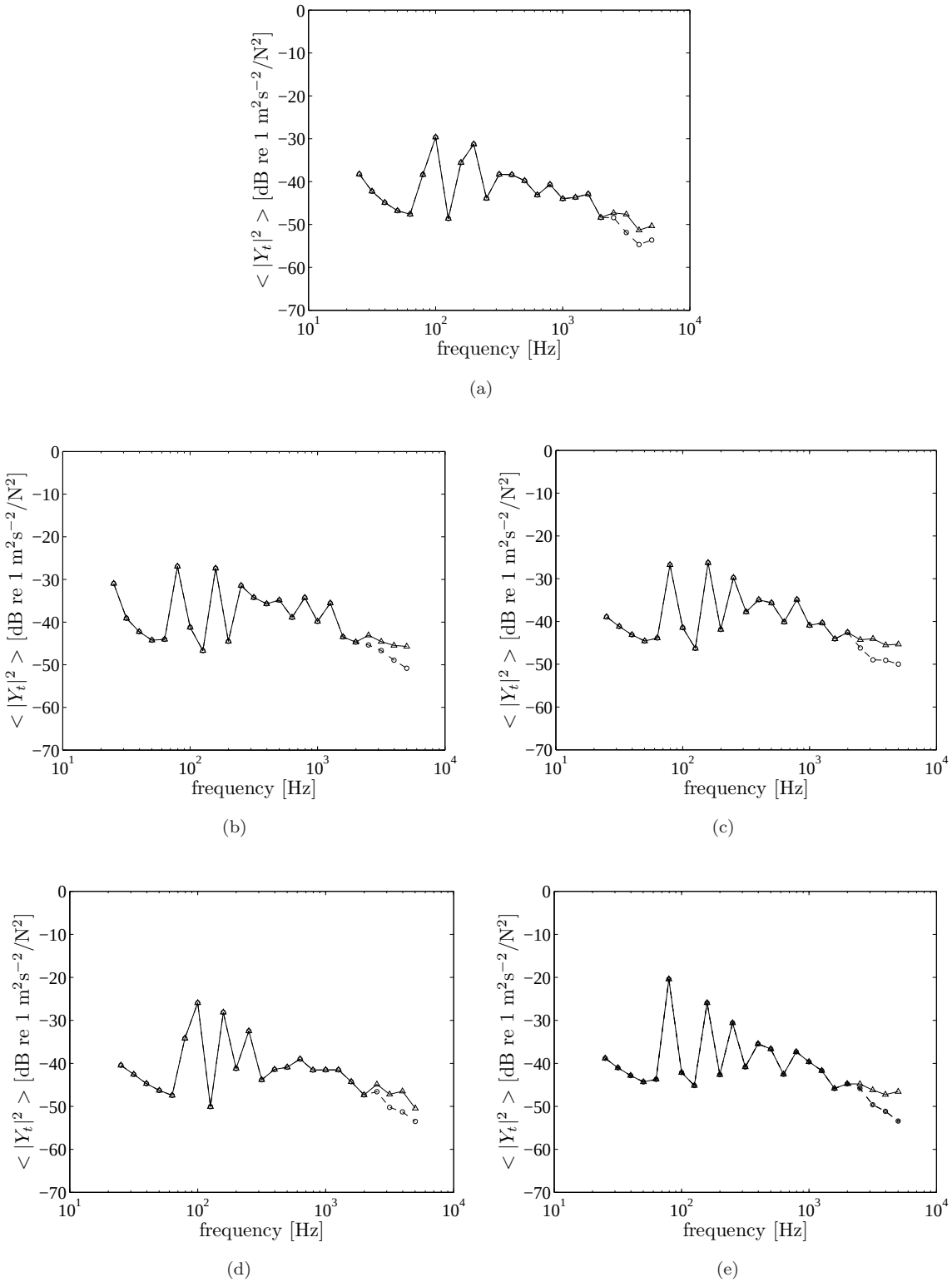


FIGURE 7.28: Experimental results of spatially averaged squared-transfer mobility of 3 mm free-free perforated plates ($10 \log_{10} \langle |Y_t|^2 \rangle$) in $\frac{1}{3}$ octave bands: (a) unperforated, (b) $d_o = 5$ mm, $\tau = 20\%$, (c) $d_o = 10$ mm, $\tau = 20\%$, (d) $d_o = 15$ mm, $\tau = 7\%$ and (e) $d_o = 25$ mm, $\tau = 20\%$ (-∘- before correction, -△-corrected).

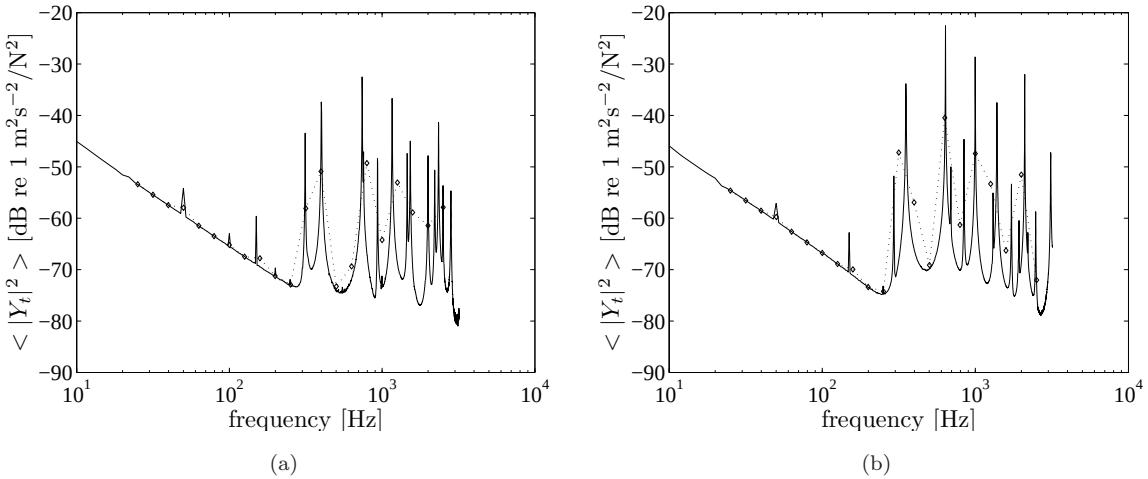


FIGURE 7.29: Experimental results of spatially averaged squared-transfer mobility of 12 mm free-free perforated plates ($20 \log_{10} |Y_p|$); $\cdot \diamond \cdot$ $\frac{1}{3}$ octave bands: (a) unperforated and (b) $d_o = 25$ mm, $\tau = 20\%$.

### 7.2.4 Structural damping

The damping loss factor $\eta$ usually has to be determined from measurements because it is difficult to predict. One method to determine $\eta$ is through the measurement of the input power $W_{in}$ and spatially averaged squared velocity of the plate $\langle |v^2| \rangle$. Under steady state conditions, the power injected to the plate is equal to the power dissipated by the plate. The input power $W_{in}$ is given by

$$W_{in} = \frac{1}{2} \Re\{Y_p\} \, |F|^2 \tag{7.12}$$

where $Y_p$ is the input mobility and $|F|^2$ is the squared input force amplitude. The dissipated power $W_{diss}$ is proportional to the vibrational kinetic energy $E_k$ and can be expressed as

$$W_{diss} = \omega \eta E_k = \frac{1}{2} \omega \eta M \left\langle \left| v^2 \right| \right\rangle \tag{7.13}$$

where $\omega$ is the circular frequency and $M$ is the total plate mass.

Therefore, as $W_{in} = W_{diss}$ in steady state, the damping loss factor $\eta$ can be written as

$$\eta = \frac{\Re\{Y_p\}}{\omega M} \left( \frac{|F|^2}{\langle |v^2| \rangle} \right) = \frac{\Re\{Y_p\}}{\omega M \, \langle |Y_t|^2 \rangle} \tag{7.14}$$

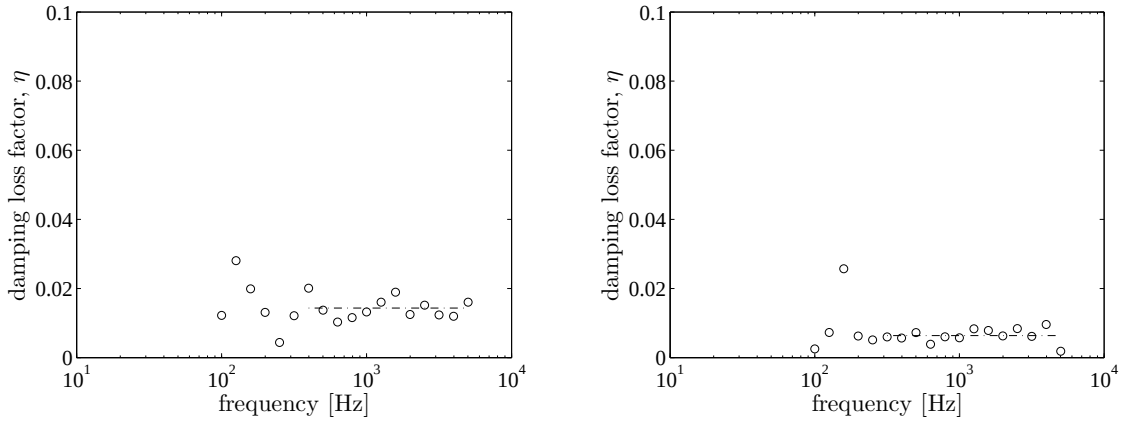


FIGURE 7.30: Structural damping loss factor: ∘ experiment, $-\cdot-$linear regression; (a) $t_p = 1.5$ mm, $d_o = 15$ mm, $\tau = 44\%$, simply supported (b) $t_p = 3$ mm, $d_o = 10$ mm, $\tau = 20\%$, free-free.

where $\langle |Y_t|^2 \rangle$ is the spatially averaged squared transfer mobility.

Two example results are plotted in Figure 7.30(a) and Figure 7.30(b) for the 1.5 mm and 3 mm plates under different boundary conditions in $\frac{1}{3}$ octave bands. The results converge above roughly 400 Hz for most of the plates. Below 400 Hz, they fluctuate around the mean value. A single number is found for the loss factor by taking the average of the results over frequency above 400 Hz. This region is most relevance since the damping only has a significant effect on the radiation efficiency in the edge mode region, i.e. from about 700 Hz up to the critical frequency for the plate dimensions given. All the results are listed in Tables 7.7, 7.8 and 7.9. The tables show that the plate damping is quite small (between 0.001 and 0.025) and the boundary conditions have no significant effect on the damping. The standard deviation (std) is between 14% and 58% of the mean.

TABLE 7.7: Measured damping loss factors $\eta$ for 1.5 mm plates

| Plate parameters | | simply supported | | free-free | |
|---|---|---|---|---|---|
| $d_o$ (mm) | $\tau$ (%) | $\eta$ | std | $\eta$ | std |
| - | - | 0.021 | 0.0057 | 0.019 | 0.0081 |
| 5 | 5 | 0.025 | 0.0039 | 0.024 | 0.0039 |
| 8 | 12 | 0.022 | 0.0053 | 0.024 | 0.0056 |
| 10 | 19 | 0.022 | 0.0030 | 0.021 | 0.0049 |
| 15 | 44 | 0.014 | 0.0075 | 0.015 | 0.0075 |

TABLE 7.8: Measured damping loss factors $\eta$ for 3 mm plates

| Plate parameters | | simply supported | | free-free | |
|---|---|---|---|---|---|
| $d_o$ (mm) | $\tau$ (%) | $\eta$ | std | $\eta$ | std |
| - | - | 0.015 | 0.0055 | 0.015 | 0.0064 |
| 5 | 20 | 0.008 | 0.0027 | 0.008 | 0.0043 |
| 10 | 20 | 0.007 | 0.0040 | 0.006 | 0.0020 |
| 15 | 7 | 0.010 | 0.0037 | 0.011 | 0.0041 |
| 25 | 20 | 0.010 | 0.0057 | 0.008 | 0.0034 |

TABLE 7.9: Measured damping loss factors $\eta$ for 12 mm plates

| Plate parameters | | free-free | |
|---|---|---|---|
| $d_o$ (mm) | $\tau$ (%) | $\eta$ | std |
| - | - | 0.001 | 0.0013 |
| 25 | 20 | 0.003 | 0.0025 |

## 7.3 Sound power measurements using reciprocal technique

To measure the radiation efficiency, in addition to the spatially averaged squared mobility, a measurement is required of the sound power for a unit squared input force. Although this can be measured directly by attaching a shaker to the plate and measuring the radiated sound, here a reciprocal technique is used.

Reciprocal measurement techniques have been used in many practical cases of sound radiation from vibrating structures, structural response to incident sound and sound transmission through partitions e.g. in vehicles for both airborne and structure borne transmission. These techniques are often less costly, less time consuming, more convenient and sometimes more accurate than the equivalent direct measurement [54]. They may also be less labour intensive, if for example, vibration sources are involved which would have to be replaced by vibration generators in a direct method.

In the case of the present experiments, particular attention has to be paid to the noise from the shaker if using the direct method. Although it has been shown that the shaker noise is negligible compared with the radiated sound of an aluminium 3 mm solid plate in the room [88], it is believed that the shaker alone produces a different

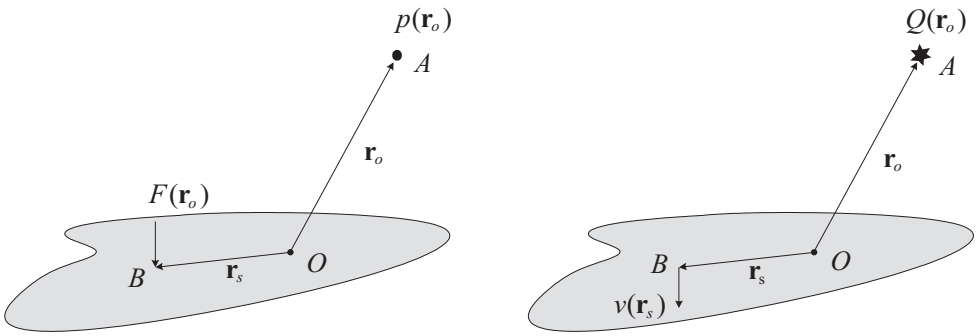


FIGURE 7.31: Basic concept of reciprocal measurement of an elastic structure excited by a point force.

noise level than when it is attached to the plate. In addition, as the perforated plate has a much lower radiation efficiency, especially at low frequency, the shaker noise may contaminate the measured sound power. The measurement also requires careful attention to other background noise from in and outside the room which could add errors in the measurement. Therefore, in this experiment, the reciprocal technique is chosen as an alternative method with less significant effect from background noise to the accuracy of the measurement.

### 7.3.1 Theory

Lyamshev [93] proposed that the transfer function between a point force $F$ exciting a *linear* elastic structure and the resulting sound pressure $p$ at a particular observation point is equivalent to the transfer function between a volume velocity $Q$ of a point monopole located at the former observation point and the resulting vibration velocity $v$ produced at the former excitation point, in the same direction as the excitation force. As shown in Figure 7.31, this gives

$$\frac{p(\mathbf{r}_o)}{F(\mathbf{r}_s)} \equiv -\frac{v(\mathbf{r}_s)}{Q(\mathbf{r}_o)} \tag{7.15}$$

where $\mathbf{r}_o$ and $\mathbf{r}_s$ are the position vectors of the observation point and of the excitation point on the structure respectively. This should be equally true if the structure is perforated.

If the direct method experiment is conducted in a reverberant chamber, the radiated power $W_{rad}$ normalised by the mean-square force $\overline{F^2}$ at point $B$ in Figure 7.31 is given

by

$$\frac{W_{rad}}{\overline{F^2}} = \frac{S\bar{\alpha}}{4\rho c}\left\langle \frac{\overline{p^2}}{\overline{F^2}} \right\rangle \tag{7.16}$$

where $S\bar{\alpha}$ is the room absorption, $\rho$ is the air density, $c$ is the sound speed and $\left\langle \overline{p^2} \right\rangle$ is the spatially-averaged mean square pressure in the room due to radiation by the plate. In a reverberant field the sound pressure is approximately the same at any location $A$, so Eq.(7.16) can be approximated by

$$\frac{W_{rad}}{\overline{F^2}} = \frac{S\bar{\alpha}}{4\rho c}\frac{\overline{p^2}}{\overline{F^2}} \tag{7.17}$$

Using the principle of reciprocity from Eq.(7.15), Eq.(7.17) can then be written as

$$\frac{W_{rad}}{\overline{F^2}} = \frac{S\bar{\alpha}}{4\rho c}\frac{\overline{v_Q^2}}{\overline{Q^2}} \tag{7.18}$$

where $\overline{v_Q^2}$ is the mean-square plate velocity at point $B$ due to the sound excitation from a monopole source of mean-square volume velocity $\overline{Q^2}$ at point $A$.

The source volume velocity $Q$ in the reciprocal measurement can itself be determined from a sound power measurement. In the diffuse field, the radiated sound power $W_Q$ of a compact source is given by [94]

$$W_Q = \rho c \overline{Q^2}\frac{k^2}{4\pi} \tag{7.19}$$

where $k$ is the wavenumber. If the source is operated in the reverberant chamber, the sound power $W_Q$ can be obtained by measuring the spatially averaged mean-square pressure $\left\langle \overline{p^2} \right\rangle$ in the room. It can be written as

$$W_Q = \frac{S\bar{\alpha}}{4\rho c}\left\langle \overline{p_Q^2} \right\rangle \tag{7.20}$$

After rearranging Eq.(7.19) and Eq.(7.20), the mean-square volume velocity $\overline{Q^2}$ is given by

$$\overline{Q^2} = \frac{S\bar{\alpha}\pi}{\rho^2 c^2 k^2} \left\langle \overline{p_Q^2} \right\rangle = \frac{S\bar{\alpha}\pi}{\rho^2 \omega^2} \left\langle \overline{p_Q^2} \right\rangle \tag{7.21}$$

since $k = \omega/c$. Hence, substituting this into Eq.(7.18) gives

$$\frac{W_{rad}}{\overline{F^2}} = \frac{S\bar{\alpha}}{4\rho c} \frac{\overline{v_Q^2}\, \rho^2 \omega^2}{S\bar{\alpha}\, \pi \left\langle \overline{p_Q^2} \right\rangle} = \frac{\overline{a_Q^2}}{\left\langle \overline{p_Q^2} \right\rangle} \frac{\rho}{4\pi c} \tag{7.22}$$

where $a_Q = j\omega v_Q$ is the plate acceleration and $\left\langle \overline{p_Q^2} \right\rangle$ is averaged over microphone positions. The acceleration could also be averaged over source positions in the room equivalent to the averaging in Eq.(7.16). However it is not very critical to average for different source positions since the sound is assumed to be diffuse irrespective of the source position in the room. Note that the absorption of the room $S\bar{\alpha}$ cancels out in Eq.(7.22). The radiation efficiency is finally obtained by using Eq.(7.22) together with the spatially averaged transfer mobility $\langle |Y_t|^2 \rangle$ in Eq.(7.2).

### 7.3.2 Experimental setup and procedure

Figure 7.32 shows the experimental setup of the reciprocal measurement which was carried out in the large reverberation chamber at the ISVR. The room has average dimensions 9.15 × 6.25 × 6.10 m, giving a volume of 348 m$^3$ and a surface area of 302 m$^2$. The room is constructed with non-parallel walls to give a good diffuse field and the internal surfaces are finished with a hard gloss paint to give a high reflection coefficient. The diffuse field is a situation where the room has many overlapping acoustic modes instead of distinct individual modes (direct field). The 'Schroeder frequency' determines the transition frequency (cross-over frequency) above which the diffuse field applies. It is given by [95]

$$f_s = 2000\sqrt{\frac{T_{60}}{V_R}} \tag{7.23}$$

For a minimum reverberation time of the room, i.e. 3 s, and for the given room volume, the Schroeder frequency is $f_s = 185$ Hz. The diffuse field cannot be assumed below this frequency.

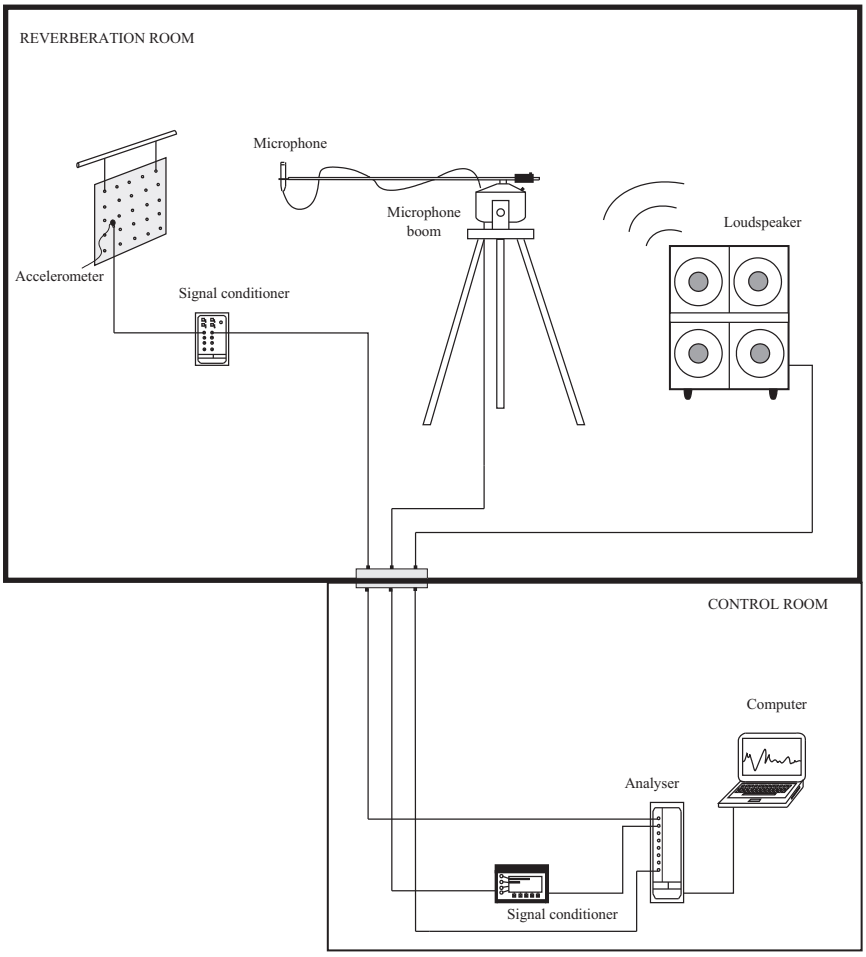


FIGURE 7.32: Experimental setup for reciprocity measurement.

Figure 7.33 shows the interior of the room and the equipment used in the measurement.

The loudspeaker was located close to one corner of the room, about 2 m from the wall. It was fed with random broadband noise up to 10 kHz. Before starting the sound power measurement, the microphone was calibrated using Brüel & Kjær piston calibrator type 4231. This was done for each plate sample. The microphone used to measure the sound pressure was a Brüel & Kjær pressure microphone type 40AG. The spatial averaging of the sound pressure across the room was achieved by using a Brüel & Kjær rotating microphone boom type 3923. The signal from the microphone was first conditioned (converted and amplified) by Brüel & Kjær Nexus conditioning amplifier Type 2690 before it was processed in a Data Physics analyser DP240.

The nearest microphone position to the loudspeaker was ensured to be more than 2 m. This fulfills the standard given by ANSI S1.21-1972 [96] that the minimum distance $d_{min}$ between the microphone and the sound source shall not be less than $d_{min} = 0.08(V_R/T_{60})^{1/2}$, where $V_R$ is the room volume and $T_{60}$ is the reverberation

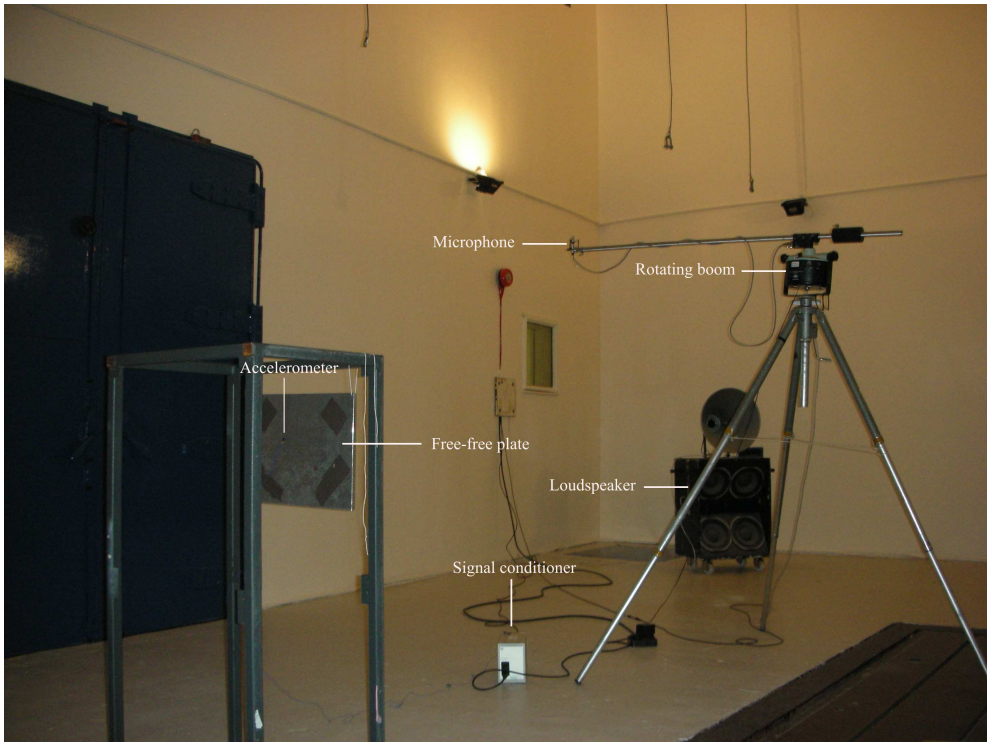


FIGURE 7.33: Equipment setup in the reverberation chamber.

time. This is half of the cross-over wavelength ($\lambda_s = c/2f_s$) from the 'Schroeder frequency', $f_s$ in Eq.(7.23). Assuming $T_{60} \geq 1$ s (it is actually in the range 3−14 s), the minimum microphone distance required is $d_{min} \leq 1.49$ m.

Figure 7.34 plots the averaged sound pressure level (SPL) spectrum in $\frac{1}{3}$ octave bands used as the acoustic excitation as well as the noise floor in the room (i.e. measured when the loudspeaker was switched off). The SPL falls below 80 Hz, but between 80 and 2.5 kHz the spectrum is almost flat; it slowly decreases at high frequency. Above 40 Hz, the background noise can be considered negligible (signal-to-noise ratio greater than 10 dB).

For the free-free boundary condition, the plates were hung using soft ropes from a stiff frame, as for the mobility measurement (see Figure 7.33). For the simply supported boundary condition, the plate (and the frame) was mounted horizontally on a rigid frame. Soft foam was placed under each corner of the frame to prevent vibration being transfered from the base. The plate was located away from the centre of the room, but more than 2 m from the walls. For the simply supported boundary conditions, the plate (and the frame) was placed horizontally 0.65 m from the floor. For the free-free boundary conditions, hung vertically, the centre of the plate was roughly 0.9 m from

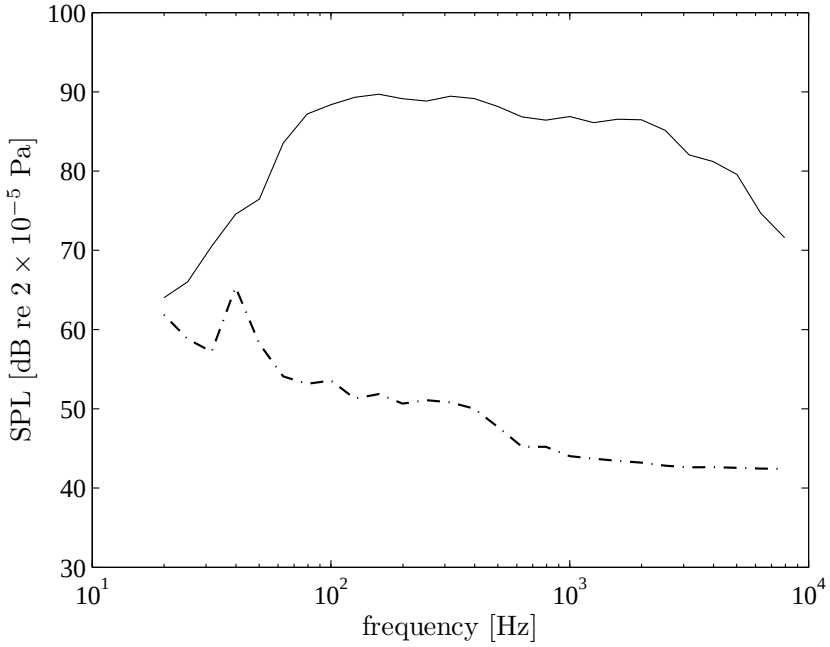


FIGURE 7.34: Sound pressure level in the chamber (—) and its noise floor (– · –) in $\frac{1}{3}$ octave bands.

the floor.

The distance between the plate and the loudspeaker was about 5 m. This ensures that the direct field from the sound source is negligible and the plate was excited predominantly by the diffuse field. This requires that the distance to the plate must be greater than the reverberation radius, $r_R = 0.056\sqrt{V_R/T_{60}}$ [95]. Assuming again that $T_{60} \geq 1$ s, this gives $r_R \leq 1$ m.

At the same location as used for the force gauge transducer in the mobility measurement, a PCB accelerometer was attached to the plate to measure its acceleration. The mass of the accelerometer 0.8 gram has negligible effect on the response. Figure 7.35 plots the mean square acceleration of the various plates in $\frac{1}{3}$ octave bands together with the corresponding noise floor i.e. when there was no sound excitation. For each boundary condition, the plate acceleration at low frequency has a similar level to the noise floor. This is due to the low level of sound excitation at very low frequencies as seen in Figure 7.34, combined with the small values of radiation efficiency expected. Thus, the data at these frequencies are rejected. The free-free plates have much lower vibration than the simply supported plates, as seen in Figure 7.35(a), (c) and (e). For some plates, the squared acceleration is still within 3 dB of the noise floor up to 300 Hz. However, for each boundary condition, the results will be plotted from 100 Hz

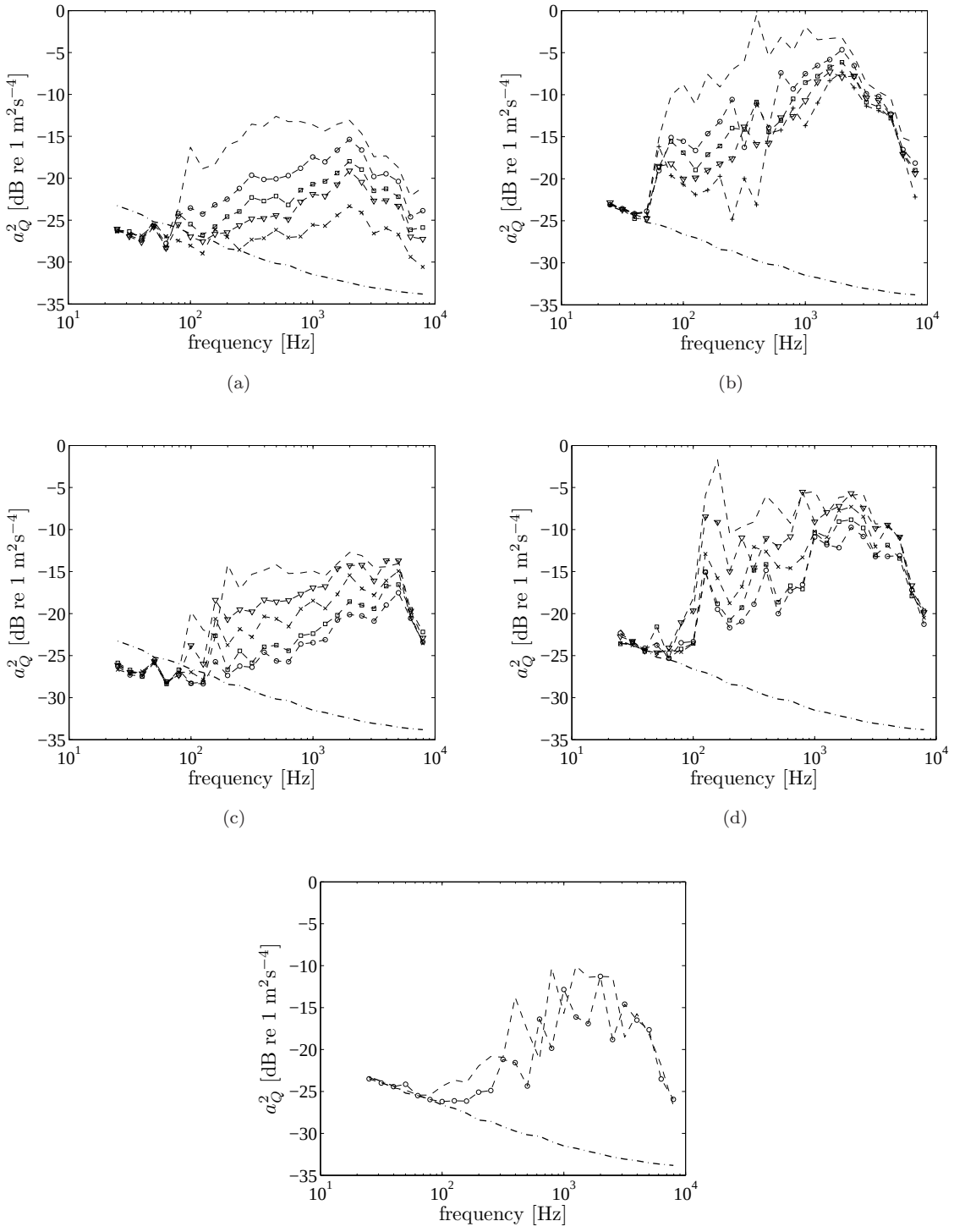


FIGURE 7.35: Plate squared acceleration: $--$ unperforated, $-\cdot-$ noise floor, (a) and (b) ($t_p = 1.5$ mm) -o- $d_o = 5$ mm; $\tau = 5\%$, -□- $d_o = 8$ mm; $\tau = 12\%$, -▽- $d_o = 10$ mm; $\tau = 19\%$, -x- $d_o = 15$ mm; $\tau = 44\%$, (c) and (d) ($t_p = 3$ mm) -o- $d_o = 5$ mm; $\tau = 20\%$, -□- $d_o = 10$ mm; $\tau = 20\%$; -▽- $d_o = 15$ mm; $\tau = 7\%$, -x- $d_o = 25$ mm; $\tau = 20\%$, (e) ($t_p = 12$ mm) -o- $d_o = 25$ mm; $\tau = 20\%$ (free-free: (a), (c) and (e); simply supported: (b) and (d)).

although care should be taken for some of the free-free plates as the data up to 300 Hz might be influenced by the noise floor of the accelerometer.

### 7.3.3 Sound power results

The normalised sound power of the plates determined from Eq.(7.22) is displayed in Figure 7.36 in $\frac{1}{3}$ octave bands. It can be seen that the plate sound power shows different levels according to the diameter of the holes and perforation ratio of the plates. Similar to the radiation efficiency trend, according to the theory, the sound power also reduces as the perforation ratio increases and as the hole size reduces. This can be seen clearly for the free-free plates in Figure 7.36(a) and (c) and also for the simply supported plates in Figure 7.36(b) and (d), although there are some fluctuations below 1 kHz. For the free-free plates, the trend also shows the sound power increases toward the critical frequency.

## 7.4 Radiation efficiency results

### 7.4.1 Radiation efficiency results for simply supported plates

Figure 7.37 presents the radiation efficiency in dB (radiation index, $10\log_{10}\sigma$) for the 1.5 mm simply supported plates along with corresponding predictions. Although the measured and predicted results show similar trends, it can be seen that the measured radiation efficiencies exceed the theoretical predictions by about 5−10 dB. Figure 7.38 shows the radiation efficiency for the 3 mm simply supported plates. Again the experimental results are considerably higher than the predictions.

The measured results cover the range 100 Hz−5 kHz. The upper limit is determined by the mobility measurements which had a maximum frequency of 6.4 kHz, meaning that the highest $\frac{1}{3}$ octave band covered is 5 kHz.

Regarding the sound radiation from a vibrating plate in an unbaffled condition, the radiated sound from one side can 'communicate' with the radiated sound from the other side of the plate. This communication, particularly at the plate edges for a solid

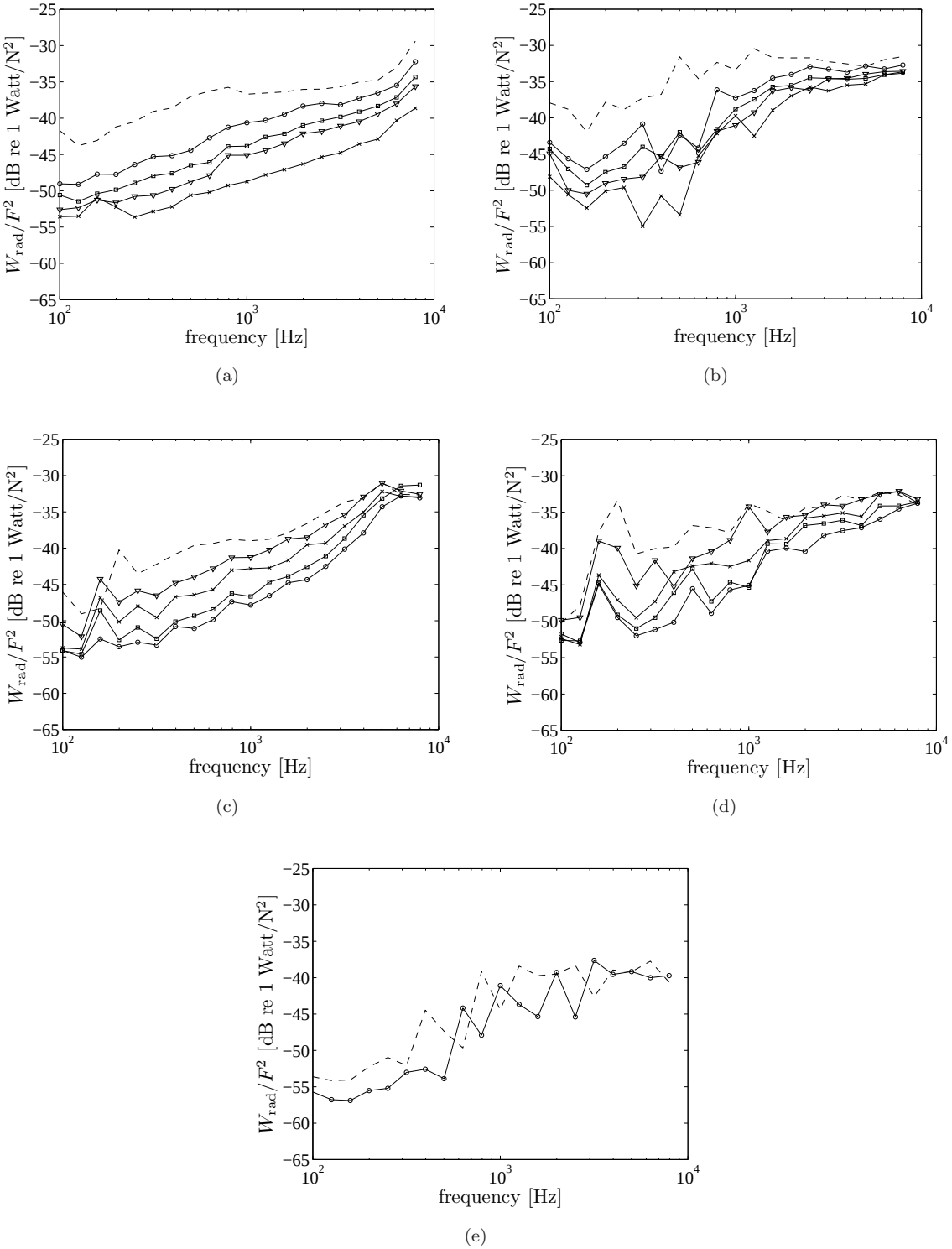


FIGURE 7.36: Plate normalised sound power: −− unperforated, (a) and (b) ($t_p$ = 1.5 mm) -o- $d_o$ = 5 mm; $\tau$ = 5%, -□- $d_o$ = 8 mm; $\tau$ = 12%, -▽- $d_o$ = 10 mm; $\tau$ = 19%, -x- $d_o$ = 15 mm; $\tau$ = 44%, (c) and (d) ($t_p$ = 3 mm) -o- $d_o$ = 5 mm; $\tau$ = 20%, -□- $d_o$ = 10 mm; $\tau$ = 20%; -▽- $d_o$ = 15 mm; $\tau$ = 7%, -x- $d_o$ = 25 mm; $\tau$ = 20%, (e) ($t_p$ = 12 mm) -o- $d_o$ = 25 mm; $\tau$ = 20% (free-free: (a), (c) and (e); simply supported: (b) and (d)).

plate, creates cancellation of the sound radiation. The effectiveness of this cancellation depends on the acoustic wavelength. The longer the wavelength, the more effective the cancellation, as explained in Chapter 3. Conversely, in the baffled condition this sort of communication is not possible. Therefore, a baffled plate has a higher radiation efficiency, as already shown in Figure 3.6.

Figure 7.39 shows a diagram of one side of the plate edges. This illustrates that the path length for the sound to propagate from one side of the plate to the other is approximately 110 mm. In order for the plate to be considered as unbaffled, this has to be less than about half an acoustic wavelength. It means that the frequency should be less than $f = 343/(2 \times 0.11) \approx 1.5$ kHz. Above this frequency, the radiated sound from the back of the plate is blocked by the frame and the plate becomes effectively baffled. This may explain the disagreement in the results at least above 1 kHz. Moreover, the nature of the radiated sound from the back of the plate is also modified by the frame. So the sound radiation from the back will be more directional than that from the front. This could also reduce the effectiveness of the cancellation process. Hence the plate may also be effectively baffled at lower frequencies than 1.5 kHz.

Figure 7.40 compares some of the results with predictions for both baffled and unbaffled conditions. The results of the perforated baffled plate were calculated using the discrete sources model from Chapter 6. They could only be calculated for the 3 mm plate with small hole density, i.e. plates numbered 9 and 10 in Table 7.1. For greater hole densities, the model needs more sources which then results in excessive calculation times. The results for the unperforated plates are calculated by the wavenumber approach of Section 2.2. It can be seen that above around 1 kHz the measured results follow the trend of the baffled plate results rather than the unbaffled results. Thus the frame used for the simply supported boundary conditions does not allow unbaffled results to be obtained.

Figure 7.41 displays the measured and predicted effect of perforation (EoP) for 1.5 mm simply supported plates. This shows the level difference between the curves in Figure 7.37(a) and those in (b)−(e). Above 500 Hz, the measured results follow the trend of the predictions although at some frequencies the measured effect is about $2 - 5$ dB less than the predictions. Below 500 Hz, high fluctuations occur due to the disagreement, particularly in the corner mode region, between the measured radiation

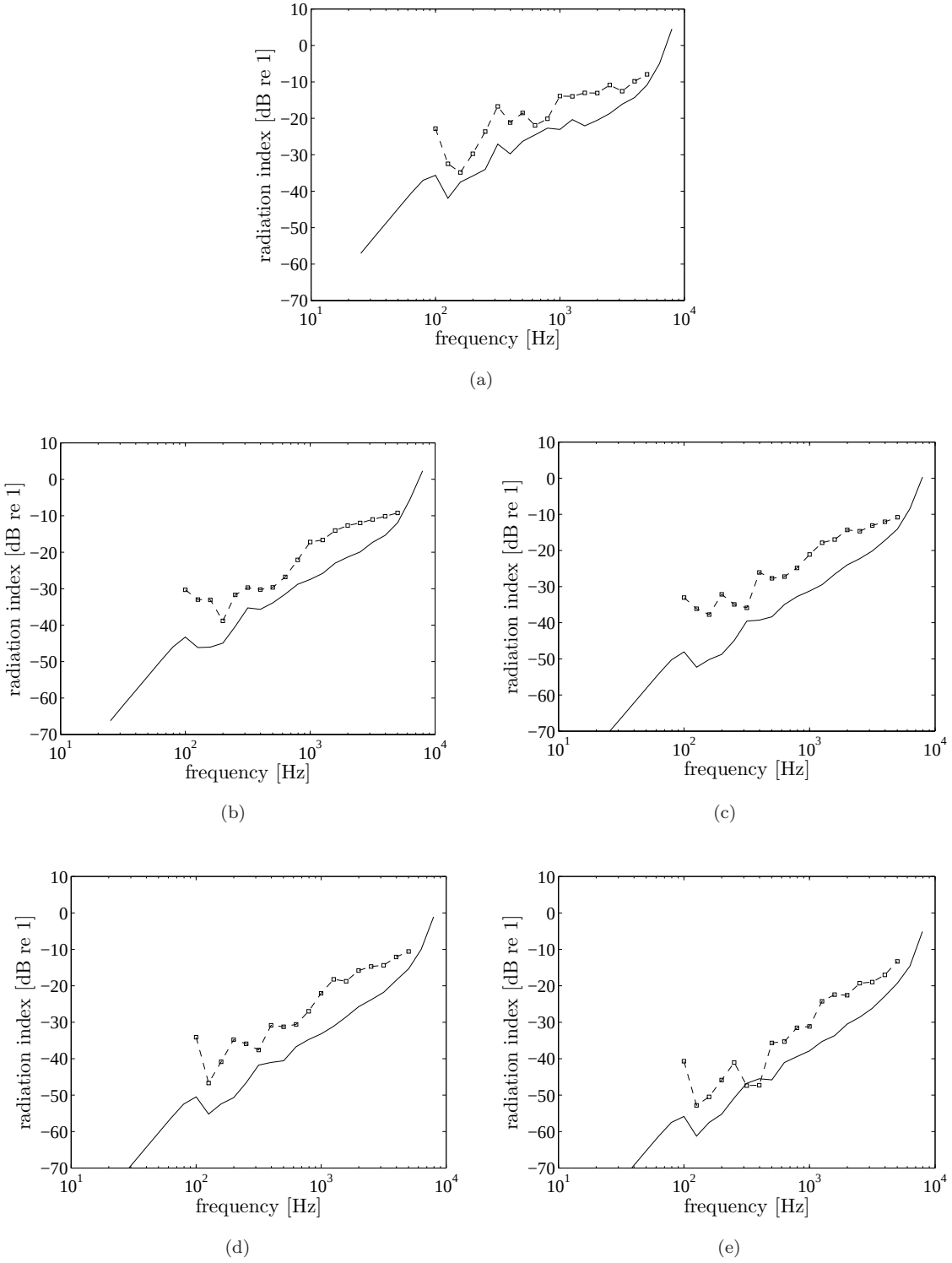


FIGURE 7.37: Radiation efficiency of unbaffled 1.5 mm simply supported perforated plates: — theoretical, -□- experiment; (a) unperforated, (b) $d_o = 5$ mm; $\tau = 5\%$, (c) $d_o = 8$ mm; $\tau = 12\%$, (d) $d_o = 10$ mm; $\tau = 19\%$ and (e) $d_o = 15$ mm; $\tau = 44\%$.

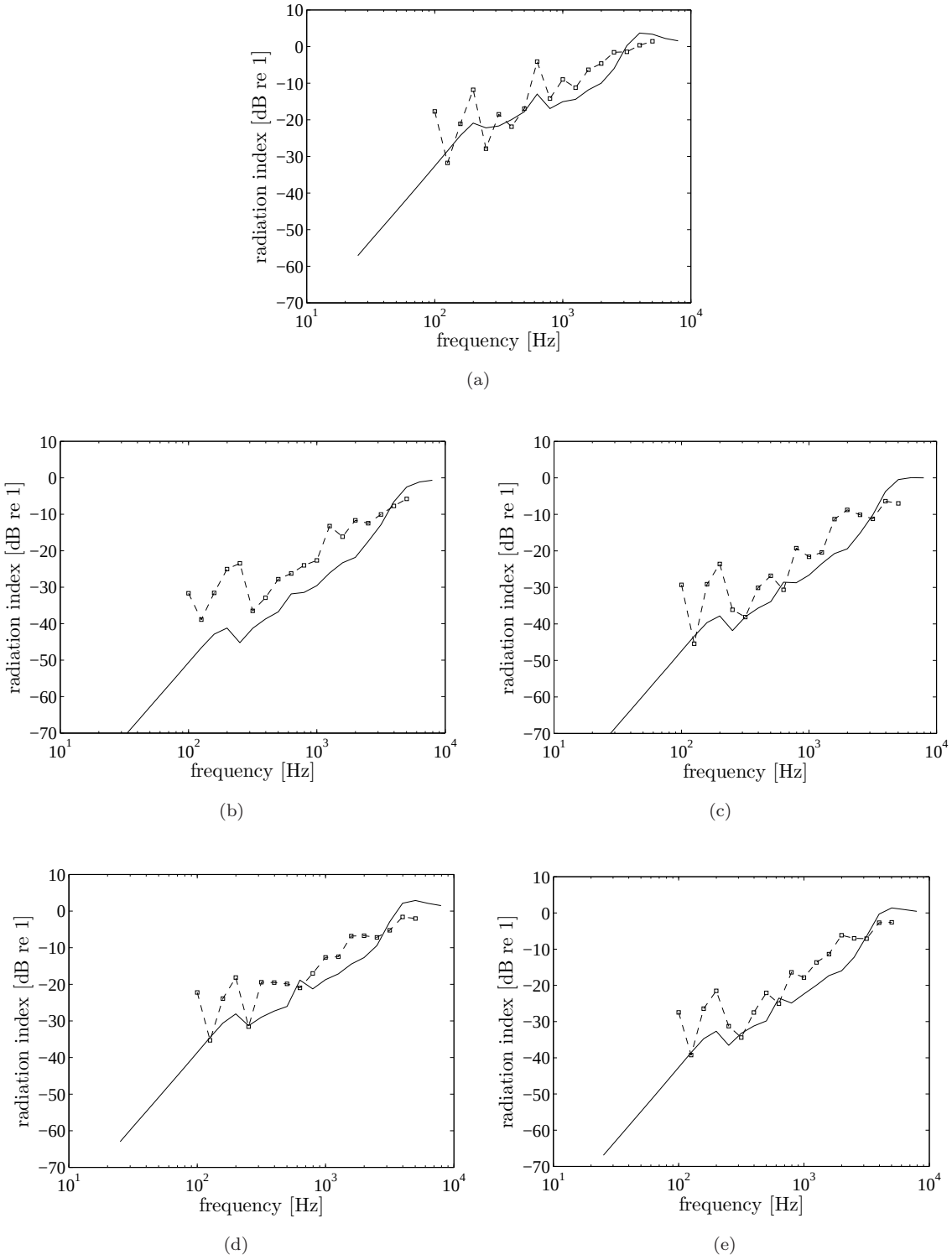


FIGURE 7.38: Radiation efficiency of unbaffled 3 mm simply supported perforated plates: — theoretical, -□- experiment; (a) unperforated, (b) $d_o = 5$ mm; $\tau = 20\%$, (c) $d_o = 10$ mm; $\tau = 20\%$, (d) $d_o = 15$ mm; $\tau = 7\%$ and (e) $d_o = 25$ mm; $\tau = 20\%$.

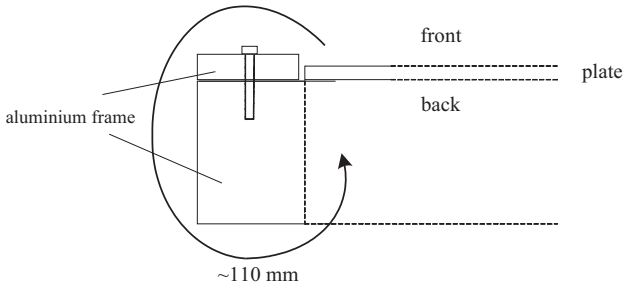


FIGURE 7.39: Illustration of the sound path at the frame edges.

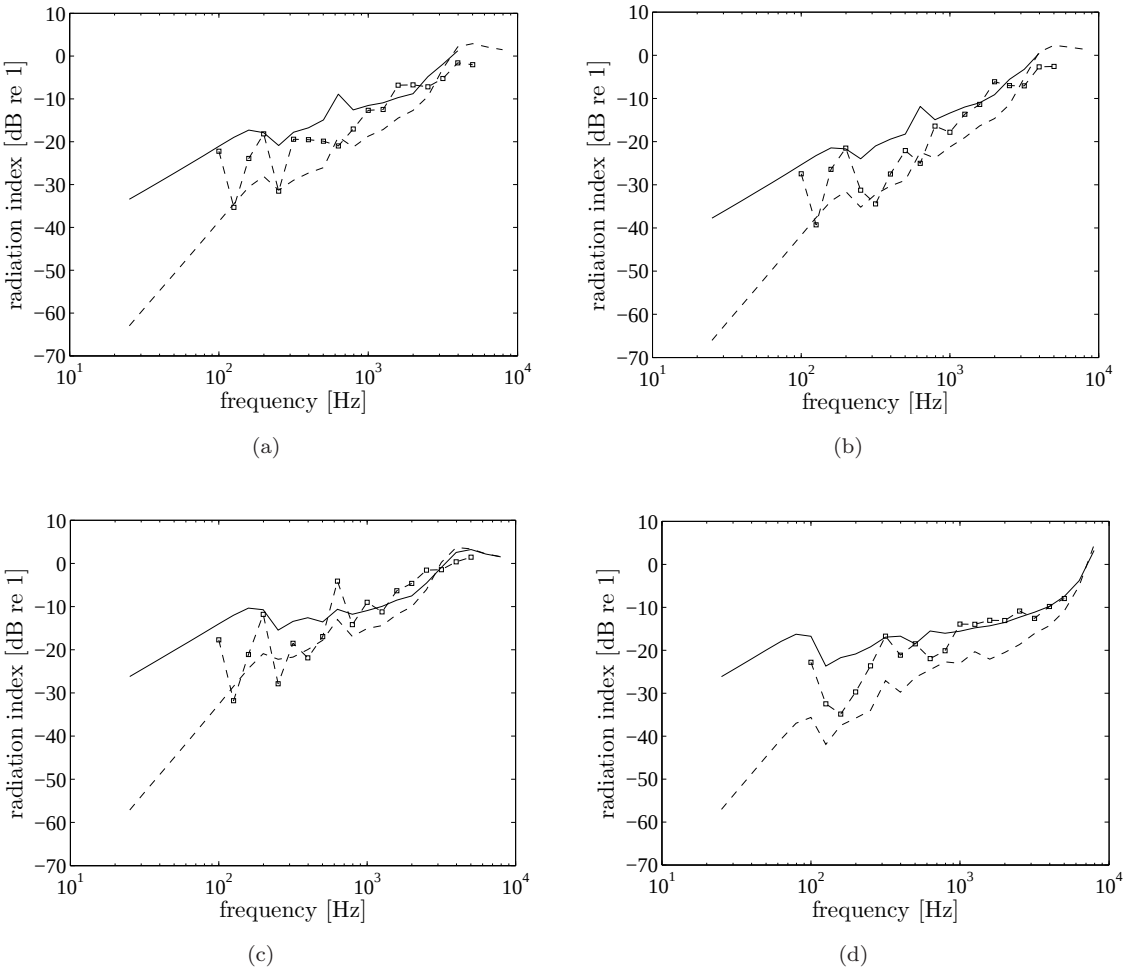


FIGURE 7.40: Comparison of measured radiation efficiency of perforated simply supported plates with baffled model. −−unbaffled, —baffled; ($t_p$ = 3 mm): (a) $d_o$ = 15 mm; $\tau$ = 7%, (b) $d_o$ = 25 mm; $\tau$ = 20%, (c) unperforated and ($t_p$ = 1.5 mm): (d) unperforated.

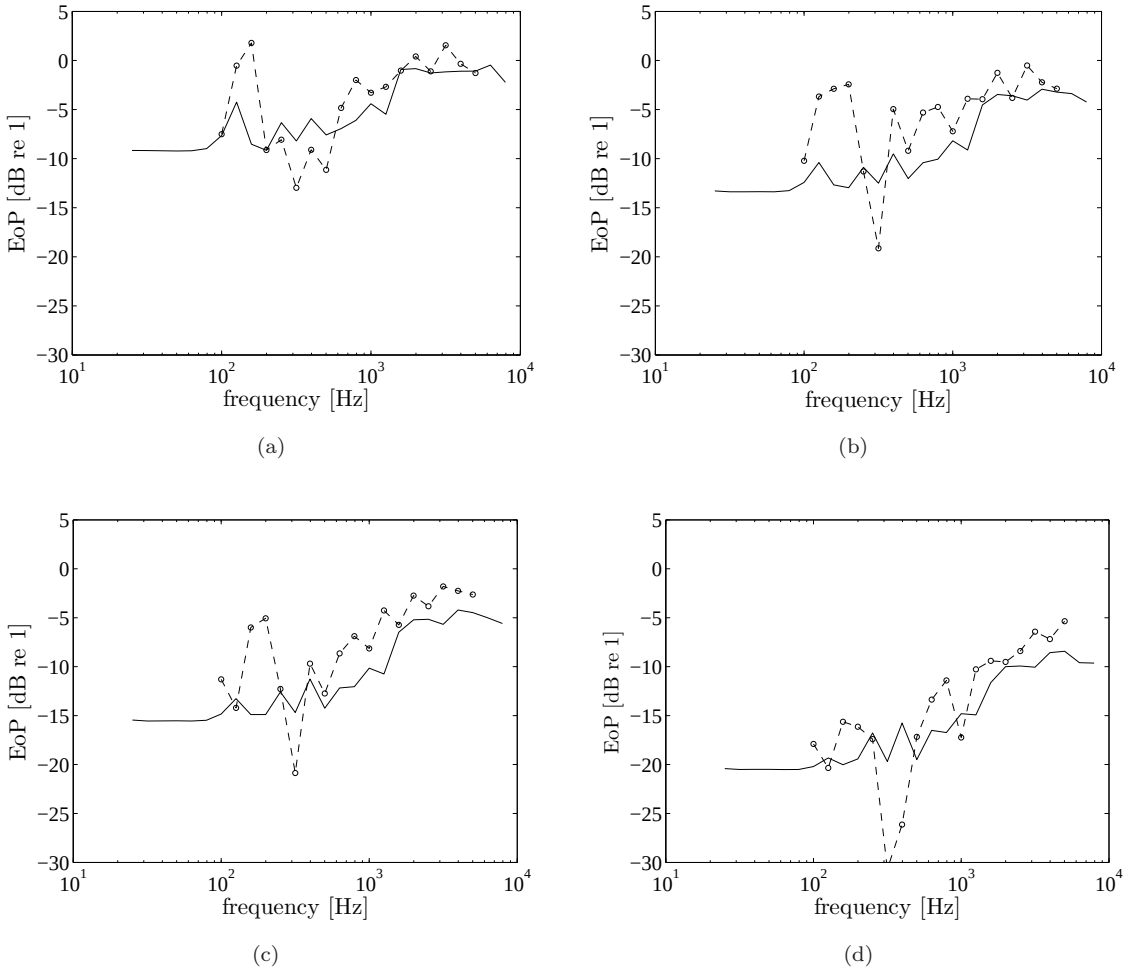


FIGURE 7.41: Effect of perforation on unbaffled 1.5 mm simply supported perforated plates: —theoretical (simply supported), -o-experiment; (a) $d_o = 5$ mm; $\tau = 5\%$, (b) $d_o = 8$ mm; $\tau = 12\%$, (c) $d_o = 10$ mm; $\tau = 19\%$ and (d) $d_o = 15$ mm; $\tau = 44\%$.

efficiencies and the predictions. The result for the plate with 44% perforation ratio in Figure 7.41(d) seems to have good agreement with the prediction. However, this is most affected by the change of its bending stiffness, as already explained, which is not taken into account in these results.

Equivalent results are shown for the 3 mm simply supported plates in Figure 7.42. Here more fluctuations can be seen below 1 kHz. Above 1 kHz where the baffled condition begins, the measured effect of perforation is mostly less than the prediction by 2−5 dB. This can also be seen in Figure 6.11 where the baffled plate has lower EoP than does the unbaffled plate.

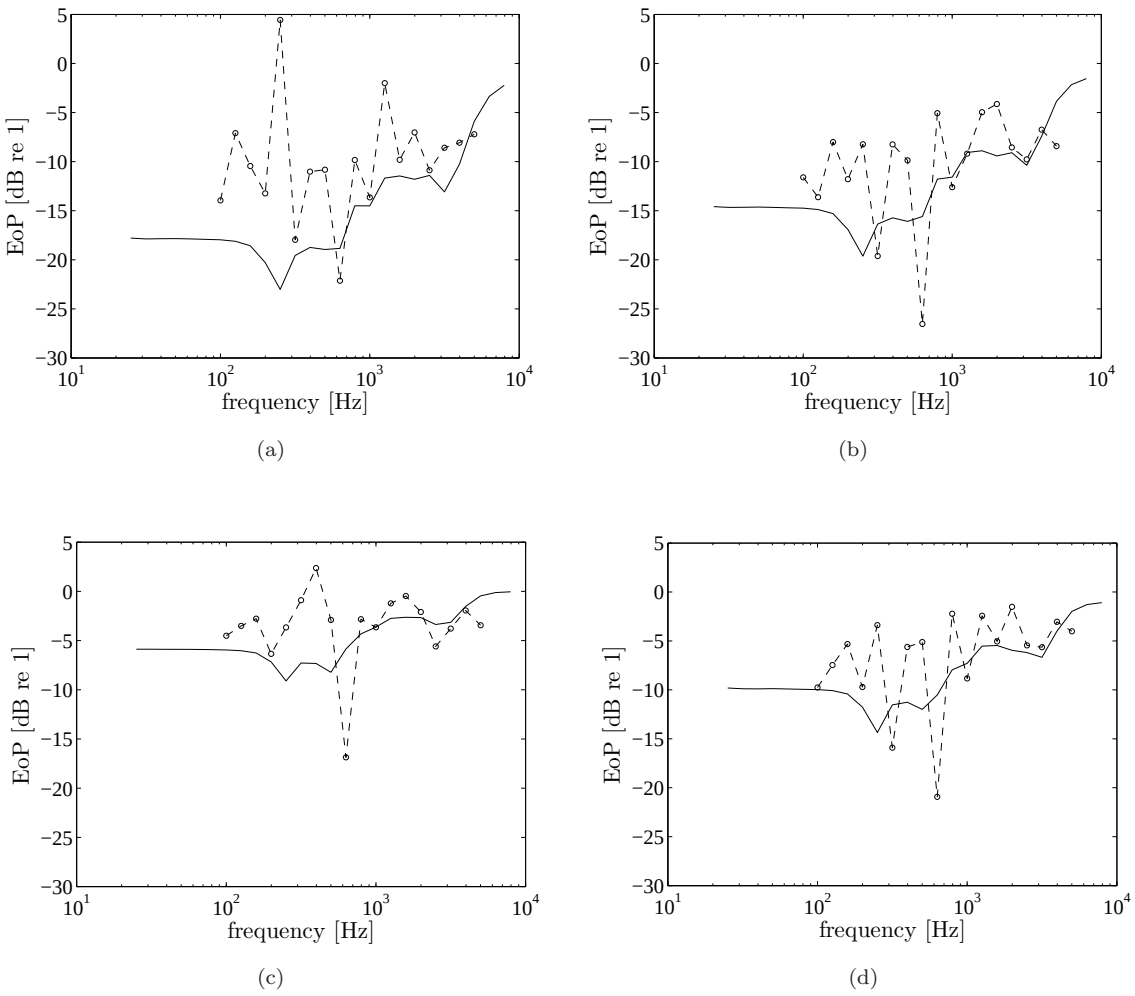


FIGURE 7.42: Effect of perforation on unbaffled 3 mm simply supported perforated plates: —theoretical (simply supported), $-\circ-$experiment; (a) $d_o = 5$ mm; $\tau = 20\%$, (b) $d_o = 10$ mm; $\tau = 20\%$, (c) $d_o = 15$ mm; $\tau = 7\%$ and (d) $d_o = 25$ mm; $\tau = 20\%$.

### 7.4.2 Radiation efficiency results for free-free plates

The measured radiation efficiencies for free-free boundary conditions are shown in Figure 7.43 for 1.5 mm plates and in Figure 7.44 for 3 mm plates. These show good agreement with the predictions, although the latter are for simply supported boundary conditions.

For the 12 mm plates, the results are plotted in Figure 7.45. It can be seen that the measured radiation efficiencies show high fluctuations relative to the predictions. This is due the low modal density especially below the critical frequency (1 kHz).

For the 1.5 mm plates the measured results are greater than the predictions in the

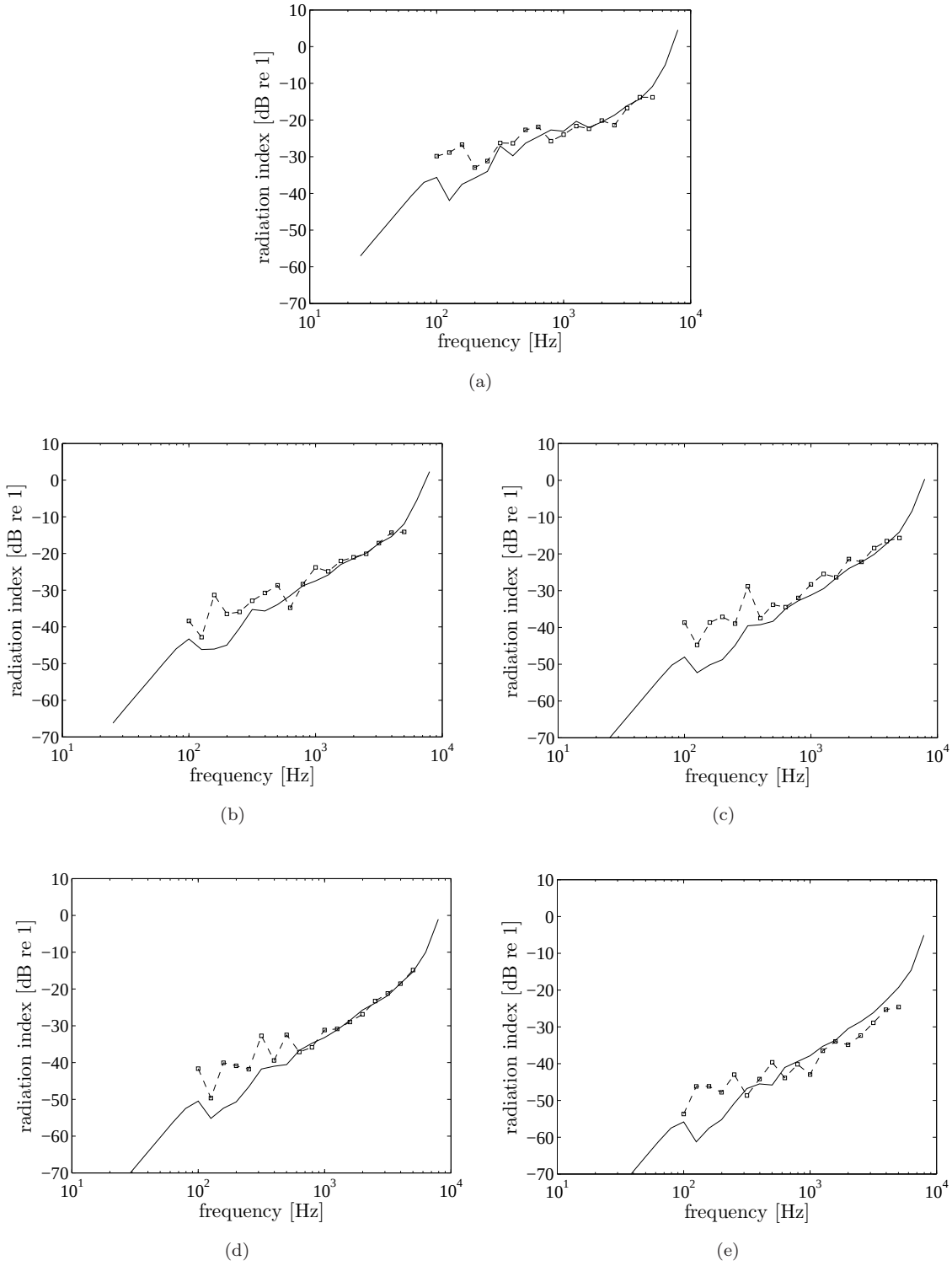


FIGURE 7.43: Radiation efficiency of unbaffled 1.5 mm free-free perforated plates: — theoretical (simply supported), -□-experiment; (a) unperforated, (b) $d_o = 5$ mm; $\tau = 5\%$, (c) $d_o = 8$ mm; $\tau = 12\%$, (d) $d_o = 10$ mm; $\tau = 19\%$ and (e) $d_o = 15$ mm; $\tau = 44\%$.

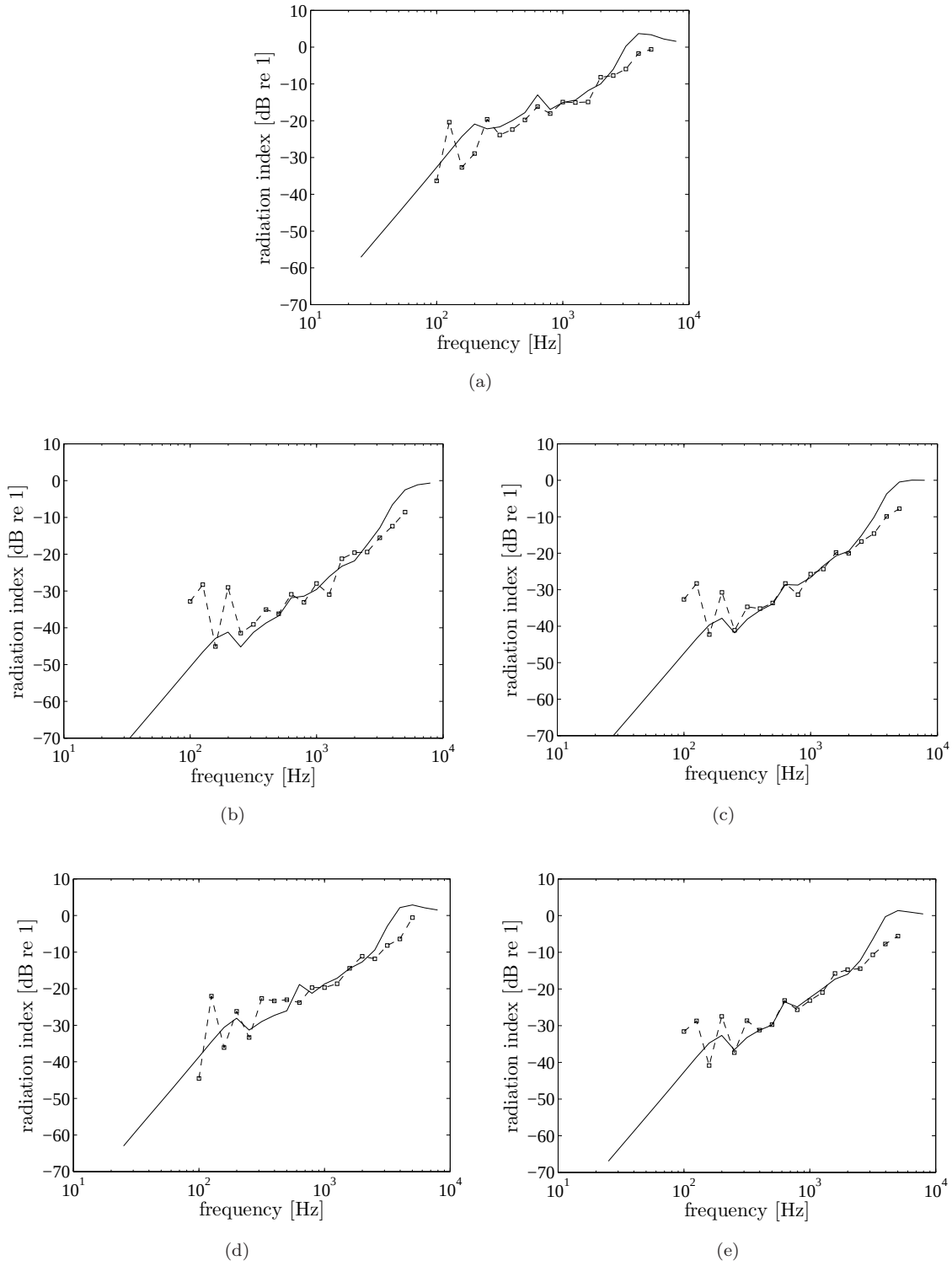


FIGURE 7.44: Radiation efficiency of unbaffled 3 mm free-free perforated plates: — theoretical (simply supported), -□-experiment; (a) unperforated, (b) $d_o = 5$ mm; $\tau = 20\%$, (c) $d_o = 10$ mm; $\tau = 20\%$, (d) $d_o = 15$ mm; $\tau = 7\%$ and (e) $d_o = 25$ mm; $\tau = 20\%$.

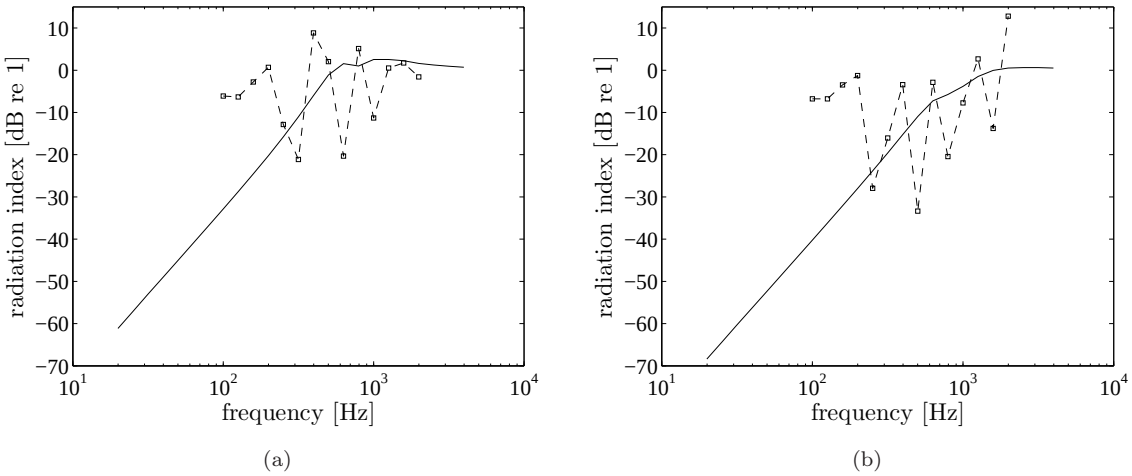


FIGURE 7.45: Radiation efficiency of unbaffled 12 mm free-free perforated plates: — theoretical (simply supported), -□-experiment; (a) unperforated and (b) $d_o = 25$ mm; $\tau = 20\%$.

region 100−300 Hz. Below 200 Hz (i.e. for centre frequency band 100,125 and 160 Hz), this could be due to errors from the measured spatially mean-square sound pressure $\left\langle \overline{p_Q^2} \right\rangle$ as the field is not diffuse below this frequency (the cross-over frequency is 185 Hz). This could also be due to unreliable measured data, as they are still very close to the noise floor (within 5 dB, see Figure 7.35(a)) particularly for the plates in Figure 7.43(c), (d) and (e). This could be improved by trying to increase the acoustic excitation level or using an accelerometer which is more sensitive at low frequency. However this has not been done.

The 3 mm plates show a similar effect for 100−300 Hz where high fluctuations appear. Especially for 100−200 Hz, these are again likely to be because the measured data is below the cross-over frequency of the room. In addition, it should be noted that in the experiments only one mechanical force excitation position was applied. This could be possible source of discrepancies between measurement and prediction below 300 Hz. As explained in Chapter 2, the variability of the radiation efficiency due to the use of a single force position could lead to up to around ±5 dB differences in the corner mode region for a 3 mm thick plate compared with the result for an average over force positions. This variability then converges in the edge mode region and above the critical frequency.

Above 3 kHz the measured radiation efficiency of the 3 mm plates, particularly for the perforated plates, is lower than the measurements. The trend suggests that the

measured result tends toward a higher critical frequency. This can be explained as in Section 5.5 that because of the perforation, the bending stiffness and the plate mass are changed, resulting to the resonance frequency shift. For the plate samples with 20% perforation ratio and all have similar XLE and YLE, the critical frequency is expected to be 4.8 kHz.

The good agreement found between the measured results for free-free boundary conditions and the theoretical result for the simply supported boundary conditions also raises an interesting finding. The hypothesis has been made in Chapter 4 that for an unbaffled plate, the boundary condition has less effect on the radiation efficiency than for a baffled plate because the process of cancellation can still happen through the plate edges effectively. Moreover, the cancellation becomes more effective if the plate is perforated, particularly along the plate edges for the higher hole density. This may explain the satisfactory agreement between the results of the free-free boundary condition in the experiment and the theoretical predictions of the simply supported boundary condition. As already shown in Figure 4.11 and Figure 4.12 in Chapter 4, the results for a simply supported plate and a guided-guided plate show the almost same radiation efficiency even in the corner mode region. Meanwhile for the same case, differences up to 10 dB in the corner mode region and 5 dB in the edge mode region are found for the baffled plates in Figure 4.5 and Figure 4.7. This at least shows that, for the unbaffled case, the condition of the plate edges does not give a significant effect to the sound radiation. However, to validate this hypothesis more fully, a model for the unbaffled free-free plate would be required.

The effect of perforation (EoP) for 1.5 mm free-free plates is shown in Figure 7.46. In an average sense, this has good agreement with the predictions, particularly above 400 Hz. For the plate with the highest perforation ratio (44%) in Figure 7.46(d), again, the effect of perforation on material properties should be taken into account.

A satisfactory agreement between the measured EoP and the prediction can also be seen in Figure 7.47 for the 3 mm free-free plates above 400 Hz. The measured results follow the trend of the prediction up to frequencies above the critical frequency (4 kHz). For each 3 mm perforated plate, a peak appears at 1.6 kHz, which is roughly 3 dB greater than the prediction. This comes from the measured radiation efficiency for the solid plate (see Figure 7.44(a)) where at 1.6 kHz, the measured result is 3 dB

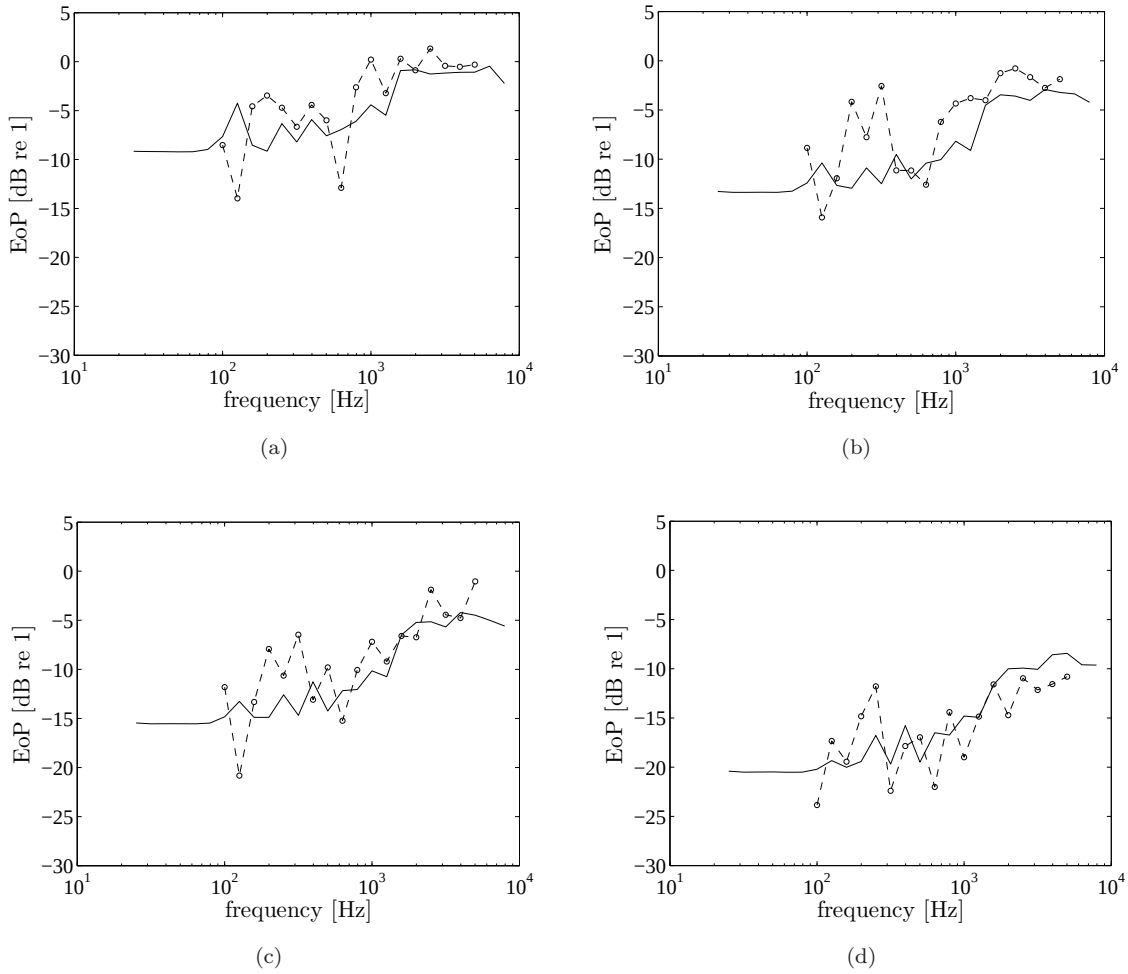


FIGURE 7.46: Effect of perforation on unbaffled 1.5 mm free-free perforated plates: —theoretical (simply supported), $-\circ-$experiment; (a) $d_o = 5$ mm; $\tau = 5\%$, (b) $d_o = 8$ mm; $\tau = 12\%$, (c) $d_o = 10$ mm; $\tau = 19\%$ and (d) $d_o = 15$ mm; $\tau = 44\%$.

lower than the prediction. This illustrates that it is not easy to obtain a reliable result of the EoP because one has to deal with four input errors, i.e. from the sound power and the mobility measurements on the perforated and the unperforated plates.

For the 12 mm plate, a poor agreement of the effect of perforation with the prediction can be seen in Figure 7.48. This is obviously due to poor agreement of the results from the radiation efficiency, accentuated by taking the ratio of two measurements.

### 7.4.3 Comparison with existing measured data

To complement the validation of the model, comparison is made with existing measured data. The data was the experiment made by Pierri [56] in 1977 at ISVR for 1.22 mm

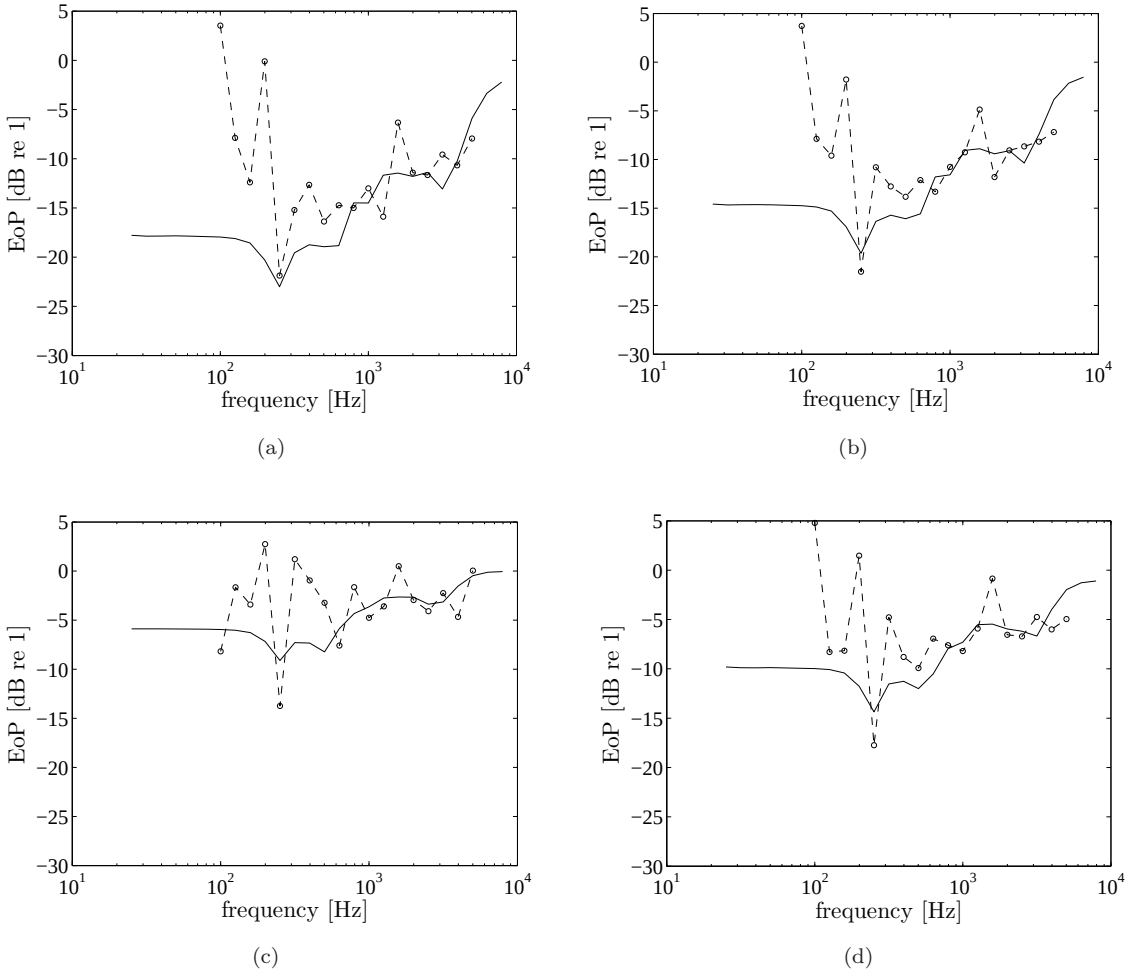


FIGURE 7.47: Effect of perforation on unbaffled 3 mm free-free perforated plates: — theoretical (simply supported), $-\circ-$experiment; (a) $d_o = 5$ mm; $\tau = 20\%$, (b) $d_o = 10$ mm; $\tau = 20\%$, (c) $d_o = 15$ mm; $\tau = 7\%$ and (d) $d_o = 25$ mm; $\tau = 20\%$.

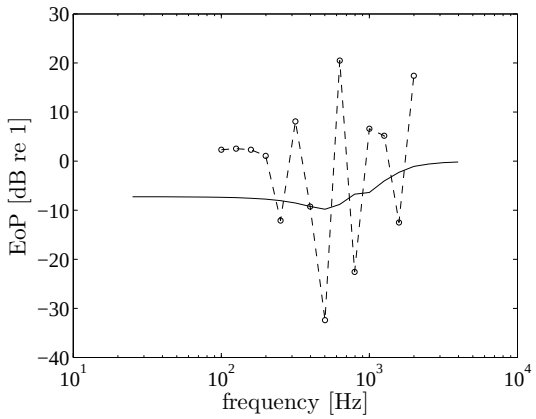


FIGURE 7.48: Effect of perforation on unbaffled 12 mm free-free perforated plate:— theoretical (simply supported), -o-experiment; $d_o = 25$ mm; $\tau = 20\%$.

thick perforated steel plates having dimensions of $0.3 \times 0.3$ m. The results can be seen in Figure 1.3 in Chapter 1.

The measurement of the radiation efficiency was conducted using the direct method, where the plate was excited by a broadband force from a shaker and the radiated sound pressure was measured across the reverberant room. The plate sample was supported by the edges with very soft foam rubber so that free-free boundary conditions could be assumed.

Figure 7.49 shows a comparison of the radiation index from the model with that from the established measured data. The damping loss factor is not known. In the calculation it is assumed to be very low, i.e. $\eta = 0.001$. It can be seen that a good agreement is achieved with these results, including the unperforated plate. For the plate having 41.5% perforation ratio, the measured data is greater than the prediction by roughly 10 dB. This could be due to the effect of noise from the shaker. As the radiated sound was very low from this plate, the shaker noise might have a significant contribution to the measured data.

## 7.5 Radiation efficiency results for plates near a rigid surface

This section describes experimental results for the radiation efficiency for a plate located close to a rigid surface. For this, the measurement setup was similar to the previous case. The only difference was the arrangement of the plate. The plate was supported on a soft pieces of foam placed under each corner of the plate on the floor of the reverberant chamber. This still produced the free-free boundary conditions as the plate edges can move freely on the very soft foam. The thicknesses of the foam used were 1, 2 and 4 cm. This thickness thus becomes the distance of the plate from the rigid surface $D$. The arrangement is shown in Figure 7.50.

The radiation efficiency of a plate located close to a rigid surface is very small at low frequency, particularly for the perforated plates. This causes problems in measuring such a small acceleration. Figure 7.51 plots the plate squared acceleration for unperforated and perforated plates. It can be seen that, for the perforated plate in

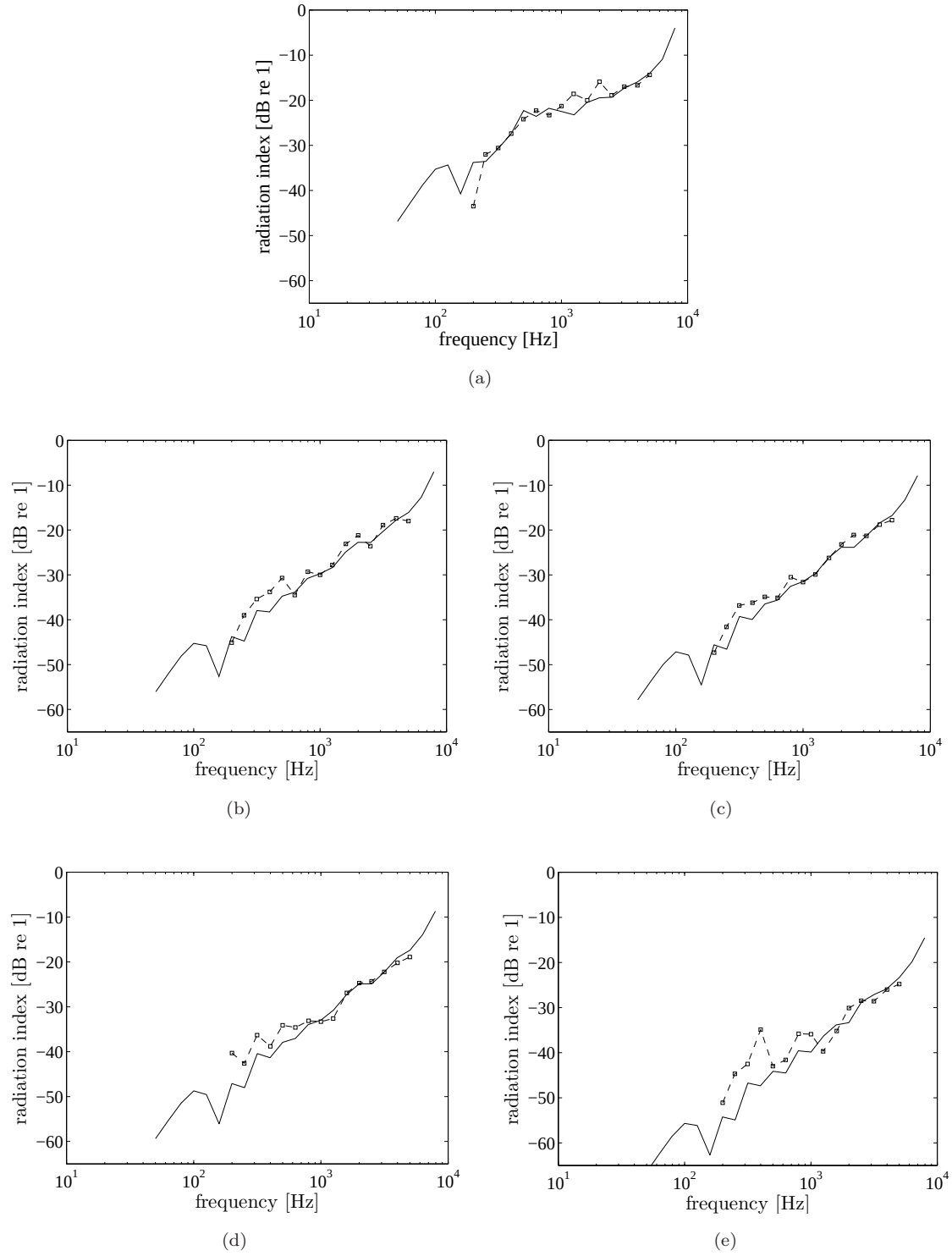


FIGURE 7.49: Comparison of the radiation index from analytical calculation (—) with that from existing measured data (-□-); (a) unperforated, (b) $d_o = 5.6$ mm; $\tau = 5.7\%$, (c) $d_o = 7.1$ mm; $\tau = 9.4\%$, (d) $d_o = 8.8$ mm; $\tau = 14.1\%$ and (e) $d_o = 15$ mm; $\tau = 41.5\%$ (mild steel; $0.3 \times 0.3 \times 0.0012$ m, $\eta = 0.001$).

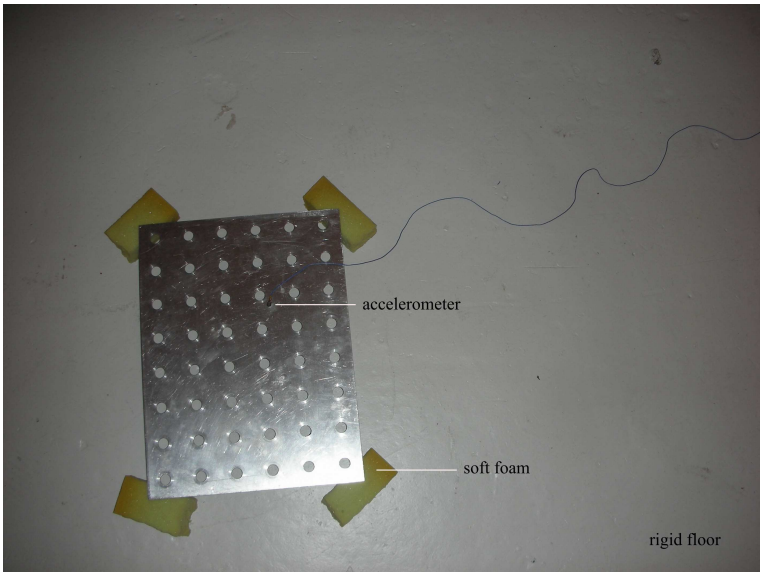


FIGURE 7.50: A perforated plate placed close to a rigid surface.

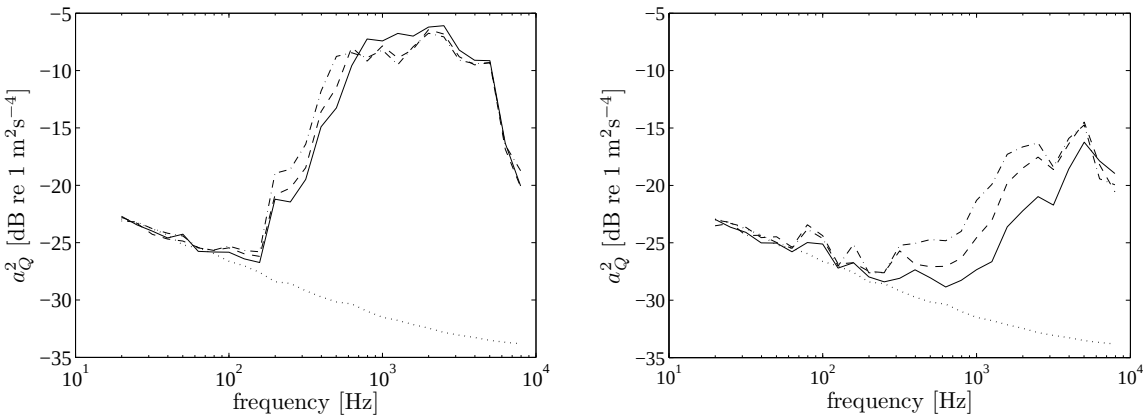


FIGURE 7.51: Squared acceleration of plates near rigid surface ($t_p = 3$ mm): (a) unperforated and (b) $d_o = 5$ mm, $\tau = 20\%$ (—$D = 1$ cm, − − $D = 2$ cm, − · −$D = 4$ cm, · · · noise floor).

Figure 7.51(b), the noise floor contaminates the data up to 400 Hz for $D = 1$ cm. Meanwhile for the solid plate in Figure 7.51(a), the contamination appears to be only up to 160 Hz. However to ensure a signal-to-noise of 10 dB would limit the frequency range to 400 Hz and above for the unperforated plate and to 2 kHz and above for the perforated plate in Figure 7.51(b).

Figure 7.52 shows these results in the form of the measured normalised sound power for the unperforated 3 mm plate. It can be seen that, below 630 Hz, the plate radiates less sound as it is moved closer to the rigid surface. Above 2 kHz, the plate radiates almost the same power for the three different distances. The radiation efficiency is

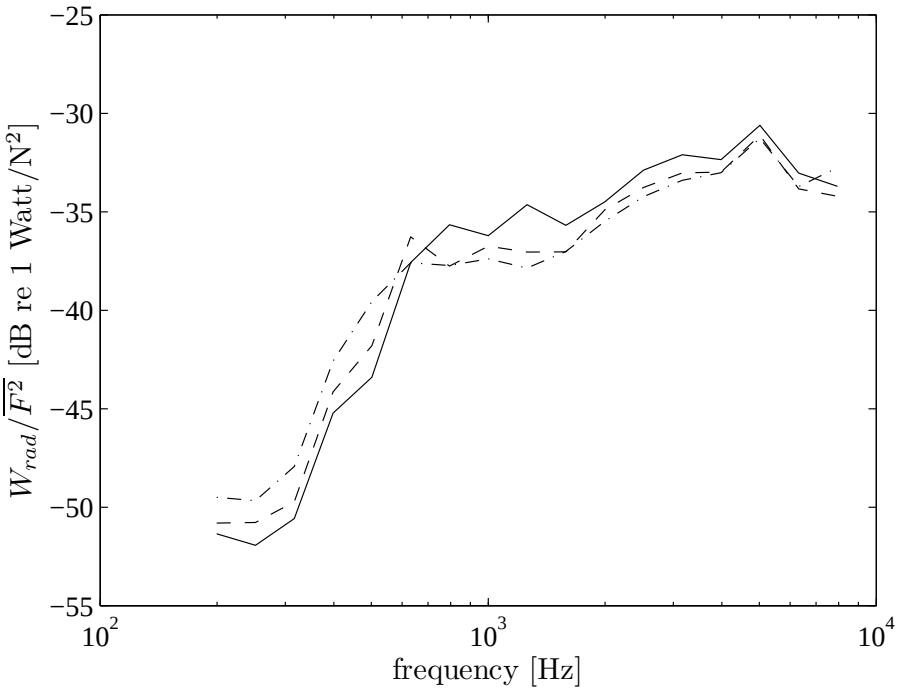


FIGURE 7.52: Measured normalised sound power of a plate near a rigid surface (unperforated, $t_p = 3$ mm): —$D = 1$ cm, − − $D = 2$ cm, − · −$D = 4$ cm.

shown in Figure 7.53, along with the results without the rigid surface. This shows that the effect of the rigid surface occurs below about 600 Hz where the results are less than the measured result without the rigid surface. Above 600 Hz, the measured radiation efficiency from the plate close to the rigid surface starts to exceed that of the plate in the absence of the rigid surface by 5−6 dB on average. These results are consistent with the theory in Chapter 5 for the unperforated plate (see Figure 5.34), although there is less difference between the predictions for different distances than between the corresponding measurements.

The measured radiation efficiency for the 3 mm unperforated plates is plotted together with the predictions in Figure 7.54 for different distances from the rigid surface. In an average sense, a good agreement can be seen between the measured result and the prediction. The data below 200 Hz is contaminated by the noise floor from the accelerometer so that the low frequency trend of 60 dB/decade could not be validated.

The effect of the rigid surface is shown in Figure 7.55, comparing the data from measurement and theoretical calculation. A good agreement is found above 700 Hz.

Figure 7.56 plots the radiation index for the perforated 3 mm plates having 5 mm

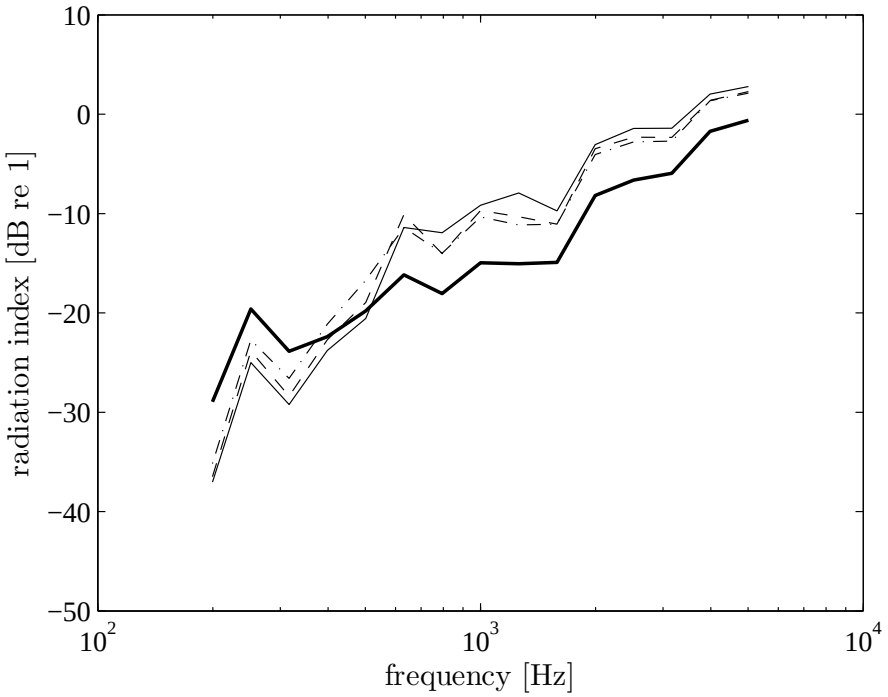


FIGURE 7.53: Measured radiation index of a plate near a rigid surface ($t_p = 3$ mm, unperforated): —absence of rigid surface, —$D = 1$ cm, − − $D = 2$ cm, − · −$D = 4$ cm.

diameter holes. This shows generally good agreement between predictions and measurements. At high frequencies the measured data deviates toward a higher critical frequency, as already seen in Figure 7.44 for the case without the rigid surface. At low frequencies discrepancies occur due to contamination by the measurement noise of the accelerometer particularly for the smaller distances (see Figure 7.51).

Figure 7.57 shows some measured results compared with the predictions for the 1.5 mm perforated plates with various hole diameters and plate distances. The fluctuations at low frequency are again due to noise contamination, but otherwise generally good agreement is seen.

Figure 7.58 presents one example of the effect of the rigid surface from the measured data together with the theory. As expected from the latter, the perforated plate located close to a rigid surface will radiated less sound than that without the reflecting rigid surface, below a certain frequency. The plate at a closer distance will produce a lower sound radiation over a wider frequency range. At higher frequency, the sound radiation exceeds that from the plate in the absence of the surface by up to 5 dB (see Figure 5.39). A reasonably good agreement between the experiment and the theory can be seen in this region.

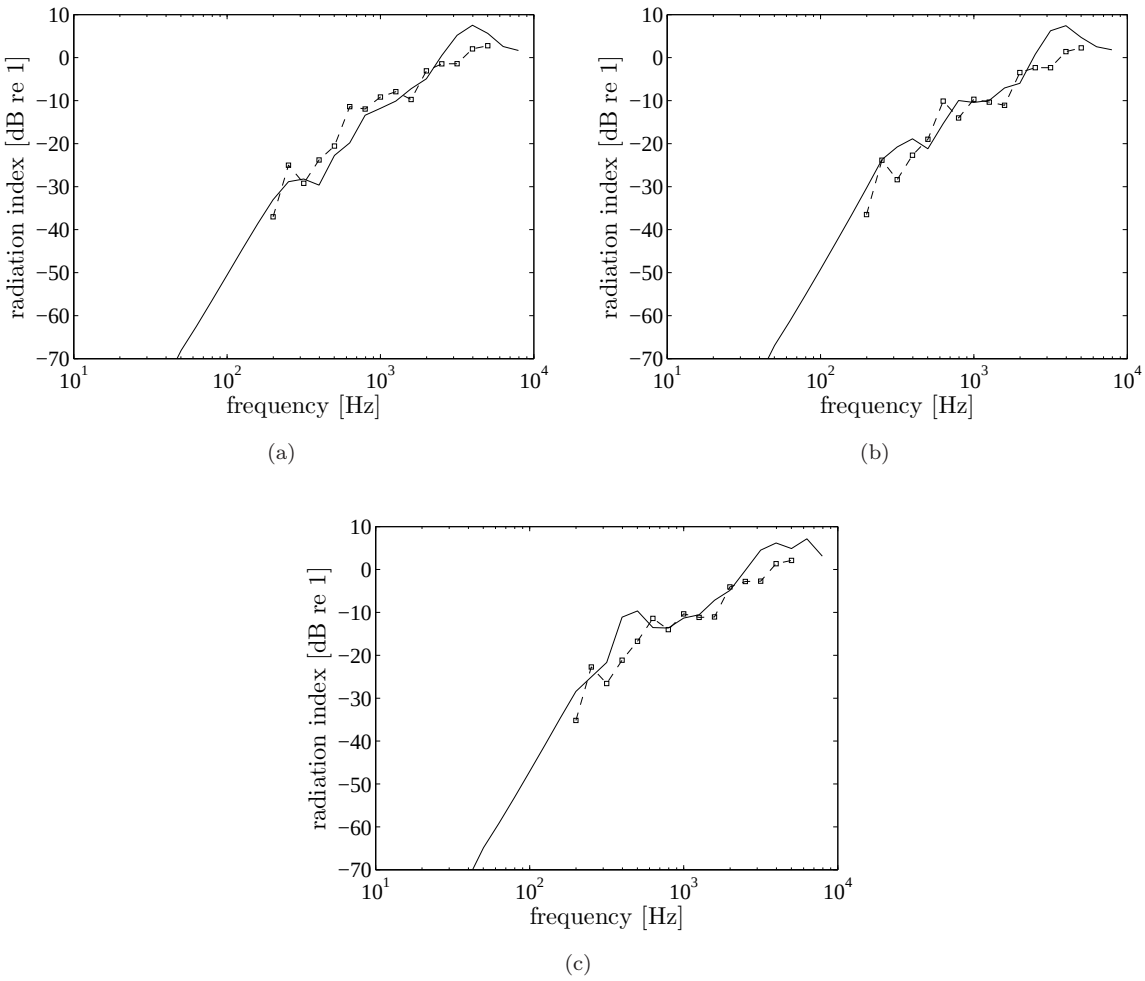


FIGURE 7.54: Radiation efficiency of 3 mm solid plates near a rigid surface: — theoretical, -□- experiment; (a) $D = 1$ cm, (b) $D = 2$ cm and (c) $D = 4$ cm.

Generally, the measured data has a reasonably good agreement with the model. As for the case of the stand-alone plate in the previous section, the experiment was conducted in free-free conditions, while the model is for a simply supported plate. This experiment again confirms that the edge conditions is less sensitive for the unbaffled case.

The foam placed at the corners to support the plate (see Figure 7.50) may affect the sound radiation, particularly in the corner mode region, as the foam is a sound absorption material. However, the measured results for the solid 3 mm thick plate in Figure 7.54 seem to be well predicted even in the corner mode region below 700 Hz. For the perforated plates, the measured data are affected by the accelerometer noise below this frequency.

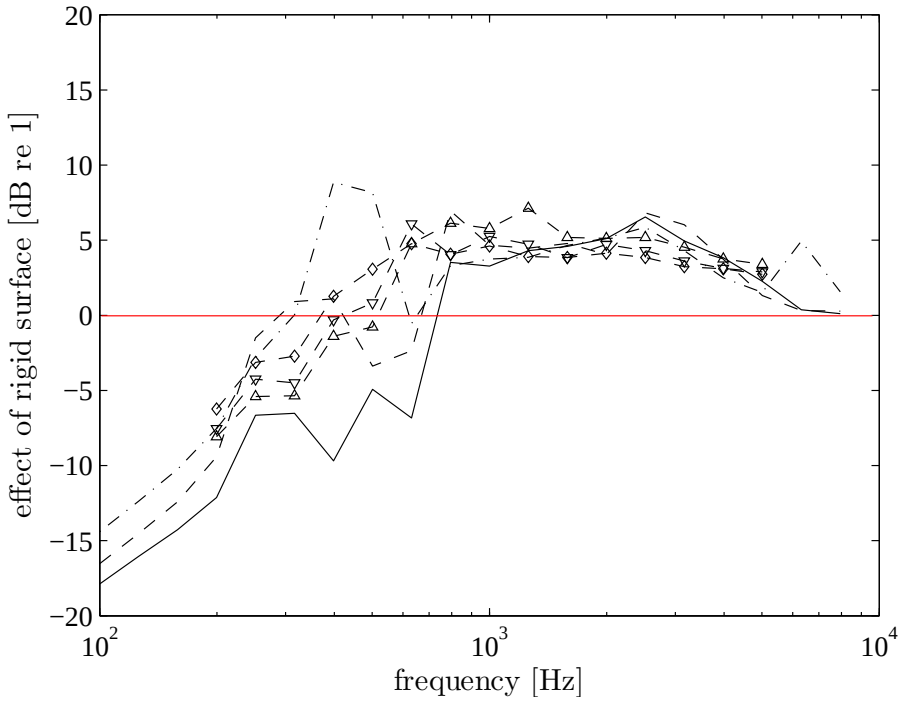


FIGURE 7.55: Measured effect of rigid surface on sound radiation of an unbaffled plate (unperforated, $t_p = 3$ mm): ($\triangle$)—$D = 1$ cm, ($\triangledown$)$--$ $D = 2$ cm, ($\Diamond$)$-\cdot-$ $D = 4$ cm (experiment: marked line, theoretical: unmarked line).

## 7.6 Summary

The theoretical predictions of radiation efficiency of perforated plates have been successfully validated through experiments. The measurements included the spatially averaged mobility and the sound power per unit mean-square force, the latter being obtained using a reciprocity technique.

In terms of the mechanical measurement, i.e. the mobility, the application of simply supported boundary conditions has been very well achieved; a good agreement was obtained against the prediction. However, for the acoustic measurement, it was found that the constructed frame did not allow the unbaffled condition to be fully obtained. Above around 1 kHz, the condition changed to be effectively baffled due to the blocking of the radiated sound field by the frame. In this frequency range the measurements showed good agreement with predictions for a baffled perforated plate.

For free-free boundary conditions, a very good agreement was obtained with the prediction for the radiation efficiency of the perforated plates even though the predictions are based on simply supported boundaries. It is believed that, for the unbaffled case,

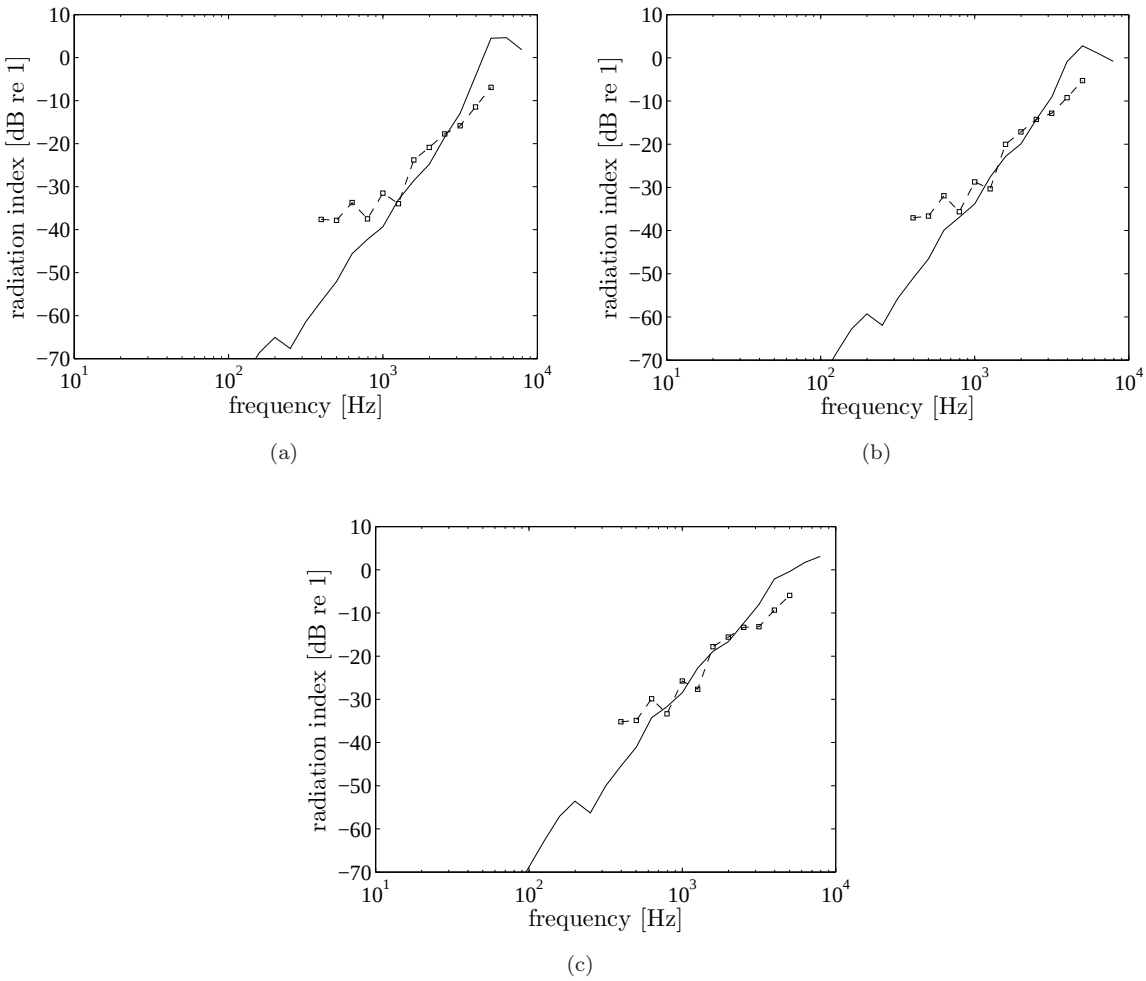


FIGURE 7.56: Radiation efficiency of 3 mm perforated plates near a rigid surface ($d_o = 5$ mm, $\tau = 20\%$): — theoretical, -□- experiment; (a) $D = 1$ cm, (b) $D = 2$ cm and (c) $D = 4$ cm.

the sound radiation is less sensitive to the conditions at the plate edges, as demonstrated in Chapter 4 using guided boundaries.

For a plate close to a rigid surface, problems occurred in the validation at low frequencies where the data is contaminated by the accelerometer noise due to a very small response and very low radiation efficiency. Apart from this, a reasonably good agreement is also achieved between the model and the measured data.

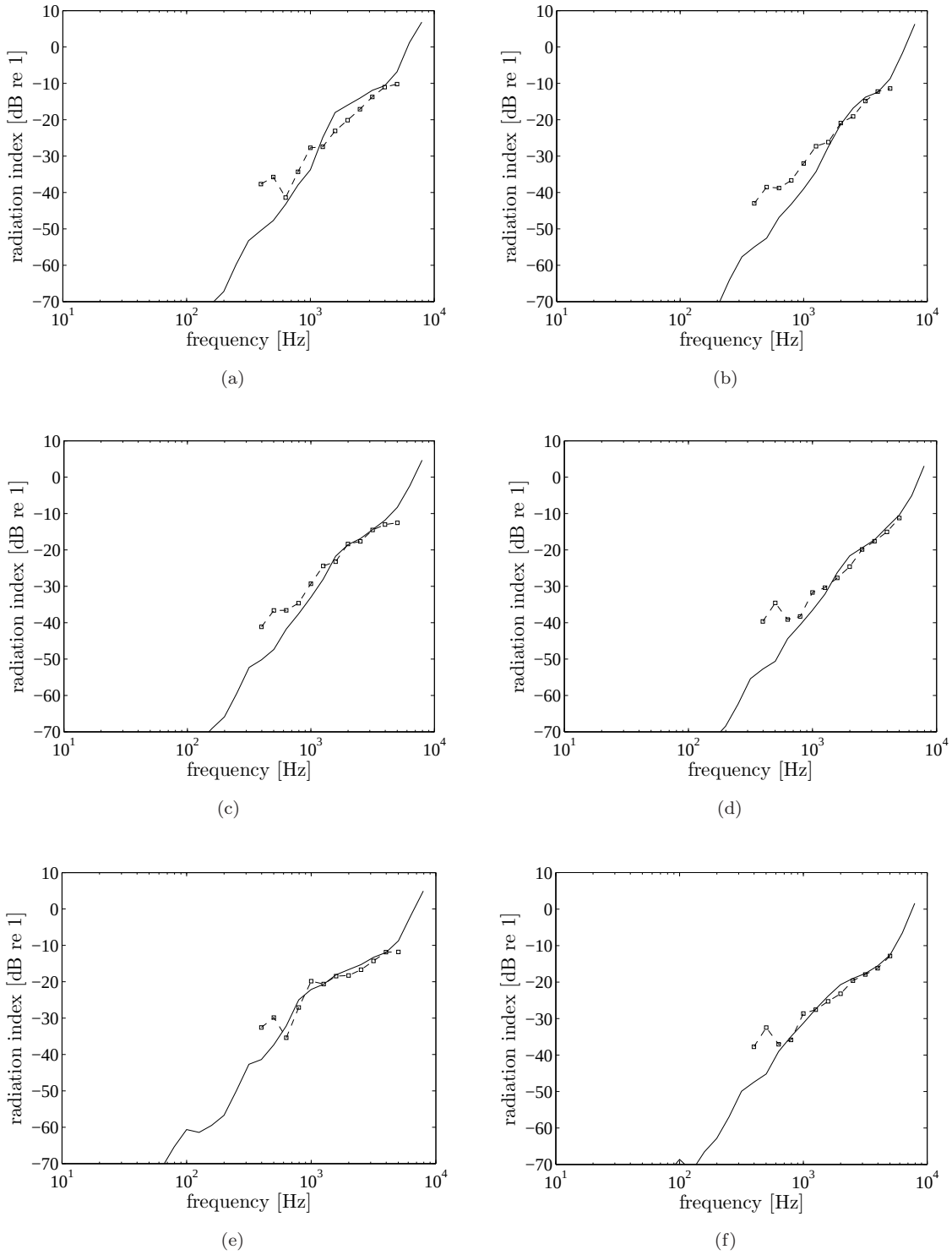


FIGURE 7.57: Radiation efficiency of perforated 1.5 mm plates near a rigid surface: —theoretical , -□-experiment; $D = 1$ cm: (a) $d_o = 5$ mm, $\tau = 5\%$, (b) $d_o = 8$ mm, $\tau = 12\%$; $D = 2$ cm: (c) $d_o = 8$ mm, $\tau = 12\%$, (d) $d_o = 10$ mm, $\tau = 19\%$; $D = 4$ cm: (e) $d_o = 5$ mm, $\tau = 5\%$, (f) $d_o = 10$ mm, $\tau = 19\%$.

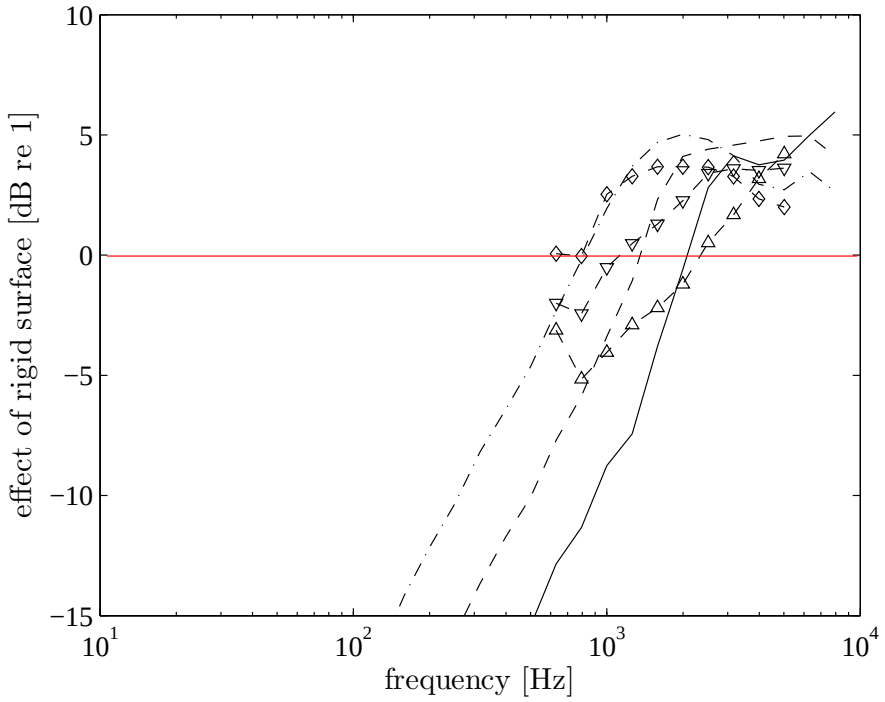


FIGURE 7.58: Measured effect of rigid surface on sound radiation of an unbaffled perforated plate ($t_p = 1.5$ mm, $d_o = 10$ mm, $\tau = 19\%$): ($\triangle$)—$D = 1$ cm, ($\triangledown$)$--$ $D = 2$ cm, ($\Diamond$)$-\cdot-$ $D = 4$ cm (experiment: marked line, theoretical: unmarked line).

# Chapter 8

# Conclusions

The primary work of this thesis relates to the sound radiation from a perforated plate. Models have been investigated for baffled and unbaffled plates, before introducing the effect of perforation. This chapter summarises the main conclusions of this thesis and makes recommendations for further work.

## 8.1 Baffled plates

Several methods for calculating the radiation efficiency of a baffled plate have been investigated. The emphasis is placed on methods which calculate the sound radiation for a point force excitation averaged over all possible locations on the plate. The average radiation efficiency is obtained using a summation over all modes of vibration.

The wavenumber domain approach to determine the sound power has been found to be more efficient than the spatial domain approach. Due to the oscillatory nature of its integrand, the latter needs a high resolution of integration segments to obtain an accurate result. Apart from this, both methods give the same results. Although appearing attractive, the FFT method does not provide an efficient way for calculating the average radiation efficiency. Although the FFT itself is fast, the need to calculate the modified Green's function to avoid the singularity increases the calculation time.

The FFT method is also not efficient for calculations on a mode-by-mode basis. However, it has been used successfully to calculate the radiation efficiency from a baffled

plate for a single forcing position. Selecting 20 points scattered over the surface of the plate, the variation of radiation efficiency due to the location of a single point force position has been determined. The largest variations occur in the corner mode regions where a range of roughly ±5 dB is found in $\frac{1}{3}$ octave band results for a 3 mm thick plate. It is also found that this variability does not depend strongly on the plate damping or the plate dimensions, but increases as the plate thickness is reduced.

The effect of boundary conditions on the radiation efficiency of a baffled plate has been considered by comparing the results for simply supported and guided-guided plates and also combinations of these boundary conditions. It has been shown that the guided-guided plate has a radiation efficiency which is up to about 10 dB lower in the corner mode regions and up to 5 dB lower in the edge mode regions than that of a simply supported plate. This confirms that, for the baffled plate, the sound radiation is sensitive to the condition of the plate edges.

## 8.2 Unbaffled plates

Two methods for calculating the radiation efficiency of an unbaffled plate have been implemented. The iterative method using the FFT appears to have convergence problems at low frequencies. It is also found that it cannot cope with higher order plate modes. The method proposed by Laulagnet gives a much better result. This gives results directly in the form of the radiation from the forced response and can be studied in terms of modal contributions, in the same way as for the baffled plate. The calculation can be performed up to very high frequency. It is found that, below the critical frequency, the radiation efficiency of an unbaffled plate is lower than that of a baffled plate. The difference reduces as the frequency increases. Above the critical frequency the results are identical.

The ratio between the average radiation efficiency of unbaffled and baffled plates has been used to develop an empirical formula. This gives a very good agreement with the analytical calculations for unbaffled plates over a wide range of frequency.

The effect of boundary conditions on the radiation efficiency is found to be much less significant for the unbaffled plate than for the baffled case, even in the corner mode

region. The difference between the radiation efficiency of a simply supported plate and a guided-guided plate is found to be less than 2 dB for frequencies above the fundamental mode of the simply supported plate for damping loss factor $\eta = 0.1$. As the damping is reduced to be very small ($\eta = 0.01$), the difference increases to be 3−4 dB, while for the baffled plate it is around 10 dB. Good agreement is found between predicted radiation efficiencies for simply supported plates and measured results for free-free boundaries.

## 8.3 Perforated plates

To calculate sound radiation from a perforated plate, three methods have been implemented. For a perforated plate in an equally perforated baffle a method by Fahy and Thompson has been implemented. The results are presented particularly in terms of the effect of perforation (EoP). From this, a simple approximate formula for the EoP with a 20 dB dependency has been proposed which gives a good agreement up to half the critical frequency. It is also shown that the EoP for a perforated plate in a perforated baffle does not depend on the plate dimensions.

By extending Laulagnet's model for an unbaffled plate, a model of a perforated unbaffled plate has been developed. In this case, the EoP is found to depend on the plate thickness and dimensions. A proposed approximate formula for the EoP gives a good agreement with the theory up to half the critical frequency. This formula can be used for the purpose of an engineering design guide in considering perforation for noise control.

A perforated baffled plate model has been developed by discretising the plate and the holes into discrete elementary sources. Due to practical limitations on the number of elements that can be used, this could only be used for plates with a moderate number of holes. Using this model, it was found that the assumption of a continuous impedance on the plate surface is only valid when the distance between holes is less than an acoustic wavelength for a plate moving with uniform velocity (rectangular piston) and less than half an acoustic wavelength when a plate is in bending vibration below its critical frequency.

It is shown using each model that the radiation efficiency can be reduced by increasing the perforation ratio or by increasing the hole density (reducing the hole size for the same perforation ratio).

Experimental results for free-free plate boundary conditions give a good agreement with the theory, although the latter is for simply supported edges. This is consistent with the finding that the boundary conditions have a less significant effect on the radiation efficiency for the unbaffled case.

The realisation of simply supported boundary conditions experimentally has been satisfactorily achieved from a mechanical point of view. In the acoustical measurements, however, the frame designed to support the plate prevents the condition from being unbaffled. The frame blocks the radiated sound from interacting with the other side of the plate. It appears that above approximately 1.5 kHz, the condition becomes baffled rather than unbaffled.

The model for the perforated unbaffled plate has also been extended to consider the situation where the plate is located close to a reflecting rigid surface. It is found that, at low frequencies, the radiation efficiency is less than that of the unbaffled plate without the presence of the rigid surface. As the frequency increases, the sound radiation becomes more than (for a solid plate) or almost similar to (for a perforated plate) the radiation from the plate without the rigid surface. Experiments also give a satisfactory agreement between the measured data and the theory for this situation.

The changes in the mass and bending stiffness due to perforation have also been considered. The natural frequencies are reduced slightly and the frequency average mobility is increased. The critical frequency is also increased slightly by these changes, as confirmed in the measurements. As a result, for the lighter plate sample (1.5 mm thick) with a large perforation (44% perforation ratio), the level of measured radiation efficiency is found to be up to 5 dB less than the theory neglecting this effect.

It has been shown that perforation of a vibrating plate has a good potential as a noise control measure. For a 20% perforation ratio, the radiated sound power can be reduced by a substantial amount, in the range of $10-20$ dB. However, allowance should also be made for the increase of the plate vibration due to perforation.

## 8.4 Recommendations for further work

Models have been developed for the sound radiation from a plate with simply supported and guided-guided boundary conditions. Further work is required to develop models for other plate boundary conditions, such as clamped or free. An efficient analytical or numerical model is desirable in order to calculate results for the multi-modal responses. For this it is necessary to solve the Fourier transform of mode shape functions for these edge conditions.

To improve the experimental validation for the radiation efficiency of a simply supported plate, it is necessary to reduce the frame height and width as much as possible while still providing a sufficient restraint. In practice this may not be feasible. An alternative would be to construct a more 'open' supporting structure by using a perforated beam.

It has been shown that introducing perforation into a plate can change the resonance frequencies and critical frequency. This needs a further, more rigorous investigation, as the existing models still have some limitations. The proposed prediction model should be tested for various plate dimensions and thicknesses; it should take account of the perforation array and geometry. Its effect on the radiation efficiency also has to be modelled. This can be extended to develop formulae to allow the trade-off to be investigated between the effect on stiffness or structural integrity and sound radiation.

The empirical formulae for the unbaffled plate need improvement particularly in the edge mode region and around the critical frequency. An analytical approach is preferred which involves the understanding of the physical phenomena.

Finally, the models involving the effect of the array of holes, especially on the end corrections of the hole impedance, need further investigation. The end corrections for holes due to a vibrating, instead of a static plate also need to be investigated.

# References


[1] B. Berglund, T. Lindvall, and D. H. Schwela. Guidelines for community noise. Technical report, World Health Organization, 1999. [http://www.who.int/docstore/peh/noise/guidelines2.html].

[2] I. H. Findell. *Fundamentals of human response to sound*, chapter 3 in Fundamentals of Noise and Vibration (Eds. F. J. Fahy and J. G. Walker). E & FN Spon, 1998.

[3] K. D. Kryter. *The handbook of hearing and the effects of noise: physiology, psychology, and public health*. Academic Press, Boston, 1994.

[4] F. J. Fahy and P. Gardonio. *Sound and Structural Vibration: Radiation, Transmission and Response*. Academic Press, London, 2nd edition, 2006.

[5] G. Maidanik. Response of ribbed panels to reverberant acoustic fields. *Journal of the Acoustical Society of America*, 34:809–826, 1962.

[6] C. E. Wallace. Radiation resistance of a rectangular panel. *Journal of the Acoustical Society of America*, 51:946–952, 1972.

[7] L. Cremer, M. Heckl, and B. A. T. Petersson. *Structure-borne sound*. Springer, Berlin, 3rd edition, 2005.

[8] E. G. Williams. *Fourier Acoustics: Sound Radiation and Nearfield Acoustical Holography*. Academic Press, London, 1999.

[9] L. Rayleigh. *The Theory of Sound*. 2nd edition, 1896.

[10] I. L. Vér and C. I. Holmer. *Interaction of sound waves with solid structures*, chapter 11 in Noise and Vibration Control (Ed. L. L. Beranek). McGraw-Hill, 1971.

[11] F. G. Leppington, E. G. Broadbent F. R. S, and K. H. Heron. The acoustic radiation efficiency of rectangular panels. *Proceedings of the Royal Society London*, A 382:245–271, 1982.

[12] G. Xie, D. J. Thompson, and C. J. C. Jones. The radiation efficiency of baffled plates and strips. *Journal of Sound and Vibration*, 280:181–209, 2005.

[13] M. Bonilha and F. J. Fahy. An approximation to the frequency-average radiation efficiency of flat plates. *Acoustical Society of America*, 138$^{\text{th}}$ meeting, Colombus, Ohio, 1999.

[14] F. G. Leppington, E. G. Broadbent F. R. S, and S. M. Mead. Resonant and non-resonant acoustic properties of elastic panels. I. The radiation problem. *Proceedings of the Royal Society London*, A 406:139–171, 1986.

[15] G. Maidanik. Radiation efficiency of panels. *Journal of the Acoustical Society of America*, 35:115, 1963.

[16] F. G. Leppington, E. G. Broadbent F. R. S, and K. H. Heron. Acoustic radiation from rectangular panels with constrained edges. *Proceedings of the Royal Society London*, A 393:67–84, 1984.

[17] W. L. Li. Vibroacoustic analysis of rectangular plates with elastic rotational edge restraints. *Journal of the Acoustical Society of America*, 120(2):769–779, 2006.

[18] M. C. Gomperts. Radiation from rigid baffled, rectangular plates with general boundary conditions. *Acustica*, 30:320–327, 1974.

[19] M. C. Gomperts. Sound radiation from baffled, thin, rectangular plates. *Acustica*, 37:93–102, 1977.

[20] A. Berry, J. L. Guyader, and J. Nicolas. A general formulation for the sound radiation from rectangular, baffled plates with arbitrary boundary conditions. *Journal of the Acoustical Society of America*, 88(6):2792–2802, 1990.

[21] A. Berry. A new formulation for sound radiation of fluid loaded plates. *Journal of the Acoustical Society of America*, 96(2):2792–2802, 1994.

[22] E. G. Williams and J. D. Maynard. Numerical evaluation of the rayleigh integral for planar radiators using the FFT. *Journal of the Acoustical Society of America*, 72(6):2020–2030, 1982.

[23] E. G. Williams. A series expansion of the acoustic power radiated from planar sources. *Journal of the Acoustical Society of America*, 73(5):1520–1524, 1983.

[24] W. L. Li. An analytical solution for the self and mutual radiation resistances of a rectangular plate. *Journal of Sound and Vibration*, 245(1):1–16, 2001.

[25] P. Vitiello, P. A. Nelson, and M. Petyt. Numerical studies of the active control of sound transmission through double partitions. Technical report, ISVR Technical Report 183, University of Southampton, 1989.

[26] K. A. Cunefare and G. H. Koopmann. Global optimum active noise control: surface and far field effects. *Journal of the Acoustical Society of America*, 90:365, 1991.

[27] S. J. Elliott and M. E. Johnson. Radiation modes and the active control of sound power. *Journal of the Acoustical Society of America*, 94:2194–2204, 1993.

[28] P. Gardonio, E. Bianchi, and S. J. Elliott. Smart panel with multiple decentralized units for the control of sound transmission. Part I: Theoretical predictions. *Journal of Sound and Vibration*, pages 163–192, 2004.

[29] E. G. Williams. Numerical evaluation of the radiation from unbaffled, finite plates using the FFT. *Journal of the Acoustical Society of America*, 74(1):343–347, 1983.

[30] N. Atalla, J. Nicolas, and C. Gauthier. Acoustic radiation of an unbaffled vibrating plate with general elastic boundary conditions. *Journal of the Acoustical Society of America*, 99(3):1484–1494, 1996.

[31] A. D. Pierce. Variational formulations in acoustic radiation and scattering. *Physical Acoustics*, XXII, 1993.

[32] P. Labrecque, D. Couture, and Y. Champoux. Experimental investigation of the vibroacoustic behavior of structures for validation purposes. *Applied Acoustics*, 46:197–210, 1995.

[33] B. Laulagnet. Sound radiation by a simply supported unbaffled plate. *Journal of the Acoustical Society of America*, 103(5):2451–2462, 1998.

[34] H. Nelisse, O. Beslin, and J. Nicolas. A generalized approach for the acoustic radiation from a baffled or unbaffled plate with arbitrary boundary conditions, immersed in a light or heavy fluid. *Journal of Sound and Vibration*, 211(2):207–225, 1998.

[35] O. Beslin and J. Nicolas. A hierarchical functions set for predicting very high order plate bending modes with any boundary conditions. *Journal of Sound and Vibration*, 202(5):633–655, 1997.

[36] C. H. Oppenheimer and S. Dubowsky. A radiation efficiency for unbaffled plates with experimental validation. *Journal of Sound and Vibration*, 199(3):473–489, 1997.

[37] F. J. Fahy and D. J. Thompson. The effect of perforation on the radiation efficiency of vibrating plates. *Proceedings of the Institute of Acoustics*, 26, 2004.

[38] C. S. Desai and J. F. Abei. *Introduction to the Finite Element Method*. Van Nostrand Reinhold, 1972.

[39] M. Petyt. *Finite Element Techniques for acoustics*, chapter 11 in Noise and Vibration (Ed. R. G. White and J. G. Walker). Ellis Horwood Ltd, 1982.

[40] S. M. Kirkup. *The Boundary Element Method in Acoustics*. Integrated Sound Software, 2007.

[41] M. Petyt and C. J. C. Jones. *Advanced Applications in Acoustics, Noise and Vibration*, chapter numerical methods in acoustics (Eds. F. J. Fahy and J. G. Walker). Spon Press, 2004.

[42] B. Nolte and L. Gaul. Sound energy flow in the acoustic near field of a vibrating plate. *Mechanical Systems and Signal Processing*, 10(3):351–364, 1996.

[43] P. O. Mattei. Sound energy by baffled and constrained plates. *Journal of Sound and Vibration*, 179(1):63–77, 1995.

[44] Z. G. Zhao, Q. B. Huang, and Z. He. Calculation of sound radiant efficiency and sound radiant modes of arbitrary shape structures by BEM and general eigenvalue decomposition. *Applied Acoustics*, doi:10.1016/j.apacoust.2007.04.003.

[45] R. J. Astley, G. J. Macaulay, J−P. Coyotte, and L. Cremers. Three-dimensional wave-envelope elements of variable order for acoustic radiation and scattering. Part I. Formulation in the frequency domain. *Journal of the Acoustical Society of America*, 1:49–63, 1998.

[46] R. J. Astley, J−P. Coyotte, and L. Cremers. Three-dimensional wave-envelope elements of variable order for acoustic radiation and scattering. Part II. Formulation in the time domain. *Journal of the Acoustical Society of America*, 1:64–72, 1998.

[47] P. Cordonnier-Cloarec, S. Pauzin, and D. Biron. Contribution to the study of sound transmission and radiation of corrugated steel structure. *Journal of Sound and Vibration*, 157(3):515–530, 1992.

[48] C. H. Hansen and D. A. Bies. Near field determination of the complex radiation efficiency and acoustic intensity distribution for a resonality vibrating surface. *Journal of Sound and Vibration*, 62(1):93–110, 1979.

[49] C. C. Sung and J. T. Jan. The response of and sound power radiated by a clamped rectangular plate. *Journal of Sound and Vibration*, 207(3):301–317, 1997.

[50] G. Xie, D. J. Thompson, and C. J. C. Jones. A modelling approach for the vibroacoustic behaviour of aluminium extrusions used in railway vehicles. *Journal of Sound and Vibration*, 293:921–932, 2006.

[51] D. J. Thompson, I. Back, and A. N. Thite. Measurement of sound radiation by a steel valve cover. Technical report, ISVR, University of Southampton, 2002.

[52] P. Ramachandran and S. Narayanan. Evaluation of modal density, radiation efficiency and acoustic response of longitudinally stiffened cylindrical shell. *Journal of Sound and Vibration*, pages 154–174, 2007.

[53] J. Zheng, F. J. Fahy, and D. Anderton. Application of vibro-acoustic reciprocity technique to the prediction of sound radiated by a motored I.C. engine. *Applied Acoustics*, 42:333–346, 1994.

[54] F. J. Fahy. The vibro-acoustic reciprocity principle and applications to noise control. *Acustica*, 81:544–558, 1995.

[55] N. Hashimoto. Measurement of sound radiation efficiency by the discrete calculation method. *Applied Acoustics*, 62:429–446, 2001.

[56] R. A. Pierri. Study of a dynamic absorber for reducing the vibration and noise radiation of plate-like structures. Master's thesis, Institute of Sound and Vibration Reseach, University of Southampton, 1977.

[57] D. Takahashi and M. Tanaka. Flexural vibration of perforated plates and porous elastic materials under acoustic loading. *Journal of the Acoustical Society of America*, 112(4):1456–1464, 2002.

[58] Y. Y. Lee, E. W. M. Lee, and C. F. Ng. Sound absorption of a finite flexible micro-perforated panel backed by an air cavity. *Journal of Sound and Vibration*, 287:227–243, 2005.

[59] M. Toyoda and D. Takahashi. Reduction of acoustic radiation by impedance control with a perforated absorber system. *Journal of Sound and Vibration*, 286:601–614, 2005.

[60] M. Toyoda, M. Tanaka, and D. Takahashi. Reduction of acoustic radiation by perforated board and honeycomb layer systems. *Applied Acoustics*, 68:71–85, 2007.

[61] D. Y. Maa. Microperforated panel wideband absorber. *Noise Control Engineering Journal*, pages 77–84, November-December 1987.

[62] *Noise Control: Principles and Practice*. Brüel & Kjær, 1986.

[63] M. H. A. Janssens and W. J. van Vliet. Noise from steel bridges: research into the effect of perforations of bridge components (in dutch). Technical report, TNO report TPD-HAG-RPT-960057, 1996.

[64] K. A. Burgemeister and C. H. Hansen. Calculating resonance frequencies of perforated panels. *Journal of Sound and Vibration*, 196(4):387–399, 1996.

[65] Forskitt, J. R. Moon, and P. A. Brook. Elastic properties of plates perforated by elliptical holes. *Applied Mathematical Modelling*, 15:182–190, 1991.

[66] S. D. Snyder and N. Tanaka. Calculating total acoustic power output using modal radiation efficiencies. *Journal of the Acoustical Society of America*, 97(3):1702–1709, 1995.

[67] W. L. Li and H. J. Gibeling. Determination of the mutual radiation resistances of a rectangular plate and their impact on the radiated sound power. *Journal of Sound and Vibration*, 229(5):1213–1233, 2000.

[68] A. J. Keane and W. G. Price. *Statistical Energy Analysis: An Overview, with Applications in Structural Dynamics*. Cambridge University Press, 1997.

[69] E. W. Weisstein. Fast fourier transform. From MathWorld−−A Wolfram Web Resource. http://mathworld.wolfram.com/FastFourierTransform.html.

[70] L. L. Beranek. *Noise and Vibration Control*. McGraw-Hill, 1971.

[71] F. J. Fahy. *Foundation of Engineering Acoustics*. Elsevier Academic Press, 2005.

[72] M. C. M. Wright. *Mathematics of Acoustics*. Imperial College Press, 2005.

[73] A. D. Pierce. *Acoustics*. Acoustical Society of America, 1989.

[74] I. B. Crandall. *Theory of Vibration System and Sound*. Van Nostrand, New York, 1926.

[75] P. M. Morse and U. Ingard. *Theoretical Acoustics*. McGraw-Hill, New York, 1968.

[76] N. Atalla and F. Sgard. Modelling of perforated plates and screens using rigid frame porous models. *Journal of Sound and Vibration*, 303:195–208, 2007.

[77] D. Y. Maa. Potential of microperforated panel absorber. *Journal of the Acoustical Society of America*, 104(4):2861–2866, 1998.

[78] L. V. King. On the electrical and acoustic conductivities of cylindrical tubes bounded by infinite flanges. *Philosophical Magazine*, 21(7):128–144, 1936.

[79] J. F. Allard. *Propagation of Sound in Porous Media*. Elsevier, London, 1993.

[80] C. L. Morfey. *Dictionary of Acoustics*. Academic Press, 2001.

[81] F. P. Mechel and I. L. Vér. *Sound-absorbing Materials and Sound Absorbers*, chapter 8 in Noise and Vibration Control Engineering: Principles and Applications (Eds. L. L. Beranek and I. L. Vér). John Wiley and Sons, Inc., 1992.

[82] L. E. Kinsler, A. R. Frey, A. B. Coppens, and J. V. Sanders. *Fundamentals of Acoustics*. John Wiley and Sons, 3rd edition, 1982.

[83] R. Bailey and R. Hicks. Behavior of perforated plates under plane stress. *Journal of Mechanical Engineering Science*, 2:143–161, 1960.

[84] W. J. O'Donnel and B. F. Langer. Design of perforated plates. *Journal of Engineering for Industry*, 84:307–320, 1962.

[85] J. P. Duncan and R. W. Uphold. Equivalent elastic of perforated bars and plates. *Journal of Mechanical Engineering Science*, 5:53–65, 1963.

[86] D. C. Patil, Gawade. S. S, and Mali. K. D. Dynamic response analysis of rectangular perforated plates with varying sizes of circular perforation holes. *In. Proc. ICSV 14 Cairns Australia*, 9-12 July 2007.

[87] A. I. Soler and W. S. Hill. Effective bending properties for stress analysis of rectangular tubesheets. *Journal of Engineering for Power*, 2:143–161, 1960.

[88] L. Robertson. Determination of the radiation efficiency of perforated plates. Technical report, ISVR BEng Project Dissertation, University of Southampton, 2003.

[89] P. Gardonio and M. J. Brennan. *Moblity and Impedance Methods in Structural Dynamics*, chapter 9 in Advanced Applications in Acoustics, Noise and Vibration (Eds. F. J. Fahy and J. G. Walker). Spon Press, 2004.

[90] J. B. Ochs and J. C. Snowdown. Transmissibility across simply supported thin plates. I. rectangular and square plates with and without damping layers. *Journal of the Acoustical Society of America*, 58:832–840, 1975.

[91] O. Lacour, M. A. Galland, and D. Thenail. Preliminary experiments on noise reduction in cavities using active impedance changes. *Journal of Sound and Vibration*, 230:69–99, 2000.

[92] J. P. Maillard and C. R. Fuller. Advanced time domain wave-number sensing for structural acoustic systems. Part III. Experiments on active broadband radiation

control of a simply supported plate. *Journal of the Acoustical Society of America*, 98(5):2613–2621, 1995.

[93] L. M. Lyamshev. A method for solving the problem of sound radiation by thin elastic shells and plates. *Soviet Physics Acoustics*, 5:122–124, 1959.

[94] A. C. Geerlings, D. J. Thompson, and J. W. Verheij. Model-based acoustic substitution source methods for assesing shielding measures applied trains. *Applied Acoustics*, 62:979–1000, 2001.

[95] M. R. Schroeder. The schroeder frequency revisited. *Journal of the Acoustical Society of America*, 99:3240–3241, 1996.

[96] ANSI S1-1972. *Methods for Determination of Sound Power Level of Small Sources in Reverberation Rooms*. Acoustical Society of America, Standards Secretariat, New York, 1972.

# Appendix A

# Sound Radiation by a Uniformly Vibrating Perforated Strip

Fahy and Thompson [37] developed a model of radiation of a uniformly vibrating perforated strip set in an infinite baffle which may have a different impedance from the plate (i.e. different perforation). For a strip set in a rigid infinite baffle, the specific acoustic impedance associated with the baffle $z_{h2}$ is set to be very large compared with that associated with the perforation of the plate $z_{h1}$ ($|z_{h1}/z_{h2}| \rightarrow 0$). Conversely for an unbaffled perforated strip, the specific acoustic impedance $z_{h2}$ should be very low ($|z_{h1}/z_{h2}| \rightarrow \infty$). The complete mathematical derivation of the method can be found in reference [37].

Figure A.1 presents the radiation efficiency of a perforated strip with width $L$ plotted against the non-dimensional parameter $kL$. Results are given for the case of a perforated strip set in a similarly perforated baffle ($z_{h2} = z_{h1}$) and in a rigid baffle. For the rigid baffle, the results are proportional to $kL$ at low $kL$, i.e. they have a frequency dependence of 10 dB/decade. The perforation of the baffle drastically changes the frequency dependence of the radiation efficiency to 30 dB/decade. The results are proportional to $(kL)^3$ and the radiation efficiency for the perforated baffled is lower than that for the rigid baffle.

As mentioned in the Chapter 1, for an unbaffled strip, it is found that the matrix to be inverted is singular or nearly singular, which affects the quality of the solution. Figure A.2 shows the radiation efficiency of the unbaffled perforated strip compared

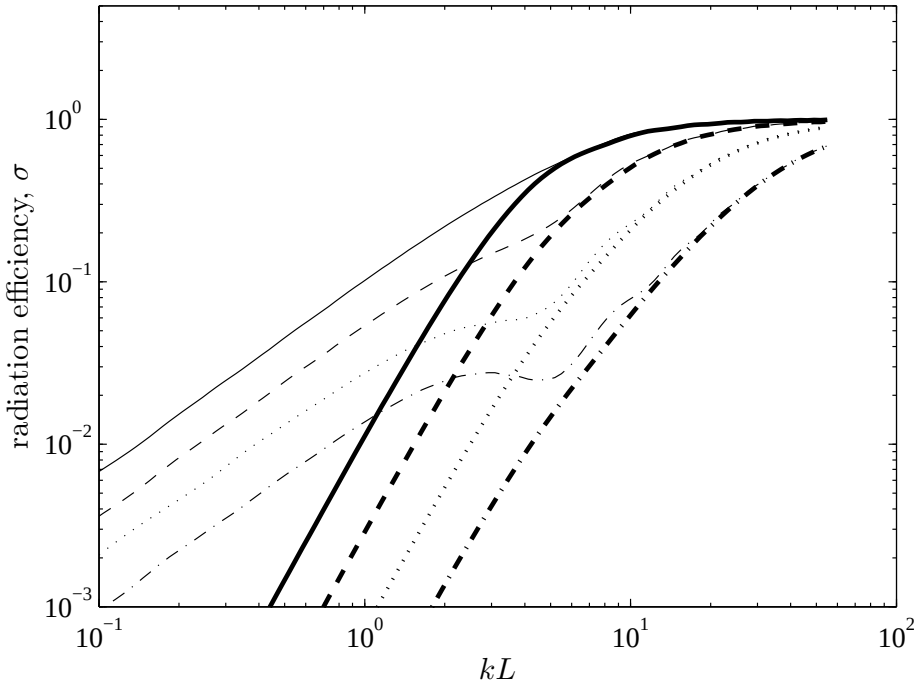


FIGURE A.1: Radiation efficiency of a strip-piston in a perforated baffle (thick line) and in a rigid baffle (thin line): $-$$h/kL = 0.44$, $--h/kL = 0.22$, $\cdots h/kL = 0.11$, $-\cdot-h/kL = 0.055$.

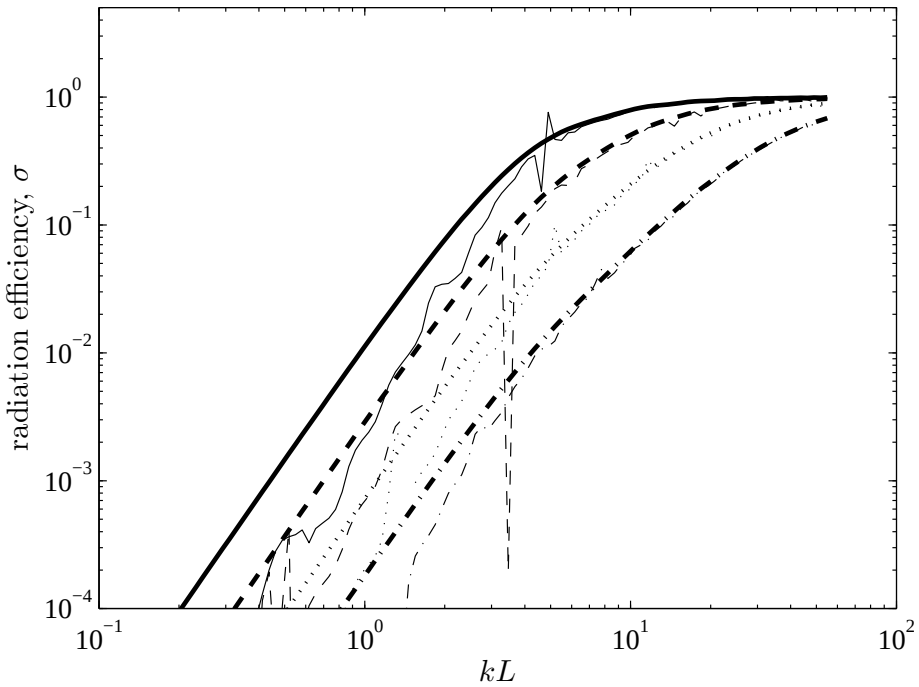


FIGURE A.2: Radiation efficiency of a strip-piston in a perforated baffle (thick line) and in a low impedance baffle ($z_{h1} = 0.1 z_{h2}$, thin line): $-$$h/kL = 0.44$, $--h/kL = 0.22$, $\cdots h/kL = 0.11$, $-\cdot-h/kL = 0.055$.

with that of the perforated strip set in the rigid perforated baffle. The results for the unbaffled perforated strip are expected to be lower than those for the perforated baffle but have the same frequency dependence at low $kL$. As seen in the figure, the inverted near-singular matrix gives poor quality results.

In both Figure A.1 and Figure A.2 results are presented for different $h/kL$ where $h$ is the non-dimensional specific acoustic impedance as defined in Section 5.1.4. The strip itself has implicitly an infinite length. Consequently, an arbitrary number of holes can be introduced even though they are limited in the strip width direction.

# Appendix B

# Mobility of a Simply Supported Rectangular Plate

For a rectangular plate having dimensions $a \times b \times t_p$, its mobility $Y$ for each frequency $\omega$ is defined by

$$Y(\omega) = j\omega \sum_{m=1}^{\infty} \sum_{m=1}^{\infty} \frac{\psi_{mn}(x_2, y_2)\psi_{mn}(x_1, y_1)}{M_{mn}\left[\omega_{mn}^2(1 + j\eta) - \omega^2\right]} \tag{B.1}$$

where $M_{mn}$ is the modal mass, $\eta$ is the damping loss factor, $(x_1, y_1)$ and $(x_2, y_2)$ are the excitation point and response point co-ordinates respectively.

The $(m, n)$ natural frequency $\omega_{mn}$ is given by [89]

$$\omega_{mn} = \sqrt{\frac{Et_p^2}{12\rho_p(1 - \nu^2)}} \left(\frac{\pi}{a}\right)^2 q_{mn} \tag{B.2}$$

where $E$ is the Young's modulus, $\nu$ is the Poisson's ratio, $\rho_p$ is the plate density and

$$q_{mn} = \sqrt{G_x^4(m) + G_y^4(n) \left(\frac{a}{b}\right)^4 + 2 \left(\frac{a}{b}\right)^2 \left[\nu H_x(m) H_y(n) + (1 - \nu) J_x(m) J_y(n)\right]}$$

For a simply supported boundary condition, $G_x = m, G_y = n$ and $H_x = J_x = m^2, H_y = J_y = n^2$, which gives

$$q_{mn} = \frac{1}{b^2}\left[(mb)^2 + (na)^2\right]$$

The mode shape function $\psi_{mn}(x, y)$ can be approximated as the product of the characteristic beam function $\phi_m(x)$ and $\phi_n(y)$ that gives

$$\psi_{mn}(x, y) = \phi_m(x)\phi_n(y) \tag{B.3}$$

The mode shape function of a simply supported beam for mode $m$ is written as

$$\phi_m = \sin\left(\frac{m\pi x}{a}\right) \tag{B.4}$$

in which case the mode shape $\psi_{mn}(x, y)$ is exact.

The modal mass is defined as

$$M_{mn} = \int_S \rho_p t_p \psi_{mn}(x, y) dx dy \tag{B.5}$$

For simply supported edges, the modal mass $M_{mn}$ is given by

$$M_{mn} = \frac{1}{4}\rho_p abt_p \tag{B.6}$$

# Appendix C

# Fourier transform of mode shape functions

For a simply supported plate with dimensions $a \times b$ lying in the $xy$ plane, the mode shape function $\varphi_{mn}$ is given by

$$\varphi_{mn}(x, y) = \sin\left(\frac{m\pi x}{a}\right) \sin\left(\frac{n\pi y}{b}\right) \tag{C.1}$$

The Fourier transform of $\varphi_{mn}$ in the wavenumber domain is given by

$$\widetilde{\varphi}_{mn}(k_x, k_y) = \int_0^a \int_0^b \varphi_{mn} e^{-j(k_x x + k_y y)}\, dx\, dy \tag{C.2}$$

Substituting Eq.(C.2)

$$\widetilde{\varphi}_{mn}(k_x, k_y) = \underbrace{\int_0^a \sin\left(\frac{m\pi x}{a}\right) e^{-jk_x x}\, dx}_{X} \overbrace{\int_0^b \sin\left(\frac{n\pi y}{b}\right) \varphi_{mn} e^{-jk_y y}\, dy}^{Y} \tag{C.3}$$

For convenience, only the first part (for $x$ direction) is derived. The technique is similar for the $y$ direction.

$$X = \int_0^a \sin\left(\frac{m\pi x}{a}\right) e^{-jk_x x}\, dx \tag{C.4}$$

Integrating by parts, $X$ can be written as

$$X = \int_0^a u \frac{dv}{dx} dx = uv - \int_0^a v \frac{du}{dx}\, dx \tag{C.5}$$

where from Eq.(C.5) the integrand is defined as

$$\begin{aligned} u &= \sin\left(\frac{m\pi x}{a}\right) \\ \frac{du}{dx} &= \frac{m\pi}{a}\cos\left(\frac{m\pi x}{a}\right) \\ \frac{dv}{dx} &= e^{-jk_x x} \\ v &= -\frac{1}{jk_x} e^{-jk_x x} \end{aligned} \tag{C.6}$$

This gives

$$X = -\frac{1}{jk_x}\sin\left(\frac{m\pi x}{a}\right) e^{-jk_x x} + \frac{m\pi}{jk_x a} \underbrace{\int_0^a \cos\left(\frac{m\pi x}{a}\right) e^{-jk_x x}\, dx}_{Z} \tag{C.7}$$

Solving the integral $Z$ using Eq.(C.5), the integrand is

$$\begin{aligned} u &= \cos\left(\frac{m\pi x}{a}\right) \\ \frac{du}{dx} &= -\frac{m\pi}{a}\sin\left(\frac{m\pi x}{a}\right) \\ \frac{dv}{dx} &= e^{-jk_x x} \\ v &= -\frac{1}{jk_x} e^{-jk_x x} \end{aligned} \tag{C.8}$$

Eq.(C.7) is now written as

$$\begin{aligned} X = & -\frac{1}{jk_x}\sin\left(\frac{m\pi x}{a}\right)e^{-jk_x x}+ \\ & +\frac{m\pi}{jk_x a}\left[-\frac{1}{jk_x}\cos\left(\frac{m\pi x}{a}\right)e^{-jk_x x}-\frac{m\pi}{jk_x a}\int_0^a \sin\left(\frac{m\pi x}{a}\right)e^{-jk_x x}\,dx\right] \\ = & -\frac{1}{jk_x}\sin\left(\frac{m\pi x}{a}\right)e^{-jk_x x}+\left(\frac{m\pi}{k_x^2 a}\right)\cos\left(\frac{m\pi x}{a}\right)e^{-jk_x x}+ \\ & +\left(\frac{m\pi}{k_x a}\right)^2\int_0^a \sin\left(\frac{m\pi x}{a}\right)e^{-jk_x x}\,dx \end{aligned} \tag{C.9}$$

Rearranging Eq.(C.9) yields

$$\begin{aligned} \left[1-\left(\frac{m\pi}{k_x a}\right)^2\right]\int_0^a \sin\left(\frac{m\pi x}{a}\right)e^{-jk_x x}\,dx = & \\ = -\frac{1}{jk_x}\sin\left(\frac{m\pi x}{a}\right)e^{-jk_x x}+\left(\frac{m\pi}{k_x^2 a}\right)\cos\left(\frac{m\pi x}{a}\right)e^{-jk_x x}\Big|_0^a & \\ = \left(-\frac{1}{jk_x}\sin(m\pi)\,e^{-jk_x a}+\left(\frac{m\pi}{k_x^2 a}\right)\cos(m\pi)\,e^{-jk_x a}\right)+\left(0+\frac{m\pi}{k_x^2 a}\right) & \end{aligned} \tag{C.10}$$

For $m = 0, 1, 2, ...$; $\sin(m\pi) = 0$ and $\cos(m\pi) = (-1)^m$. Hence Eq.(C.10) yields

$$\left[1-\left(\frac{m\pi}{k_x a}\right)^2\right]\int_0^a \sin\left(\frac{m\pi x}{a}\right)e^{-jk_x x}\,dx = \frac{m\pi}{k_x^2 a}\left[(-1)^m e^{-jk_x a}-1\right] \tag{C.11}$$

Therefore

$$\int_0^a \sin\left(\frac{m\pi x}{a}\right)e^{-jk_x x}\,dx = \frac{\frac{m\pi}{k_x^2 a}\left[(-1)^m e^{-jk_x a}-1\right]}{\left[1-\left(\frac{m\pi}{k_x a}\right)^2\right]} \tag{C.12}$$

Multiplying both the numerator and denominator on the right side of Eq.(C.12), by $\left(\frac{k_x a}{m\pi}\right)^2$ gives

$$\int_0^a \sin\left(\frac{m\pi x}{a}\right)e^{-jk_x x}\,dx = \frac{\frac{a}{m\pi}\left[(-1)^m e^{-jk_x a}-1\right]}{\left[\left(\frac{k_x a}{m\pi}\right)^2-1\right]} \tag{C.13}$$

By including the Fourier transform of the sinusoidal wave function for the $y$-direction (Y in Eq.(C.3)), the Fourier transform of the mode shape function for the simply supported plate can be expressed as

$$\widetilde{\varphi}_{mn}(k_x, k_y) = \frac{\dfrac{ab}{mn\pi^2}\left[(-1)^m e^{-jk_x a} - 1\right]\left[(-1)^n e^{-jk_y b} - 1\right]}{\left[\left(\dfrac{k_x a}{m\pi}\right)^2 - 1\right]\left[\left(\dfrac{k_y b}{n\pi}\right)^2 - 1\right]} \tag{C.14}$$

In terms of non-dimensional wavenumber ($\alpha$, $\beta$) where $\alpha = k_x/k$ and $\beta = k_y/k$ and by expanding the exponential component where $e^{\pm jz} = \cos z \pm j \sin z$ gives

$$\widetilde{\varphi}_{mn}(k_x, k_y) = \frac{k^{-2}\left(\dfrac{m\pi}{ka}\right)\left(\dfrac{n\pi}{kb}\right)(\varepsilon + j\vartheta)(\gamma + j\varsigma)}{\left[\alpha^2 - \left(\dfrac{m\pi}{ka}\right)^2\right]\left[\beta^2 - \left(\dfrac{n\pi}{kb}\right)^2\right]} \tag{C.15}$$

where

$$\varepsilon = (-1)^m \cos(\alpha ka) - 1,\ \vartheta = (-1)^{m+1} \sin(\alpha ka)$$

$$\gamma = (-1)^n \cos(\beta kb) - 1,\ \varsigma = (-1)^{n+1} \sin(\beta kb)$$

A similar procedure can be applied to the Fourier transform of the cosine functions for the guided-guided boundary conditions.